Constraining the early evolution of Earth's photosynthetic pathways : an isotopic approach

Laureline Patry

DOCTORAT SCIENCES BRETAGNE DE LA MER LOIRE ET DU LITTORAL

UBO
Université de Bretagne Occidentale

THESE DE DOCTORAT DE

L'UNIVERSITE
DE BRETAGNE OCCIDENTALE

ECOLE DOCTORALE N° 598
Sciences de la Mer et du littoral
Spécialité : Géosciences Marines

Par
Laureline PATRY

Contraindre l'évolution précoce des voies photosynthétiques de la Terre
Une approche isotopique

Thèse présentée et soutenue à Plouzané, le 8 décembre 2022
Unité de recherche : UMR 6538 GEO-OCEAN

Rapporteurs avant soutenance :

Catherine CHAUVEL — IPGP / DR CNRS
Pascal PHILIPPOT — Université de Montpellier / DR CNRS

Composition du Jury :

Présidente du Jury
Magali ADER — IPGP / Professeure des universités

Catherine CHAUVEL — IPGP / DR CNRS
Pascal PHILIPPOT — Université de Montpellier / DR CNRS
Bleuenn GUEGUEN — UBO / Ingénieure de recherche

Directeur de thèse HDR
Christophe HEMOND — UBO / Professeur des universités

Encadrant de thèse
Pierre BONNAND — UBO / Maître de Conférence

Constraining the Early Evolution of Earth's Photosynthetic Pathways:

An Isotopic Approach

Laureline A. Patry

Abstract

The origin of oxygenic photosynthesis is one of the most dramatic evolutionary events that the Earth has ever experienced. During the Great Oxidation Event (GOE) ca. 2.5 to 2.3 billion years ago (Ga), O_2 accumulated permanently in the atmosphere, forever changing the chemistry of the Earth's surface and marine environments. Earth's modern biosphere owes its existence to this planet-defining metabolism, and understanding its origin is a primary challenge for Earth system science. However, due to uncertainties in the primary nature of geochemical signals of oxygen in ancient and altered rocks, exactly when oxygenic photosynthesis evolved on Earth remains highly debated. This PhD work focused on novel geochemical and isotopic signatures preserved in chemical sedimentary rocks and other marine sediments from the Canadian Superior Craton, deposited between 2.93 and 2.8 Ga, to better understand the evolution of photosynthetic pathways on the early Earth. Iron isotope chemostratigraphy of stromatolitic carbonates and deep-water sediments preserved in drill core from the 2.93 Ga Red Lake Greenstone Belt reveals complex iron redox cycling across a shallow-to-deep transect, with coupling between Fe and S cycling that is best explained by offshore photosynthetic activity. Comparative REE systematics of three Mesoarchean carbonate platforms of the Superior Craton, preserved on three different Greenstone Belts (2.93 Ga Red Lake, 2.86 Ga Woman Lake, and 2.80 Ga Steep Rock Lake) and representing Earth's earliest known large carbonate platforms, provide clear evidence for estuarine processes, hydrothermal inputs, and crucially, for the production of free oxygen, as tracked by important negative Ce anomalies of unprecedented magnitude for the Archean. High-precision La-Ce geochronology was successfully applied to samples from all three sites, yielding three clear isochrons that constrain the timing of La/Ce fractionation, and thus Ce oxidation, to the time of deposition. These results constitute the first geochronological constraint on the origin of oxygenic photosynthesis and place it firmly within the Mesoarchean, with important implications for our current understanding of Earth's biological and geochemical evolution.

Résumé

L'origine de la photosynthèse oxygénique est l'un des événements évolutifs les plus dramatiques que la Terre n'ait jamais connus. Au cours du Grand événement d'oxydation (GOE), il y a environ 2,5 à 2,3 milliards d'années (Ga), l'O_2 s'est accumulé de façon permanente dans l'atmosphère, modifiant à jamais la chimie de la surface de la Terre et des environnements marins. La biosphère moderne de la Terre doit son existence à ce métabolisme, et la compréhension de son origine est un défi majeur pour les Sciences de Terre. Cependant, en raison des incertitudes quant à la nature primaire des signaux géochimiques de l'oxygène dans les roches anciennes et altérées, la chronologie de l'évolution de la photosynthèse oxygénique sur Terre reste très débattue. Ce travail de thèse s'est concentré sur de nouvelles signatures géochimiques et isotopiques préservées dans des roches sédimentaires chimiques et d'autres sédiments marins du Craton Supérieur canadien, déposés entre 2,93 et 2,8 Ga, afin de mieux comprendre l'évolution des voies photosynthétiques sur la Terre primitive. La chimiostratigraphie isotopique du fer des carbonates stromatolithiques et des sédiments d'eaux profondes préservés dans une carotte de la ceinture de schistes verts de Red Lake (2,93 Ga) révèle un cycle complexe d'oxydoréduction du fer sur un transect de faible profondeur à grande profondeur, avec un couplage entre le cycle du fer et du soufre qui est mieux expliqué par l'activité photosynthétique marine. La systématique comparative des REE de trois plateformes carbonatées Mésoarchéennes du Craton Supérieur, préservées sur trois ceintures de schistes verts différents (2,93 Ga Red Lake, 2,86 Ga Woman Lake et 2,80 Ga Steep Rock Lake) et représentant les plus anciennes plateformes carbonatées épaisses connues sur Terre, fournit des preuves de processus estuariens, d'apports hydrothermaux et, surtout, de la production d'oxygène libre, comme le montrent d'importantes anomalies négatives en Ce d'une ampleur sans précédent pour l'Archéen. La géochronologie La-Ce de haute précision a été appliquée avec succès aux échantillons des trois sites, produisant trois isochrones claires qui datent le fractionnement La/Ce, et donc l'oxydation du Ce, au moment du dépôt. Ces résultats constituent la première contrainte géochronologique sur l'origine de la photosynthèse oxygénique et la placent fermement dans le Mésoarchéen, avec des implications importantes pour notre compréhension de l'évolution biologique et géochimique de la Terre.

Acknowledgments

First of all, I would like to thank my PhD supervisor Pierre Bonnand for his unwavering support. Although this thesis has turned out differently than either of us expected when I started, I am sincerely grateful for all of his help and support until the end. Thanks also to Christophe Hemond and Marc-Andre Gutscher for their support and for having accepted to be my PhD directors at different stages of this thesis.

Many thanks to Stefan Lalonde for allowing me to be part of his ERC EARTHBLOOM project and for all of the scientific collaborations. Thanks also to all the people involved in the project who also supported me through this thesis, particularly Pierre Sans Jofre, Martin Homann, Dylan Wilmeth, Munira Afroz, and Brittany Ramsay.

I would also like to thank Maud Boyet for her warm welcome to the Laboratoire Magmas et Volcans in Clermont-Ferrand. Thanks also to Delphine Auclair for her welcome and all the funny discussions.

Many thanks to all the people of the Pôle Spectrométrie Océan, Bleuenn Guéguen, Marie-Laure Rouget, Céline Liorzou, and especially Philippe Nonotte for his support from the beginning to the end of my PhD.

I would like to thank all my various office mates and friends, Malcolm Hodgskiss, Charlotte Guérin, Munira Afroz, Peggy Rimmelin-Maury, Edgar Lenhof, and Jérémy Devesa, who made my time in the office so much more enjoyable.

Thanks so much to my family and to all my friends, Alice Pesty, Aurore Verdier, Lauriane Cannamela, Michael Allouche, Camille Rubio, and Yoann Lallaizon, for being part of my life and motivating me to be the best version of myself.

Finally, I am most appreciative to my partner for his unconditional support, love, and encouragement through the numerous highs and lows of the past three years.

Table of Contents

List of Figures

Chapter 1 : Introduction

Chapter 2 : Geological context

Chapter 3 : Material and methods

Chapter 4 : Iron Isotope Systematics of Earth's Earliest Thick Carbonate Platform

Chapter 5 : Comparative Rare Earth Element Systematics from Three Mesoarchean carbonate platform

Chapter 6 : Archean origins of oxygenic photosynthesis confirmed by La-Ce geochronology

Appendices

List of Tables

Chapter 3 : Material and methods

Appendices

CHAPTER 1:

INTRODUCTION

This doctoral thesis presents new research at the intersection of the geological, biological, and isotope geochemical sciences, with the overarching goal of better understanding of biogeochemical cycling and the evolution of Earth's earliest photosynthetic communities. Accordingly, in this chapter, the geological, biogeochemical, and isotope geochemical context of this thesis work is introduced to the reader via a synthesis of current knowledge and the literature works supporting the current state of the art. In the final section of this chapter, the original goals of the thesis work are summarized, and the organization of the individual chapters are presented.

1.1 The Precambrian Earth

1.1.1 Evolution of Earth's different envelopes

Since its formation, the Earth has never ceased to evolve, and these changes have contributed to define the different periods of what is now known as the "Geological Time Scale". This geological time scale is divided into 4 main Eons: Hadean, Archean, Proterozoic and Phanerozoic (Fig. 1.1). The first three eons together form the Precambrian.

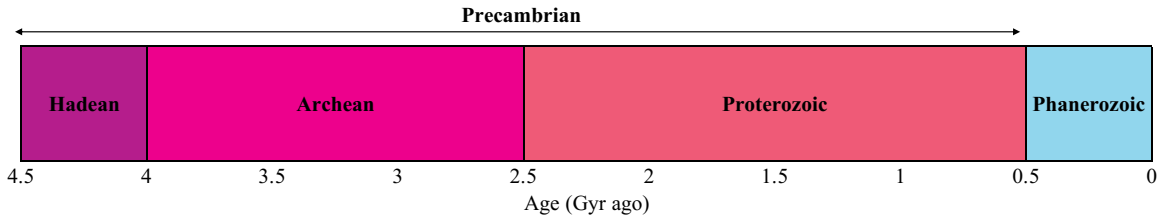

Figure 1.1. Geological time scale representing the four Eons: Hadean, Archean, Proterozoic and Phanerozoic through time.

The Hadean Eon, named by geologist Preston Cloud in 1976 (Harland et al., 1989) after the Greek god Hades, is the oldest eon encompassing Earth's first 550 million years. This Eon is characterized by Earth's initial accretion, the stabilization of its core and crust,

and the development of its atmosphere and oceans. The Archean Eon, which lasted from 4 to 2.5 billion years ago, was named after the Greek word for “pertaining to the beginning” by American geologist James Dwight Dana in 1872. With Earth’s crust having cooled enough to form the first continents, the Archean represents the beginning of the rock record and the earliest known form of life. The Proterozoic Eon extended from 2.5 billion to 541 million years ago and is mostly characterized by the formation and breakup of supercontinents, compelling changes of the ocean’s composition, and the accumulation of oxygen in Earth’s atmosphere significantly increasing the biological activity. The Phanerozoic Eon, covering from 541 million years ago to the present, is the current geological eon and the one where Earth has experiences abundant animal and plant life, minus the relatively short periods of extinctions.

1.1.1.1 Lithosphere

The lithosphere is the rigid outer layer of Earth divided into two parts (the crust and the upper mantle), its formation and evolution depend on the thermal energy of the planet's interior and is modulated by solar radiation. The lithosphere is the long-term archive of the Earth's history, recording the interactions with the underlying asthenospheric mantle and the overlying hydrosphere and atmosphere. Stable and billion years old remnants of continental lithosphere called “Cratons” (Fig. 1.2) that survived cycles of merging and rifting of continents are essential tools in understanding the early history of Earth.

The oldest known terrestrial rocks are the Acasta gneisses located in the Slave Craton, Northern Canada with components dated at ~4.02 Ga (Bowring and Williams, 1999). Nevertheless, the oldest terrestrial zircons from the 3.3 Ga Jack Hills formation, Yilgarn Craton, Western Australia indicate the presence of felsic magmas and surface water

from ~4.4 Ga (Wilde et al., 2001; Valley et al., 2002; Cavosie et al., 2007). But there is considerable controversy about the setting in which these Hadean zircons were generated and so their significance for continental crustal growth (Harrison, 2009; Kemp et al., 2010).

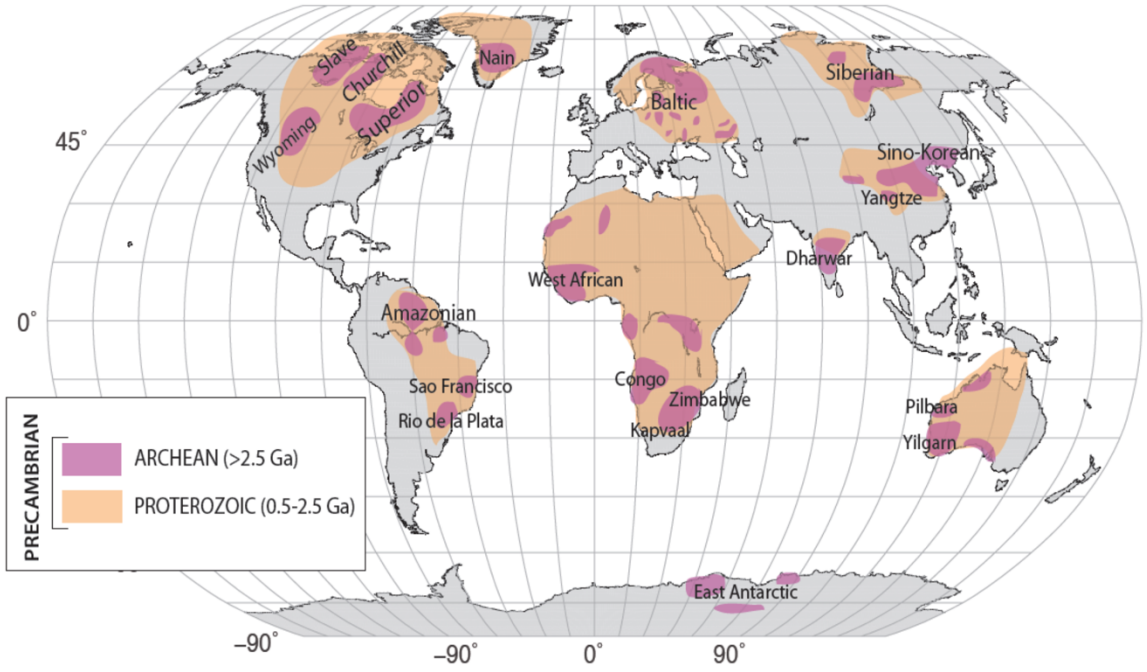

Figure 1.2. Distribution of Archean cratons and Proterozoic continental crust in the world (Petrescu, 2017).

Records of Archean oceanic crusts called "Greenstone Belt", because of the green minerals (chlorites) produced by the low-grade metamorphism (Condie, 1981), are mainly composed of volcanic (basalt, gabbro, serpentinite, and komatiite) and sedimentary rocks (Banded iron formation, chert, carbonate, black shales and sandstone). With a warmer mantle reflected by the abundance of komatiites (Jaupart et al., 2007; Coltice et al., 2009) and partial melting rates about twice as high as today, the Archean oceanic crusts were thicker and much less dense (Smithies et al., 2003). This led to rock instability and a vertical tectonic phenomenon named “Sagduction” (Goodwin and Smith, 1980), when the gravitational sinking of superficial greenstone cover sequences generates concomitant

exhumation of the deeper granitic crust into large domes (François et al., 2014). Thicker oceanic crust and presence of sagduction do not mean that there was no subduction during the Archean. In fact, the granitic-gneissic or TTG (Tonalite, Trondhjemite, and Granodiorite) basement record of Archean continental crust reinforces the idea of the presence of subduction during the Archean. Indeed, the TTG which groups metamorphic plutonic rocks of tonalitic to granitic composition (Martin et al., 1983), that are poor in alkali feldspar but rich in quartz and plagioclase, seem to be mostly able to form in context of subduction (van Hunen and Moyen, 2012; Roman and Arndt, 2020). Although Archean tectonics is still a hotly debated topic, it is widely believed that plate tectonics appearance was around 3 Ga (van Kranendonk, 2011; Tang et al., 2016; Condie, 2018; Cawood et al., 2018). However, a recent study by Windley et al. (2021), proposes that plate tectonics was operating since the Eoarchean (i.e., 4 Ga ago), in the form of Accretionary Cycle Plate Tectonics and that around 2.7-2.5 Ga plate tectonics started to appear in a form of the Wilson Cycle as we know today (Fig. 1.3).

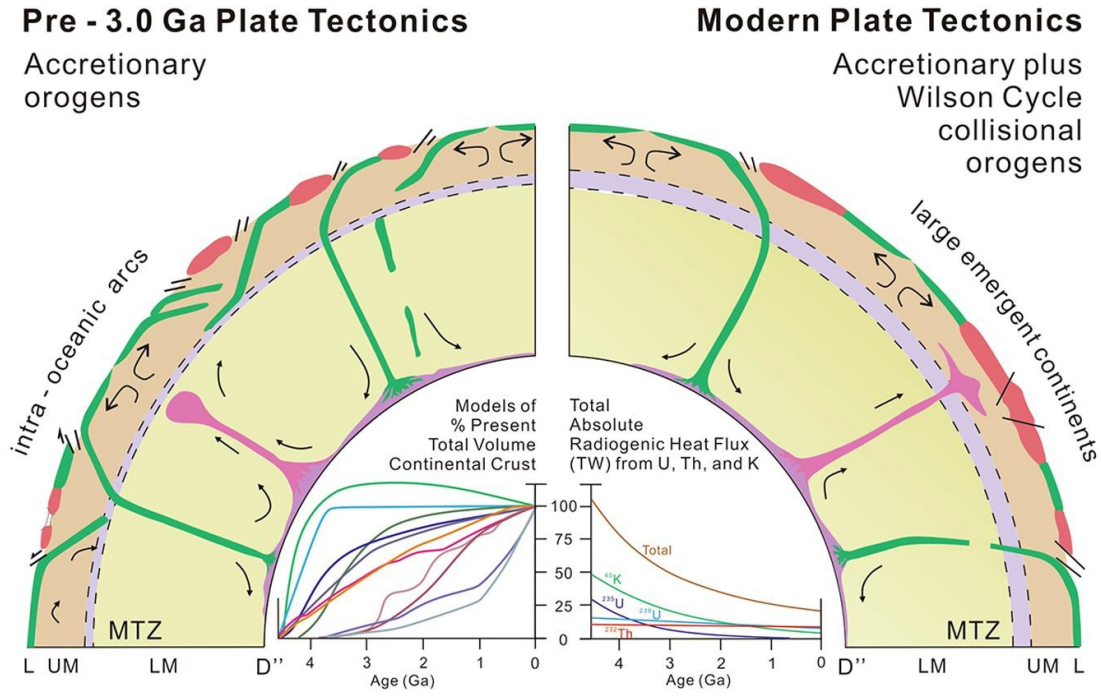

Figure 1.3. Schematic diagram illustrating the two types of plate tectonics in Earth's history proposed by Windley et al. (2021): the Accretionary cycle plate tectonics before 3 Ga and the "Modern" Wilson cycle plate tectonics after 2.7 Ga.

The evolution of the lithosphere during the history of the Earth is complex, nevertheless 5 main steps determined by Hawkesworth et al. (2016) can be retained: The first stage corresponds to the initial accretion and differentiation of the core/mantle system, and the development of an ocean of magma within the first 5-10 million years (Kamber, 2015). The second stage refers to the period before 3.0 Ga when crust started to be formed for the first time in a pre-plate tectonic regime (as it is widely thought) or in an accretionary cycle plate tectonics (as proposed by Windley et al., 2021, see above). The third stage began ca. 3.0 Ga when Archean cratons stabilized, crustal growth rates changed thickening the continental crust and is characterized by early plate tectonics involving collisional orogenies, development of supercontinent cycles and hot subduction with shallow slab breakoff until 1.7 Ga (Sizova et al., 2014). The fourth stage, extending from 1.7 to 0.75 Ga, referred to as the "boring billion" (Holland, 2006) and more recently as "Earth middle age" (Cawood and Hawkesworth, 2014) has been a period of great stability and is particularly marked by the absence of preserved passive margins, of orogenic gold and volcanic-hosted massive sulfide deposits, of glacial deposits and iron formations, and by the absence of significant anomalies in the paleoseawater Sr isotope record and in Hf isotopes in detrital zircon (Cawood and Hawkesworth, 2015). The last and fifth stage started with the supercontinent Rodinia breakup around 0.75 Ga and corresponds to the development of the modern cold subduction that has likely been controlled by changes in mantle temperature enabling the development of high- to ultrahigh-pressure metamorphic rocks (Brown, 2006). This last stage, marked by a strongly episodic age distribution related to the cycles of the Gondwanaland and Pangea supercontinents, also witnessed the increase of oxygen levels in the deep oceans and in the atmosphere.

1.1.1.2 Atmosphere

The Earth's primitive atmosphere was the product of late-accretionary and internal heat-driven processes acting on late-accreting material that mixed with the outer hot parts (early mantle) of Earth (Shaw, 2008). It is widely assumed that this primitive degassed atmosphere was dominated by CO_2 and N_2 (Fig. 1.4), however the possibility of a more reduced early phase and an early surface environment dominated by reduced carbon compounds cannot be ruled out, as the precise conditions of the initial degassing remain open to supposition (Holland, 1984). There is a wide consensus that fifty percent or more of Earth's surface volatiles may have been degassed from the early mantle by about 4 Ga (Shaw, 2008).

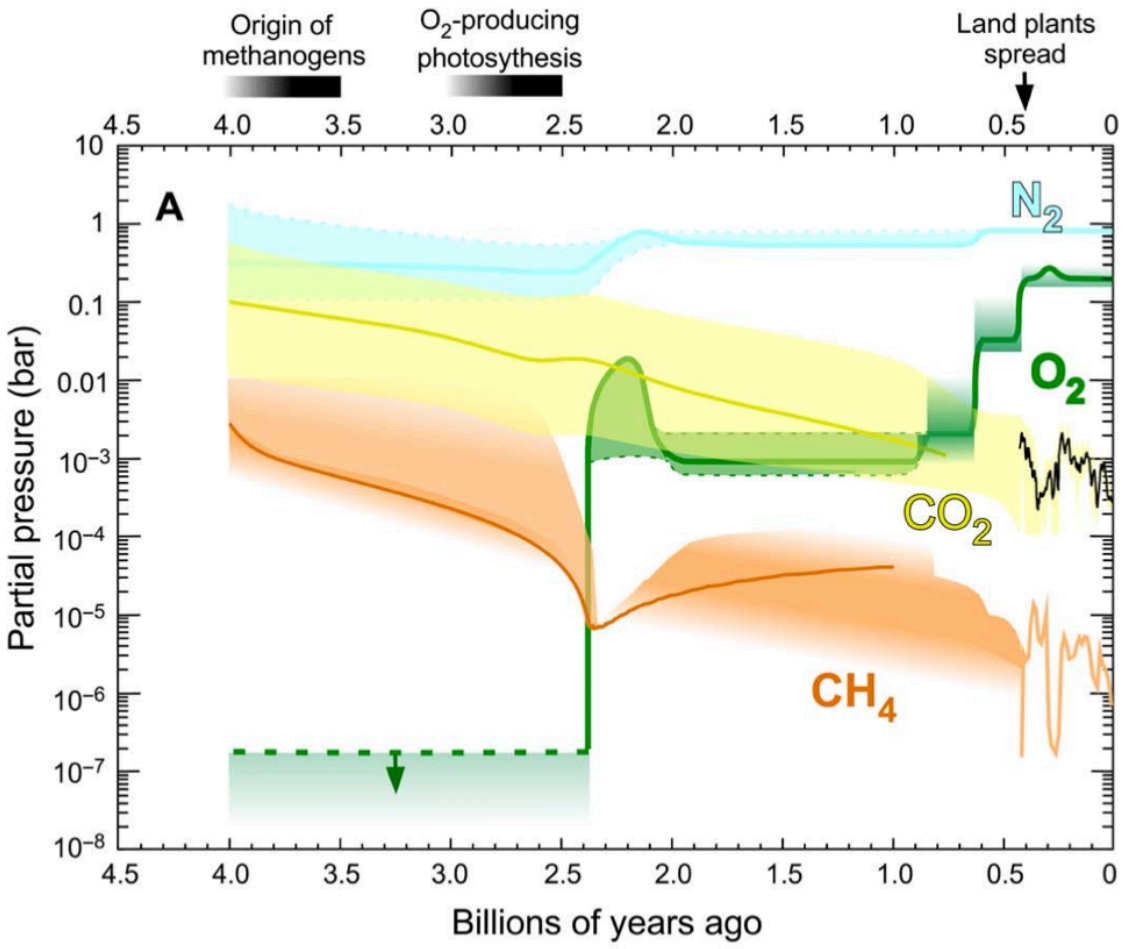

Figure 1.4. Evolution of major atmospheric gases (N_2, O_2, CO_2, CH_4) over time (Catling and Zahnle, 2020).

For the early Earth, models of stellar evolution predict that the sun was only about 70 to 75% as bright as today (Gough, 1981; Gilliland, 1989; Feulner, 2012). This would result in a completely frozen world over the first 2 billion years if the early Earth had its current albedo and greenhouse effect (Sagan and Mullen, 1972). Yet the geological evidence suggests presence of liquid water and even life in the Archean, this inconsistency is called the "Faint Young Sun Paradox" (FYSP; Sagan and Mullen, 1972; Kasting, 1993). Warm conditions under a faint sun implies that some effects must have been compensating, such as either higher concentrations of atmospheric greenhouse gases or a lower planetary albedo, or both. Sagan and Mullen (1972) suggested that ammonia (NH_3) could have offset the lower insolation, but ammonia appears less likely because it would have to be shielded against photodissociation by ultraviolet radiation (Abelson, 1966; Sagan and Mullen, 1972) and because it would be washed out by rain (Levine et al., 1980) then dissolved as NH_4^+ in the oceans (Kasting, 1982; Walker, 1982).

Earth's modern atmosphere is mainly composed of N_2 (78.08%), O_2 (20.95%), Ar (0.93%) and CO_2 (0.036%) and has an atmospheric pressure about 1.013 bar which corresponds to partial pressures (P) of P_{N2}= 0.78 bar, P_{O2}= 0.2 bar and P_{CO2}= 0.36 mbar. In 2013, Marty et al. showed from nitrogen and argon isotopes that P_{N2} during the Archean was between 0.5 and 1.1 bar and argued that N_2 did not play a significant role in explaining the FYSP. The hypothesis of a low nitrogen pressure throughout the Archean is further supported by Avice et al., (2018) who suggested similar or lower P_{N2} level than present-day and by Gebauer et al. (2020) who suggested P_{N2} <420 mbar at the time of the appearance of life. Furthermore, total air pressure from 2.7 billion years ago is constrained to less than half of modern levels, with P_{atm}=0.23 bar, and these data place an upper cap of around 0.5 bar for late Archean (Som et al., 2012, 2016). However, Goldblatt et al. (2009),

using a radiative-convective climate model, concluded that nitrogen (N_2) levels about twice as high as present day would have contributed to warming the early Earth, and the hypothesis that P_{N2} across the Hadean and Archean was above today's values is supported by several other studies (Barry and Hilton, 2016; Mallik et al., 2018; Johnson and Goldblatt, 2018). It thus remains debated the role of atmospheric N_2 as well as total atmospheric pressure in resolving the FYSP.

The role that clouds could play in resolving the Faint Young Sun Paradox (FYSP) has been studied by Goldblatt et al (2011), nevertheless they concluded that no matter how many high clouds (which tend to warm the surface with downwelling infrared) or low clouds (which tend to reflect sunlight) there were, it would not be enough forcing to resolve the FYSP.

Carbon dioxide (CO_2) is an attractive solution to the FYSP because of Earth's carbonate-silicate cycle thermostat that stabilizes Earth climate on geological timescales (Walker et al., 1981; Krissansen-Totton et al., 2018). Indeed, if global temperatures and CO_2 are low, CO_2 removal from precipitation is slow, as are weathering rates of silicates on the continents and seabed. Geological CO_2 emissions then increase atmospheric CO_2 levels, which increases global temperatures. Paleosols were used to estimate CO_2 pressure during the Archean and the results place P_{CO2} between 10 to 2500 times present atmospheric level (PAL) in the period between 2.2 Ga and 2.77 Ga (Kasting, 1987; Sheldon, 2006; Driese et al., 2011; Kanzaki and Murakami, 2015).

Methane is also of particular interest because of its potentially large greenhouse heating effects and long photochemical lifetime in an oxygen-poor atmosphere (Pavlov et

al., 2001). The possibility of methanogenic bacteria producing a high flux of biogenic CH_4 on the early Earth (Kharecha et al., 2005) is supported by evidence for the activity of methanogens and methanotrophs from light carbon isotopes in Archean kerogen (Stüeken and Buick, 2018). In addition, presence of Sulfur-Mass Independent Fractionation (S-MIF), a proxy for atmospheric anoxia, indicates significantly higher pCH_4 in deep geological time, placing pCH_4 at >20 ppmv, the minimum required to generate the particulate sulfur S_8 necessary to S-MIF preservation in sediments (Zahnle et al., 2006). Thus, methane may have played an important role in heating the early earth. Higher methane concentrations may also have participated in the more rapid loss of hydrogen to space because of UV photolysis of CH_4 in the upper atmosphere (Catling et al., 2001). The deuterium-to-hydrogen (D/H) ratio estimated from serpentine minerals, for a 3.7-billion-year-old seawater, is 2.5% lighter than today, which can be explain by a rapid loss of hydrogen in the Archean but also by isotopic fractionation (Pope et al., 2012; Kurokawa et al., 2018). Hydrogen escape to space may have been one of the main causes of the rise of atmospheric oxygen (Zahnle et al., 2013) about 2.32 billion years ago (Bekker et al., 2004) known as the Great Oxidation Event (GOE) and marked by the appearance of red beds (Holland, 1984; Eriksson and Cheney, 1992; Song et al., 2017).

Finally, although some argue that the Archean climate was warm, glacial rocks from 2.7, 2.9, and 3.42 billion years ago and recent isotope analyses combined with the current understanding of geological carbon cycle feedbacks suggest surface temperatures between 0° and 40°C (Catling and Zahnle, 2020). Despite the problem of the FYSP and the various possible mechanisms for overcoming it, the early earth clearly possessed a clement, habitable environments and a large liquid hydrosphere.

1.1.1.3 Hydrosphere

The earliest evidence of liquid water on Earth comes from oxygen isotopes evidence of the oldest terrestrial zircons from the Jack Hills Formation in Western Australia and is dated at 4.4 Ga (Mojzsis et al., 2001; Valley et al., 2002). The origin of water on Earth has been debated for several decades and it would come either from carbonaceous chondrites, comets or from the solar nebula. The average deuterium/hydrogen ratio (D/H) of carbonaceous chondrites is close to the current D/H of the terrestrial ocean, while those of comets and the solar nebula are respectively higher by a factor of two and lower by a factor of seven than the terrestrial ocean (Robert, 2001). However, Genda and Ikoma, (2008), investigating the early evolution of D/H in the ocean in a hydrogen-rich atmosphere, showed that even if the values pointed to a similarity between the terrestrial ocean and the carbonaceous chondrites, this did not necessarily mean that the origin of the water on Earth came from the carbonaceous chondrites and that the possibility of a nebular origin should not be excluded.

The existence of metasediments going back to at least 3.8 Ga constrains the presence of oceans and provides important clues to the early marine environment and hydrosphere. Marine sediments as old as at least 3.8 Ga are found in the Isua supracrustral rocks in West Greenland (Appel et al., 1998) as well as in the Nuvvuagittuq Greenstone Belt, Northern Quebec (Cates and Mojzsis, 2007) and in the case of the latter may be as old as ~4.3 Ga based on the short lived ^{146}Sm-^{142}Nd chronometer (O'Neil et al., 2012) although this age is controversial (Cates et al., 2013). Slightly younger marine sediments that are ~3.7 Ga are found in the Nulliak supracrustal rocks of the Saglek Block, northeastern Labrador (Nutman et al., 1989; Yoshida et al., 2021). While all these Eoarchean sedimentary occurrences are highly metamorphosed, at least upper amphibolite

facies, a large variety of well preserved (upper greenschist or lower) metasediments deposited between 3.5 and 2.5 billion years ago are found on a wide variety of Archean cratons. Their analysis over the past few decades, as well as theoretical considerations, constitute the basis of current knowledge on the Earth's early hydrosphere.

While the pH of the early oceans is poorly constrained, they were almost certainly more acidic due to higher atmospheric pCO_2, likely in the pH 6.5 to 7.5 range (Grotzinger and Kasting, 1993). There are significantly more rock record constraints, but also controversy, surrounding the temperature of the ancient oceans. Studies of oxygen ($\delta^{18}O$) and silicon ($\delta^{30}Si$) isotopic compositions of Paleoarchean cherts indicate seawater temperatures between 55 and 85°C (Knauth and Lowe, 1978, 2003; Robert and Chaussidon, 2006). While the interpretation of the silicon isotope data is highly theoretical, the $\delta^{18}O$ of both cherts and carbonates is remarkably low for the first two billion years of sedimentary records, with the conclusion that Earth's early hydrosphere was significantly different than today (Kasting et al., 2006, Fig. 1.5).

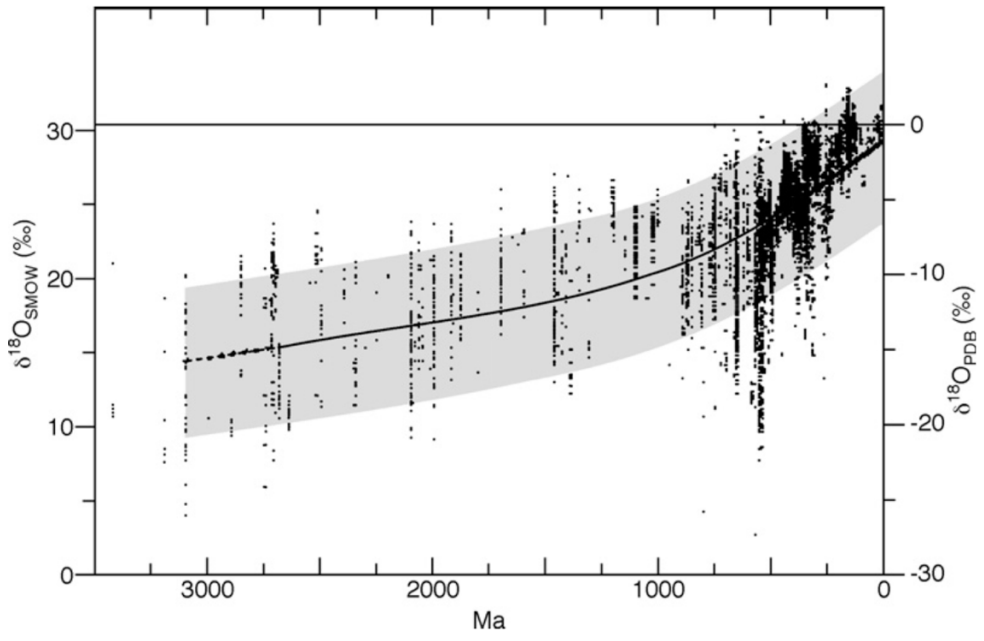

Figure 1.5. $\delta^{18}O$ values from about 10 000 ancient marine calcites over time, from Archean to the present (Kasting et al., 2006).

The isotope fractionation of oxygen between water and authigenic oxide minerals generally shows important temperature dependence, with isotope fractionation decreasing with increasing temperature. As a result, at higher paleoseawater temperatures, the $\delta^{18}O$ of oxide minerals (which are generally heavier than their formation waters) approaches that of seawater in which they formed, which is isotopically lower. Thus, a palaeothermometry interpretation of the low $\delta^{18}O$ isotope compositions of Archean cherts and carbonates indicates high seawater temperatures, first estimated by Knauth and Lowe, (1978).

The interpretation of the unusually low $\delta^{18}O$ data in a paleothermometer framework depends on the assumption of the $\delta^{18}O$ value of seawater, which has long been believed to be strongly buffered by water-rock interaction during seafloor hydrothermal circulation (Muehlenbachs et al., 1974). However, light $\delta^{18}O$ values have also been reported in ancient iron oxides, whose $\delta^{18}O$ value is largely independent of temperature but highly dependent on the water formation value (Galili et al., 2019). This would indicate that rather than being hot, the ancient oceans had an oxygen isotope composition far from modern seawater. Killingsworth et al. (2019) similarly observed unusually light $\delta^{18}O$ values in GOE-era sulfates, which they suggested also indicates a hydrological cycle anchored on lighter ocean water than today.

This would only be possible by inefficient oxygen isotope exchange during hydrothermal circulation at mid-ocean ridges. Indeed, this might have been possible if the oceanic crust was much hotter than today, so that water did not circulate at the same depths as today (Kasting et al., 2006). Finally, it has been recently suggested that most Archean chert and carbonate records may have an inherent bias to high temperature precipitation, for example by their association with large impacts and deposition from what may have

been superheated surface waters during massive evaporation events associated with ultra-large impacts (Lowe and Byerly, 2015). Photosynthesis itself is today limited to approximately 73°C (Loiacono et al., 2012; Bennett et al., 2022) which probably places an approximate upper limit on paleoseawater temperatures wherever microbial photosynthetic structures (e.g., stromatolites) are found. In any case, the temperature of seawater during the Archean remains largely open.

The first oceans were anoxic and Fe (II)-rich (ferruginous), and these conditions persisted in the deep-ocean for most of Earth's history (Kato et al., 1996; Poulton and Canfield, 2011; Li et al., 2013). During these "ferruginous" ocean periods, dissolved iron came mainly from hydrothermal sources or from sediments during anoxic diagenesis (Poulton and Raiswell, 2002; Raiswell et al., 2006). Large deposits of iron-enriched marine chemical sediments called Banded Iron Formations (BIFs) attest of the abundance of Fe and thus iron-bearing conditions over time. The oldest BIFs are 3.8 Ga old (Isua, West Greenland) and the youngest are 527 Ma old (Taxkorgan terrane, Western China, Li et al. 2018). BIFs are part of Archean cratons from 3.5 to 2.5 Ga, and they disappear from the geological record at about 1.8 Ga, to reappear between 0.8 and 0.5 Ga (Fig. 1.6; James and Trendall, 1982; Klein, 2005).

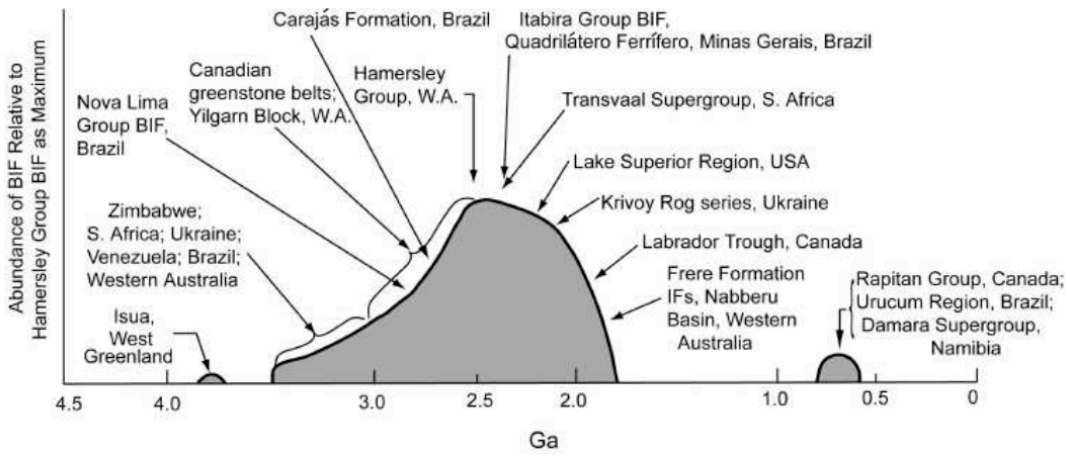

Figure 1.6. Schematic diagram showing the relative abundance of Precambrian BIFs as a function of time, with identification of several of the major BIFs or regions of BIFs (Klein, 2005).

These important changes in the composition of seawater, especially with respect to iron, are intimately linked with the redox evolution of the Earth, as discussed in section 1.2 below. Initially, it was thought that BIF disappeared due to complete oxidation of the large Archean and Paleoproterozoic dissolved iron reservoir. However, Canfield (1998) proposed another hypothesis, where atmospheric oxygenation after the GOE generated oxidation of pyrite, supplying sulfates to the Proterozoic Ocean, and thus titrated dissolved Fe (II) from the ocean and thereby terminating global BIF deposition. Such dramatic changes would have had important effects on biogeochemical cycling (Habicht et al., 2002; Planavsky et al., 2012) and even biological evolution (Anbar and Knoll, 2002) as discussed below.

1.1.1.4 Biosphere

The oldest evidence of life may be in the highly ^{13}C-depleted graphite in Eoarchean rocks such as the 3.8 Ga Isua supracrustal belt in West Greenland (Schidlowski, 2001), the 3.8 Ga Nuvvuagittuq Greenstone Belt in Northern Quebec (Papineau et al., 2011) or the 3.95 Ga Saglek block from the Nulliak supracrustal rocks in Western Labrador (Tashiro et al., 2017). However, due to the high degree of metamorphism (amphibolite to granulite-facies) of these rocks (van Zuilen, 2019), it is not impossible that these carbonaceous materials are in fact derived from abiotic processes such as extensive re-equilibration of the isotopic compositions between carbonates/metamorphic fluids and graphite (Chacko et al., 2001) or through thermal decomposition of carbonate minerals (Ueno et al., 2002). Older ^{13}C-depleted graphite preserved in the 4.1 Ga detrital zircons from Jack Hills in Western Australia with $\delta^{13}C_{PDB}$ values as low as -24 +/- 5‰ could be considered as the potential oldest trace of life (Bell et al., 2015).

While ambiguous in highly metamorphosed rocks deposited prior to 3.7 Ga, the presence of life on Earth from ca. 3.5 Ga onwards is much less controversial and indeed widely accepted based on available rock records evidence. There are only a few recognized places on Earth where well-preserved sedimentary rocks were deposited between 3.5 and 2.8 Ga, and they are largely restricted to three cratons: the Pilbara craton in Western Australia, the Kaapvaal craton in South Africa, and the Superior craton of Eastern Canada. The Pilbara craton is divided into three terranes: the East Pilbara Granite-Greenstone Terrane comprised of 3655–2850 granitic complexes and 3515-3000 Ma greenstones of the Pilbara supergroup, the West Pilbara Granite-Greenstone Terrane comprised of two distinct greenstone belts (ca. 3270 Ma Roebourne Group and ca. 3120 Ma Whundo Group), and the Kurrana Granite-Greenstone Terrane comprised of ca. 3190 Ma gneisses and a few older greenstone enclaves (van Kranendonk, 2006). Here, the East Pilbara Terrane is host to particularly well-studied cherty sedimentary units preserving some of Earth's earliest life traces, notably the ca. 3480 Ma Dresser Formation and the ca. 3400 Strelley Pool Chert. On the Kaapvaal craton, the Barberton Greenstone Belt hosts the Barberton Supergroup, which was deposited over the period 3.55 to 3.20 Ga and is subdivided into three units: the 3547 to 3258 Ma volcanic-dominated Onverwatch Group, 3258 to 3223 Ma Fig Tree Group, and 3223 to 3219 Ma Moodies Group. Cherts of the Onverwatch Group and sandstones and conglomerates of the Moodies Group are particularly known for their abundant life traces (Homann, 2019). The Superior Craton of East-Central Canada is the largest known Archean craton and records a complex history spanning 4.3 to 2.57 Ga. It is comprised of northern and southern subprovinces dominated by high-grade gneiss, with a central region comprised of multiples granite-greenstone belts preserving abundant metasediments. The greenstone belt-hosted metasediments of the Superior Craton contain some of the earliest and thickest Archean carbonate successions known for the Archean

(Kusky and Hudleston, 1999) and similarly includes abundant evidence for ancient microbial life, largely in the form of preserved stromatolitic structures (Hofmann, 1985; McIntyre and Fralick, 2017). These three cratons paint a unified picture of a rich biosphere that had already emerged by 3.5 Ga and colonized multiple environments of the early Archean Earth.

The multiple lines of evidence for ancient life in the cratons described above is found in both morphological and chemical forms. In terms of morphological evidence, a variety of sedimentary structures may be preserved that implicates the activity of microbes in their formation. In the 3.48 Ga Dresser and 3.40 Ga Strelley Pool Formations (Pilbara), ~3.47 Ga, ~3.42 Ga, and ~3.33 Ga cherts of the Onverwacht Group (Barberton), and multiple carbonate platforms of Superior Craton overlapping 2.94 to 2.80 Ga, chert and carbonate metasediments preserve abundant stromatolites (Hofmann, 1985; van Kranendonk, 2006; Riding et al., 2014a; Homann, 2019), organo-sedimentary structures that accrete towards the sun by the grain-binding and carbonate-cementing activity of photosynthetic microbial communities (Riding, 2000). Similar morphological evidence in the form of microbially-induced sedimentary structures (MISS), which include fossilized microbial mats and microbially-influenced desiccation cracks, are also preserved on the Pilbara and Barberton Cratons (Noffke, 2009; Noffke et al., 2013). Additional morphological evidence for early Archean life that has proven more controversial is the purported presence of microfossilized remains of individual cells, most often preserved in cherts. Early excitement over cell-like structures preserved in chert, including some reported to reflect the presence of cyanobacteria as far back as 3.47 Ga (Schopf, 1993), generated significant debate as to their primary, biological origin (Brasier et al., 2002; Wacey et al., 2016). Further investigations have revealed a large diversity of kerogenous,

microfossil-like structures preserved in Archean rocks across the globe, including spherical, lenticular, and tubular forms, however important questions continue to surround their bio- and syn-genecity in all except the most convincing cases (Lepot, 2020). Nonetheless, the ensemble of morphological evidence is best explained by a thriving microbial biosphere influencing sedimentary environments since at least 3.5 Ga.

Abundant geochemical evidence supports this interpretation and provides additional insight into Earth's early microbial biosphere. Carbon stable isotope compositions of preserved kerogen in sediments deposited between 3.5 and 2.8 Ga generally fall in the -25 to -35‰ range and are rarely lighter than -40‰, consistent with biological carbon acquisition by several possible autotrophic carbon fixation pathways, but light enough to exclude important methanotrophy (Havig et al., 2017). Similarly, nitrogen stable isotope data indicate predominately diazotrophic and anaerobic nitrogen cycling over this period (Stüeken et al., 2015). Both records contrast to data from sediments deposited after 2.7 Ga, when isotopically light C isotope compositions and heavy N isotope compositions indicate important roles for aerobic carbon cycling (methanotrophy) and aerobic nitrogen cycling (diazotrophy) in the run-up to the Great Oxidation Event starting ca. 2.45 Ga (Eigenbrode and Freeman, 2006; Thomazo et al., 2011; Ader et al., 2016; Kipp et al., 2018; see also Section 1.2). Additional insights into the evolving metabolic capabilities of Earth's early biosphere come from the sulfur stable isotope compositions of sedimentary pyrites. Already in the 3.48 Ga Dresser Formation (East Pilbara), stable isotope fractionation of sulfur preserved in both pyrites and barites, as well as variable mass dependent overprinting of photochemically-generated sulfur mass independent fraction (S-MIF; see section 1.2), point to non-negligible biological sulfate reduction and perhaps S-disproportionation (Philippot et al., 2007; Ueno et al., 2008; Wacey et al., 2015). Similarly,

iron stable isotope compositions in oxides and pyrites that deviate strongly from crustal values are consistently found in sediments deposited between 3.8 and 2.5 Ga, with a large negative excursion peaking ca. 2.7 Ga (Johnson et al., 2008) ; these are also best explained by microbial redox cycling, although the relative role of partial iron oxidation *vs.* dissimilatory iron reduction in generating the large range in compositions observed is subject to debate (Rouxel et al., 2005).

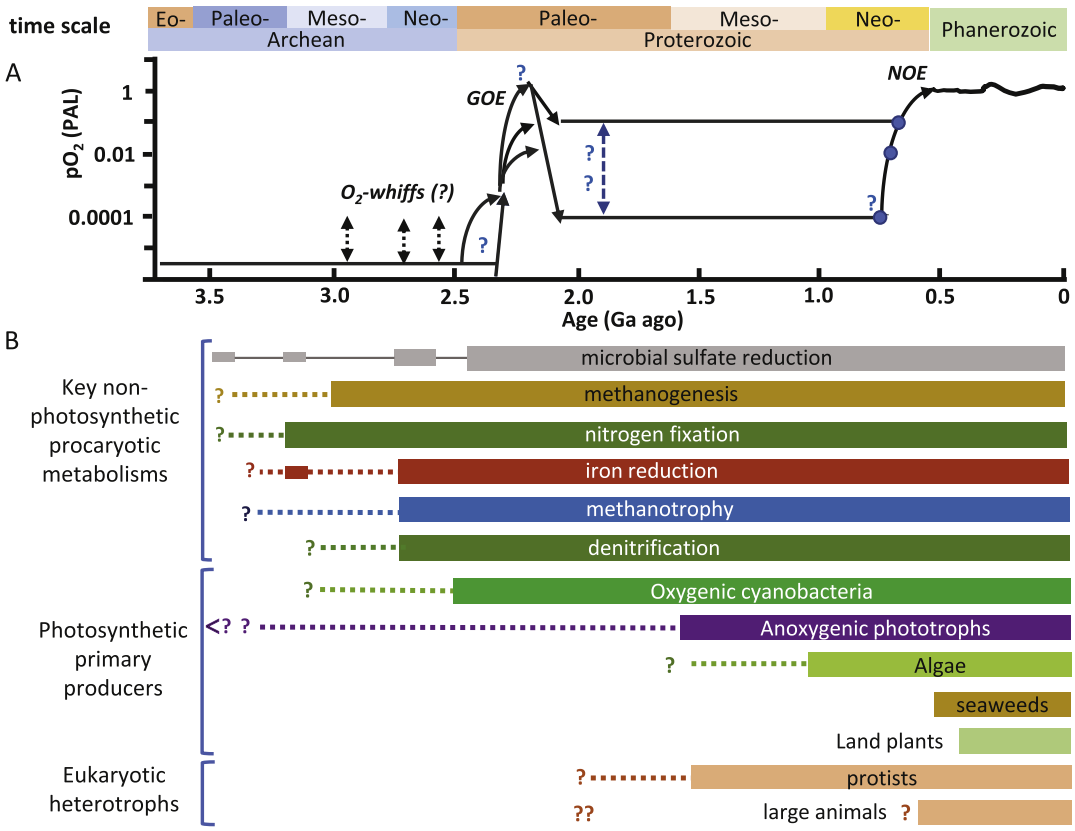

Figure 1.7. Synthesis of the evolution of atmospheric oxygen and microbial metabolism as recorded in Earth's ancient rock record. Figure from Lepot (2020).

The emergent picture, supported by both morphological and geochemical fossil evidence, is that the Earth was colonized by an important microbial biosphere already by 3.5 Ga, and that diversification occurred relatively early, with evidence for most major microbial metabolisms appearing in the rock record in the 3.5 to 2.8 Ga range (Fig. 1.7). Evidence for the origins of oxygenic photosynthesis, however, have proven highly

controversial. Early organic geochemical investigations of Archean sediments tentatively identified the presence of 2-methyl-hopane compounds in drill core from the 2.7 Ga Fortescue Group (Western Australia), which were thought to indicate the presence of cyanobacteria already at this time. However, it was later revealed that these biomarkers were unlikely to be primary components of the sediment, but rather represent later contaminants (Rasmussen et al., 2008; French et al., 2015). Furthermore, it was later revealed that 2-methyl-hopane compounds are also produced by anoxygenic phototrophs under strictly anoxic conditions. As currently available biomarker and microfossil evidence (discussed above) for an Archean origin for oxygenic photosynthesis is widely considered ambiguous at present, most workers over the last decade have focused on the detection of free oxygen itself to better constrain the origin of oxygenic photosynthesis on Earth. As we shall see below, Earth's oxygenation and redox history is complex, and there remain important uncertainties regarding the fidelity of geochemical proxies for ancient O_2 production, including some that are directly addressed by this thesis.

1.2 Earth's surface oxygenation

The Precambrian witnessed a dramatic evolution in Earth surface oxygenation, including the first significant accumulation of atmospheric oxygen around the Archean-Proterozoic boundary. This important transition in Earth history was first discovered in the late 1960s by Preston Cloud while studying Banded Iron Formations (BIFs). Hypothesizing that BIFs must have formed in anoxic oceans because oxidized iron is insoluble, he concluded that the abundance of BIFs implied the presence of soluble iron in ionic form capable of being transported over great distances to the sites of deposition and that the absence of BIF deposition after 2 billion years must be explained by the increase in oxygen concentrations in the atmosphere around that time. This first rise of oxygen now known as

the 'Great Oxidation Event' or GOE (Holland, 2002, 2006) is well-defined in the rock record by multiple lines of evidence that points to irreversible oxidation of Earth's atmosphere ca. 2.5 to 2.3 Ga (Lyons et al., 2014).

One common possible mechanism to explain the increase in atmospheric oxygen is that oxygen would be a secondary consequence of the Earth's cooling (Holland (1962) caused by a change from submarine to subaerial volcanics (Kump and Barley, 2007) or decrease in degassing pressure (Gaillard et al., 2011) that both act to increase the oxidizing potential of volcanic degassing and volcanic sulfur emissions, and therefore lead to the rise of oxygen in the atmosphere. However, splitting of H_2O and escape of hydrogen to space represents clearly recognized mechanism for planetary oxidation on other solar system bodies, and its calculated effect on Earth's atmosphere over geological time could also readily explain the GOE (Zahnle et al., 2013). Finally, many workers look to a strong biological role in driving the GOE, that being the splitting of CO_2 and massive worldwide burial of reduced carbon, and to a lesser degree reduced sulfur, that would remove reducing equivalents from Earth's surface; on short geological timescales, biological productivity and carbon burial is often evoked for regulating atmospheric O_2 (Berner, 2006). Indeed, there exists potential evidence for massive carbon burial associated with the GOE in the form of a large, synchronous, and global positive isotope excursion in the $\delta^{13}C$ of carbonates, known as the Lomagundi-Jatuli Event. This event, considered as the largest and longest positive carbon isotope excursion in Earth history, implicates such an intense degree of burial of isotopically light reduced carbon that it would have increased pO_2 between 12 to 22 times present atmospheric level (Karhu and Holland, 1996). However, as we see below, this excursion happened after the initial oxidation of the atmosphere as tracked by other proxies, and some today suggest that it reflects instead a response to the

GOE, whether as the result of increased nutrient availability (Bekker and Holland, 2012) or as the result of weathering of exotic redox sensitive components influencing the carbon cycle such as siderite weathering (Bachan and Kump, 2015).

The GOE is characterized by the first appearance of red beds on land (Holland, 1984; Eriksson and Cheney, 1992; Song et al., 2017), the disappearance of redox-sensitive minerals such as pyrite (FeS_2) from ancient fluvial and deltaic deposits (Canfield, 2005; Holland, 2006), and an enrichment of Cr and U in iron formations (Konhauser et al., 2011; Partin et al., 2013). However, it was the discovery of mass-independent fractionation of sulfur isotopes (S-MIF), resulting from photochemical SO_2 processing in an oxygen depleted atmosphere, and its disappearance from sedimentary records between 2.2 and 2.45 Ga, that is considered the most irrefutable proof for the GOE (Farquhar et al., 2000; Bekker et al., 2004; Guo et al., 2009). S-MIF of diagenetic pyrite from the Transvaal Supergroup, South Africa, would constrain the age of the GOE at 2.33 Ga and suggest a rapid oxygenation of Earth's atmosphere within 1-10 million years followed by the slow rise of oceanic sulfates (Luo et al., 2016). Detrital pyrite and uranite from the 2.415 Ga South African Koegas Subgroup indicate that the rise of oxygen is at least younger than 2.415 Ga (Johnson et al., 2014). However, Reinhard et al. (2013b) showed using geochemical modeling that S-MIF is susceptible to undergo a crustal memory effect that generates an extension of the visibility of the S-MIF signal about 10 to 100 million years after the beginning of oxygenation when the signal ceased to be produced in the atmosphere. Furthermore, the S-MIF record from around the world (Transvaal Basin in South Africa, Huronian Supergroup in North America and Hamersley Basin in Australia) appears to be asynchronous, arguing in favor of regional-scale modulation of the S-MIF crustal memory effect (Philippot et al., 2018). This S-MIF recycling effect has been confirmed by coupled

S and O stable isotopes measured on barites from the Turee Creek Basin, Western Australia, showing clearly that S-MIF signals were transferred from the paleo-continent under an oxygenated atmosphere (Killingsworth et al., 2019). The GOE was not only accompanied by profound perturbations to Earth's surface environments and atmosphere, but the biosphere was also profoundly affected, with carbon and triple oxygen isotope evidence indicating dramatic swings, and potentially even a collapse, in productivity (Hodgskiss et al., 2019).

The evolution of the Earth's surface geochemistry has been closely linked to the presence of O_2 and the evolution of photosynthetic cyanobacteria. Oxygenic photosynthesis appeared after anoxygenic photosynthesis (Hohmann-Marriott and Blankenship, 2011) so the direct ancestors of cyanobacteria may have been anoxygenic (Johnson et al., 2013; Fischer et al., 2016), or lacked photosynthetic machinery, acquiring it later via lateral transfer (Soo et al., 2017). Microfossils have been used for understanding the evolution of early phototrophs (Schopf, 1993) however (Brasier et al., 2002) reinterpreted as secondary artefacts the most ancient microfossil-like structures purported to represent cyanobacteria. Moreover, the Precambrian microfossil record is now known to be inconclusive (Butterfield, 2015; Schirrmeister et al., 2016) and molecular biomarkers (Brocks et al., 1999) are also considered unreliable in rocks older than ~2 Ga (French et al., 2015) .So, evidence for cyanobacterial origins relies on geochemical data, i.e., abundances or isotopic compositions of redox-sensitive elements indicative of free oxygen.

While it had been long hypothesized that the origin of cyanobacteria might be the cause for the GOE itself, intriguingly the possibility that they existed for hundreds of millions of years prior to the GOE is becoming more and more likely. Multiple redox

proxies (trace element and metal isotope) indicate the presence of O_2 oases prior to the GOE between 2.5 Ga and 3 Ga (Anbar et al., 2007; Crowe et al., 2013; Planavsky et al., 2014; Riding et al., 2014; Wang et al., 2018; Thoby et al., 2019). In 2018, Eickmann et al. suggested with S and Fe isotopes measurement the presence of oxygenated near-shore shallow marine environments ca. 2.96 Ga, despite of the clear presence of an overall reduced atmosphere. Moreover, models of the oxidation of crustal sulfide minerals without concomitant accumulation of oxygen in atmosphere (Reinhard et al., 2013a) also suggest localized oxygenic photosynthesis before the GOE. Prior to 2.5 Ga, the discrepancy between persistent MIF-S, which indicates the presence of an anoxic atmosphere, and redox proxies implying the presence of localized oxygen pre-GOE, was initially explained by the idea of marine oxygen oases, whereby O_2 produced in the upper water column of the oceans wafted over the continents and effectuated early oxidative weathering (Anbar et al., 2007). Model studies indicate that under reducing Archean ocean and atmospheric conditions, cyanobacterial productivity could have generated upper water column dissolved O_2 concentrations of a few micromolar in nutrient-rich nearshore environments (Olson et al., 2013), however degassing and transport under such conditions remained problematic. This problem can be resolved by a benthic terrestrial and shallow-water biosphere populated by cyanobacteria producing O_2 and driving oxidative weathering more locally but with little effect on atmospheric composition (Stüeken et al., 2012; Lalonde and Konhauser, 2015).

However, the syngenetic nature of many of these signals is questioned, leaving the Archean origins of oxygenic photosynthesis in doubt. For example, the isotopically light Mo isotope compositions reported by Planavsky et al. (2014) for outcrop samples from the Ijzermign BIF of the 2.95 Ga Mozaan Group, Pongola Supergroup, South Africa, interpreted to represent oxic Mo cycling in the presence of Mn oxides, was shown to be

absent in drill core samples (Albut et al., 2019). Furthermore, non-crustal Cr isotope compositions reported in the Ijzermign BIF by Crowe et al. (2013) that were also interpreted to represent the presence of O_2 were shown to be absent in drill cores that were subsequently analzyed and reported by Albut et al. (2018). In the 2.5 Ga Mount McRae shale where the idea of a whiff of O_2 was first proposed based on Mo and Re enrichments, it was shown that the Mo-rich intervals show signs of important sulfur remobilization, with Mo concentrated in the latest stage mineralization phases (Slotznick et al., 2022). In a more general study, Planavsky et al. (2020) examined the presence or absence of Ce anomalies in a large Archean and Paleoproterozoic sedimentary geochemical database and concluded that appreciable Ce anomalies are found mostly in surface outcrop samples but are absent from most drill core samples throughout the Archean. These observations of redox proxy mobilization and resetting complicate heavily the challenge of identifying the origins of oxygenic photosynthesis in the Archean rock record.

Recent advances in radiometric isotope geochemistry may be the solution to resolve this challenge. At least three currently applied redox tracers form radiogenic parent-daughter pairs that can be used for dating isotope system closure on timescales are suitable for ancient Earth studies. These are Re-Os (Kendall et al., 2015), U-Th-Pb (Li et al., 2012) and La-Ce (Bonnand et al., 2020). All the above examples represent unique breakthrough papers that confirmed or rejected closure of the redox sensitive isotope system in question using radiometric isotope decay. At the same time, such applications are limited to the above references at present. In this thesis work, I specifically explore the La-Ce chronometer, applied here in an attempt to directly date Ce oxidation events in deep geological time, and provide new constraints on the earliest production of O_2 by cyanobacteria.

1.3 The Ce redox proxy and La-Ce geochronology

The rare earth elements (REE) have very similar chemical properties, but cerium is the only REE, except for Eu, for which anomalies due to redox reactions are detected in aqueous solutions and their precipitates. Oxidation of Ce^{3+} to Ce^{4+} and subsequent decoupling of Ce from the other REEs (due to formation of less soluble Ce (IV) species and/or preferential adsorption of Ce (IV) species on particle surfaces) can explain the appearance of Ce anomalies (Bau and Dulski, 1996). Positive Ce anomalies can be found in marine hydrogenetic Fe-Mn crusts (Fig. 1.8; Bau and Dulski, 1996) and in Fe-Mn nodules (Amakawa et al., 1991; Bau et al., 2014) when Ce (IV) is adsorbed on the surface of Fe-Mn (oxyhydr)oxides under oxic conditions, leaving residual seawater depleted in Ce relative to the other trivalent REE (German and Elderfield, 1990). Modern seawater is characterized by a strong negative Ce anomaly (Fig. 1.8), a positive yttrium (Y) anomaly and an enrichment in heavy rare earth element (HREE) compared to light rare earth element (LREE). In addition to seawater, negative cerium anomalies can be found in riverine waters and in authigenic carbonate that have captured the signature of seawater during their formation (Fig. 1.8). Therefore, REE spectra in authigenic carbonates and chemical sedimentary rocks (i.e., BIF), have been used to know the characteristic of seawater and its redox conditions over geological time.

The development of Ce anomalies being generally attributed to oxidizing environments (see chapter 6, section 6.3.4 for further discussion), widespread occurrence of negative Ce anomalies in sediments beginning ca. 2.5 Ga was used to argue in favor of the presence of oxidized Precambrian surface waters (Towe, 1991; Riding et al., 2014). However, as explained in the previous section, these signals may be subject to post-depositional alteration, therefore, determining whether these signals are primary or

secondary is of critical importance and the use of radioactive decay systems proves to be essential.

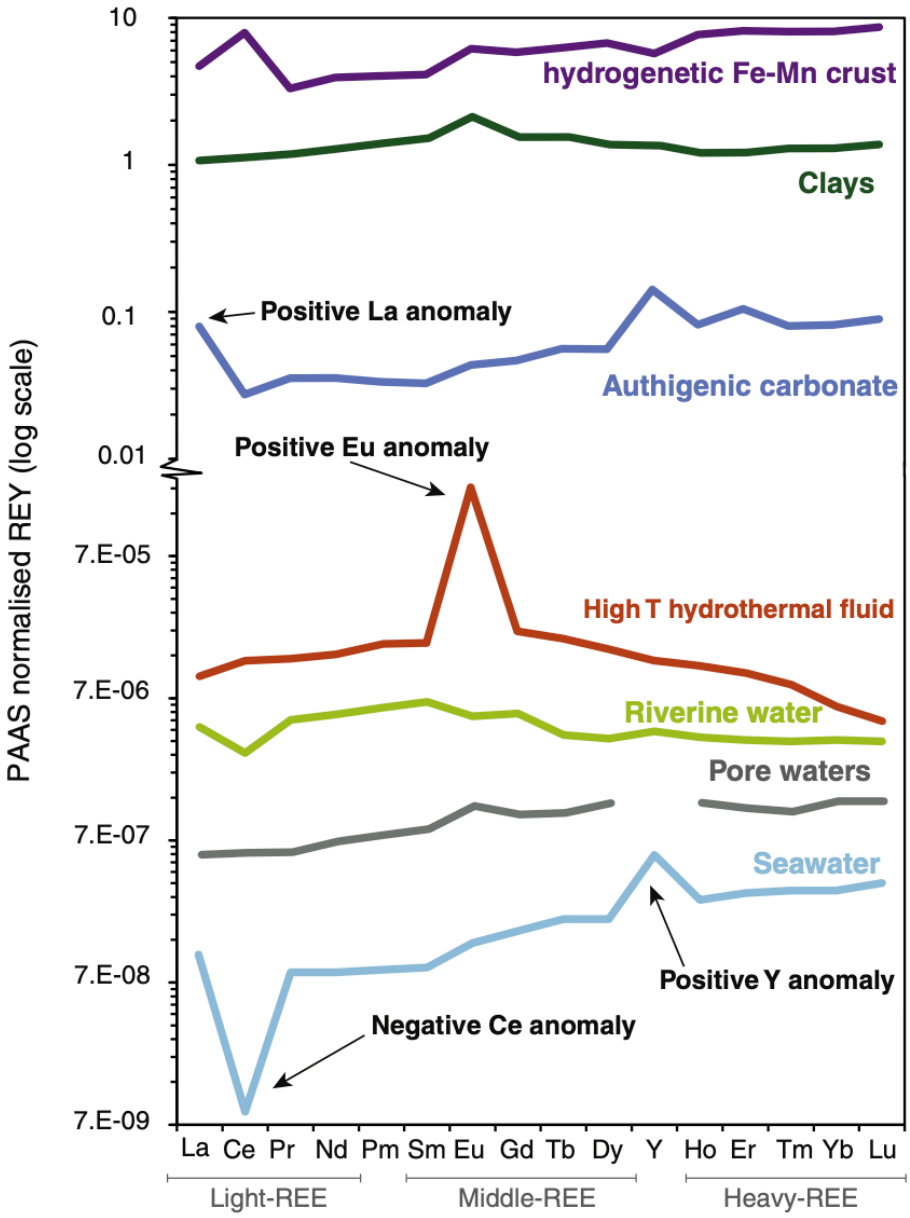

Figure 1.8. Post-Archean Australian Shale (PAAS) normalized REE+Y (REY) patterns showing typical REY signatures and anomalies of La, Ce, Eu and Y in different environments and minerals (Tostevin et al., 2016).

For several decades, radioactive decay systems (Lu-Hf, Sm-Nd, Re-Os, Rb-Sr, etc.) have been used to date geological events and to establish temporal constraints on the differentiation history of the Earth. For example, the Rb-Sr geochronometer, based on the

β^- decay of radioactive ^{87}Rb to ^{87}Sr, has a half life of about 49 Ga and the Sm-Nd system, based on the α decay of radioactive ^{147}Sm to ^{143}Nd, has a long half-life of about 106 Ga.
In this thesis, I used the La-Ce system to determine the La-Ce closure age and whether the cerium anomalies were primary or in fact secondary artifacts. In this system with a half-life of 102 Ga (Sonzogni, 2003), ^{138}La decays into two parallel processes: 34 % of the isotope undergoes $\beta-$ decay (conversion of a neutron into a proton) transforming into the stable ^{138}Ce, while the remaining 66% of ^{138}La disintegrates by electronic capture (conversion of a proton to a neutron by interaction with an electron) leading to the formation of stable ^{138}Ba (Bortoluzzi and Ferraro, 2020). This system was used for the first time in 1982 by Tanaka and Masuda in combination with the Sm-Nd system to determine the age of a gabbro from the upper zone of the Bushveld complex in South Africa and confirm that the ages obtained with the two systems were consistent. These two systems combined were later used for ocean island basalt (OIB) source determination (Dickin, 1987), to constrain the evolution of the moon (Tanimizu and Tanaka, 2002), to characterize the nature of the sediments involved in the genesis of lavas (Bellot, 2016; Bellot et al., 2018) and to study the behavior of LREE in mid-ocean ridge basalts (MORBs) and OIBs (Schnabel, 2019).

Hayashi et al. (2004) were the first to attempt to deduce the origin of negative cerium anomalies and constrain their age of formation in ancient sedimentary rocks using the La-Ce isotopic systematics. The calculated initial Ce isotopic ratios in samples from the 3.25 Ga Barberton Greenstone Belt, South Africa, indicated that the Ce anomalies were not primary and with two different models, they deduced that these negative cerium anomalies appeared during episodes of alterations younger than 1.1 Ga. Recently, Bonnand et al. (2020) constrained the timing of Ce anomalies in 3.22 Ga BIFs from the Moodies

Group, Barberton Greenstone Belt, South Africa, to the last 100 million years with the La-Ce geochronometer leading to an isochron of 60 ± 32 Ma, unquestionably confirming these anomalies as secondary artefacts.

1.4 Summary and PhD presentation

The origin of oxygenic photosynthesis is one of the most dramatic evolutionary events that the Earth has ever experienced. Earth's modern biosphere owes its existence to this planet-defining metabolism, and understanding its origin is a paramount challenge in Earth system science. However, due to uncertainties in the primary nature of ancient signals of oxygen in ancient and altered rocks, exactly when oxygenic photosynthesis evolved remains largely unresolved. This PhD work focuses on novel chemical and isotopic signals (Ce anomalies, Fe isotopes, Ce isotopes) preserved in chemical sedimentary rocks and other marine sediments deposited between 2.93 and 2.8 Ga to better understand the evolution of photosynthetic pathways on the early Earth.

After this introductory Chapter 1, a general geologic context of the samples examined in this work is detailed in Chapter 2. I also provide some general characteristics of the diverse lithologies examined (carbonates, BIFs, and black shales) as well as information related to their analysis and interpretation as environmental and redox proxies. Chapter 3 detail the analytical methodologies used to obtain elemental and isotopic data.

Chapters 4, 5, and 6 present results and discussion in the form of scientific articles (i.e., with abstracts). In Chapter 4, rare earth element (REE) and Fe isotope analyses are reported from diverse sediments associated with a shallow water stromatolitic Archean carbonate platform preserved in the 2.93 Ga Red Lake Greenstone Belt, Ontario, Canada.

This thick accumulation of carbonates interbedded with deep-water pyritic black shales and BIF provides an unparalleled opportunity to study the Mesoarchean iron cycle and microbial metabolisms driving it in a deep-to-shallow transect. Chapter 5 presents a comparative rare earth element (REE) systematics from three Canadian Mesoarchean carbonate platform displaying negative cerium anomalies: Red Lake, Woman Lake and Steep Rock. In Chapter 6, La-Ce geochronology is used to date the cerium anomalies from the three Mesoarchean platforms studied in Chapter 5 to definitively determine whether those anomalies, used to argue the presence of pre-GOE oxygen, are primary or secondary. At the time of submission of this thesis, Chapter 4 were in advanced stages of preparation for submission to *Geology* and Chapter 6 for *Nature*, which is at times reflected in their formatting.

Chapter 7 concludes the thesis with a summary of the principal findings as well as perspectives for future workers looking to geochemically examine ancient sediments bearing evidence of photosynthetic activity and/or working on Ce isotope systematics.

1.5 References

Abelson, P.H., 1966, Chemical Events on the Primitive Earth: Proceedings of the National Academy of Sciences, v. 55, p. 1365–1372, doi:10.1073/pnas.55.6.1365.

Ader, M., Thomazo, C., Sansjofre, P., Busigny, V., Papineau, D., Laffont, R., Cartigny, P., and Halverson, G.P., 2016, Interpretation of the nitrogen isotopic composition of Precambrian sedimentary rocks: Assumptions and perspectives: Chemical Geology, v. 429, p. 93–110, doi:10.1016/j.chemgeo.2016.02.010.

Albut, G., Babechuk, M.G., Kleinhanns, I.C., Benger, M., Beukes, N.J., Steinhilber, B., Smith, A.J.B., Kruger, S.J., and Schoenberg, R., 2018, Modern rather than Mesoarchaean oxidative weathering responsible for the heavy stable Cr isotopic signatures of the 2.95 Ga old Ijzermijn iron formation (South Africa): Geochimica et Cosmochimica Acta, v. 228, p. 157–189, doi:10.1016/j.gca.2018.02.034.

Albut, G., Kamber, B.S., Brüske, A., Beukes, N.J., Smith, A.J.B., and Schoenberg, R., 2019, Modern weathering in outcrop samples versus ancient paleoredox information in drill core samples from a Mesoarchaean marine oxygen oasis in Pongola Supergroup, South Africa: Geochimica et Cosmochimica Acta, v. 265, p. 330–353, doi:10.1016/j.gca.2019.09.001.

Amakawa, H., Ingri, J., Masuda, A., and Shimizu, H., 1991, Isotopic compositions of Ce, Nd and Sr in ferromanganese nodules from the Pacific and Atlantic Oceans, the Baltic and Barents Seas, and the Gulf of Bothnia: Earth and Planetary Science Letters, v. 105, p. 554–565, doi:10.1016/0012-821X(91)90192-K.

Anbar, A.D. et al., 2007, A Whiff of Oxygen Before the Great Oxidation Event? Science, v. 317, p. 1903–1906, doi:10.1126/science.1140325.

Anbar, A.D., and Knoll, A.H., 2002, Proterozoic Ocean Chemistry and Evolution: A Bioinorganic Bridge? Science, v. 297, p. 1137–1142, doi:10.1126/science.1069651.

Appel, Fedo, Moorbath, and Myers, 1998, Recognizable primary volcanic and sedimentary features in a low-strain domain of the highly deformed, oldest known (≈ 3.7–3.8 Gyr) Greenstone Belt, Isua, West Greenland: Terra Nova, v. 10, p. 57–62, doi:10.1046/j.1365-3121.1998.00162.x.

Avice, G., Marty, B., Burgess, R., Hofmann, A., Philippot, P., Zahnle, K., and Zakharov, D., 2018, Evolution of atmospheric xenon and other noble gases inferred from Archean to Paleoproterozoic rocks: Geochimica et Cosmochimica Acta, v. 232, p. 82–100, doi:10.1016/j.gca.2018.04.018.

Bachan, A., and Kump, L.R., 2015, The rise of oxygen and siderite oxidation during the Lomagundi Event: Proceedings of the National Academy of Sciences, v. 112, p. 6562–6567, doi:10.1073/pnas.1422319112.

Barry, P.H., and Hilton, D.R., 2016, Release of subducted sedimentary nitrogen throughout Earth's mantle: Geochemical Perspectives Letters, p. 148–159, doi:10.7185/geochemlet.1615.

Bau, M., and Dulski, P., 1996, Distribution of yttrium and rare-earth elements in the Penge and Kuruman iron-formations, Transvaal Supergroup, South Africa: Precambrian Research, v. 79, p. 37–55, doi:10.1016/0301-9268(95)00087-9.

Bau, M., Schmidt, K., Koschinsky, A., Hein, J., Kuhn, T., and Usui, A., 2014, Discriminating between different genetic types of marine ferro-manganese crusts and nodules based on rare earth elements and yttrium: Chemical Geology, v. 381, p. 1–9, doi:10.1016/j.chemgeo.2014.05.004.

Bekker, A., and Holland, H.D., 2012, Oxygen overshoot and recovery during the early Paleoproterozoic: Earth and Planetary Science Letters, v. 317–318, p. 295–304, doi:10.1016/j.epsl.2011.12.012.

Bekker, A., Holland, H.D., Wang, P.-L., Rumble Iii, D., Stein, H.J., Hannah, J.L., Coetzee, L.L., and Beukes, N.J., 2004, Dating the rise of atmospheric oxygen:, www.nature.com/nature.

Bell, E.A., Boehnke, P., Harrison, T.M., and Mao, W.L., 2015, Potentially biogenic carbon preserved in a 4.1 billion-year-old zircon: Proceedings of the National Academy of Sciences, v. 112, p. 14518–14521, doi:10.1073/pnas.1517557112.

Bellot, N., 2016, Application du système isotopique 138La-138Ce en contexte de subduction intra-océanique : les Petites Antilles et les Mariannes: PhD diss., Université Blaise Pascal-Clermont Ferrand II.

Bellot, N., Boyet, M., Doucelance, R., Bonnand, P., Savov, I.P., Plank, T., and Elliott, T., 2018, Origin of negative cerium anomalies in subduction-related volcanic samples: Constraints from Ce and Nd isotopes: Chemical Geology, v. 500, p. 46–63, doi:10.1016/j.chemgeo.2018.09.006.

Bennett, A.C., Murugapiran, S.K., Kees, E.D., Sauer, H.M., and Hamilton, T.L., 2022, Temperature and Geographic Location Impact the Distribution and Diversity of Photoautotrophic Gene Variants in Alkaline Yellowstone Hot Springs: Microbiology Spectrum, v. 10, doi:10.1128/spectrum.01465-21.

Berner, R.A., 2006, GEOCARBSULF: A combined model for Phanerozoic atmospheric O2 and CO2: Geochimica et Cosmochimica Acta, v. 70, p. 5653–5664, doi:10.1016/j.gca.2005.11.032.

Bonnand, P., Lalonde, S. v., Boyet, M., Heubeck, C., Homann, M., Nonnotte, P., Foster, I., Konhauser, K.O., and Köhler, I., 2020, Post-depositional REE mobility in a Paleoarchean banded iron formation revealed by La-Ce geochronology: A cautionary tale for signals of ancient oxygenation: Earth and Planetary Science Letters, v. 547, doi:10.1016/j.epsl.2020.116452.

Bortoluzzi, M., and Ferraro, V., 2020, 138La as a useful isotope for gamma spectroscopy without radioactive sources: Spectroscopy Europe, www.spectroscopyeurope.com.

Bowring, S.A., and Williams, I.S., 1999, Priscoan (4.00-4.03 Ga) orthogneisses from northwestern Canada: Contributions to Mineralogy and Petrology, v. 134, p. 3–16, doi:10.1007/s004100050465.

Brasier, M.D., Green, O.R., Jephcoat, A.P., Kleppe, A.K., van Kranendonk, M.J., Lindsay, J.F., Steele, A., and Grassineau, N. v., 2002, Questioning the evidence for Earth's oldest fossils: Nature, v. 416, p. 76–81, doi:10.1038/416076a.

Brocks, J.J., Logan, G.A., Buick, R., and Summons, R.E., 1999, Archean Molecular Fossils and the Early Rise of Eukaryotes: Science, doi:10.1126/science.285.5430.1033.

Brown, M., 2006, Duality of thermal regimes is the distinctive characteristic of plate tectonics since the Neoarchean: Geology, v. 34, p. 961, doi:10.1130/G22853A.1.

Butterfield, N.J., 2015, Proterozoic photosynthesis - a critical review: Palaeontology, v. 58, p. 953–972, doi:10.1111/pala.12211.

Canfield, D.E., 1998, A new model for Proterozoic ocean chemistry: Nature, v. 396, p. 450–453, doi:10.1038/24839.

Canfield, D.E., 2005, THE EARLY HISTORY OF ATMOSPHERIC OXYGEN: Homage to Robert M. Garrels: Annual Review of Earth and Planetary Sciences, v. 33, p. 1–36, doi:10.1146/annurev.earth.33.092203.122711.

Cates, N.L., and Mojzsis, S.J., 2007, Pre-3750 Ma supracrustal rocks from the Nuvvuagittuq supracrustal belt, northern Québec: Earth and Planetary Science Letters, v. 255, p. 9–21, doi:10.1016/j.epsl.2006.11.034.

Cates, N.L., Ziegler, K., Schmitt, A.K., and Mojzsis, S.J., 2013, Reduced, reused and recycled: Detrital zircons define a maximum age for the Eoarchean (ca. 3750–

3780Ma) Nuvvuagittuq Supracrustal Belt, Québec (Canada): Earth and Planetary Science Letters, v. 362, p. 283–293, doi:10.1016/j.epsl.2012.11.054.

Catling, D.C., and Zahnle, K.J., 2020, The Archean atmosphere:, http://advances.sciencemag.org/.

Catling, D.C., Zahnle, K.J., and McKay, C.P., 2001, Biogenic Methane, Hydrogen Escape, and the Irreversible Oxidation of Early Earth: Science, v. 293, p. 839–843, doi:10.1126/science.1061976.

Cavosie, A.J., Valley, J.W., and Wilde, S.A., 2007, Chapter 2.5 The Oldest Terrestrial Mineral Record: A Review of 4400 to 4000 Ma Detrital Zircons from Jack Hills, Western Australia, *in* p. 91–111, doi:10.1016/S0166-2635(07)15025-8.

Cawood, P.A., and Hawkesworth, C.J., 2014, Earth's middle age: Geology, v. 42, p. 503–506, doi:10.1130/G35402.1.

Cawood, P.A., and Hawkesworth, C.J., 2015, Temporal relations between mineral deposits and global tectonic cycles: Geological Society, London, Special Publications, v. 393, p. 9–21, doi:10.1144/SP393.1.

Cawood, P.A., Hawkesworth, C.J., Pisarevsky, S.A., Dhuime, B., Capitanio, F.A., and Nebel, O., 2018, Geological archive of the onset of plate tectonics: Philosophical Transactions of the Royal Society A: Mathematical, Physical and Engineering Sciences, v. 376, p. 20170405, doi:10.1098/rsta.2017.0405.

Chacko, T., Cole, D.R., and Horita, J., 2001, Equilibrium Oxygen, Hydrogen and Carbon Isotope Fractionation Factors Applicable to Geologic Systems: Reviews in Mineralogy and Geochemistry, v. 43, p. 1–81, doi:10.2138/gsrmg.43.1.1.

Coltice, N., Bertrand, H., Rey, P., Jourdan, F., Phillips, B.R., and Ricard, Y., 2009, Global warming of the mantle beneath continents back to the Archaean: Gondwana Research, v. 15, p. 254–266, doi:10.1016/j.gr.2008.10.001.

Condie, K.C., 2018, A planet in transition: The onset of plate tectonics on Earth between 3 and 2 Ga? Geoscience Frontiers, v. 9, p. 51–60, doi:10.1016/j.gsf.2016.09.001.

Condie, K.C., 1981, Archean Greenstone belts (Elsevier, Ed.).

Crowe, S.A., Døssing, L.N., Beukes, N.J., Bau, M., Kruger, S.J., Frei, R., and Canfield, D.E., 2013, Atmospheric oxygenation three billion years ago: Nature, v. 501, p. 535–538, doi:10.1038/nature12426.

Dickin, A.P., 1987, La–Ce dating of Lewisian granulites to constrain the 138La β-decay half-life: Nature, v. 325, p. 337–338, doi:10.1038/325337a0.

Driese, S.G., Jirsa, M.A., Ren, M., Brantley, S.L., Sheldon, N.D., Parker, D., and Schmitz, M., 2011, Neoarchean paleoweathering of tonalite and metabasalt: Implications for reconstructions of 2.69Ga early terrestrial ecosystems and paleoatmospheric chemistry: Precambrian Research, v. 189, p. 1–17, doi:10.1016/j.precamres.2011.04.003.

Eickmann, B., Hofmann, A., Wille, M., Bui, T.H., Wing, B.A., and Schoenberg, R., 2018, Isotopic evidence for oxygenated Mesoarchaean shallow oceans: Nature Geoscience, v. 11, p. 133–138, doi:10.1038/s41561-017-0036-x.

Eigenbrode, J.L., and Freeman, K.H., 2006, Late Archean rise of aerobic microbial ecosystems: Proceedings of the National Academy of Sciences, v. 103, p. 15759–15764, doi:10.1073/pnas.0607540103.

Eriksson, P.G., and Cheney, E.S., 1992, Evidence for the transition to an oxygen-rich atmosphere during the evolution of red beds in the lower proterozoic sequences of southern Africa: Precambrian Research, v. 54, p. 257–269, doi:10.1016/0301-9268(92)90073-W.

Farquhar, J., Bao, H., and Thiemens, M., 2000, Atmospheric influence of Earth's earliest sulfur cycle: Science, v. 289, p. 756–758, doi:10.1126/science.289.5480.756.

Feulner, G., 2012, The faint young Sun problem: Reviews of Geophysics, v. 50, doi:10.1029/2011RG000375.

Fischer, W.W., Hemp, J., and Valentine, J.S., 2016, How did life survive Earth's great oxygenation? Current Opinion in Chemical Biology, v. 31, p. 166–178, doi:10.1016/j.cbpa.2016.03.013.

François, C., Philippot, P., Rey, P., and Rubatto, D., 2014, Burial and exhumation during Archean sagduction in the East Pilbara Granite-Greenstone Terrane: Earth and Planetary Science Letters, v. 396, p. 235–251, doi:10.1016/j.epsl.2014.04.025.

French, K.L. et al., 2015, Reappraisal of hydrocarbon biomarkers in Archean rocks: Proceedings of the National Academy of Sciences of the United States of America, v. 112, p. 5915–5920, doi:10.1073/pnas.1419563112.

Gaillard, F., Scaillet, B., and Arndt, N.T., 2011, Atmospheric oxygenation caused by a change in volcanic degassing pressure: Nature, v. 478, p. 229–232, doi:10.1038/nature10460.

Galili, N. et al., 2019, The geologic history of seawater oxygen isotopes from marine iron oxides: Science, v. 365, p. 469–473, doi:10.1126/science.aaw9247.

Gebauer, S., Grenfell, J.L., Lammer, H., de Vera, J.-P.P., Sproß, L., Airapetian, V.S., Sinnhuber, M., and Rauer, H., 2020, Atmospheric Nitrogen When Life Evolved on Earth: Astrobiology, v. 20, p. 1413–1426, doi:10.1089/ast.2019.2212.

Genda, H., and Ikoma, M., 2008, Origin of the ocean on the Earth: Early evolution of water D/H in a hydrogen-rich atmosphere: Icarus, v. 194, p. 42–52, doi:10.1016/j.icarus.2007.09.007.

German, C.R., and Elderfield, H., 1990, Application of the Ce anomaly as a paleoredox indicator: The ground rules: Paleoceanography, v. 5, p. 823–833, doi:10.1029/PA005i005p00823.

Gilliland, R.L., 1989, Solar evolution: Global and Planetary Change, v. 1, p. 35–55, doi:10.1016/0921-8181(89)90015-5.

Goldblatt, C., Claire, M.W., Lenton, T.M., Matthews, A.J., Watson, A.J., and Zahnle, K.J., 2009, Nitrogen-enhanced greenhouse warming on early Earth: Nature Geoscience, v. 2, p. 891–896, doi:10.1038/ngeo692.

Goodwin, A.M., and Smith, I.E.M., 1980, Chemical discontinuities in Archean metavolcanic terrains and the development of Archean crust: Precambrian Research, v. 10, p. 301–311, doi:10.1016/0301-9268(80)90016-9.

Gough, D.O., 1981, Solar Interior Structure and Luminosity Variations, *in* Physics of Solar Variations, Dordrecht, Springer Netherlands, p. 21–34, doi:10.1007/978-94-010-9633-1_4.

Grotzinger, J.P., and Kasting, J.F., 1993, New Constraints on Precambrian Ocean Composition: The Journal of Geology, v. 101, p. 235–243, doi:10.1086/648218.

Guo, Q. et al., 2009, Reconstructing Earth's surface oxidation across the Archean-Proterozoic transition: Geology, v. 37, p. 399–402, doi:10.1130/G25423A.1.

Habicht, K.S., Gade, M., Thamdrup, B., Berg, P., and Canfield, D.E., 2002, Calibration of Sulfate Levels in the Archean Ocean: Science, v. 298, p. 2372–2374, doi:10.1126/science.1078265.

Harland, W., Armstrong, R.L., Cox, A. v., Craig, L.E., Smith, A.G., and Smith D. G., 1989, A Geologic Time Scale: Cambridge, Cambridge University Press.

Harrison, T.M., 2009, The Hadean Crust: Evidence from 4 Ga Zircons: Annual Review of Earth and Planetary Sciences, v. 37, p. 479–505, doi:10.1146/annurev.earth.031208.100151.

Havig, J.R., Hamilton, T.L., Bachan, A., and Kump, L.R., 2017, Sulfur and carbon isotopic evidence for metabolic pathway evolution and a four-stepped Earth system

progression across the Archean and Paleoproterozoic: Earth-Science Reviews, v. 174, p. 1–21, doi:10.1016/j.earscirev.2017.06.014.

Hawkesworth, C.J., Cawood, P.A., and Dhuime, B., 2016, Tectonics and crustal evolution: GSA Today, v. 26, p. 4–11, doi:10.1130/GSATG272A.1.

Hayashi, T., Tanimizu, M., and Tanaka, T., 2004, Origin of negative Ce anomalies in Barberton sedimentary rocks, deduced from La-Ce and Sm-Nd isotope systematics, *in* Precambrian Research, Elsevier B.V., v. 135, p. 345–357, doi:10.1016/j.precamres.2004.09.004.

Hofmann, H.J., 1985, Archean Stromatolites from Uchi Greenstone Belt, Northwestern Ontario: Geological Association of Canada Special Paper.

Hohmann-Marriott, M.F., and Blankenship, R.E., 2011, Evolution of photosynthesis: Annual Review of Plant Biology.

Holland, H.D., 1984, The Chemical Evolution of the Atmosphere and Oceans: Princeton University Press, 598 p.

Holland, H.D., 2006, The oxygenation of the atmosphere and oceans: Philosophical Transactions of the Royal Society B: Biological Sciences, v. 361, p. 903–915, doi:10.1098/rstb.2006.1838.

Holland, H.D., 2002, Volcanic gases, black smokers, and the great oxidation event: Geochimica et Cosmochimica Acta, v. 66, p. 3811–3826, doi:10.1016/S0016-7037(02)00950-X.

Homann, M., 2019, Earliest life on Earth: Evidence from the Barberton Greenstone Belt, South Africa: Earth-Science Reviews, v. 196, doi:10.1016/j.earscirev.2019.102888.

van Hunen, J., and Moyen, J.-F., 2012, Archean Subduction: Fact or Fiction? Annual Review of Earth and Planetary Sciences, v. 40, p. 195–219, doi:10.1146/annurev-earth-042711-105255.

James, H.L., and Trendall, A.F., 1982, Banded Iron Formation: Distribution in Time and Paleoenvironmental Significance, *in* Mineral Deposits and the Evolution of the Biosphere, Berlin, Heidelberg, Springer Berlin Heidelberg, p. 199–217, doi:10.1007/978-3-642-68463-0_11.

Jaupart, C., Labrosse, S., and Mareschal, J.-C., 2007, Temperatures, Heat and Energy in the Mantle of the Earth, *in* Treatise on Geophysics, Elsevier, p. 253–303, doi:10.1016/B978-044452748-6.00114-0.

Johnson, C.M., Beard, B.L., and Roden, E.E., 2008, The iron isotope fingerprints of redox and biogeochemical cycling in modern and ancient earth: Annual Review of Earth and Planetary Sciences, v. 36, p. 457–493, doi:10.1146/annurev.earth.36.031207.124139.

Johnson, J.E., Gerpheide, A., Lamb, M.P., and Fischer, W.W., 2014, O2 constraints from Paleoproterozoic detrital pyrite and uraninite: Geological Society of America Bulletin, v. 126, p. 813–830, doi:10.1130/B30949.1.

Johnson, B.W., and Goldblatt, C., 2018, EarthN: A New Earth System Nitrogen Model: Geochemistry, Geophysics, Geosystems, v. 19, p. 2516–2542, doi:10.1029/2017GC007392.

Johnson, J.E., Webb, S.M., Thomas, K., Ono, S., Kirschvink, J.L., and Fischer, W.W., 2013, Manganese-oxidizing photosynthesis before the rise of cyanobacteria: Proceedings of the National Academy of Sciences, v. 110, p. 11238–11243, doi:10.1073/pnas.1305530110.

Kamber, B.S., 2015, The evolving nature of terrestrial crust from the Hadean, through the Archaean, into the Proterozoic: Precambrian Research, v. 258, p. 48–82, doi:10.1016/j.precamres.2014.12.007.

Kanzaki, Y., and Murakami, T., 2015, Estimates of atmospheric CO2 in the Neoarchean–Paleoproterozoic from paleosols: Geochimica et Cosmochimica Acta, v. 159, p. 190–219, doi:10.1016/j.gca.2015.03.011.

Karhu, J.A., and Holland, H.D., 1996, Carbon isotopes and the rise of atmospheric oxygen: Geology, v. 24, p. 867, doi:10.1130/0091-7613(1996)024<0867:CIATRO>2.3.CO;2.

Kasting, J.F., 1993, Earth's Early Atmosphere: Science, v. 259, p. 920–926, doi:10.1126/science.11536547.

Kasting, J.F., 1982, Stability of ammonia in the primitive terrestrial atmosphere: Journal of Geophysical Research, v. 87, p. 3091, doi:10.1029/JC087iC04p03091.

Kasting, J.F., 1987, Theoretical constraints on oxygen and carbon dioxide concentrations in the Precambrian atmosphere: Precambrian Research, v. 34, p. 205–229, doi:10.1016/0301-9268(87)90001-5.

Kasting, J.F., Howard, M.T., Wallmann, K., Veizer, J., Shields, G., and Jaffrés, J., 2006, Paleoclimates, ocean depth, and the oxygen isotopic composition of seawater: Earth and Planetary Science Letters, v. 252, p. 82–93, doi:10.1016/j.epsl.2006.09.029.

Kato, Y., Kawakami, T., Kano, T., Kunugiza, K., and Swamy, N.S., 1996, Rare-earth element geochemistry of banded iron formations and associated amphibolite from the Sargur belts, south India: Journal of Southeast Asian Earth Sciences, v. 14, p. 161–164, doi:10.1016/S0743-9547(96)00054-2.

Kemp, A.I.S., Wilde, S.A., Hawkesworth, C.J., Coath, C.D., Nemchin, A., Pidgeon, R.T., Vervoort, J.D., and DuFrane, S.A., 2010, Hadean crustal evolution revisited: New constraints from Pb–Hf isotope systematics of the Jack Hills zircons: Earth and Planetary Science Letters, v. 296, p. 45–56, doi:10.1016/j.epsl.2010.04.043.

Kendall, B., Creaser, R.A., Reinhard, C.T., Lyons, T.W., and Anbar, A.D., 2015, Transient episodes of mild environmental oxygenation and oxidative continental weathering during the late Archean: Science Advances, v. 1, doi:10.1126/sciadv.1500777.

Kharecha, P., Kasting, J., and Sieffert J., 2005, A coupled atmosphere-ecosystem model of the early Archean Earth: Geobiology, v. 3, p. 53–76, doi:10.1111/j.1472-4669.2005.00049.x.

Killingsworth, B.A., Sansjofre, P., Philippot, P., Cartigny, P., Thomazo, C., and Lalonde, S. v., 2019, Constraining the rise of oxygen with oxygen isotopes: Nature Communications, v. 10, p. 4924, doi:10.1038/s41467-019-12883-2.

Kipp, M.A., Stüeken, E.E., Yun, M., Bekker, A., and Buick, R., 2018, Pervasive aerobic nitrogen cycling in the surface ocean across the Paleoproterozoic Era: Earth and Planetary Science Letters, v. 500, p. 117–126, doi:10.1016/j.epsl.2018.08.007.

Klein, C., 2005, Some Precambrian banded iron-formations (BIFs) from around the world: Their age, geologic setting, mineralogy, metamorphism, geochemistry, and origins: American Mineralogist, v. 90, p. 1473–1499, doi:10.2138/am.2005.1871.

Knauth, L.P., and Lowe, D.R., 2003, High Archean climatic temperature inferred from oxygen isotope geochemistry of cherts in the 3.5 Ga Swaziland Supergroup, South Africa: Geological Society of America Bulletin, v. 115, p. 566–580, doi:10.1130/0016-7606(2003)115<0566:HACTIF>2.0.CO;2.

Knauth, L.P., and Lowe, D.R., 1978, Oxygen isotope geochemistry of cherts from the Onverwacht Group (3.4 billion years), Transvaal, South Africa, with implications for secular variations in the isotopic composition of cherts: Earth and Planetary Science Letters, v. 41, p. 209–222, doi:10.1016/0012-821X(78)90011-0.

Konhauser, K.O. et al., 2011, Aerobic bacterial pyrite oxidation and acid rock drainage during the Great Oxidation Event: Nature, v. 478, p. 369–373, doi:10.1038/nature10511.

van Kranendonk, M.J., 2011, Onset of Plate Tectonics: Science, v. 333, p. 413–414, doi:10.1126/science.1208766.

van Kranendonk, M., 2006, Volcanic degassing, hydrothermal circulation and the flourishing of early life on Earth: A review of the evidence from c. 3490-3240 Ma rocks of the Pilbara Supergroup, Pilbara Craton, Western Australia: Earth-Science Reviews, v. 74, p. 197–240, doi:10.1016/j.earscirev.2005.09.005.

Krissansen-Totton, J., Arney, G.N., and Catling, D.C., 2018, Constraining the climate and ocean pH of the early Earth with a geological carbon cycle model: Proceedings of the National Academy of Sciences, v. 115, p. 4105–4110, doi:10.1073/pnas.1721296115.

Kump, L.R., and Barley, M.E., 2007, Increased subaerial volcanism and the rise of atmospheric oxygen 2.5 billion years ago: Nature, v. 448, p. 1033–1036, doi:10.1038/nature06058.

Kurokawa, H., Foriel, J., Laneuville, M., Houser, C., and Usui, T., 2018, Subduction and atmospheric escape of Earth's seawater constrained by hydrogen isotopes: Earth and Planetary Science Letters, v. 497, p. 149–160, doi:10.1016/j.epsl.2018.06.016.

Kusky, T.M., and Hudleston, P.J., 1999, Growth and demise of an Archean carbonate platform, Steep Rock Lake, Ontario, Canada: Canadian Journal of Earth Sciences, v. 36, p. 565–584, doi:10.1139/e98-108.

Lalonde, S. V., and Konhauser, K.O., 2015, Benthic perspective on Earth's oldest evidence for oxygenic photosynthesis: Proceedings of the National Academy of Sciences, v. 112, p. 995–1000, doi:10.1073/pnas.1415718112.

Lepot, K., 2020, Signatures of early microbial life from the Archean (4 to 2.5 Ga) eon: Earth-Science Reviews, v. 209, p. 103296, doi:10.1016/j.earscirev.2020.103296.

Levine, J.S., Augustsson, T.R., and Hoell, J.M., 1980, The vertical distribution of tropospheric ammonia: Geophysical Research Letters, v. 7, p. 317–320, doi:10.1029/GL007i005p00317.

Li, W., Czaja, A.D., van Kranendonk, M.J., Beard, B.L., Roden, E.E., and Johnson, C.M., 2013, An anoxic, Fe(II)-rich, U-poor ocean 3.46 billion years ago: Geochimica et Cosmochimica Acta, v. 120, p. 65–79, doi:10.1016/j.gca.2013.06.033.

Li, W., Johnson, C.M., and Beard, B.L., 2012, U–Th–Pb isotope data indicate phanerozoic age for oxidation of the 3.4Ga Apex Basalt: Earth and Planetary Science Letters, v. 319–320, p. 197–206, doi:10.1016/j.epsl.2011.12.035.

Li, Z.-Q., Zhang, L.-C., Xue, C.-J., Zheng, M.-T., Zhu, M.-T., Robbins, L.J., Slack, J.F., Planavsky, N.J., and Konhauser, K.O., 2018, Earth's youngest banded iron formation implies ferruginous conditions in the Early Cambrian ocean: Scientific Reports, v. 8, p. 9970, doi:10.1038/s41598-018-28187-2.

Loiacono, S.T., Meyer-Dombard, D.R., Havig, J.R., Poret-Peterson, A.T., Hartnett, H.E., and Shock, E.L., 2012, Evidence for high-temperature in situ nifH transcription in an alkaline hot spring of Lower Geyser Basin, Yellowstone National Park: Environmental Microbiology, v. 14, p. 1272–1283, doi:10.1111/j.1462-2920.2012.02710.x.

Lowe, D.R., and Byerly, G.R., 2015, Geologic record of partial ocean evaporation triggered by giant asteroid impacts, 3.29–3.23 billion years ago: Geology, v. 43, p. 535–538, doi:10.1130/G36665.1.

Luo, G., Ono, S., Beukes, N.J., Wang, D.T., Xie, S., and Summons, R.E., 2016, Rapid oxygenation of Earth's atmosphere 2.33 billion years ago: Science Advances, v. 2, doi:10.1126/sciadv.1600134.

Lyons, T.W., Reinhard, C.T., and Planavsky, N.J., 2014, The rise of oxygen in Earth's early ocean and atmosphere: Nature, v. 506, p. 307–315, doi:10.1038/nature13068.

Mallik, A., Li, Y., and Wiedenbeck, M., 2018, Nitrogen evolution within the Earth's atmosphere–mantle system assessed by recycling in subduction zones: Earth and Planetary Science Letters, v. 482, p. 556–566, doi:10.1016/j.epsl.2017.11.045.

Martin, H., Chauvel, C., and Jahn, B.-M., 1983, Major and trace element geochemistry and crustal evolution of Archaean granodioritic rocks from eastern Finland: Precambrian Research, v. 21, p. 159–180, doi:10.1016/0301-9268(83)90039-6.

Marty, B., Zimmermann, L., Pujol, M., Burgess, R., and Philippot, P., 2013, Nitrogen Isotopic Composition and Density of the Archean Atmosphere: Science, v. 342, p. 101–104, doi:10.1126/science.1240971.

McIntyre, T., and Fralick, P., 2017, Sedimentology and Geochemistry of the 2930 Ma Red Lake-Wallace Lake Carbonate Platform, Western Superior Province, Canada: The Depositional Record, v. 3, p. 258–287, doi:10.1002/dep2.36.

Mojzsis, S.J., Harrison, T.M., and Pidgeon, R.T., 2001, Oxygen-isotope evidence from ancient zircons for liquid water at the Earth's surface 4,300 Myr ago: Nature, v. 409, p. 178–181, doi:10.1038/35051557.

Muehlenbachs, K., Anderson, A.T., and Sigvaldason, G.E., 1974, Low-O18 basalts from Iceland: Geochimica et Cosmochimica Acta, v. 38, p. 577–588, doi:10.1016/0016-7037(74)90042-8.

Noffke, N., 2009, The criteria for the biogeneicity of microbially induced sedimentary structures (MISS) in Archean and younger, sandy deposits: Earth-Science Reviews, v. 96, p. 173–180, doi:10.1016/j.earscirev.2008.08.002.

Noffke, N., Christian, D., Wacey, D., and Hazen, R.M., 2013, Microbially Induced Sedimentary Structures Recording an Ancient Ecosystem in the *ca.* 3.48 Billion-Year-Old Dresser Formation, Pilbara, Western Australia: Astrobiology, v. 13, p. 1103–1124, doi:10.1089/ast.2013.1030.

Nutman, A.P., Fryer, B.J., and Bridgwater, D., 1989, The early Archaean Nulliak (supracrustal) assemblage, northern Labrador: Canadian Journal of Earth Sciences, v. 26, p. 2159–2168, doi:10.1139/e89-181.

O'Neil, J., Carlson, R.W., Paquette, J.-L., and Francis, D., 2012, Formation age and metamorphic history of the Nuvvuagittuq Greenstone Belt: Precambrian Research, v. 220–221, p. 23–44, doi:10.1016/j.precamres.2012.07.009.

Papineau, D., de Gregorio, B.T., Cody, G.D., O'Neil, J., Steele, A., Stroud, R.M., and Fogel, M.L., 2011, Young poorly crystalline graphite in the >3.8-Gyr-old Nuvvuagittuq banded iron formation: Nature Geoscience, v. 4, p. 376–379, doi:10.1038/ngeo1155.

Partin, C.A., Lalonde, S. V., Planavsky, N.J., Bekker, A., Rouxel, O.J., Lyons, T.W., and Konhauser, K.O., 2013, Uranium in iron formations and the rise of atmospheric oxygen: Chemical Geology, v. 362, p. 82–90, doi:10.1016/j.chemgeo.2013.09.005.

Pavlov, A.A., Brown, L.L., and Kasting, J.F., 2001, UV shielding of NH3 and O2 by organic hazes in the Archean atmosphere: Journal of Geophysical Research: Planets, v. 106, p. 23267–23287, doi:10.1029/2000JE001448.

Petrescu, L., 2017, Precambrian Lithospheric Structure and Evolution: Evidence from Broadband Seismology in Eastern Canada: PhD diss., Imperial College London,.

Philippot, P. et al., 2018, Globally asynchronous sulphur isotope signals require re-definition of the Great Oxidation Event: Nature Communications, v. 9, p. 2245, doi:10.1038/s41467-018-04621-x.

Philippot, P., van Zuilen, M., Lepot, K., Thomazo, C., Farquhar, J., and van Kranendonk, M.J., 2007, Early Archaean Microorganisms Preferred Elemental Sulfur, Not Sulfate: Science, v. 317, p. 1534–1537, doi:10.1126/science.1145861.

Planavsky, N.J. et al., 2014, Evidence for oxygenic photosynthesis half a billion years before the Great Oxidation Event: Nature Geoscience, v. 7, p. 283–286, doi:10.1038/ngeo2122.

Planavsky, N.J., Bekker, A., Hofmann, A., Owens, J.D., and Lyons, T.W., 2012, Sulfur record of rising and falling marine oxygen and sulfate levels during the Lomagundi event: Proceedings of the National Academy of Sciences, v. 109, p. 18300–18305, doi:10.1073/pnas.1120387109.

Planavsky, N.J., Robbins, L.J., Kamber, B.S., and Schoenberg, R., 2020, Weathering, alteration and reconstructing Earth's oxygenation: Interface Focus, v. 10, p. 20190140, doi:10.1098/rsfs.2019.0140.

Pope, E.C., Bird, D.K., and Rosing, M.T., 2012, Isotope composition and volume of Earth's early oceans: Proceedings of the National Academy of Sciences, v. 109, p. 4371–4376, doi:10.1073/pnas.1115705109.

Poulton, S.W., and Canfield, D.E., 2011, Ferruginous Conditions: A Dominant Feature of the Ocean through Earth's History: Elements, v. 7, p. 107–112, doi:10.2113/gselements.7.2.107.

Poulton, S.W., and Raiswell, R., 2002, The low-temperature geochemical cycle of iron: From continental fluxes to marine sediment deposition: American Journal of Science, v. 302, p. 774–805, doi:10.2475/ajs.302.9.774.

Raiswell, R., Tranter, M., Benning, L.G., Siegert, M., De'ath, R., Huybrechts, P., and Payne, T., 2006, Contributions from glacially derived sediment to the global iron (oxyhydr)oxide cycle: Implications for iron delivery to the oceans: Geochimica et Cosmochimica Acta, v. 70, p. 2765–2780, doi:10.1016/j.gca.2005.12.027.

Rasmussen, B., Fletcher, I.R., Brocks, J.J., and Kilburn, M.R., 2008, Reassessing the first appearance of eukaryotes and cyanobacteria: Nature, v. 455, p. 1101–1104, doi:10.1038/nature07381.

Reinhard, C.T., Lalonde, S. V., and Lyons, T.W., 2013a, Oxidative sulfide dissolution on the early Earth: Chemical Geology, v. 362, p. 44–55, doi:10.1016/j.chemgeo.2013.10.006.

Reinhard, C.T., Planavsky, N.J., and Lyons, T.W., 2013b, Long-term sedimentary recycling of rare sulphur isotope anomalies: Nature, v. 497, p. 100–103, doi:10.1038/nature12021.

Riding, R., 2000, Microbial carbonates: the geological record of calcified bacterial-algal mats and biofilms: Sedimentology, v. 47, p. 179–214, doi:10.1046/j.1365-3091.2000.00003.x.

Riding, R., Fralick, P., and Liang, L., 2014a, Identification of an Archean marine oxygen oasis: Precambrian Research, v. 251, p. 232–237, doi:10.1016/j.precamres.2014.06.017.

Riding, R., Fralick, P., and Liang, L., 2014b, Identification of an Archean marine oxygen oasis: Precambrian Research, v. 251, p. 232–237, doi:10.1016/j.precamres.2014.06.017.

Robert, F., 2001, The Origin of Water on Earth: Science, v. 293, p. 1056–1058, doi:10.1126/science.1064051.

Robert, F., and Chaussidon, M., 2006, A palaeotemperature curve for the Precambrian oceans based on silicon isotopes in cherts: Nature, v. 443, p. 969–972, doi:10.1038/nature05239.

Roman, A., and Arndt, N., 2020, Differentiated Archean oceanic crust: Its thermal structure, mechanical stability and a test of the sagduction hypothesis: Geochimica et Cosmochimica Acta, v. 278, p. 65–77, doi:10.1016/j.gca.2019.07.009.

Rouxel, O.J., Bekker, A., and Edwards, K.J., 2005, Iron isotope constraints on the Archean and Paleoproterozoic ocean redox state: Science, v. 307, p. 1088–1091, doi:10.1126/science.1105692.

Sagan, C., and Mullen, G., 1972, Earth and Mars: Evolution of Atmospheres and Surface Temperatures: Science, v. 177, p. 52–56, doi:10.1126/science.177.4043.52.

Schidlowski, M., 2001, Carbon isotopes as biogeochemical recorders of life over 3.8 Ga of Earth history: evolution of a concept: Precambrian Research, v. 106, p. 117–134, doi:10.1016/S0301-9268(00)00128-5.

Schirrmeister, B.E., Sanchez-Baracaldo, P., and Wacey, D., 2016, Cyanobacterial evolution during the Precambrian: International Journal of Astrobiology, v. 15, p. 187–204, doi:10.1017/s1473550415000579.

Schnabel, C., 2019, 138La-138Ce systematics in terrestrial samples and chondrites: PhD diss., Universität zu Köln.

Schopf, J.W., 1993, Microfossils of the Early Archean Apex Chert: New Evidence of the Antiquity of Life: Science, v. 260, p. 640–646, doi:10.1126/science.260.5108.640.

Shaw, G.H., 2008, Earth's atmosphere – Hadean to early Proterozoic: Geochemistry, v. 68, p. 235–264, doi:10.1016/j.chemer.2008.05.001.

Sheldon, N.D., 2006, Precambrian paleosols and atmospheric CO2 levels: Precambrian Research, v. 147, p. 148–155, doi:10.1016/j.precamres.2006.02.004.

Sizova, E., Gerya, T., and Brown, M., 2014, Contrasting styles of Phanerozoic and Precambrian continental collision: Gondwana Research, v. 25, p. 522–545, doi:10.1016/j.gr.2012.12.011.

Slotznick, S.P., Johnson, J.E., Rasmussen, B., Raub, T.D., Webb, S.M., Zi, J.-W., Kirschvink, J.L., and Fischer, W.W., 2022, Reexamination of 2.5-Ga "whiff" of oxygen interval points to anoxic ocean before GOE: Science Advances, v. 8, doi:10.1126/sciadv.abj7190.

Smithies, R.H., Champion, D.C., and Cassidy, K.F., 2003, Formation of Earth's early Archaean continental crust: Precambrian Research, v. 127, p. 89–101, doi:10.1016/S0301-9268(03)00182-7.

Som, S.M., Buick, R., Hagadorn, J.W., Blake, T.S., Perreault, J.M., Harnmeijer, J.P., and Catling, D.C., 2016, Earth's air pressure 2.7 billion years ago constrained to less than half of modern levels: Nature Geoscience, v. 9, p. 448–451, doi:10.1038/ngeo2713.

Som, S.M., Catling, D.C., Harnmeijer, J.P., Polivka, P.M., and Buick, R., 2012, Air density 2.7 billion years ago limited to less than twice modern levels by fossil raindrop imprints: Nature, v. 484, p. 359–362, doi:10.1038/nature10890.

Song, H. et al., 2017, The onset of widespread marine red beds and the evolution of ferruginous oceans: Nature Communications, v. 8, p. 399, doi:10.1038/s41467-017-00502-x.

Sonzogni, A.A., 2003, Nuclear Data Sheets for A = 138: Nuclear Data Sheets, v. 98, p. 515–664, doi:10.1006/ndsh.2003.0004.

Soo, R.M., Hemp, J., Parks, D.H., Fischer, W.W., and Hugenholtz, P., 2017, On the origins of oxygenic photosynthesis and aerobic respiration in Cyanobacteria: Science.

Stüeken, E.E., and Buick, R., 2018, Environmental control on microbial diversification and methane production in the Mesoarchean: Precambrian Research, v. 304, p. 64–72, doi:10.1016/j.precamres.2017.11.003.

Stüeken, E.E., Buick, R., Guy, B.M., and Koehler, M.C., 2015, Isotopic evidence for biological nitrogen fixation by molybdenum-nitrogenase from 3.2 Gyr: Nature, v. 520, p. 666–669, doi:10.1038/nature14180.

Stüeken, E.E., Catling, D.C., and Buick, R., 2012, Contributions to late Archaean sulphur cycling by life on land: Nature Geoscience, v. 5, p. 722–725, doi:10.1038/ngeo1585.

Tanaka, T., and Masuda, A., 1982, The La–Ce geochronometer: a new dating method: Nature, v. 300, p. 515–518, doi:10.1038/300515a0.

Tang, M., Chen, K., and Rudnick, R.L., 2016, Archean upper crust transition from mafic to felsic marks the onset of plate tectonics: Science, v. 351, p. 372–375, doi:10.1126/science.aad5513.

Tanimizu, M., and Tanaka, T., 2002, Coupled Ce–Nd isotope systematics and rare earth elements differentiation of the moon: Geochimica et Cosmochimica Acta, v. 66, p. 4007–4014, doi:10.1016/S0016-7037(02)00961-4.

Tashiro, T., Ishida, A., Hori, M., Igisu, M., Koike, M., Méjean, P., Takahata, N., Sano, Y., and Komiya, T., 2017, Early trace of life from 3.95 Ga sedimentary rocks in Labrador, Canada: Nature, v. 549, p. 516–518, doi:10.1038/nature24019.

Thomazo, C., Ader, M., and Philippot, P., 2011, Extreme 15N-enrichments in 2.72-Gyr-old sediments: evidence for a turning point in the nitrogen cycle: Geobiology, v. 9, p. 107–120, doi:10.1111/j.1472-4669.2011.00271.x.

Tostevin, R., Shields, G.A., Tarbuck, G.M., He, T., Clarkson, M.O., and Wood, R.A., 2016, Effective use of cerium anomalies as a redox proxy in carbonate-dominated marine settings: Chemical Geology, v. 438, p. 146–162, doi:10.1016/j.chemgeo.2016.06.027.

Towe, K.M., 1991, Aerobic carbon cycling and cerium oxidation: significance for Archean oxygen levels and banded iron-formation deposition: Global and Planetary Change, v. 5, p. 113–123, doi:10.1016/0921-8181(91)90132-G.

Ueno, Y., Ono, S., Rumble, D., and Maruyama, S., 2008, Quadruple sulfur isotope analysis of ca. 3.5 Ga Dresser Formation: New evidence for microbial sulfate reduction in the early Archean: Geochimica et Cosmochimica Acta, v. 72, p. 5675–5691, doi:10.1016/j.gca.2008.08.026.

Ueno, Y., Yurimoto, H., Yoshioka, H., Komiya, T., and Maruyama, S., 2002, Ion microprobe analysis of graphite from ca. 3.8 Ga metasediments, Isua supracrustal belt, West Greenland: Relationship between metamorphism and carbon isotopic composition: Geochimica et Cosmochimica Acta, v. 66, p. 1257–1268, doi:10.1016/S0016-7037(01)00840-7.

Valley, J.W., Peck, W.H., King, E.M., and Wilde, S.A., 2002, A cool early Earth: Geology, v. 30, p. 351, doi:10.1130/0091-7613(2002)030<0351:ACEE>2.0.CO;2.

Wacey, D., Noffke, N., Cliff, J., Barley, M.E., and Farquhar, J., 2015, Micro-scale quadruple sulfur isotope analysis of pyrite from the ~3480Ma Dresser Formation: New insights into sulfur cycling on the early Earth: Precambrian Research, v. 258, p. 24–35, doi:10.1016/j.precamres.2014.12.012.

Wacey, D., Saunders, M., Kong, C., Brasier, A., and Brasier, M., 2016, 3.46 Ga Apex chert 'microfossils' reinterpreted as mineral artefacts produced during phyllosilicate exfoliation: Gondwana Research, v. 36, p. 296–313, doi:10.1016/j.gr.2015.07.010.

Walker, J.C.G., 1982, Climatic factors on the Archean earth: Palaeogeography, Palaeoclimatology, Palaeoecology, v. 40, p. 1–11, doi:10.1016/0031-0182(82)90082-7.

Walker, J.C.G., Hays, P.B., and Kasting, J.F., 1981, A negative feedback mechanism for the long-term stabilization of Earth's surface temperature: Journal of Geophysical Research, v. 86, p. 9776, doi:10.1029/JC086iC10p09776.

Wang, X. et al., 2018, A Mesoarchean shift in uranium isotope systematics: Geochimica et Cosmochimica Acta, v. 238, p. 438–452, doi:10.1016/j.gca.2018.07.024.

Wilde, S.A., Valley, J.W., Peck, W.H., and Graham, C.M., 2001, Evidence from detrital zircons for the existence of continental crust and oceans on the Earth 4.4 Gyr ago: Nature, v. 409, p. 175–178, doi:10.1038/35051550.

Windley, B.F., Kusky, T., and Polat, A., 2021, Onset of plate tectonics by the Eoarchean: Precambrian Research, v. 352, p. 105980, doi:10.1016/j.precamres.2020.105980.

Yoshida, S., Ishikawa, A., Aoki, S., and Komiya, T., 2021, Occurrence and chemical composition of the Eoarchean carbonate rocks of the Nulliak supracrustal rocks in the Saglek Block of northeastern Labrador, Canada: Island Arc, v. 30, doi:10.1111/iar.12381.

Zahnle, K.J., Catling, D.C., and Claire, M.W., 2013, The rise of oxygen and the hydrogen hourglass: Chemical Geology, v. 362, p. 26–34, doi:10.1016/j.chemgeo.2013.08.004.

Zahnle, K., Claire, M., and Catling, D., 2006, The loss of mass-independent fractionation in sulfur due to a Palaeoproterozoic collapse of atmospheric methane: Geobiology, v. 4, p. 271–283, doi:10.1111/j.1472-4669.2006.00085.x.

van Zuilen, M.A., 2019, The Significance of Carbonaceous Matter to Understanding Life Processes on Early Earth, *in* Earth's Oldest Rocks, Elsevier, p. 945–963, doi:10.1016/B978-0-444-63901-1.00038-1.

CHAPTER 2:

GEOLOGICAL CONTEXT

2.1 Regional geology and sample sites

In this study, all samples came from three different Mesoarchean carbonate platforms that are all located (Fig. 2.1) in the Superior Province in Canada: Red Lake (2.93 Ga), Woman Lake (2.85 Ga) and Steep Rock (2.80 Ga). The Superior Province is the largest known Archean craton, covering about 23% of the Earth's exposed Archean crust (Thurston et al., 1991). It lies in the south-central zone of the Canadian Shield and extends from northwestern Quebec to the shores of Lake Superior in Ontario and south to the northern fringes of the United States. The Superior Province has been divided into various subprovinces by Card and Ciesielski, (1986) (e.g., Uchi Subprovince, English River Subprovince, Wabigoon Subprovince, Quetico Subprovince, etc.) based on unique rock types that are primarily Meso-Neoarchean and have undergone significant deformation.

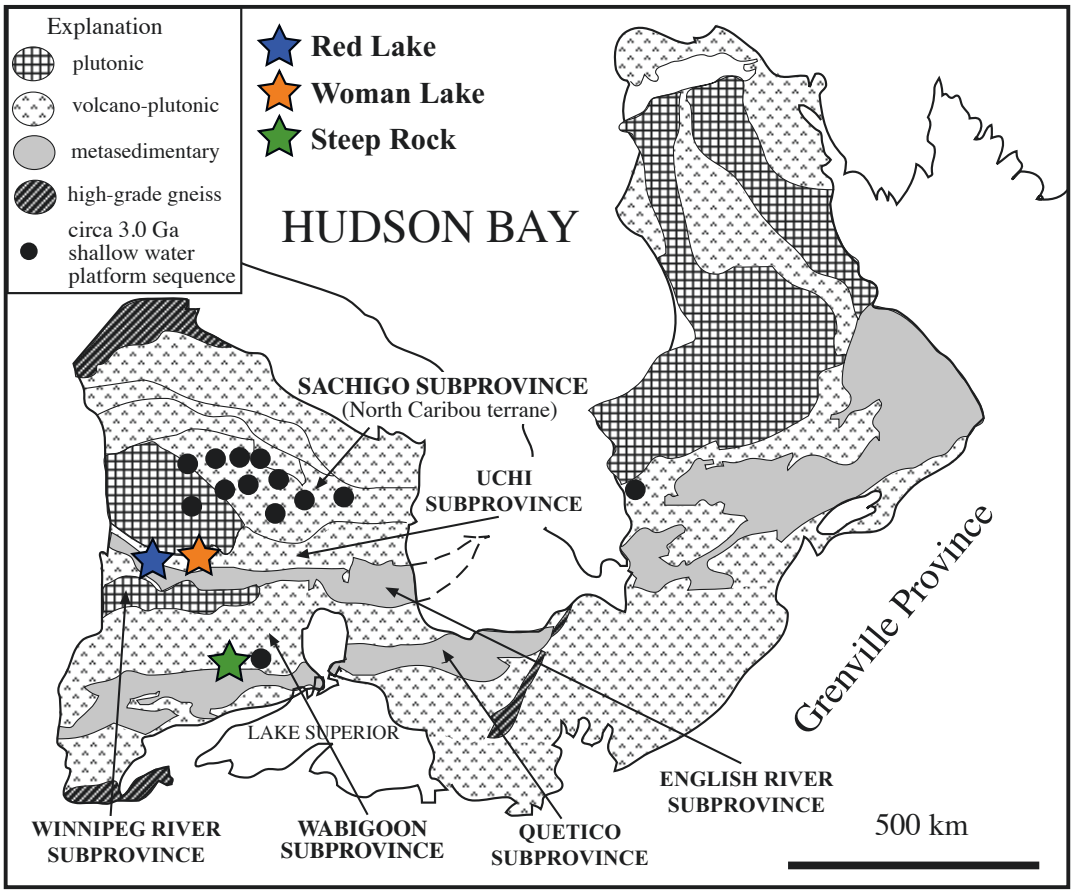

Figure 2.1. Geological map modified from Kusky and Polat, (1999) with the three different study site location (Red Lake, Woman Lake and Steep Rock) in the Superior Craton in Western Ontario, Canada.

2.1.1 Red Lake

The Red Lake carbonate platform is located in the Superior Province on the southern margin of the Uchi Subprovince between the North Caribou Terrane in the North and the English River Subprovince in the South and is part of the Red Lake Greenstone Belt. The latter is mainly composed of a complex succession of metavolcanic-metasedimentary rocks and comprise the Confederation, Slate Bay, Bruce Channel, Huston, Balmer and Ball assemblages. In the Eastern part of the belt is the Balmer assemblage, dated at 2992-2960 Ma by U-Pb on zircons, and includes tholeiitic basalts, basaltic komatiites, komatiite lava flows, and minor interbedded units of felsic metavolcanic rocks and metasedimentary rocks (Corfu and Andrews, 1987; Hollings et al., 1999). In the Western part of the belt lies the Ball assemblage which is mainly composed of a dominantly calc-alkaline mafic to felsic volcanic sequence including minor komatiite, siliciclastic and stromatolitic carbonates (Sanborn-Barrie et al., 2001). This ~200 m-thick stromatolitic carbonate unit is constrained in age by overlying and underlying felsic volcanic rocks dated to between 2940 ± 2 Ma and 2925 ± 3 Ma (Corfu and Wallace, 1986). The metasediments of the Ball assemblage have experience at least upper greenschist to lower amphibolite phase metamorphism on the basis of rare garnet horizons in oxide facies BIF (Afroz, 2019). The Red Lake stromatolitic carbonate platform is one of the oldest carbonate platforms in the world and yet has not attracted much attention and has been the subject of few studies apart from Hofmann (1985). Recently, however, it has regained attention, as McIntyre and Fralick (2017) conducted a more thorough study of the lithofacies of the platform and also performed geochemical analyses involving REE measurements and O, Sr, and C isotopic measurements on the limestones and dolomites. Most of the platform is comprised of structures reflecting a low-energy and supratidal flat to distal platform environment. Initial geochemical data from the carbonates indicated the

possibility of the development of limited zones where oxygen production may have influenced redox conditions in the water column (McIntyre and Fralick, 2017). Another study conducted by Afroz (2019) significantly improved the knowledge of this platform by examining major and trace elements, REE systematics, and organic carbon, carbonate oxygen, and sulfur stable isotope compositions of both chemical sedimentary rocks and siliciclastic black shales. She concluded that carbonates may have formed in a mildly oxic shallow-water environment, magnetite and chert in more distal suboxic environments, and iron sulfides accumulated in a reducing anoxic environment influenced by hydrothermal fluids. The black shales accumulated during the cessation of chemical sedimentation. In addition, the intercalation of the stromatolitic carbonate successions with the deep-water sediments suggests multiple carbonate platform flooding events (Afroz, 2019). Follow-up PhD thesis work examining the entire Ball assemblage in chemostratigraphic profile across multiple drill cores (Afroz, 2023, PhD thesis in prep) reveals highly dynamic major element indicators of fluctuating water column composition and likely redox as well (e.g., Mn, S enrichments), important authigenic enrichments in redox sensitive trace elements such as Mo, Cr, U, and V, and rare Ce anomalies, both positive and negative, that further point to the likely production of free oxygen by oxygenic photosynthesizers in trace amounts, at least temporarily, during deposition of the Ball Assemblage (Afroz, 2023, thesis in prep).

The samples analyzed during this PhD were collected, in the context of the ERC EARTHBLOOM project, from the Red Lake carbonate platform in the Ball Assemblage. More precisely, samples were obtained from drill core NGI10-31 that was collared on the mainland north of Galena Island and from drill core 17-GA1 from the North coast of the Golden Arm area (Fig. 2.2). The NGI10-31 drill core is one of 11 PQ-sized diamond drill cores (approximately 4000m in total) that were donated by Goldcorp, Inc. to the

EARTHBLOOM project following their gold exploration activities in the area over the 2009-2013 period executed in partnership with Halo Resources, Ltd. The NGI10-31 core reveals a shallowing-downward sequence largely composed of stromatolitic carbonates at its base, giving way up section to black shales and sulfurized shales, and eventually to BIF and interbedded siltstone. The short NQ-sized core 17-GA1 was drilled during the summer 2017 fieldtrip by the EARTHBLOOM team using a Shaw backpack drill and samples a large calcitic dome composed of alternating layers of carbonate microbialite and former crystal fans that were likely aragonite in composition before later recrystallization to calcite. See Figure 2.3 for field images of representative microbialites.

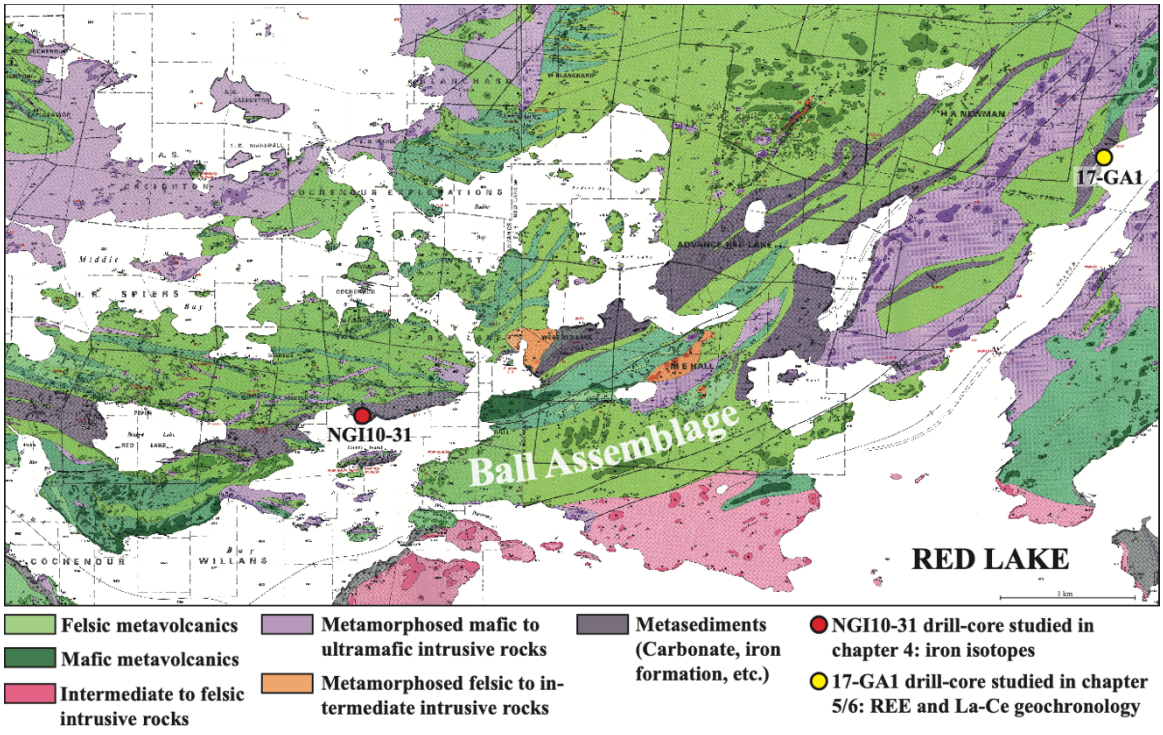

Figure 2.2. Geological map of the Ball Assemblage in Red Lake adapted from Riley (1975, 1978) showing the location of the two drill-core analyzed in this study.

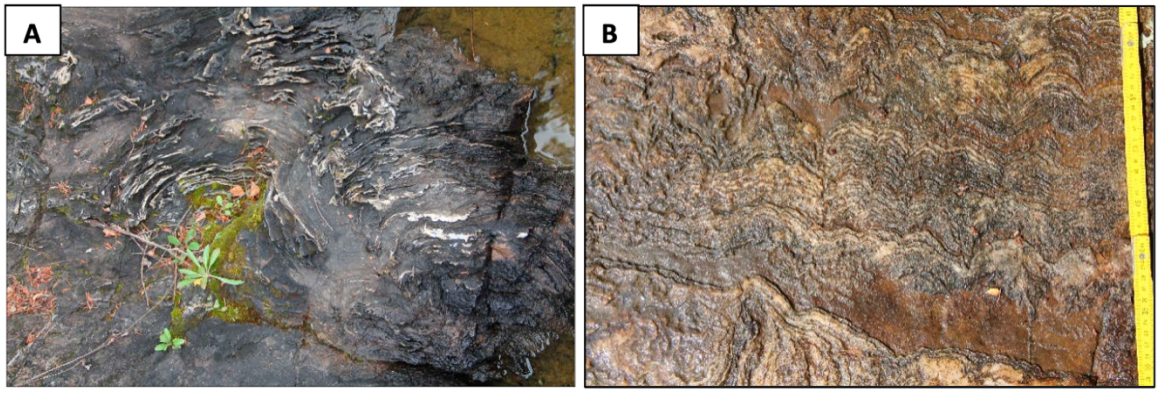

Figure 2.3. Dolomitic domal stromatolites (A) and laminated stromatolitic calcite (B) from the Red Lake carbonate platform. Figure taken from Afroz (2019).

2.1.2 Woman Lake

The 2.857 Ga Woman Lake carbonate platform from Western Ontario, Canada is located in the Uchi subprovince of the Superior province and is part of the Birch-Uchi-Confederation Greenstone Belt. It consists primarily of mafic and felsic metavolcanics and lesser metasediments, with rare chemical sediments (Fig. 2.4 and Thurston, 1980), all of which have been intruded by granitic rocks of Neoarchean age (Ayres et al., 1971; Beakhouse et al., 1999). These volcanic sequences were first recognized by Goodwin (1967) and Pryslak (1971) and then interpreted by Thurston (1980) as three major cycles occurring at 2.959 Ga, 2.840 Ga and 2.738 Ga and are estimated to be about 8.5 to 11.2 km in stratigraphic thickness. Following extensive observations and geochronological measurements, Stott and Corfu (1991) decided to instead redefine the three cycles into three lithotectonic assemblages: the Balmer (2.96 Ga), Woman (2.84 Ga) and Confederation (2.725 Ga) assemblages. The Uchi-Confederation Greenstone Belt was then stratigraphically reinterpreted in 2000 by Rogers et al., who proposed the Balmer assemblage (2.985 Ga), the Narrow Lake assemblage (2.88 Ga) and the Confederation assemblage (2.74 Ga). However, Rogers, (2002) revises the stratigraphy to include five distinct volcanic assemblages separated by unconformities, and considered Woman Lake

as its own assemblage. These five assemblages in order from oldest to youngest are the Balmer assemblage at 2.980 and 2.975 Ga, the Narrow Lake assemblage that is not directly dated but stratigraphically constrained to between 2.975 and 2.870 Ga, the Woman Lake assemblage at 2.870 Ga, the Confederation assemblage at 2.745 to 2.735 Ga and the St. Joseph assemblage at 2.725 Ga (Rogers et al., 2000; Rogers, 2002).

The Woman Lake assemblage begins with pillowed basaltic flows overlain by subaqueous intermediate ash flows, then felsic tuffs and lapilli tuffs with textures indicating local subaerial volcanism (Thurston, 1980). This volcanic sequence is capped by the Woman Lake carbonate platform. The tuff underlying the carbonate was first dated at 2.794 Ga ± 6 Ma using the U-Pb dating system by Nunes and Thurston (1980), then Rogers (2002) reported a new age of ca. 2.870 Ga (V. McNicoll, personal communication to Rogers) and recently it was dated at 2.857 Ga ± 5 Ma by Ramsay (2020), in agreement with the age presented by Rogers (2002). The Woman Lake assemblage has experience temperatures of at least 300°C (Passchier and Trouw, 2005) and thus experienced at least greenschist facies metamorphism (Hofmann et al., 1985; Ramsay, 2020).

The Woman Lake carbonate unit was studied extensively by Ramsay (2020) as part of a Master's thesis with field, petrographic and geochemical investigations to better understand the paleoenvironmental context of this platform. The platform is comprised of stratiform stromatolites interbedded with thin beds of massive carbonate grainstone, followed by laterally linked low domal stromatolites, which gradually become larger domes, then bioherms with walled pseudocolumnar stromatolites (Ramsay, 2020). The main stromatolitic morphologies here support the idea of a peritidal environment on a carbonate platform undergoing fluctuations in sea level and water energies in an overall-

deepening succession. REE patterns, major and trace element concentrations, as well as C and Sr isotope compositions all suggest that the carbonates preserve chemical signatures of ancient seawater and the surrounding environment, and more importantly, show strong evidence for free oxygen in the water column, making Woman Lake a previously-unrecognized Mesoarchean oxygen oasis (Ramsay, 2020).

The samples analyzed from Woman Lake are from the core "A" drilled at the top of the southern stratigraphy, map point 2 (Fig. 2.4) and from outcrop samples all collected during 2019 summer fieldwork. These carbonate samples are low domal silicified stromatolites, massive carbonate grainstone, banded carbonate microbialite, or fenestrated microbialite. See Figure 2.5 for field images of representative microbialites.

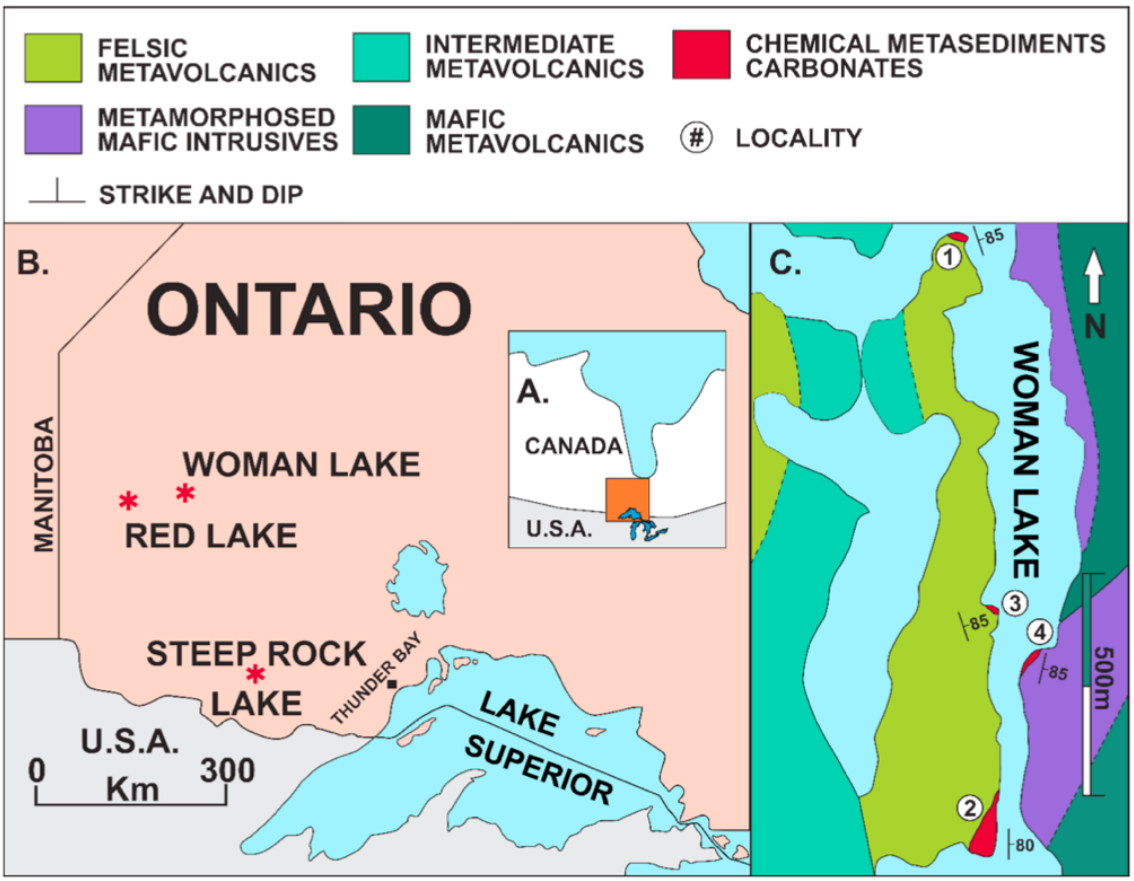

Figure 2.4. Location of Woman Lake relative to Canada (A) and relative to other carbonate platforms in Ontario (B), and its bedrock geology map (C). Figure from Ramsay (2020)

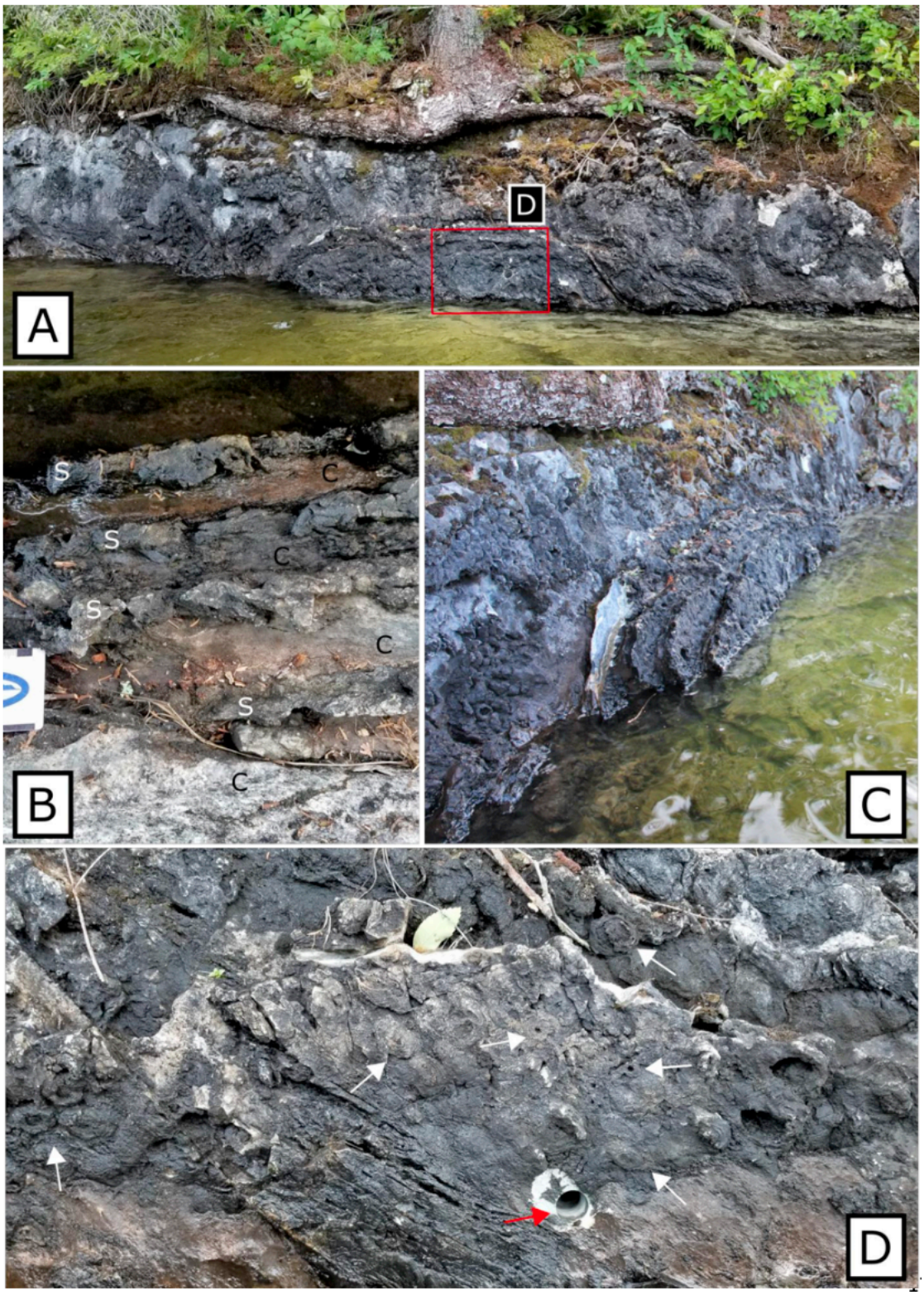

Figure 2.5. Example outcrop and microbialite photos from the Woman Lake carbonate platform (Unit M from Ramsay, 2020). Beds of laterally linked small domal stromatolites alternating with carbonate grainstone and carbonate microbialite (A), cross sectional view of carbonate and silicified stromatolite (S) beds (B). A different view of silicified stromatolite beds alternating with carbonate grainstone (C). Circular stromatolite tops (white arrows) and drill hole locality (red arrow), drill hole diameter is 6 cm (D). Figure taken from Ramsay (2020).

2.1.3 Steep Rock

The 2.8 Ga Mosher Carbonate Formation outcrops around Steep Rock Lake is part of the Steep Rock Group situated in the southern part of the Wabigoon Subprovince, 5 km north of the town of Atikokan in the Quetico Subprovince. The latter, the Lumby Lake Greenstone Belt and the Finlayson Greenstone Belt form a series of correlative sedimentary units disrupted by a major shear zone (Fig 2.6.; Fenwick, 1976; Stone and Pufahl, 1995; Fralick and King, 1996; Wyman and Hollings, 1998; Tomlinson et al., 1999; Fralick et al., 2008). These sedimentary units overlie thick successions of tholeiitic basalts and komatiites that span a time interval from 3.014 Ga near an intrusive contact at their base to 2.828 Ga ± 1 Ma in the upper part of the Lumby Lake belt beneath the sedimentary rocks (Tomlinson et al., 2003).

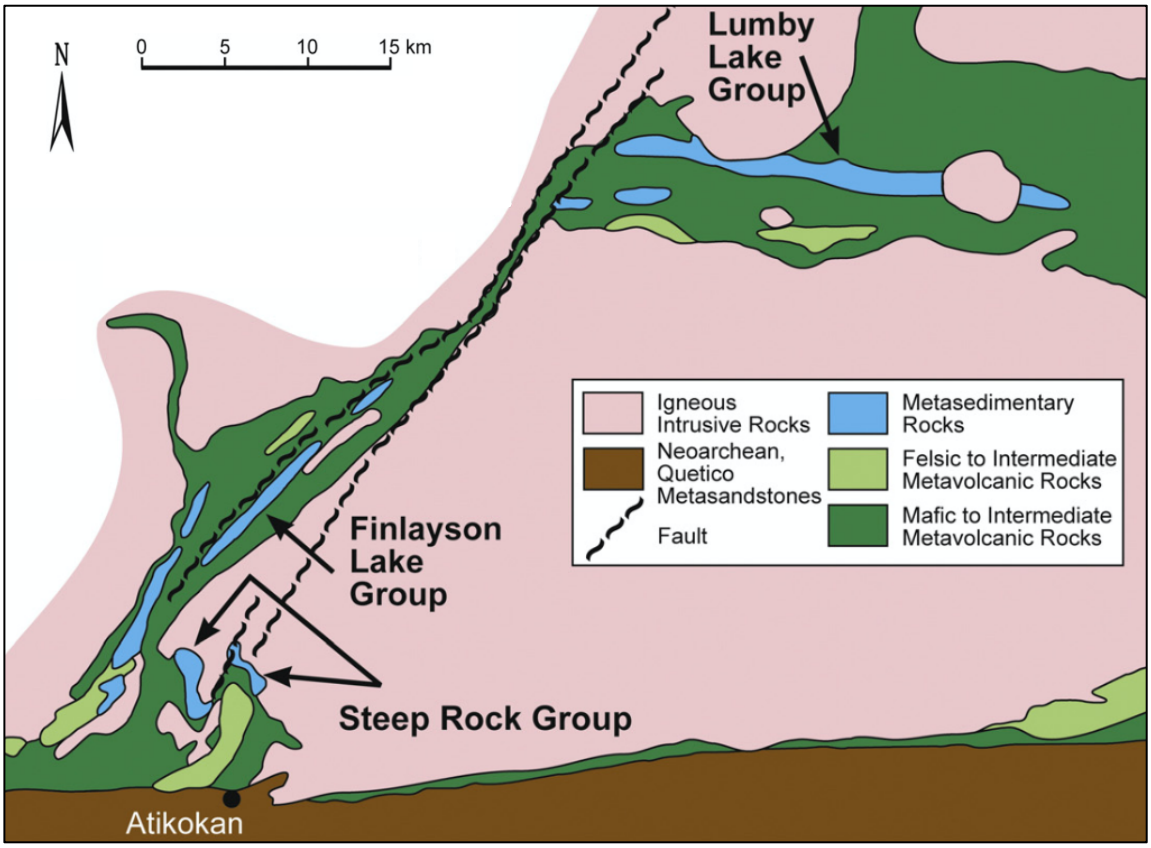

Figure 2.6. Outcrop location of the Steep Rock Group and the two correlative sedimentary successions in the Finlayson Lake and Lumby Lake Greenstone belts.

The number and names of formations included in the Steep Rock Group have been modified many times (Smyth, 1891; Lawson and Walcott, 1912; Jolliffe, 1955). According to Fralick and Riding (2015), the most practical division of the units would be as per Wilks and Nisbet (1988) into four formations: the Wagita Formation (conglomerate, sandstone), the Mosher Carbonate, the Jolliffe Ore Zone, and the Witch Bay Formation.

The sedimentary sequence begins with sandstone and conglomerate of the Wagita Formation that show evidence of erosion into the underlying volcanics and contain zircons as young as 2.779 Ga ± 22 Ma. These zircons place the current upper bound on the age of the overlying Mosher Carbonate at 2801 Ma (Fralick and Riding 2015). Zircons from volcanic rocks in the overlying Dismal Ashrock (Witch Bay Formation) show an age of 2780 ± 1 Ma (Tomlinson et al., 2003), thus constraining the depositional age of the Mosher Carbonate Formation to between 2.801 and 2.780 Ga.

The Mosher Carbonate Formation experienced lower greenschist metamorphism and contains a remarkable and well-preserved assemblage of diverse stromatolite morphologies and associated carbonate sediments that have been the subject of numerous studies (e.g. Smyth, 1891; Lawson and Walcott, 1912; Jolliffe, 1955; Hofmann, 1971; Wilks and Nisbet, 1985, 1988; Kusky and Hudleston, 1999). Stromatolite morphologies show a general trend from stratiform or pseudocolumnar in the lower part, followed by branched and conical forms, to end the upper part of the formation with giant domal stromatolites. In 2015, Fralick and Riding divided the Mosher Carbonate Formation into two parts: (i) the lower Hogarth Member containing domal, pseudocolumnar, columnar and fenestral stratiform stromatolites which are interpreted to have accumulated in a relatively protected inner platform environment, and (ii) the upper Elbow Point Member with giant domes interpreted represent a platform margin deposit in which the alternating calcite-

aragonite mineralogies in each dome reflect a fluctuating redox environment offshore. Major and trace element data as well as C and Fe stable isotope data from the Mosher Carbonate Formation support the idea of an early marine oxygen oasis driven by oxygenic photosynthesis was established on this platform (Riding et al., 2014; Fralick and Riding, 2015; Wilmeth et al., 2021).

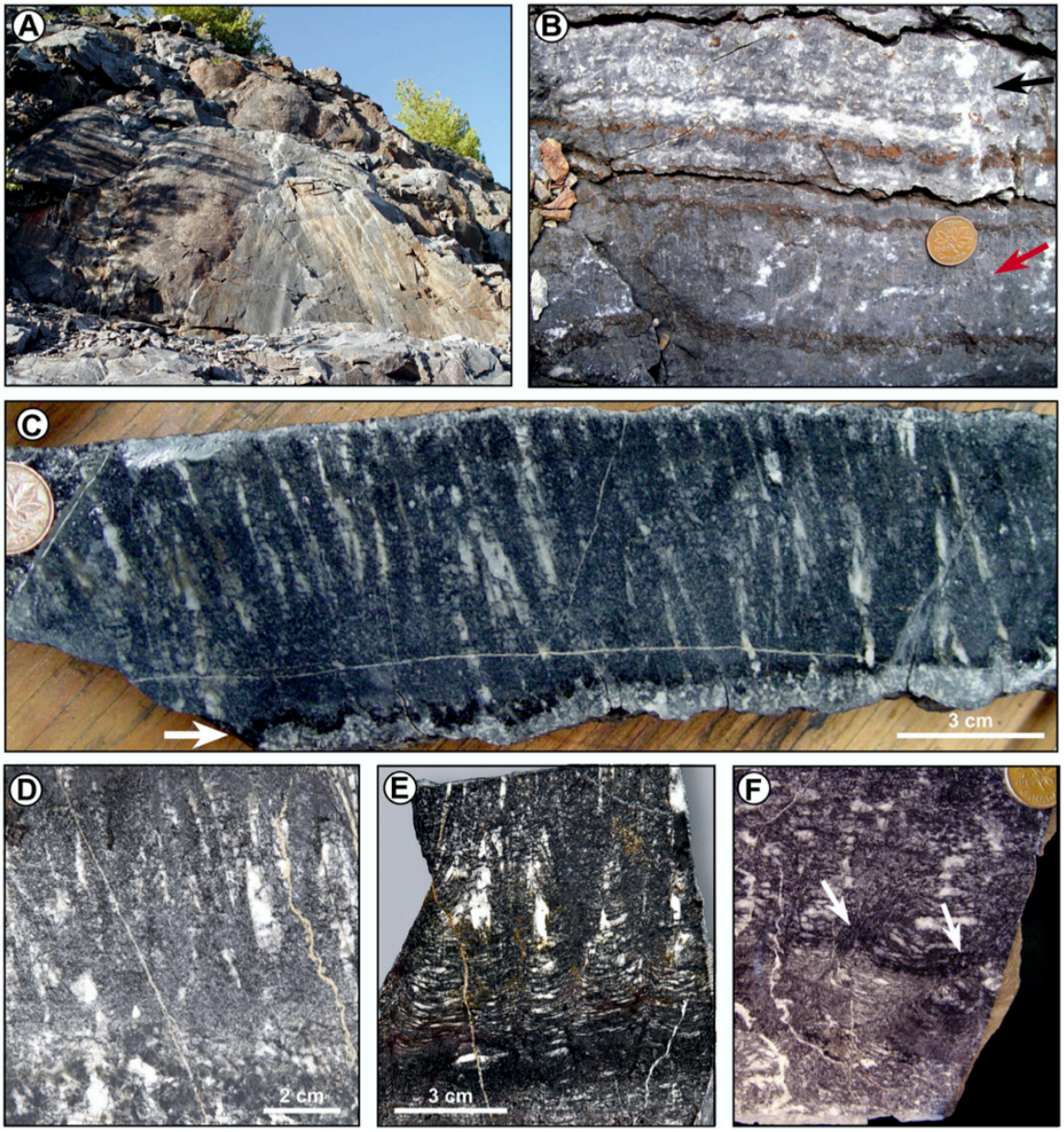

Figure 2.7. Giant domes of the Steep Rock carbonate platform (Elbow Point Member, Locality 6 from Fralick and Riding, 2015). Giant dome in outcrop (A). Close up of the giant domes that are composed of cuspate fenestral fabric (black arrow) and crystal fan fabric (red arrow). (B). Close up of a crystal fan layer growing on an iron- and carbon-rich horizon (white arrow) (C). Crystal fans growing from underlying sediment (D) and nucleated (E, F) on the upturned edges of underlying cuspate fenestral fabric (white arrows on F) and appearing to overprint the cuspate fabric. Coins are 19 mm in diameter. Figure taken from Fralick and Riding, 2015.

The samples analyzed in this thesis from Steep Rock are from outcrops from both the Hogarth Member and Elbow Point Member. These carbonate samples are mainly carbonate grainstone, laminar carbonate, and carbonate with crystal fans. See Figure 2.7 for field images of representative microbialites.

2.2 Sedimentary Lithologies

Several different sedimentary lithologies were examined in this thesis, and many have the potential to record paleogeochemical and paleoenvironmental signals from the time of their deposition. However, these different lithologies also differ with respect to their (1) own specific depositional conditions and environments, (2) different biological controls or contributions, and (3) different chemical or isotopic proxy signals that they are most apt to record or preserve. In this section, the above three aspects of the three main lithologies studied in this thesis (carbonate, BIF, and shale) are briefly synthesized; additional details concerning these aspects are further discussed in the individual chapters presenting the research findings of this thesis.

2.2.1 Carbonates

Carbonate rocks are chemically and biochemically formed sedimentary rocks of carbonate composition, predominantly limestones and dolostones. Limestones are composed of calcium carbonate ($CaCO_3$: calcite, aragonite), including high-Mg varieties, while dolostones are mainly composed of dolomite i.e., $CaMg(CO_3)_2$. Generally, carbonates form above pH>6.5 in alkaline environments where carbonate ions (CO_3^{2-}) associate with dissolved Ca^{2+} (or Mg^{2+}) ions, and carbonate precipitation occurs readily

upon saturation. They can form in reduced environments (e.g., at depth in the Baltic Sea) as well as in oxygenated environments (e.g., Bahamas) when aqueous conditions reach carbonate mineral saturation. The precipitation of carbonate minerals is also closely linked to biology since many metabolic processes, such as photosynthetic uptake of CO_2 and/or HCO_3^- by cyanobacteria, and ammonification, denitrification and sulfate reduction by other bacteria, can increase alkalinity and stimulate carbonate precipitation (Riding, 2000). Microbial structures such as biofilms, stromatolites and microbial mats, all formed by bacteria, have thus been important components of carbonate sediments since the Archean.

As carbonates that precipitate directly from seawater may record the chemical characteristics of seawater of the time, and because of their close connection to microbial processes, they are regarded as valuable archives in the reconstruction of the different paleoenvironments preserved in Earth history (Riding, 2000; Kamber et al., 2014). However, one must be sure that the recorded signals reflect the original signal created during sample formation (primary signals), and not that of post-depositional processes (secondary signals). Diagenetic effects, i.e., physical and chemical changes at low pressure and temperature that affect the sediments after deposition but before metamorphism, should also be considered when interpreting geochemical proxy data. The major processes of diagenesis are:

(1) dissolution by which the constituent ions of a carbonate mineral are released into solution, as a consequence of the increase of $CaCO_3$ solubility controlled by either (i) decreases in temperature, salinity, or pH, or (ii) increases in pressure, fluid pCO_2, or rates of respiration of organic matter (James and Jones, 2015);

(2) recrystallization, which is the consequence of pH-controlled dissolution and re-precipitation cycles that change the orientation, shape and volume of mineral (Bathurst, 1972; Gorski and Fantle, 2017);

(3) inversion, also called neomorphism, which is when a mineral is replaced by a more stable polymorph of similar chemical composition but with different atomical arrangement and crystal structure as a result of an increase in pressure and/or temperature, or pH-driven dissolution-precipitation cycles (Bathurst, 1972);

(4) dolomitization, which is the process of dolomite formation, often by altering calcite/aragonite into dolomite, driven by a variety of proposed processes such as meteoric-seawater mixing, evaporative or hydrothermal fluid alteration, and early microbially-driven diagenesis as well as later burial diagenesis (Machel, 2004; James and Jones, 2015);

(5) cementation, which can be abiotic or biotically-induced and consists in the precipitation of authigenic cement due to the augmentation of CO_3^{2-} inducing $CaCO_3$ supersaturation, driven by water mass mixing, fluid flow, elevated alkalinity, an increase in temperature, salinity or by microbial anaerobic metabolisms (Irwin et al., 1977; Berner, 1980; Given and Wilkinson, 1987);

(6) compaction, which is a mechanical compression of the sediments due to the increase in the overload pressure with the deposition and burial of overlying sediments, leading to dewatering and loss of porosity (Croizé et al., 2013).

Geochemical indicators such as $\delta^{18}O$, $\delta^{13}C$, $^{87}Sr/^{86}Sr$, as well as selected trace element ratios, have been applied for over half a century to identify signatures of diagenetic alteration in carbonate rocks, which are generally considered more sensitive to post-depositional alteration than the other lithologies examined in this thesis. Nevertheless, traditional isotope systems ($\delta^{18}O$, $\delta^{13}C$, $\delta^{34}S$) have sometimes proven less sensitive to

alteration than previously thought (Swart, 2015). Furthermore, the fact that certain isotope systems may act at the same time as a paleoenvironmental proxy and as an indicator of diagenetic alteration (e.g., $\delta^{18}O$ may reflect depositional temperature or may reflect the degree of diagenetic alteration) means that additional constraints are often required (Fantle et al., 2020). Novel non-traditional stable isotopic proxies such as $\delta^{44}Ca$ and $\delta^{26}Mg$ are currently emerging as useful tools to distinguish primary from secondary signals in altered carbonate (Blättler et al., 2015; Lau et al., 2017; Ahm et al., 2018). Importantly, most carbonate diagenetic metamorphic processes, and late alteration processes do not appear to affect the rare earth element (REE) geochemical signatures, which often remain similar to those of seawater for carbonates of marine origin, confirming their usefulness in reconstructing the seawater composition and redox conditions of ancient marine environments (Hood et al., 2018; Liu et al., 2019; Luo et al., 2021).

2.2.2 BIF

Banded Iron Formations (BIFs) are chemically precipitated sedimentary rocks composed primarily of silica (40-60 wt.% SiO_2) and Fe (15-40 wt.% Fe). Layers containing magnetite (Fe_3O_4) and/or hematite (Fe_2O_3) which alternate with microcrystalline silica layers (chert, quartz) form their distinctive macro- to micro-bands (Bekker et al., 2014). The majority of BIFs formed during the Archean and Paleoproterozoic, from 3.5 to 1.8 Ga, with a brief reappearance ca. 0.7 Ga associated with the Neoproterozoic Snowball Earth events (Klein, 2005). This temporal distribution is related to the special conditions necessary for their formation. First, in view of their high iron concentrations, a precursor sediment precipitated from seawater with Fe(II) concentrations above 100 μM is implied (Holland, 1973, 1984). The accumulation of Fe(II) is best explained by the presence of a reducing atmosphere or one with a low oxidizing potential (Holland, 1984; Bekker et al.,

2004), low marine concentrations of sulfate and thus sulfide (Habicht et al., 2002), and/or a high hydrothermal flux of iron (Kump and Seyfried, 2005). Secondly, the deposition of BIFs requires an oxidative process converting Fe^{2+} to solid-phase iron oxyhydroxide particles that will deposit and accumulate on the seafloor. Three main oxidation mechanisms were originally proposed: (i) oxidation of Fe(II) by oxygenic cyanobacteria at the interface between oxygenated shallow waters and reduced upwelling iron-rich waters (Cloud, 1965, 1973) or (ii) oxidation of Fe(II) by anoxygenic photosynthesis, commonly known as "photoferrotrophy", that uses Fe(II) instead of H_2O as an electron donor and thus producing Fe(III) instead of O_2 (Baur, 1978; Ehrenreich and Widdel, 1994), or finally (iii) ultraviolet photooxidation of Fe(II) (Cairns-Smith, 1978). However, with new geochemical insights from non-traditional isotopic systems such as Fe, Cr, U, Mo, Cu, it is now generally believed that the key process for the deposition of Banded Iron Formations is microbial (i.e. enzymatic) oxidation of Fe(II) (Czaja et al., 2013; Konhauser et al., 2017) with microbial reduction of Fe(III) such as DIR likely playing an important role in Fe(II) supply to the water column, as well as in BIF diagenesis (Johnson et al., 2008; Heimann et al., 2010; Li et al., 2011, 2015).

BIFs were deposited in deep-water environments near or above continental slopes and during periods of sea level high stand (Simonson and Hassler, 1996; Krapež et al., 2003; Fralick and Pufahl, 2006). In a transgressive sequence they are generally underlain by organic-rich shales with which they are in some cases interbedded e.g., the 2.48 Ga Dales Gorge Member of the Brockman Iron formation in Western Australia alternating 17 layers of BIF with 16 layers of shales (Trendall and Blockley, 1970), and are often considered the most distal, sediment starved facies of platform sedimentation, although shallow water examples of iron oxide chemical sedimentation also exist (see review by

Bekker et al., 2014). Considering that their precursor minerals precipitated directly from ancient seawater, and that their generally low concentrations of crustal-derived elements (such as Al, Ti, Zr, Th, Nb, and Sc) can be used to confirm their authigenic origin, elemental enrichments in BIFs have been widely examined as proxy indicators for the chemical composition of seawater in deep geological time (Bau and Dulski, 1996; Bolhar et al., 2004), including the nutrients available in ancient seawater for the ancient marine microbial biosphere (Konhauser et al., 2007; Planavsky et al., 2010).

2.2.3 Black Shales

Black shales are dark-colored, organic matter-rich sedimentary rocks that accumulate slowly in low energy environments. They may contain authigenic iron sulfide minerals, but are mostly dominated by fine detrital components (silts and clays) representative of their crustal provenance. The depositional processes of these reduced sediments involve a series of relationships between factors such as organic productivity, the rate of clastic sedimentation, water column depth, and the rapidity of oxidation through which sinking organic matter is remineralized. In most cases, they accumulate under anoxic bottom water and/or bottom sediment conditions in marine or continental sedimentary basins (Wignall, 1994). Indeed, under oxic conditions, organic matter is rapidly degraded by aerobic respiration in the water column and the upper sediment-water interface, favoring the preservation of sediments with low levels of organic matter. In contrast, in suboxic or anoxic conditions, partial degradation (due to lower energetic efficiency) of organic matter by anaerobic bacteria via denitrification, Mn(IV) reduction, Fe(III) reduction, sulfate reduction, and/or methanogenesis (Fig. 2.8), generally leads to enhanced delivery and preservation of organic matter in sediments. Under euxinic conditions (both anoxic and sulfidic), the degradation of organic matter is even less efficient, organic matter is

preservation is further enhanced. Anoxia in the modern marine environment can occur today under certain conditions as the result of a combination of physical and biological factors. For example, in cases of intense upwelling, oxygen poor and nutrient-rich bottom waters mix with oxygen-rich surface waters and result in very high primary productivity. Exportation and decomposition of this new organic matter consumes all available oxygen, leading to the enrichment in organic matter in the sediments (Kämpf and Chapman, 2016).

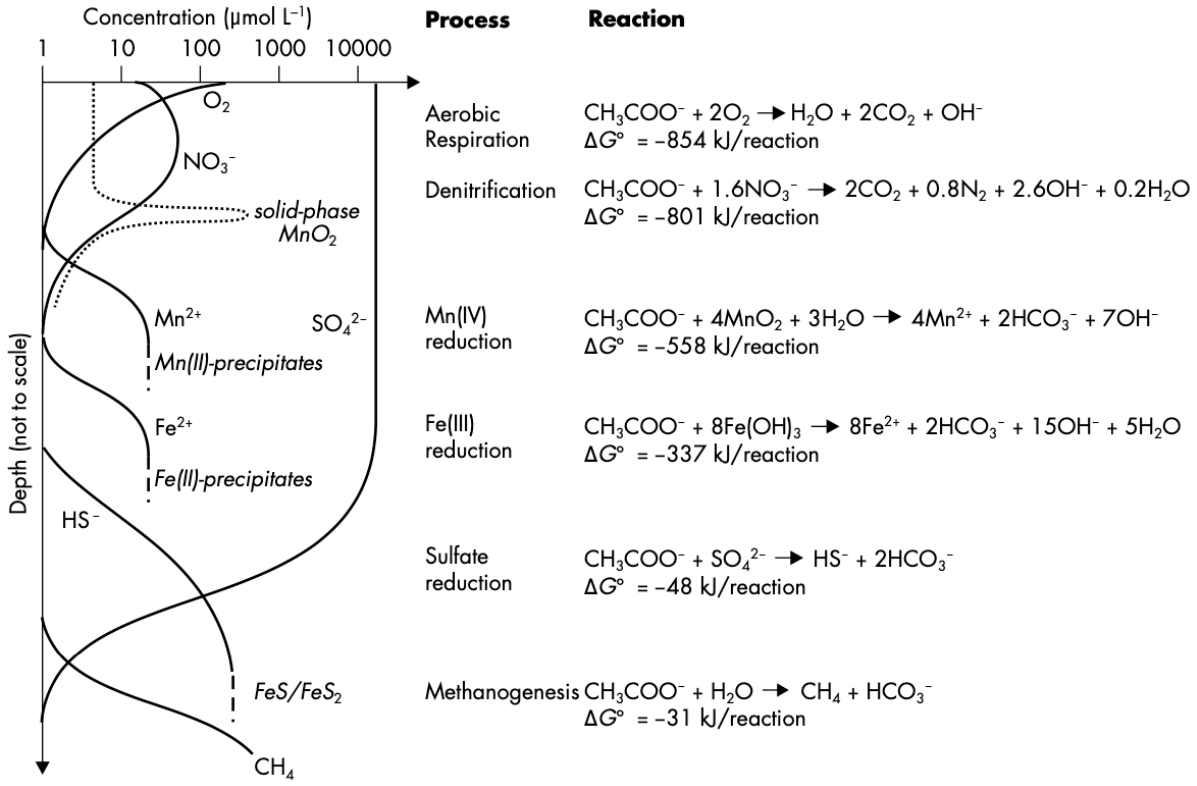

Figure 2.8. Schematic of a typical marine sediment porewater profile showing the successive utilization of terminal electron acceptors that develop during the decomposition of marine sedimentary organic matter. Reproduced from Konhauser (2007).

Organic rich sediments are also frequently deposited in silled basins with a positive water balance and a close, shallow connection to the open ocean/sea, such as in the modern Black Sea (Stewart et al., 2007). Silled basins are often characterized by low-salinity surface water outflow and a higher-salinity deeper water inflow. The difference in density

between the low and high salinity waters results in the formation of a permanent halocline and stratification that prevents convection and oxygen supply in the lower parts of the water column, thus leading to the development of anoxic conditions. Oxygen minimum zones (OMZs) and Ocean anoxic events (OAEs) are characterized by oxygen depletion of intermediate waters in significant portions or even entire ocean basins. The development of weakly oxic to anoxic conditions with increased preservation of organic matter is thought to be driven by several factors during OAE events, such as (i) the intensification of deep-water formation at high latitudes, (ii) the origin of warm and salty bottom waters at low latitudes, (iii) the increase in freshwater runoff from the continents associated with high rates of nutrient input, and (iv) an increase in primary production associated with extreme greenhouse conditions.

Black shales are generally highly enriched in many redox-sensitive and/or sulfide-forming metals and metalloids, including Cr, V, Mo, Re, U, As, Cd, Ag, Cu, Ni, Zn, Co, Pb and P (Vine and Tourtelot, 1970), which makes them a particularly attractive potential paleoenvironmental archive. Enrichments in redox–sensitive elements such as S, Mo, Re, Os, as well as Fe, Mo and Cr isotope compositions, may serve as important indicators of changes in oxygen levels in the ancient atmosphere and oceans. Indeed, several studies that examined these geochemical proxies in ancient marine black shales have provided important geochemical evidence for establishment of Archean oxygen oases between ca. 2.6 and 3 Ga (e.g., Wille et al., 2007; Czaja et al., 2012; Stüeken et al., 2012).

Detailed methods relating to the preparation and geochemical analyses of Archean sediment samples representing all three lithology types are provided in the following Chapter.

2.3 References

Afroz, M., 2019, Sedimentology and Geochemistry of the 2.93 Ga Basinal Facies of the Red Lake Carbonate Platform: MSc diss., Lakehead University.

Ahm, A.-S.C., Bjerrum, C.J., Blättler, C.L., Swart, P.K., and Higgins, J.A., 2018, Quantifying early marine diagenesis in shallow-water carbonate sediments: Geochimica et Cosmochimica Acta, v. 236, p. 140–159, doi:10.1016/j.gca.2018.02.042.

Ayres, L.D., Lumbers, S.B., Milne, V.G., and Robeson, D.W., 1971, Ontario geological map 2197.

Bathurst, R.G., 1972, Carbonate sediments and their diagenesis: Elsevier.

Bau, M., and Dulski, P., 1996, Distribution of yttrium and rare-earth elements in the Penge and Kuruman iron-formations, Transvaal Supergroup, South Africa: Precambrian Research, v. 79, p. 37–55, doi:10.1016/0301-9268(95)00087-9.

Baur, M.E., 1978, Thermodynamics of heterogeneous iron—Carbon systems: Implications for the terrestrial primitive reducing atmosphere: Chemical Geology, v. 22, p. 189–206, doi:10.1016/0009-2541(78)90031-1.

Beakhouse, G.P., Heaman, L.M., and Creaser, R.A., 1999, Geochemical and U–Pb zircon geochronological constraints on the development of a Late Archean greenstone belt at Birch Lake, Superior Province, Canada: Precambrian Research, v. 97, p. 77–97, doi:10.1016/S0301-9268(99)00021-2.

Bekker, A., Holland, H.D., Wang, P.-L., Rumble Iii, D., Stein, H.J., Hannah, J.L., Coetzee, L.L., and Beukes, N.J., 2004, Dating the rise of atmospheric oxygen:, www.nature.com/nature.

Bekker, A., Planavsky, N.J., Krapež, B., Rasmussen, B., Hofmann, A., Slack, J.F., Rouxel, O.J., and Konhauser, K.O., 2014, Iron Formations: Their Origins and Implications for

Ancient Seawater Chemistry, *in* Treatise on Geochemistry, Elsevier, p. 561–628, doi:10.1016/B978-0-08-095975-7.00719-1.

Berner, R.A., 1980, Early diagenesis: a theoretical approach: (No.1) Princeton University Press.

Blättler, C.L., Miller, N.R., and Higgins, J.A., 2015, Mg and Ca isotope signatures of authigenic dolomite in siliceous deep-sea sediments: Earth and Planetary Science Letters, v. 419, p. 32–42, doi:10.1016/j.epsl.2015.03.006.

Bolhar, R., Kamber, B.S., Moorbath, S., Fedo, C.M., and Whitehouse, M.J., 2004, Characterisation of early Archaean chemical sediments by trace element signatures: Earth and Planetary Science Letters, v. 222, p. 43–60, doi:10.1016/j.epsl.2004.02.016.

Cairns-Smith, A.G., 1978, Precambrian solution photochemistry, inverse segregation, and banded iron formations: Nature, v. 276, p. 807–808, doi:10.1038/276807a0.

Card, K.D., and Ciesielski, A., 1986, Subdivisions of the Superior Province of the Canadian Shield.: Geoscience Canada.

Cloud, P., 1973, Paleoecological Significance of the Banded Iron-Formation: Economic Geology, v. 68, p. 1135–1143, doi:10.2113/gsecongeo.68.7.1135.

Cloud, P.E., 1965, Significance of the Gunflint (Precambrian) Microflora: Science, v. 148, p. 27–35, doi:10.1126/science.148.3666.27.

Corfu, F., and Andrews, A.J., 1987, Geochronological constraints on the timing of magmatism, deformation, and gold mineralization in the Red Lake greenstone belt, northwestern Ontario: Canadian Journal of Earth Sciences, v. 24, p. 1302–1320, doi:10.1139/e87-126.

Corfu, F., and Wallace, H., 2011, U–Pb zircon ages for magmatism in the Red Lake greenstone belt, northwestern Ontario: Canadian Journal of Earth Sciences, v. 23, p. 27–42, doi:10.1139/e86-004.

Croizé, D., Renard, F., and Gratier, J.-P., 2013, Compaction and Porosity Reduction in Carbonates: A Review of Observations, Theory, and Experiments, *in* p. 181–238, doi:10.1016/B978-0-12-380940-7.00003-2.

Czaja, A.D., Johnson, C.M., Beard, B.L., Roden, E.E., Li, W., and Moorbath, S., 2013, Biological Fe oxidation controlled deposition of banded iron formation in the ca. 3770Ma Isua Supracrustal Belt (West Greenland): Earth and Planetary Science Letters, v. 363, p. 192–203, doi:10.1016/j.epsl.2012.12.025.

Czaja, A.D., Johnson, C.M., Roden, E.E., Beard, B.L., Voegelin, A.R., Nägler, T.F., Beukes, N.J., and Wille, M., 2012, Evidence for free oxygen in the Neoarchean ocean based on coupled iron–molybdenum isotope fractionation: Geochimica et Cosmochimica Acta, v. 86, p. 118–137, doi:10.1016/j.gca.2012.03.007.

Ehrenreich, A., and Widdel, F., 1994, Anaerobic oxidation of ferrous iron by purple bacteria, a new type of phototrophic metabolism: Applied and Environmental Microbiology, v. 60, p. 4517–4526, doi:10.1128/aem.60.12.4517-4526.1994.

Fantle, M.S., Barnes, B.D., and Lau, K. v., 2020, The Role of Diagenesis in Shaping the Geochemistry of the Marine Carbonate Record: Annual Review of Earth and Planetary Sciences, v. 48, p. 549–583, doi:10.1146/annurev-earth-073019-060021.

Fenwick, K.G., 1976, Geology of the Finlayson Lake area, district of Rainy River: Ontario Division of Mines, Ministry of Natural Ressources.

Fralick, P., Hollings, P., and King, D., 2008, Stratigraphy, geochemistry, and depositional environments of Mesoarchean sedimentary units in western Superior Province: Implications for generation of early crust, *in* Special Paper 440: When Did Plate Tectonics Begin on Planet Earth?, Geological Society of America, p. 77–96, doi:10.1130/2008.2440(04).

Fralick, P., and King, D., 1996, Meso-Archean evolution of Western Superior Province: evidence from metasedimentary sequences near Atikokan: Vancouver, BC: Lithoprobe Secretariat University of British Columbia.

Fralick, P., and Pufahl, P.K., 2006, Iron Formation in Neoarchean Deltaic Successions and the Microbially Mediated Deposition of Transgressive Systems Tracts: Journal of Sedimentary Research, v. 76, p. 1057–1066, doi:10.2110/jsr.2006.095.

Fralick, P., and Riding, R., 2015, Steep Rock Lake: Sedimentology and geochemistry of an Archean carbonate platform: Earth-Science Reviews, v. 151, p. 132–175, doi:10.1016/j.earscirev.2015.10.006.

Given, R.K., and Wilkinson, B.H., 1987, Dolomite abundance and stratigraphic age; constraints on rates and mechanisms of Phanerozoic dolostone formation: Journal of Sedimentary Research, v. 57, p. 1068–1078, doi:10.1306/212F8CF1-2B24-11D7-8648000102C1865D.

Goodwin, A.M., 1967, Volcanic studies in the Birch-Uchi Lakes Area of Ontario: Department of Mines, Miscellaneous Paper 6, p. 96.

Gorski, C.A., and Fantle, M.S., 2017, Stable mineral recrystallization in low temperature aqueous systems: A critical review: Geochimica et Cosmochimica Acta, v. 198, p. 439–465, doi:10.1016/j.gca.2016.11.013.

Habicht, K.S., Gade, M., Thamdrup, B., Berg, P., and Canfield, D.E., 2002, Calibration of Sulfate Levels in the Archean Ocean: Science, v. 298, p. 2372–2374, doi:10.1126/science.1078265.

Heimann, A., Johnson, C.M., Beard, B.L., Valley, J.W., Roden, E.E., Spicuzza, M.J., and Beukes, N.J., 2010, Fe, C, and O isotope compositions of banded iron formation carbonates demonstrate a major role for dissimilatory iron reduction in ~2.5Ga marine

environments: Earth and Planetary Science Letters, v. 294, p. 8–18, doi:10.1016/j.epsl.2010.02.015.

Hofmann, H.J., 1985, Archean Stromatolites from Uchi Greenstone Belt, Northwestern Ontario: Geological Association of Canada Special Paper.

Hofmann, H.J., 1971, Precambrian fossils, pseudofossils and problematica in Canada: Geol. surv. Bull, v. 189, p. 146.

Holland, H.D., 1984, The Chemical Evolution of the Atmosphere and Oceans: Princeton University Press, 598 p.

Holland, H.D., 1973, The Oceans; A Possible Source of Iron in Iron-Formations: Economic Geology, v. 68, p. 1169–1172, doi:10.2113/gsecongeo.68.7.1169.

Hollings, P., Wyman, D., and Kerrich, R., 1999, Komatiite–basalt–rhyolite volcanic associations in Northern Superior Province greenstone belts: significance of plume-arc interaction in the generation of the proto continental Superior Province: Lithos, v. 46, p. 137–161, doi:10.1016/S0024-4937(98)00058-9.

Hood, A. v. S., Planavsky, N.J., Wallace, M.W., and Wang, X., 2018, The effects of diagenesis on geochemical paleoredox proxies in sedimentary carbonates: Geochimica et Cosmochimica Acta, v. 232, p. 265–287, doi:10.1016/j.gca.2018.04.022.

Irwin, H., Curtis, C., and Coleman, M., 1977, Isotopic evidence for source of diagenetic carbonates formed during burial of organic-rich sediments: Nature, v. 269, p. 209–213, doi:10.1038/269209a0.

James, N.P., and Jones, B., 2015, Origin of carbonate sedimentary rocks: John Wiley & Sons.

Johnson, C.M., Beard, B.L., Klein, C., Beukes, N.J., and Roden, E.E., 2008, Iron isotopes constrain biologic and abiologic processes in banded iron formation genesis:

Geochimica et Cosmochimica Acta, v. 72, p. 151–169, doi:10.1016/j.gca.2007.10.013.

Jolliffe, A.W., 1955, Geology and iron ores of Steep Rock Lake [Ontario]: Economic Geology, v. 50, p. 373–398, doi:10.2113/gsecongeo.50.4.373.

Kamber, B.S., Webb, G.E., and Gallagher, M., 2014, The rare earth element signal in Archaean microbial carbonate: information on ocean redox and biogenicity: Journal of the Geological Society, v. 171, p. 745–763, doi:10.1144/jgs2013-110.

Kämpf, J., and Chapman, P., 2016, Upwelling Systems of the World: Cham, Springer International Publishing, doi:10.1007/978-3-319-42524-5.

Klein, C., 2005, Some Precambrian banded iron-formations (BIFs) from around the world: Their age, geologic setting, mineralogy, metamorphism, geochemistry, and origins: American Mineralogist, v. 90, p. 1473–1499, doi:10.2138/am.2005.1871.

Konhauser, K., 2007, Introduction to Geomicrobiology.

Konhauser, K.O. et al., 2017, Iron formations: A global record of Neoarchaean to Palaeoproterozoic environmental history: Earth-Science Reviews, v. 172, p. 140–177, doi:10.1016/j.earscirev.2017.06.012.

Konhauser, K.O., Amskold, L., Lalonde, S. v., Posth, N.R., Kappler, A., and Anbar, A., 2007, Decoupling photochemical Fe(II) oxidation from shallow-water BIF deposition: Earth and Planetary Science Letters, v. 258, p. 87–100, doi:10.1016/j.epsl.2007.03.026.

Krapež, B., Barley, M.E., and Pickard, A.L., 2003, Hydrothermal and resedimented origins of the precursor sediments to banded iron formation: sedimentological evidence from the Early Palaeoproterozoic Brockman Supersequence of Western Australia: Sedimentology, v. 50, p. 979–1011, doi:10.1046/j.1365-3091.2003.00594.x.

Kump, L.R., and Seyfried, W.E., 2005, Hydrothermal Fe fluxes during the Precambrian: Effect of low oceanic sulfate concentrations and low hydrostatic pressure on the composition of black smokers: Earth and Planetary Science Letters, v. 235, p. 654–662, doi:10.1016/j.epsl.2005.04.040.

Kusky, T.M., and Hudleston, P.J., 1999, Growth and demise of an Archean carbonate platform, Steep Rock Lake, Ontario, Canada: Canadian Journal of Earth Sciences, v. 36, p. 565–584, doi:10.1139/e98-108.

Kusky, T.M., and Polat, A., 1999, Growth of granite–greenstone terranes at convergent margins, and stabilization of Archean cratons: Tectonophysics, v. 305, p. 43–73, doi:10.1016/S0040-1951(99)00014-1.

Lau, K. v. et al., 2017, The influence of seawater carbonate chemistry, mineralogy, and diagenesis on calcium isotope variations in Lower-Middle Triassic carbonate rocks: Chemical Geology, v. 471, p. 13–37, doi:10.1016/j.chemgeo.2017.09.006.

Lawson, A., and Walcott, C., 1912, The Geology of Steeprock Lake, Ontario: Geo. Sur. Branch, Mem. , v. 28, p. 7–15.

Li, W., Beard, B.L., and Johnson, C.M., 2015, Biologically recycled continental iron is a major component in banded iron formations: Proceedings of the National Academy of Sciences, v. 112, p. 8193–8198, doi:10.1073/pnas.1505515112.

Li, Y.-L., Konhauser, K.O., Cole, D.R., and Phelps, T.J., 2011, Mineral ecophysiological data provide growing evidence for microbial activity in banded-iron formations: Geology, v. 39, p. 707–710, doi:10.1130/G32003.1.

Liu, X.-M., Hardisty, D.S., Lyons, T.W., and Swart, P.K., 2019, Evaluating the fidelity of the cerium paleoredox tracer during variable carbonate diagenesis on the Great Bahamas Bank: Geochimica et Cosmochimica Acta, v. 248, p. 25–42, doi:10.1016/j.gca.2018.12.028.

Luo, Y., Li, G., Xu, W., Liu, J., Cheng, J., Zhao, J., and Yan, W., 2021, The effect of diagenesis on rare earth element geochemistry of the Quaternary carbonates at an isolated coral atoll in the South China Sea: Sedimentary Geology, v. 420, p. 105933, doi:10.1016/j.sedgeo.2021.105933.

Machel, H.G., 2004, Concepts and models of dolomitization: a critical reappraisal: Geological Society, London, Special Publications, v. 235, p. 7–63, doi:10.1144/GSL.SP.2004.235.01.02.

McIntyre, T., and Fralick, P., 2017, Sedimentology and Geochemistry of the 2930 Ma Red Lake-Wallace Lake Carbonate Platform, Western Superior Province, Canada: The Depositional Record, v. 3, p. 258–287, doi:10.1002/dep2.36.

Passchier, C., and Trouw, R.A., 2005, Microtectonics: Springer, Berlin.

Planavsky, N.J., Rouxel, O.J., Bekker, A., Lalonde, S. v., Konhauser, K.O., Reinhard, C.T., and Lyons, T.W., 2010, The evolution of the marine phosphate reservoir: Nature, v. 467, p. 1088–1090, doi:10.1038/nature09485.

Pryslak, A.P., 1971, Knott Township, District of Kenora (Patricia Portion): Ontario Department of Mines and Northern Affairs, Preliminary Map P. 635.

Ramsay, B., 2020, Environmental Control of Seawater Geochemistry in a Mesoarchean Peritidal System, Woman Lake, Superior Province: MSc diss., Lakehead University.

Riding, R., 2000, Microbial carbonates: the geological record of calcified bacterial-algal mats and biofilms: Sedimentology, v. 47, p. 179–214, doi:10.1046/j.1365-3091.2000.00003.x.

Riding, R., Fralick, P., and Liang, L., 2014, Identification of an Archean marine oxygen oasis: Precambrian Research, v. 251, p. 232–237, doi:10.1016/j.precamres.2014.06.017.

Riley, R.A., 1978, Ontario Geological Survey Map 2406, Todd Township, Kenora District: Ministry of Natural Ressources.

Riley, R.A., 1975, Ontario Geological map 2265, Ball Township, Kenora district: Ontario Division of Mines.

Rogers, N., 2002, Whole-rock chemical analyses from the Birch–Uchi greenstone belt, Superior Province: Geological Survey of Canada, Open File Report, 4271.

Rogers, N., McNicoll, V., van Stall, C.R., and Tomlinson, K.Y., 2000, Lithogeochemical studies in the Uchi-Confederation Greenstone Belt, northwestern Ontario: implications for Archean tectonics: Geological Survey of Canada, Current Research, 1-11.

Sanborn-Barrie, M., Skulski, T., and Parker, J.R., 2001, Three hundred million years of tectonic history recorded by the Red Lake greenstone belt, Ontario: , p. 14, doi:10.4095/212109.

Simonson, B.M., and Hassler, S.W., 1996, Was the Deposition of Large Precambrian Iron Formations Linked to Major Marine Transgressions? The Journal of Geology, v. 104, p. 665–676, doi:10.1086/629861.

Smyth, H.L., 1891, Structural geology of Steep Rock Lake, Ont: American Journal of Science, v. s3-42, p. 317–331, doi:10.2475/ajs.s3-42.250.317.

Stewart, K., Kassakian, S., Krynytzky, M., DiJulio, D., and Murray, J.W., 2007, Oxic, suboxic, and anoxic conditions in the Black Sea, *in* The Black Sea Flood Question: Changes in Coastline, Climate, and Human Settlement, Springer Netherlands, p. 1–21, doi:10.1007/978-1-4020-5302-3_1.

Stone, D., and Pufahl, P., 1995, Project Unit 95-14. Geology of the Atikokan-Sapawe area: regional controls on gold mineralization in the Marmion batholith: Ont. Geol. Surv. Misc. Pap, v. 164, p. 45–47.

Stott, G.M., and Corfu, F., 1991, Uchi Subprovince: in Geology of Ontario, Ontario Geological Survey, Special Volume 4, Part 1, p.145-236.

Stüeken, E.E., Catling, D.C., and Buick, R., 2012, Contributions to late Archaean sulphur cycling by life on land: Nature Geoscience, v. 5, p. 722–725, doi:10.1038/ngeo1585.

Swart, P.K., 2015, The geochemistry of carbonate diagenesis: The past, present and future: Sedimentology, v. 62, p. 1233–1304, doi:10.1111/sed.12205.

Thurston, P.C., 1980, Subaerial volcanism in the Archean Uchi-Confederation volcanic belt: Precambrian Research, v. 12, p. 79–98, doi:10.1016/0301-9268(80)90024-8.

Thurston, P.C., Osmani, I.A., Stone, D., Williams, H.R., Sutcliffe, R.H., and Stott, G.M., 1991, Northwestern Superior Province: review and terrane analysis. Geology of Ontario: Ontario Geological Survey, Special, 4 (Part 1).

Tomlinson, K.Y., Davis, D.W., Stone, D., and Hart, T.R., 2003, U–Pb age and Nd isotopic evidence for Archean terrane development and crustal recycling in the south-central Wabigoon subprovince, Canada: Contributions to Mineralogy and Petrology, v. 144, p. 684–702, doi:10.1007/s00410-002-0423-0.

Tomlinson, K.Y., Hughes, D.J., Thurston, P.C., and Hall, R.P., 1999, Plume magmatism and crustal growth at 2.9 to 3.0 Ga in the Steep Rock and Lumby Lake area, Western Superior Province: Lithos, v. 46, p. 103–136, doi:10.1016/S0024-4937(98)00057-7.

Trendall, A., and Blockley, J., 1970, The iron formations of the Precambrian Hamersley Group, Western Australia with special reference to the associated crocidolite: West.Austr.Geol.Surv.Bull.

Vine, J.D., and Tourtelot, E.B., 1970, Geochemistry of black shale deposits; a summary report: Economic Geology, v. 65, p. 253–272, doi:10.2113/gsecongeo.65.3.253.

Wignall, P.B., 1994, Black Shales. No 30.: Oxford University Press, USA.

Wilks, M.E., and Nisbet, E.G., 1985, Archaean stromatolites from the Steep Rock Group, northwestern Ontario, Canada: Canadian Journal of Earth Sciences, v. 22, p. 792–799, doi:10.1139/e85-086.

Wilks, M.E., and Nisbet, E.G., 1988, Stratigraphy of the Steep Rock Group, northwest Ontario: a major Archaean unconformity and Archaean stromatolites: Canadian Journal of Earth Sciences, v. 25, p. 370–391, doi:10.1139/e88-040.

Wille, M., Kramers, J.D., Nägler, T.F., Beukes, N.J., Schröder, S., Meisel, Th., Lacassie, J.P., and Voegelin, A.R., 2007, Evidence for a gradual rise of oxygen between 2.6 and 2.5Ga from Mo isotopes and Re-PGE signatures in shales: Geochimica et Cosmochimica Acta, v. 71, p. 2417–2435, doi:10.1016/j.gca.2007.02.019.

Wilmeth, D.T., Fralick, P.W., Riding, R., and Lalonde, S. v, 2021, A Mesoarchean oxygen oasis expanded: new trace element and stable isotope data from the 2.8 Ga Mosher Carbonate, Steep Rock Lake, Canada: Abstract from Goldschmidt.

Wyman, D., and Hollings, P., 1998, Long-lived mantle-plume influence on an Archean protocontinent: Geochemical evidence from the 3 Ga Lumby Lake greenstone belt, Ontario, Canada: Geology, v. 26, p. 719, doi:10.1130/0091-7613(1998)026<0719:LLMPIO>2.3.CO;2.

CHAPTER 3:

MATERIAL AND METHODS

3.1 Field and laboratory sampling

The samples analyzed throughout this thesis were from 1) cores recovered from Goldcorp (gold exploration company) for the ERC EARTHBLOOM project, 2) cores drilled by the EARTHBLOOM team directly in the field and 3) outcrops sampled by the EARTHBLOOM team.

All rock samples were crushed, first with carbon tungsten hammer mortar, then with an agate puck mill, to generate powders without contact with steel. Pyrite (FeS_2) grains were picked from selected samples and grains less than 1 mm in size were collected using 500 μm and 1.0 mm sieves then the sulfide minerals were isolated by hand-picking under a binocular microscope.

3.2 Major and trace elements

3.2.1 Digestion

Two types of digestions were performed for the measurement of Fe isotopes and trace element concentrations: a weak leach digest on the carbonates to isolate the carbonate fraction, and a total digest on the carbonates, black shales, and BIF for true whole-rock measurements. A third digest specifically for major elements (Al, Fe, S, Mg, Si, Ca, etc.) was also performed.

3.2.1.1 Major elements

Each sample powder was digested into PFA vials in 1ml of concentrated HNO_3, 3 ml of HCl and 3ml of HF, reacted overnight in heating blocks at 90° then at 110° for an hour. All reactants were reagent grade for major element analyses. Then, they were transferred into 100 ml PFA bottles with 93ml of boric acid to neutralize the HF and keep Si from volatilizing as SiF_4. A wait of one week before measuring major elements by Horiba Jobin Yvon Ultima 2 ICP-AES (Pôle Spectrometry Océan, Brest, France) was necessary to ensure the complete neutralization of the HF.

3.2.1.2 Trace elements

Leach digest: An aliquot of each sample powder (~ 100 mg) was digested in PFA vials in 2 ml of 5% trace-metal grade acetic acid and was left overnight at room temperature. The next day, the samples were transferred into centrifuge tubes and were centrifuged at ca. 3000 g for 5 min to separate the solid and liquid phase. Then, 100µl from the liquid phase was extracted and 4.9 ml of 2% PFA-distilled HNO_3 + Indium (In) was added in 5ml tubes for the REE measurement using a ThermoFisher Scientific ElementXR HR-ICP-MS. This method has been optimized to fully digest diverse carbonates while minimizing digestion of clays, oxides, and crystalline silicates (Rongemaille et al., 2011). The rest of the liquid was evaporated, re-digested with concentrated HNO_3, evaporated then archived in 4ml 6N HCl for later Fe separation on columns.

To verify the reliability of the method, two carbonate reference materials with low REE abundances were used for this study, CAL-S and BEAN. CAL-S is an Oxfordian limestone prepared and distributed by the Centre de Recherches Pétrographiques et Géochimiques (CRPG) in Nancy and BEAN is the in-house carbonate standard from Brest,

a pure calcium carbonate powder sold by Acros Organics® (Barrat et al., 2020). Yttrium, barium and rare earth element abundances from this study are consistent with the results obtained by Barrat et al., 2020 (Tab. 3.1).

Element	CAL-S			BEAN		
	This study		Barrat et al., 2020	This study		Barrat et al., 2020
	Abundances	2SD		Abundances	2SD	
Y	1.771	0.036	1.948	4.846	0.569	5.373
Ba	1.324	0.207	1.180	87.885	10.195	88.265
La	0.765	0.013	0.745	2.012	0.206	2.028
Ce	0.283	0.009	0.286	0.794	0.089	0.786
Pr	0.083	0.003	0.083	0.287	0.030	0.282
Nd	0.340	0.015	0.342	1.237	0.145	1.237
Sm	0.057	0.001	0.060	0.254	0.032	0.256
Eu	0.015	0.001	0.015	0.091	0.009	0.068
Gd	0.089	0.004	0.090	0.379	0.045	0.378
Tb	0.014	0.001	0.013	0.057	0.005	0.055
Dy	0.096	0.004	0.097	0.357	0.043	0.360
Ho	0.025	0.001	0.026	0.083	0.009	0.084
Er	0.080	0.003	0.081	0.237	0.022	0.241
Tm	0.012	0.001	-	0.031	0.004	-
Yb	0.062	0.003	0.065	0.165	0.018	0.173
Lu	0.010	0.000	0.010	0.026	0.002	0.025

Table 3.1. Y, Ba and REE abundances (in ppm) from the carbonate reference materials CAL-S (n=3) and BEAN (n=3) obtained in this study compared to Barrat et al., 2020.

Total/bulk digest: All reagents were either PFA-distilled (HNO3 and HF) or Quartex-distilled (HCl) in the clean lab. Sample powders (~70 mg) were digested in PFA vials in 2 ml of concentrated HNO_3 and 2 ml of concentrated hydrofluoric acid (HF) and left 24h on hot plates at 80°C to react, then were evaporated. Thereafter, samples were taken up in 3 ml of concentrated HCl and 1 ml of HNO_3 (forming aqua regia) and were evaporated, after having reacted few hours at room temperature. After complete evaporation, the samples were taken up in 4 ml of 6N HCl and reacted in closed vials overnight. From these archives, 100µl was extracted from the liquid phase and added to 4.9

ml of 2% HNO_3 + In in 5 ml tubes for REE analysis by ThermoFisher Scientific ElementXR HR-ICP-MS at the Pôle Spectrometry Océan in Brest, France, while the remaining solution was stored for later Fe separation on columns.

3.2.2 Mass spectrometry

3.2.2.1 ICP-AES

Inductively Coupled Plasma Atomic Emission Spectrometer (ICP-AES) enable the simultaneous analysis of major and trace elements with a measurement range of the order of 10^3 mg L^{-1} to a few µg L^{-1}. A first step, called nebulization, allows the transformation of the liquid sample into an aerosol. The liquid sample is pumped or naturally aspirated into the nebulizer where it is pushed through a small (typically 25 – 300 µm) orfice under gas pressure (sample gas) and is transformed into a fine aerosol. Once passed through the nebulizer, the aerosol formed is mixed with an Argon plasma, reaching temperatures between 6000 and 10000°K. To avoid disturbance of the temperature and properties of Argon in the plasma, only the finest drops (< 10 µm) pass into the plasma, about 1% of the initial sample volume collected. Ionized and excited by the plasma, the characteristic atoms in the sample return to their ground state by emitting photons at specific wavelengths. The beam of photons produced by the de-excitation of the ions is diffracted by a grating, then, thanks to pivoting mirrors, a specific wavelength can be isolated and sent to a photomultiplier which transforms the photon into electrical intensity. These intensities are converted into elemental concentrations using standards of different concentrations to perform a calibration range and thus calibrate the machine.

3.2.2.2 HR-ICP-MS Element XR

The ElementXR is a High Resolution Inductively Coupled Plasma Mass Spectrometer (HR-ICP-MS) that uses a magnetic sector to separate ions according to their atomic mass, which is very suitable for the measurement of trace elements. The sample, in liquid form once passed through a nebulizer or in microparticulate form in the case of laser ablation of solid materials, is injected into an Ar plasma (between 6000 and 10000°K) which ionizes the elements. The generated ions are then accelerated in the mass spectrometer, focused into an ion beam and separated according to their m/z ratio by a magnetic sector, and collected on a single faraday detector. Although many different elements possess radiogenic or stable isotopes that fall on the same masses (isobaric interferences), or combine with other elements in the plasma to form polyatomic interferences that may also fall on the masses of interest. These may be identified and avoided or corrected by monitoring multiple isotopic masses of an element to identify interferences driving isotope ratios beyond natural abundances, or by the measurement of test solutions designed to monitor the production of polyatomic interferences, such as a mono-elemental Ba solution generating potential BaO interferences on Ce masses. Both strategies were employed in this thesis to ensure high-quality, interference-free data.

3.2.2.3 Trace element data treatment

First, all samples (rinses and standards included) were corrected for signal drift using an internal indium (In) standard that was added to the sample dilutant to ensure identical concentrations across all samples in a run. We corrected the signals of each sample by applying a correction factor determined by dividing the indium signal intensity of each sample by the mean indium value of the session. This was done separately for elements measured in low, medium, and high-resolution mode of the ElementXR based on

systematic measurement of In in all three modes. The standards for the calibration were prepared from commercial multi-element solutions (0.1, 1, and 5 ppb) that were analyzed at the beginning and end of each session, and the 1 ppb standard was further repeated every ~10 samples. Standard drift across the session was corrected by dividing the signal intensity for each measurement by the mean indium value for each group of standards (0.1, 1 or 5 ppb). Calibration slopes (in terms of V/ppb), coefficients of determinations (R^2), and relative standard deviation (RSD) of standard repeats were then determined. Data was also collected for each rinse between samples and their averages were used to calculate instrumental detection limits. Method blanks as well as international geostandards were also included as unknowns (IF-G and BHVO-2 for whole-rock digests, CAL-S for acetic acid leaches) in each sample set. The elemental concentrations in the original 6N HCl or Acetic acid (AA) archives (for total digests or leaches, respectively) were calculated by multiplying the drift-corrected elemental intensities obtained for the diluted solutions by the dilution factor and dividing all values by the slopes of the calibration curves. Finally, the preceding result was multiplied by the HCl or AA archive volume and divided by the mass of the sample powder to determine solid phase concentrations.

3.3 Iron isotopes

3.3.1 Purification

Samples were Fe-purified by anion exchange chromatography on columns filled with 2 mL Biorad AG1-X8 resin, 200-400 mesh (Fig. 3.1). Beforehand, the columns were washed with 3N HNO_3, H_2O MQ and 0.24N HCl, and were conditioned with 6N HCl. After loading sample (320ug Fe) in 6N HCl solution to the column, the matrix was washed away

with 6N HCl and Fe fraction was eluted with 0.24N HCl, the full procedure is given in Tab. 3.2. The recovered Fe fraction was dried down and taken up in 2% HNO_3 for measurement by ThermoFisher Scientific Neptune MC-ICP-MS (Pôle Spectrometry Océan, Brest, France).

2 mL AG1-X8 resin– 10 mL Bio-Rad columns		
Steps	**Acid volume**	**Type of acid**
Cleaning	10 mL	3M HNO_3
	10 mL	H_2O mmQ
	10 mL	0.24M HCl
Conditioning	4 mL	6M HCl
Sample loading	x mL	6M HCl
Elution of the matrix	1 mL	6M HCl
	1 mL	6M HCl
	10 mL	6M HCl
	10 mL	6M HCl
Elution of Fe	3 mL	0.24M HCl
	3 mL	0.24M HCl
	5 mL	0.24M HCl
	5 mL	0.24M HCl

Table 3.2. Fe separation protocol using 2 mL Bio-Rad AG1-X8 (200-400 mesh) in 10 mL Bio-Rad columns.

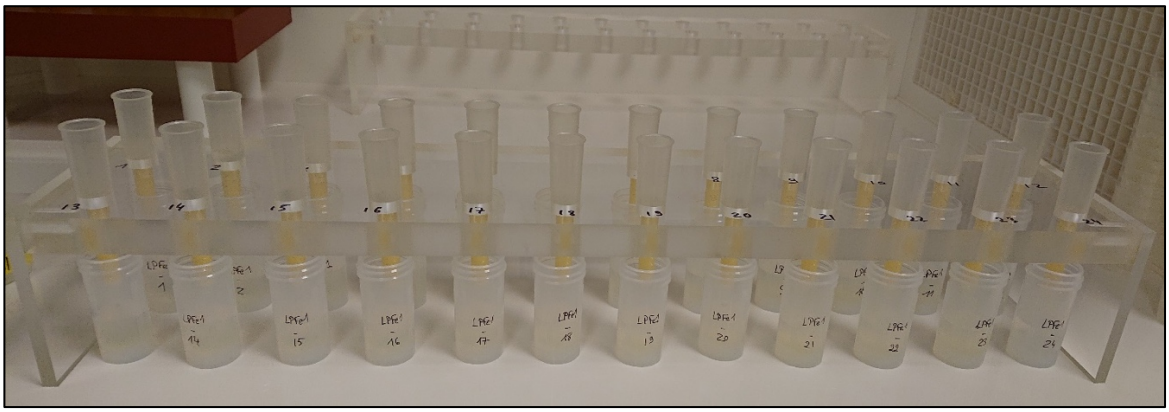

Figure 3.1. Resin AG1-X8's and 10 mL Bio-Rad columns used for the iron separation. This picture was taken at the time of the iron recovery stage.

3.3.2 MC-ICP-MS Neptune

The Thermo-Finnigan MC-ICP-MS Neptune operates like the HR-ICP-MS, but instead of having a mono-collector at the end the isotopes are collected simultaneously by an array of detectors, which in the case of the IFREMER instrument used in this study comprises 9 Faraday cups. The central cup is fixed and the other eight are mobile and can be adjusted. The central ion beam can be measured using the central Faraday cup or, for low ion intensity beams, deflected to a secondary electron multiplier (SEM) ion counting detector located behind an energy filter (RPQ).

This instrument permits high precision Fe isotope analysis without interferences of isobaric polyatomic ions such as $^{40}Ar^{16}O+$ on $^{56}Fe+$, $^{40}Ar^{16}OH+$ on $^{57}Fe+$ and $^{40}Ar^{14}N+$ on $^{54}Fe+$. Interference-free Fe isotope analysis is achieved by using the medium resolution mode (mass resolution power about 8000) and producing “flat top” peak shapes (Weyer and Schwieters, 2003). This peak is composed by a plateau on the left that corresponds to the only place where iron can be measured without interferences (Fig. 3.2). Indeed, since the Fe isotopes have a lower mass than the isobaric polyatomic ions interferences, they enter the detector first and form the left plateau. The higher plateau represents the sum of polyatomic interferences and Fe isotopes. The significantly smaller plateau on the right reflects the polyatomic interferences only. To verify the absence of instrumental artifacts generated by residual matrix elements after chemical purification of samples, we employed two methods. First, in each sample, we added 8 ppm of Ni used as internal standard to correct the instrument mass bias and secondly, we used the “sample-standard bracketing” technique with an 8-ppm standard of Fe and Ni to correct instrumental mass discrimination by normalizing the isotopic ratios of Fe to the measured mean composition of the standard that was measured before and after the sample.

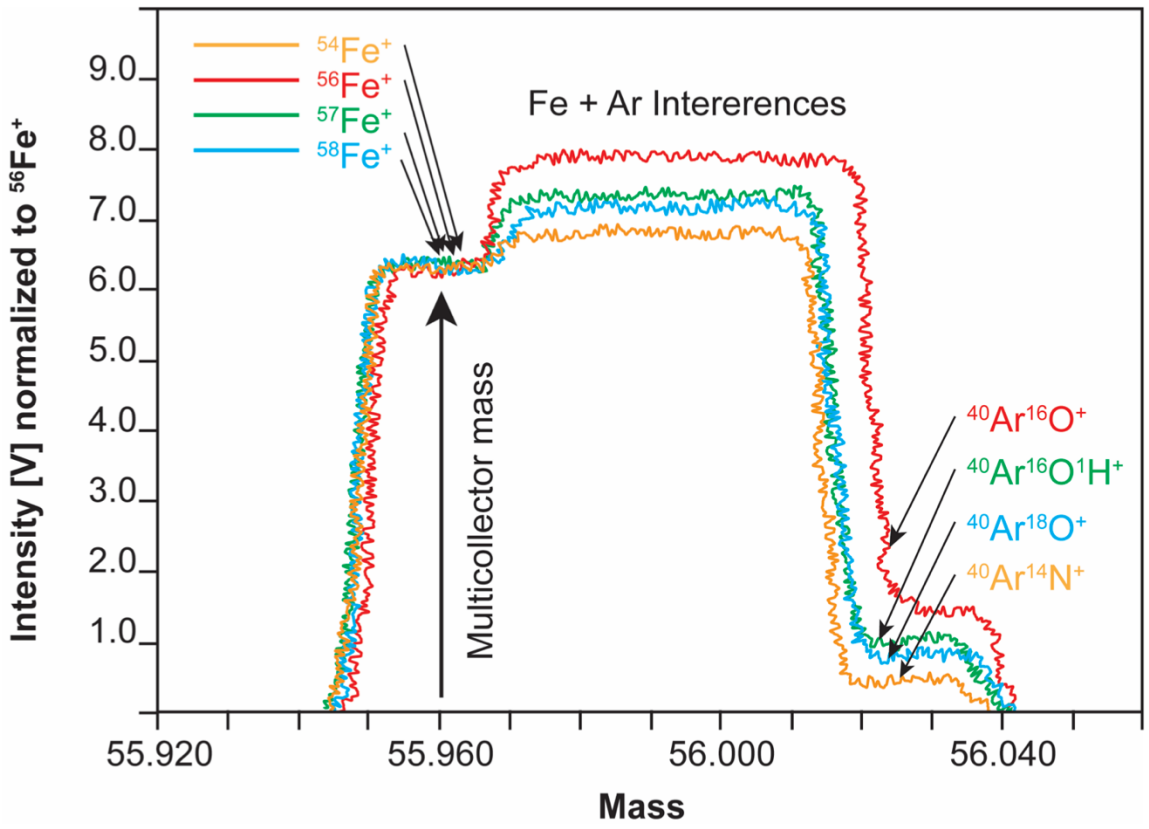

Figure 3.2. MC-ICP-MS mass scan showing all Fe isotopes and polyatomic interferences. All Fe signals are normalized to the signal of δ^{56}Fe (Wang, 2013).

The ^{54}Fe, ^{56}Fe, ^{57}Fe, ^{58}Fe-Ni, ^{60}Ni, ^{61}Ni and ^{62}Ni isotopes were collected on the faraday cups with respectively L4, L2, L1, C, H1, H2 and H4 position. Samples were analyzed one, two, or three times, and the precision of the data is given at 95% confidence levels based on the isotopic deviation of the bracketing standards analyzed during the same analysis session. The Fe isotope standard IRMM-14 demonstrated a 2SD reproducibility of 0.07 ‰ across all sessions, comparable to the external reproducibility of 0.10 ‰ from Rouxel et al. (2005). Two georeference materials, including a banded iron formation (IF-G) and a Hawaiian basalt (BHVO-2) were measured several times as different unknown duplicates passed through the same chemical purification and isotopic analyses independently for each session. IF-G showed an average value of δ^{56}Fe = 0.59 ± 0.02 ‰ (2σ) which is similar within uncertainties to the 0.64 ± 0.06 ‰ (2σ) value obtained by

Rouxel et al. (2005). The standard BHVO-2 showed an average value of $\delta^{56}Fe = 0.01 \pm 0.06$ ‰ (2σ) which is similar within uncertainties to the 0.11 ± 0.11 ‰ (2σ) value obtained by Rouxel et al. (2005). The isotopic compositions of Fe were calculated relative to the Fe isotope standard IRMM-14 using the following equations (Rouxel et al., 2005) :

$$\delta^{56}Fe=1000 * [(^{56}Fe/^{54}Fe)_{sample}/(^{56}Fe/^{54}Fe)_{IRMM\text{-}14} -1]$$

$$\delta^{57}Fe=1000 * [(^{57}Fe/^{54}Fe)_{sample}/(^{57}Fe/^{54}Fe)_{IRMM\text{-}14} -1]$$

$$\delta^{57/56}Fe=1000 * [(^{57}Fe/^{56}Fe)_{sample}/(^{57}Fe/^{56}Fe)_{IRMM\text{-}14} -1]$$

In Figure 3.3 are presented the relationships between $\delta^{56}Fe$ and $\delta^{57}Fe$ for the samples analyzed in this study. Both possible cross-plots produce a mass fractionation line, which corresponds to the natural mass dependent fractionation, which confirms that the measurements were interference-free.

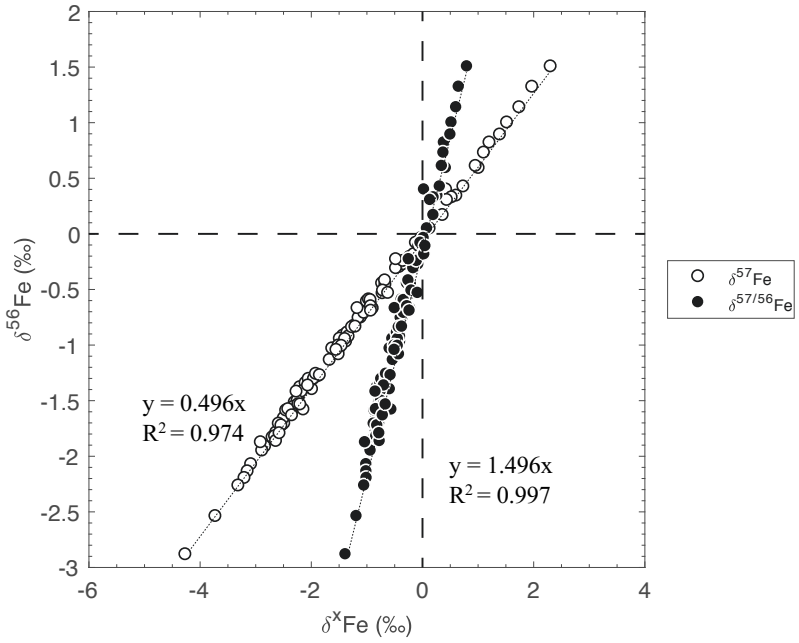

Figure 3.3. Triple isotope plot of Fe isotope values of carbonates, black shales and BIF analyzed in this study. White circles show $\delta^{56}Fe$ vs. $\delta^{57}Fe$ data and black circles represent $\delta^{56}Fe$ vs. $\delta^{57/56}Fe$ data.

3.4 Sulfur isotopes

To obtain the $\delta^{34}S$ data, the samples were sent to the Laboratoire Biogéosciences, Université de Bourgogne, Dijon, France. Sulfur isotopes were measured on isolated sulfides (pyrite and pyrrhotite) using an extraction scheme applied to recover chromium reducible sulfide (CRS). The powdered samples were stirred and reacted in a 1 M $CrCl_2$ solution (Canfield et al., 1986) to release CRS as hydrogen sulfide, which in turn was precipitated as Ag_2S. After centrifugation, the silver sulfide precipitates were rinsed several times with deionized water and dried at 50 °C for 48 h in an oven. Analyses were performed on SO_2 molecules by burning 250-500 µg of Ag_2S using a Vario PYRO cube (Elementar GmbH) connected to an IsoPrime IRMS system. International standards IAEA-S1, IAEA-S2, IAEA-S3 were used for calibration. The results are reported in delta notation against the Vienna Canyon Diablo Troilite (VCDT) standard and the reproducibility is better than ± 0.12 ‰ (2σ).

3.5 La-Ce geochronology

3.5.1 Analytical challenges of the La-Ce system

The La-Ce isotope system based on the β-decay of ^{138}La to stable ^{138}Ce has been used as a geochemical tracer, for the age determination of rocks and more recently to directly date the formation of the cerium anomalies (Shimizu et al., 1988; Bellot et al., 2018; Israel et al., 2020; Bonnand et al., 2020). The long half-life (β-decay; $t^{1/2}$ = 1.02 x 10^9 years; Sonzogni, 2003) and the low abundance (0.089 %) of ^{138}La generate very small variations in the isotopic ratio $^{138}Ce/^{142}Ce$ compared to other systems.

Cerium has four isotopes of mass 136, 138, 140 and 142 respectively. The abundances of these 4 isotopes are very contrasted: ^{136}Ce = 0.185%; ^{138}Ce = 0.251%; ^{140}Ce = 88.45%; ^{142}Ce = 11.114% (Lide, 2009). Therefore, the high abundance of ^{140}Ce, about 400 times more abundant than the isotopes ^{136}Ce and ^{138}Ce, makes Ce measurement difficult. In addition, the ^{138}Ce/^{142}Ce ratio is affected by isobaric interference on the isotopic mass 138 by barium and lanthanum, and on the isotopic mass 142 by neodymium (Tab.3.3). And finally, ^{136}Ce and ^{138}Ce are affected by the tailing effect from mass ^{140}Ce during measurement (Bonnand et al., 2019). As a result, a good chemical separation between Ce and isobaric interfering elements is essential, as well as specific analytical approaches, such as detailed below.

Element	Isotopic mass									
	134	135	136	137	138	139	140	142	143	144
Ba	2.417	6.592	7.854	11.232	71.698					
La					0.089	99.911				
Ce			0.185		0.251		88.45	11.114		
Nd								27.2	12.2	23.8

Table 3.3. Ce, Nd, La and Ba isotope relative abondances in percentage (%) (Lide et al., 2009).

3.5.2 Sample digestion

The amount of powder required for this analysis was based on the minimum amount needed for TIMS analysis, i.e., 1000ng Ce. With low and varying cerium concentrations across the 3 sites, between 535mg and 14g of powder per sample was required to reach the 1000ng of Ce. The samples were digested with 5% trace-metal grade acetic acid in either PFA vials or 250ml HDPE bottles, depending on the acetic acid volume needed (from 20ml to 374ml) relative to the amount powder, then left overnight at room temperature. The next day, the samples were centrifuged to extract the liquid phase from the solid phase using a

pipette. The pipetted liquid was then deposited into clean PFA vials and evaporated on hot plates at 90 degrees. Samples were then taken up in concentrated HNO_3 and evaporated, three times.

3.5.3 Cerium purification protocol

Chemical separation of cerium from the carbonate matrix required four steps of columns. The first column was used to remove most of the major elements (Ca, Fe, etc.), the second column managed to separate the REEs from the remaining cations and especially from Ba, the third column allowed to isolate the Ce from the other REEs, and the last column was used to remove the Na added during the third column separation protocol.

3.5.3.1 First column: removal of major elements

The first step of cerium purification was performed on TRU.Spec resin (TRansUranic-element Specific). The TRU.Spec resin comprises a solution of 13% octyl(phenyl)-N, N-diisobutylcarbamoylmethylphosphine oxide (CMPO) dissolved in 27% tributylphosphate (TBP) and supported on the inert porous polymeric substrate (60 wt%) Amberchrom CG-71ms (Horwitz et al., 1993). The TRU.Spec resin is generally used for the separation of actinides or iron. Here, we use this resin to remove a large part of the major elements but mostly calcium and iron which are in high concentrations in the samples. To achieve this separation, the samples in 1 M HNO_3 were loaded onto 1 mL of TRU resin (50-100µm) in 10 mL Bio-Rad columns. The major elements were eluted in 1 M HNO_3 and the REEs were then eluted in 0.05 M HNO_3 and 0.1 M HCl + 0.29 M HF (Fig. 3.4 and Tab.3.4).

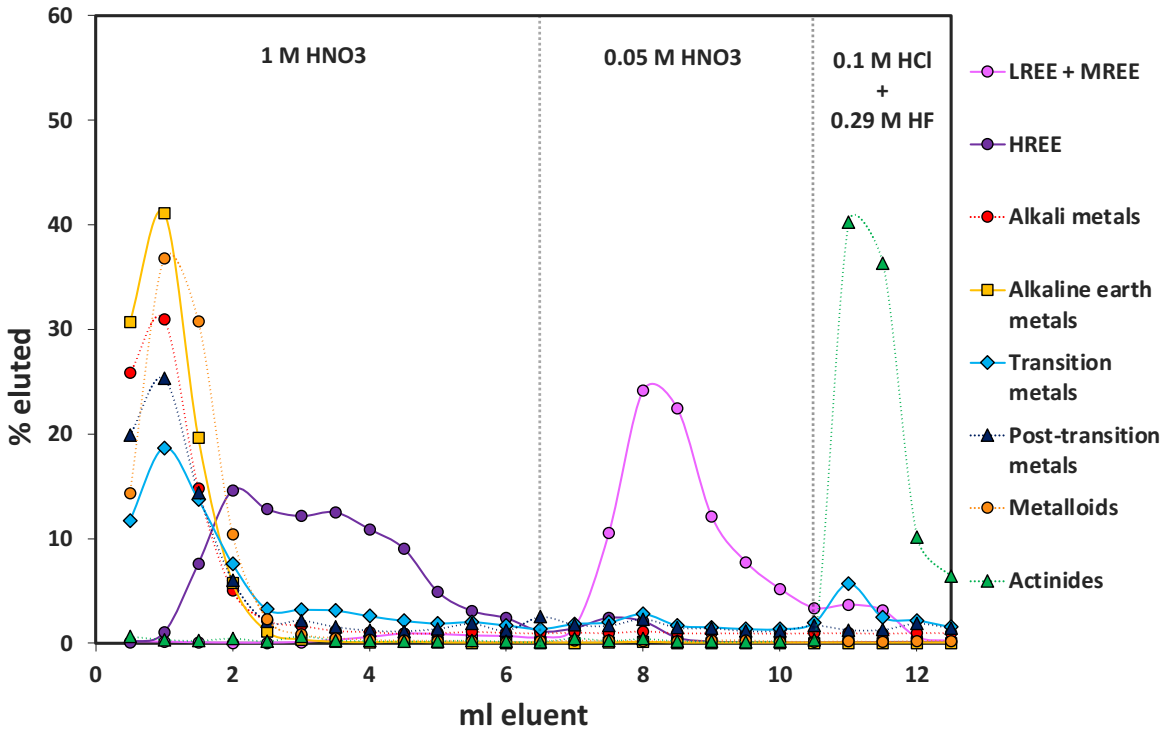

Figure 3.4. Elution curves of chemical elements during the first step of cerium purification using 1 mL TRU.Spec resin (50-100µm) in 10 mL Bio-Rad columns.

1 mL TRU resin (50-100µm) – 10 mL Bio-Rad columns		
Steps	**Acid volume**	**Type of acid**
Cleaning	20 mL	0.1M HCl + 0.29M HF
	20 mL	0.05M HNO_3
Conditioning	10 mL	1M HNO_3
Sample loading	x mL	1M HNO_3
Elution of major elements	6 mL	1M HNO_3
Elution of the matrix and REE	4 mL	0.05M HNO_3
	2.5 mL	0.1M HCl + 0.29M HF

Table 3.4. Separation protocol of the first step using 1 mL TRU.Spec resin (50-100µm) in 10 mL Bio-Rad columns.

Cerium yields were calculated from the quantitative results measured on HR-ICP-MS before and after elution on columns. The average yield of cerium after elution on TRU resin is 90.7%. Each time the TRU resin columns were used, blanks following the same

dissolution and separation steps as the samples were measured. This allows to check the purity of the analyses and to estimate the possible contaminations. The values of the blanks are given in the Table 3.5.

Elements	Ba	La	Ce	Nd	Ca	Fe
Blanks (n=7)	0.178	0.013	0.025	0.017	0.000	1.024
	0.478	0.001	0.001	0.001	0.000	0.409
	0.011	0.013	0.007	0.009	0.355	0.132
	0.008	0.001	0.006	0.001	0.037	0.059
	0.012	0.000	0.001	0.001	0.000	0.007
	0.009	0.040	0.014	0.009	0.000	0.132
	0.007	0.000	0.002	0.000	0.000	0.019

Table 3.5. Quantity (in ng) of Ba, La, Ce, Nd, Ca and Fe measured in the blanks while using the TRU.Spec resin.

3.5.3.2 Second column: REE separation from the matrix

The second step of cerium purification was performed on AGW50-X8 (200-400 mesh), an analytical grade cation exchange resin useful for separation of small peptides and amino acids, removal of cations, and metal separations. Here we use this resin to remove the remaining major cations and mostly barium. To achieve this separation, the samples in 2.5 M HCl were loaded onto 2 mL of AGW50-X8 (200- 400 mesh) in 10 mL Bio-Rad columns. The remaining major cations were eluted in 2.5 M HCl, Ba was then eluted in 2 M HNO_3 and the REEs were finally eluted in 6 M HCl (Fig. 3.5 and Tab. 3.6).

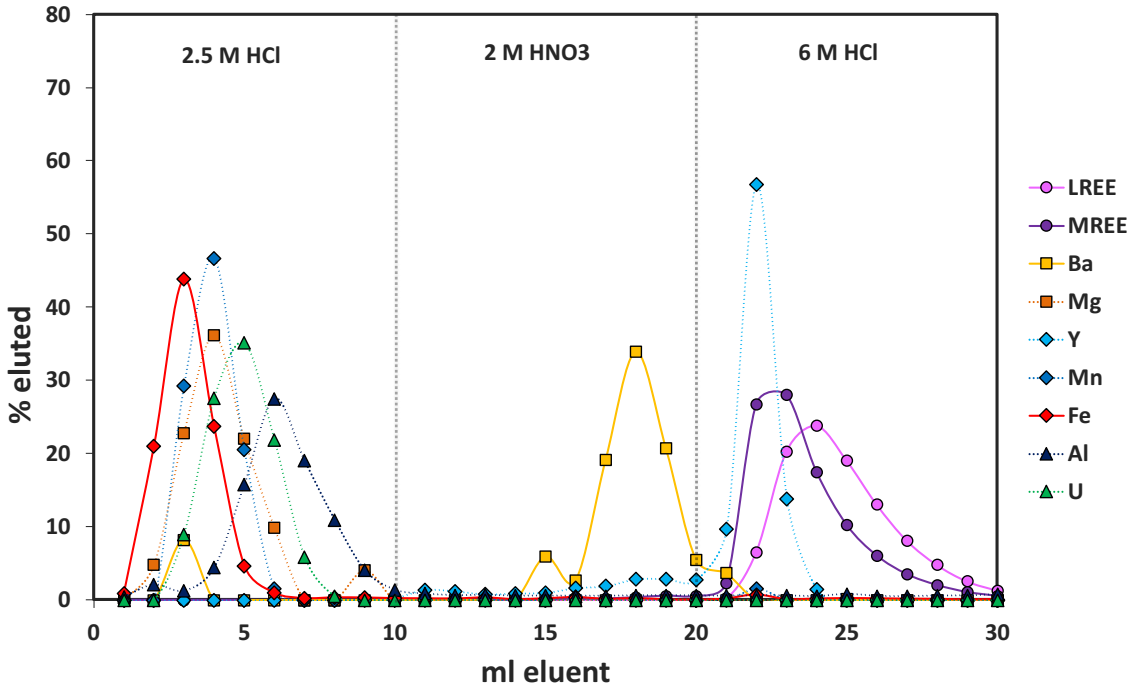

Figure 3.5. Elution curves of the remaining cations and REE during the second step of cerium purification using 2 mL AG50W-X8 (200-400 mesh) resin in 10 mL Bio-Rad columns.

2 mL AG50W-X8 resin (200-400 mesh) – Bio-Rad 10mL columns		
Steps	**Acid volume**	**Type of acid**
Cleaning	20 mL	0.3M HCl
	20 mL	6M HCl
Conditioning	20mL	2.5M HCl
Sample loading	1 mL	2.5M HCl
Matrix elution	9mL	2.5M HCl
Ba elution	10mL	2M HNO_3
LREE elution	15 mL	6M HCl

Table 3.6. Separation protocol of the second step using 2 mL AG50W-X8 (200-400 mesh) resin in 10 mL Bio-Rad columns.

The average yield of cerium after elution on AG50W-X8 resin is 92.4% and the values of the blanks while using the cationic resin are given in the Table 3.7.

Elements	Ba	La	Ce	Nd	Ca	Fe
Blanks (n=8)	0.008	0.533	0.127	0.007	0.373	0.000
	0.018	0.248	0.136	0.020	0.000	0.030
	0.009	0.000	0.000	0.000	0.190	0.000
	0.015	0.010	0.000	0.000	0.168	0.000
	0.006	0.002	0.001	0.000	0.000	0.126
	0.009	0.002	0.001	0.000	0.068	0.097
	0.037	0.000	0.002	0.000	0.057	0.204
	0.010	0.000	0.000	0.000	0.216	0.005

Table 3.7. Quantity (in ng) of Ba, La, Ce, Nd, Ca and Fe measured in the blanks while using the AG50W-X8 resin.

3.5.3.3 Third column: isolation of cerium

The third step of cerium purification was performed on Ln-Spec Eichrom resin (50-100µm) which is based on di-(2-ethylhexyl)-phosphoric acid (HDEHP) loaded on the same polymeric adsorbent (40 wt%) as used for TRU Spec, Amberchrom CG71ms (Pin and Zalduegui, 1997). This resin was used to separate Ce^{4+} from the other REEs and the oxidation of Ce from Ce^{3+} to Ce^{4+} was achieved with 20 mM of $NaBrO_3$ in 10 M HNO_3. The samples in 10 M HNO_3 + $NaBrO_3$ were loaded onto 0.4 mL Ln-Spec resin (50-100µm) in 2 mL Bio-Rad columns. The cerium was then eluted in 6 M HCl + H_2O_2 (Fig. 3.6 and Tab. 3.8).

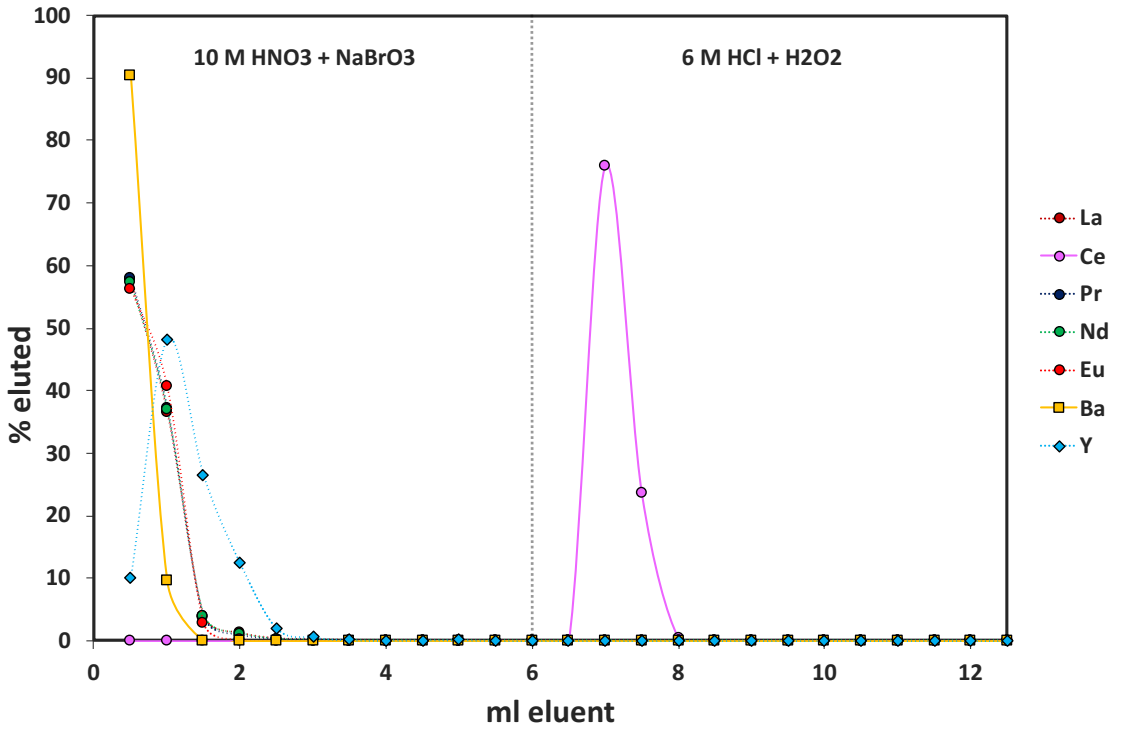

Figure 3.6. Elution curves of the rare earth elements during the third step of cerium purification using 0.4 mL LnSpec Eichrom resin (50-100µm) in 2 mL Bio-Rad columns.

0.4 mL LnSpec resin (50-100µm) – Bio-Rad 2mL columns		
Steps	**Acid volume**	**Type of acid**
Cleaning	16 mL	0.3M HCl
	16 mL	6M HCl
Conditioning	6 mL	10M HNO_3 + $NaBrO_3$
Sample loading	1 mL	10M HNO_3 + $NaBrO_3$
La, Pr, Nd, Sm and Eu elution	6 mL	10M HNO_3 + $NaBrO_3$
Ce elution	6 mL	6M HCl + H_2O_2

Table 3.8. Separation protocol of the third step using 0.4 mL LnSpec Eichrom resin (50-100µm) in 2 mL Bio-Rad columns.

The average yield of cerium after elution on Ln-Spec resin is 91.1% and the values of the blanks while using the cationic resin are given in the Table 3.9.

Elements	Ba	La	Ce	Nd	Ca	Fe
Blanks (n=8)	0.030	0.002	0.000	0.000	0.000	0.000
	0.006	0.000	0.000	0.000	0.000	0.156
	0.004	0.001	0.001	0.001	0.000	0.000
	0.013	0.000	0.000	0.000	0.000	0.000
	0.005	0.000	0.001	0.000	0.000	0.000
	0.021	0.000	0.004	0.000	0.000	0.000
	0.003	0.000	0.000	0.000	0.000	0.000
	0.001	0.000	0.000	0.000	0.000	0.445

Table 3.9. Quantity (in ng) of Ba, La, Ce, Nd, Ca and Fe measured in the blanks while using the LnSpec resin.

3.5.3.4 Fourth column: removal of Na

The last step of cerium purification was performed on AGW50-X8 (200-400 mesh), the same resin used for the second step of purification but with a different amount of resin in smaller columns. This last step is essential to remove the sodium added during the first step of purification. The samples in 2 M HCl were loaded onto 0.4 mL AG50W-X8 in 2 mL Bio-Rad columns. The remaining cations were eluted in 2 M HCl, Ba was then eluted in 2 M HNO_3 and the REEs were finally eluted in 6 M HCl (Tab. 3.10).

Even if we use the same resin (AG50W-X8) as for step 2, we cannot use it under the same conditions for this step. Indeed, for step 2, we use 2 mL of resin in 10 mL Bio-Rad columns but if we use the same amount of resin for this step, too much organic material from the resin will be in the sample and will prevent the emission of cerium on TIMS. Therefore, we reduced the volume of resin to 0.4 mL and used 2 mL Bio-Rad columns. Consequently, we had to reduce the normality from 2.5 M HCl to 2 M HCl for conditioning, loading and first elution, which was too high for this amount of resin and resulted in a loss of cerium.

0.4 mL AG50W-X8 resin (200-400 mesh) – Bio-Rad 2mL columns		
Steps	**Acid volume**	**Type of acid**
Cleaning	12 mL	0.3M HCl
	12 mL	6M HCl
Conditioning	12 mL	2M HCl
Sample loading	1 mL	2M HCl
Remaining matrix and Na elution	4mL	2M HCl
Remaining Ba elution	4mL	2M HNO_3
Ce elution	12mL	6M HCl

Table 3.10. Separation protocol of the fourth step using 0.4 mL AG50W-X8 (200-400 mesh) resin in 2 mL Bio-Rad columns.

The average yield of cerium after elution on AG50W-X8 (0.4 mL) resin is 92.3% and the values of the blanks while using the cationic resin are given in the Table 3.11.

Elements	Ba	La	Ce	Nd	Ca	Fe
Blanks (n=8)	0.037	0.000	0.276	0.000	0.000	0.046
	0.008	0.000	0.264	0.000	0.099	0.183
	0.026	0.001	0.157	0.000	0.000	0.000
	0.024	0.000	0.015	0.000	0.185	0.000
	0.020	0.000	0.001	0.000	0.000	0.938
	0.008	0.000	0.002	0.000	0.000	0.276
	0.013	0.000	0.005	0.000	0.000	0.000
	0.005	0.000	0.001	0.000	0.000	0.000

Table 3.11. Quantity (in ng) of Ba, La, Ce, Nd, Ca and Fe measured in the blanks while using the AG50W-X8 resin.

3.5.3.5 Yields

These 4 separation steps, although essential, generate a significant loss of cerium depending on the matrix. The final cerium yields are rather homogeneous for the artificial and rock standards, with an average of 82% Ce yield for BHVO-2, 85% for JDO-1, and 80% for Ce LMV. The final yields of the carbonate samples are however quite

heterogeneous, with yields varying from 1 to 100% between the three sites. The average final cerium yield for the three sites was 39%, with an average of 47% for Red Lake, 51% for Woman Lake and 16% for Steep Rock. Cerium yields appear to be clearly related to Ca concentrations as the higher the calcium concentrations, the lower the cerium yield. (Fig. 3.7). Indeed, the higher the Ca concentrations are, the more the column risks saturation by Ca and is unable to retain Ce. Although an optimal yield is desired to ensure that enough Ce is recovered for TIMS measurements (about 1000 ng), low yields are not problematic for radiogenic Ce measurements. Indeed, even if isotopic fractionation occurs on the columns, it is corrected during normalization to the $^{136}Ce/^{142}Ce$ ratio.

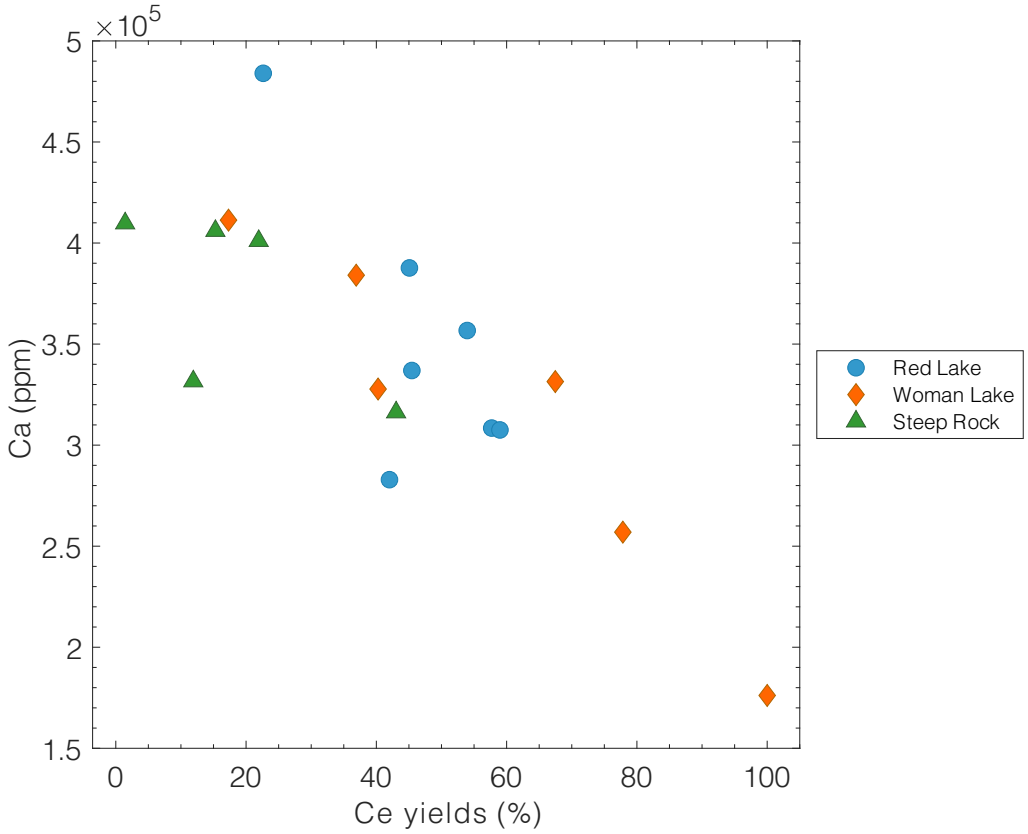

Figure 3.7. Ca concentrations (ppm) plotted against Ce yields (%), it is clear that Ca concentrations influence cerium yield as the more calcium there is, the more cerium is lost, due to the saturation of the column by calcium.

3.5.4 Mass spectrometry

3.5.4.1 TIMS Triton

Ce isotopic analyses were performed on the Thermo-Scientific Triton plus TIMS at the Laboratoire Magmas et Volcans in Clermont-Ferrand, France. The Thermo-Ionization Mass Spectrometer (TIMS) Triton is a magnetic sector mass spectrometer capable of making highly accurate measurements of isotopic ratios of elements that can be thermally ionized by passing a current through one or two thin metal filaments under clean vacuum conditions. The generated ions are then accelerated through an electrical potential gradient and focused into a beam via a series of slits and electrostatically charged plates and separated according to their m/z ratio by a magnetic sector. These mass-separated beams are then directed to collectors where the ion beam is converted into a voltage. By comparing the voltages corresponding to the different ion beams, accurate isotope ratios can be obtained.

Thermo-ionization is the most suitable method for Ce isotopic measurements in comparison with MC-ICP-MS (Willbold, 2007). On MC-ICP-MS, the plasma ionizes all the elements, and this makes it difficult to correct Ba interferences. Also, a small amount of Xe is present in the Ar, which interferes with Ce at mass 136. In TIMS, Ce can be emitted in oxide form, which allows better control of isobaric interferences, especially those from Ba because the molar enthalpy energy of BaO is higher than CeO. To measure cerium in oxide form, we deposit 1µl of H_3PO_4 (0.5 M) on the Re filament (99.99%) before depositing the sample. The sample is then very carefully deposited in 2 M HCl with a pipette on the drop of H_3PO_4 on the filament heated to 0.8 A. Once the deposit is dry, the samples are

"flashed" by heating the filaments up to about 2/3A, until a little white smoke comes out, then the current is brought down to zero very quickly.

The measurements are done in double Re filament, i.e., two filaments are positioned opposite each other, the evaporating filament on which the sample is deposited and the ionizing filament on which no deposit is made. The presence of the ionizing filament allows cerium to ionize at a lower temperature than that at which it normally does. For standards Ce LMV, the ionization filament is heated to 3800 mA while the evaporating filament is heated to approximately 800 mA. For the samples, it's much more variable, the ionization filament is heated up between 3120 to 4025 mA while the evaporating is heated up between 450 to 1300 mA. This corresponds to a pyrometer temperature between 1550 and 1750°C. The heating temperature of the evaporating filament varies because of small soldering defects or deformation of the filament feet. This is because the filament supports are reused several times. The filament posts and plates are sanded, then washed in a bath with diluted RBS25 (10% with deionized water) with ultrasound, between each use (RBS25 is an alkaline detergent which is used for washing in medical and light radioactive decontamination). Re filaments are pre-degassed for 20 min up to 4.8 A to eliminate any pollution coming from the filament, especially from Ba.

3.5.4.2 Cup configuration and corrections

For Ce isotopic measurements on TIMS, the faraday cups were positioned as shown in Table 3.12 (Bonnand et al. 2019). The samples are usually measured with an intensity between 8 and 10V on mass 158 ($^{142}Ce^{16}O$), which corresponds to an intensity of 80V on mass 156 ($^{140}Ce^{16}O$). The signal strength received in the faraday cups cannot be higher than 50V without damaging them, therefore, the ^{140}Ce is not measured. However, its emission

generates a peak tailing effect, due to the large differences in abundance of Ce isotopes, that must be corrected to not overestimate the intensities of the smallest isotopes. Part of ^{140}Ce ions lose some of their kinetic energy by colliding with residual molecules in the tube and are therefore more deflected than others by the magnetic field and increase the signal on the smaller masses 136 and 138. Consequently, the effect of peak tailing has been measured in L2, L1 and H1 cups at 152.64, 153.37 and 154.61 masses, respectively.

Faraday cup	**L4**	**L3**	**L2**	**L1**	**C**	**H1**	**H3**	**H4**
Oxides	$^{134}Ba^{16}O$	$^{136}Ce^{16}O$	PT	PT	$^{138}Ce^{16}O$	PT	$^{142}Ce^{16}O$	$^{142}Ce^{18}O$
Masses	150	152	152.64	153.37	154	154.61	158	160

Table 3.12. Cup configurations used on the Thermo-Scientific Triton plus TIMS at the Laboratoire Magmas et Volcans for Ce isotopic measurement to date cerium anomalies. L2, L1 and H1 cups are used to measure the peak tailing (PT) effect of the 140 Ce mass on the 136 and 138 Ce masses.

Moreover, since Ce is measured in oxide form, it is necessary to correct the $^{138}Ce/^{142}Ce$ ratio of CeO formed with the minor oxygen isotopes ^{18}O. For this, the $^{18}O/^{16}O$ ratio is determined in situ using an iterative calculation that integrates the mass discrimination law with direct measurements of $^{142}Ce^{18}O$ and $^{136}Ce^{16}O$ (Makishima et al., 1987; Willbold, 2007). In addition, the mass fractionation caused by the preferential evaporation of lighter atoms over heavier atoms at the beginning of analysis must also be corrected, using the exponential law applied to cerium according to Hart and Zindler (1989).

3.5.4.3 Reproducibility and precision

The artificial reference standard used for cerium measurements is Ce LMV. Figure 3.8 shows all the values obtained during these analyses; the average $^{138}Ce/^{142}Ce$ value is 0.02256983 with an external reproducibility of 21.14 ppm 2SD (n=11).

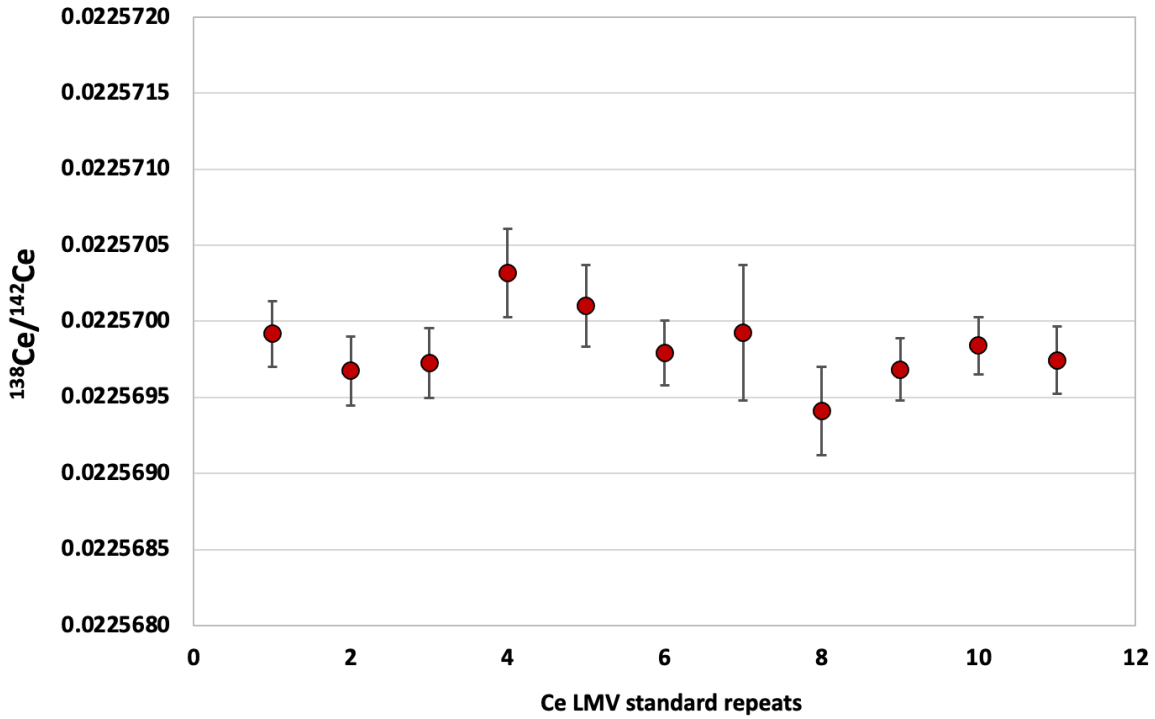

Figure 3.8. $^{138}Ce/^{142}Ce$ ratio measured for Ce LMV standard corrected from tailing, oxygen and mass fractionation. The error bars correspond to the 2SE of each measurement.

Two rock standards, JDO-1 and BHVO-2, that followed the same chemical preparation as the samples were also analyzed. The mean value of the Japanese dolomite standard JDO-1 of the $^{138}Ce/^{142}Ce$ ratio is 0.02258463 with an external reproducibility of 32.14 ppm 2SD (n=3). For the Hawaiian basalt standard BHVO-2, the mean value of the $^{138}Ce/^{142}Ce$ ratio is 0.02256337 with an external reproducibility of 5.44 ppm 2SD (n=3). This value is consistent with other BHVO-2 $^{138}Ce/^{142}Ce$ ratios from literature such as 0.02256550 (68 ppm 2SD; Doucelance et al., 2014), 0.02256460 (75 ppm 2SD; Bellot et al., 2015), 0.02256482 (26 ppm 2SD; Willig and Stracke, 2018), 0.02256499 (10 ppm 2SD; Bonnand et al., 2019) and 0.02256453 (44 ppm; Israel et al., 2020).

Uncertainty on the $^{138}La/^{142}Ce$ ratio was evaluated by independent digestions and repeat analyses of the JDo-1 international dolomite geostandard that were included in the

same ElementXR sessions used to generate the sample data. JDo-1 was duplicated a total of 6 times across all sessions, yielding and average $^{138}La/^{142}Ce$ ratio of 0.0315434 and precision of 0.00023266 (2σ). The worst 2SE error of the three duplicate JDo-1 analyses passed over the three sessions (0.00035707) was used for isochron calculation. See Appendix Tables C.3 and C.4 for the $^{138}Ce/^{142}Ce$ and $^{138}La/^{142}Ce$ values determined for the various standards analyzed alongside the samples.

3.6 References

Barrat, J.A., Bayon, G., Wang, X., le Goff, S., Rouget, M.L., Gueguen, B., and ben Salem, D., 2020, A new chemical separation procedure for the determination of rare earth elements and yttrium abundances in carbonates by ICP-MS: Talanta, v. 219, doi:10.1016/j.talanta.2020.121244.

Bellot, N., Boyet, M., Doucelance, R., Bonnand, P., Savov, I.P., Plank, T., and Elliott, T., 2018, Origin of negative cerium anomalies in subduction-related volcanic samples: Constraints from Ce and Nd isotopes: Chemical Geology, v. 500, p. 46–63, doi:10.1016/j.chemgeo.2018.09.006.

Bellot, N., Boyet, M., Doucelance, R., Pin, C., Chauvel, C., and Auclair, D., 2015, Ce isotope systematics of island arc lavas from the Lesser Antilles: Geochimica et Cosmochimica Acta, v. 168, p. 261–279, doi:10.1016/j.gca.2015.07.002.

Bonnand, P., Israel, C., Boyet, M., Doucelance, R., and Auclair, D., 2019, Radiogenic and stable Ce isotope measurements by thermal ionisation mass spectrometry: Journal of Analytical Atomic Spectrometry, v. 34, p. 504–516, doi:10.1039/c8ja00362a.

Bonnand, P., Lalonde, S. v., Boyet, M., Heubeck, C., Homann, M., Nonnotte, P., Foster, I., Konhauser, K.O., and Köhler, I., 2020, Post-depositional REE mobility in a Paleoarchean banded iron formation revealed by La-Ce geochronology: A cautionary tale for signals of ancient oxygenation: Earth and Planetary Science Letters, v. 547, doi:10.1016/j.epsl.2020.116452.

Canfield, D.E., Raiswell, R., Westrich, J.T., Reaves, C.M., and Berner, R.A., 1986, The use of chromium reduction in the analysis of reduced inorganic sulfur in sediments and shales: Chemical Geology, v. 54, p. 149–155, doi:10.1016/0009-2541(86)90078-1.

Doucelance, R., Bellot, N., Boyet, M., Hammouda, T., and Bosq, C., 2014, What coupled cerium and neodymium isotopes tell us about the deep source of oceanic carbonatites: Earth and Planetary Science Letters, v. 407, p. 175–186, doi:10.1016/j.epsl.2014.09.042.

Hart, S.R., and Zindler, A., 1989, Isotope fractionation laws: a test using calcium: International Journal of Mass Spectrometry and Ion Processes, v. 89, p. 287–301, doi:10.1016/0168-1176(89)83065-4.

Horwitz, E.P., Chiarizia, R., Dietz, M.L., Diamond, H., and Nelson, D.M., 1993, Separation and preconcentration of actinides from acidic media by extraction chromatography: Analytica Chimica Acta, v. 281, p. 361–372, doi:10.1016/0003-2670(93)85194-O.

Israel, C., Boyet, M., Doucelance, R., Bonnand, P., Frossard, P., Auclair, D., and Bouvier, A., 2020, Formation of the Ce-Nd mantle array: Crustal extraction vs. recycling by subduction: Earth and Planetary Science Letters, v. 530, doi:10.1016/j.epsl.2019.115941.

Lide, D.R., Baysinger, G., Berger, L.I., Goldberg, R.N., Kehiaian, H. v, Kuchitsu, K., Roth, D.L., and Zwillinger, D., 2009, CRC Handbook of Chemistry and Physics Editor-in-Chief.

Makishima, A., Shimizu, H., and Masuda, A., 1987, Precise measurement of cerium and lanthanum isotope ratios.: Journal of the Mass Spectrometry Society of Japan, v. 35, p. 64–72, doi:10.5702/massspec.35.64.

Pin, C., and Zalduegui, J.F.S., 1997, Sequential separation of light rare-earth elements, thorium and uranium by miniaturized extraction chromatography: Application to isotopic analyses of silicate rocks.

Rongemaille, E., Bayon, G., Pierre, C., Bollinger, C., Chu, N.C., Fouquet, Y., Riboulot, V., and Voisset, M., 2011, Rare earth elements in cold seep carbonates from the Niger delta: Chemical Geology, v. 286, p. 196–206, doi:10.1016/j.chemgeo.2011.05.001.

Rouxel, O.J., Bekker, A., and Edwards, K.J., 2005, Iron isotope constraints on the Archean and Paleoproterozoic ocean redox state: Science, v. 307, p. 1088–1091, doi:10.1126/science.1105692.

Shimizu, H., Nakai, S., Tasaki, S., Masuda, A., Bridgwater, D., Nutman, A.P., and Baadsgaard, H., 1988, Geochemistry of Ce and Nd isotopes and REE abundances in the Al~tsoq gneisses, West Greenland.

Sonzogni, A.A., 2003, Nuclear Data Sheets for A = 138: Nuclear Data Sheets, v. 98, p. 515–664, doi:10.1006/ndsh.2003.0004.

Wang, K., 2013, Iron Isotope Cosmochemistry: All Theses and Dissertations (ETDs), p. 12–2.

Weyer, S., and Schwieters, J.B., 2003, High precision Fe isotope measurements with high mass resolution MC-ICPMS: International Journal of Mass Spectrometry, v. 226, p. 355–368, doi:10.1016/S1387-3806(03)00078-2.

Willbold, M., 2007, Determination of Ce isotopes by TIMS and MC-ICPMS and initiation of a new, homogeneous Ce isotopic reference material: Journal of Analytical Atomic Spectrometry, v. 22, p. 1364, doi:10.1039/b705306a.

Willig, M., and Stracke, A., 2018, Accurate and precise measurement of Ce isotope ratios by thermal ionization mass spectrometry (TIMS): Chemical Geology, v. 476, p. 119–129, doi:10.1016/j.chemgeo.2017.11.010.

CHAPTER 4:

Iron Isotope Systematics of Earth's Earliest Thick Carbonate Platform

Abstract

The global marine carbonate factory has Archean origins, yet relatively little is known about the sedimentological, geochemical, and redox conditions associated with Earth's oldest carbonate platforms deposited from 2.96 to 2.80 Ga. Here we report rare earth element (REE) data and Fe stable isotope chemostratigraphy obtained across an exceptional transgressive sequence spanning >70 m of stromatolitic marine carbonate and >60 m of deep-water-facies (iron formation and black shales) in drill core from the ~450m thick 2.93-billion-year-old (Ga) Ball Assemblage of the Red Lake Greenstone Belt (Superior Craton, Northwestern Ontario, Canada). Major element and REE data reveal that the accretion of the stromatolitic dolostones occurred under ferruginous marine conditions with important hydrothermal influence and a combination of Eh conditions and REE residence times that were generally insufficient for Ce oxidation. However, Fe isotopes reveal a dynamic iron redox cycle spanning this shallow-to-deep transect, with $\delta^{56}Fe$ values ranging from -2.88‰ to +1.50‰ across all lithologies combined. The large range and stratigraphic evolution of $\delta^{56}Fe$ values are best explained by plume depletion of Fe via iron oxide precipitation offshore, yielding low $\delta^{56}Fe$ values in the upwelling residual Fe(II) pool. Important and remarkable secular $\delta^{56}Fe$ variations were observed in the stromatolitic carbonates that are not readily explained by a Rayleigh distillation model nor by their trace pyrite contents, instead co-varying with the latter's sulfur concentrations and stable isotope composition. Our data indicate that $\delta^{56}Fe(II)_{aq}$ values on the platform were controlled by an indirect driver linking the Fe and S cycles, which we suggest was variations in primary production. Our data indicate an important role for photosynthesis in modulating Earth's major biogeochemical cycles already by 2.93 Ga.

Résumé

Les conditions sédimentologiques, géochimiques et d'oxydoréduction associées aux plus anciennes plateformes carbonatées de la Terre déposées entre 2,96 et 2,80 Ga restent encore peu connues. Nous présentons ici des données sur les éléments des terres rares (REE) ainsi qu'une chimio-stratigraphie des isotopes stables du Fe obtenues sur une séquence transgressive couvrant plus de 70 m de carbonates marins et 60 m de faciès d'eaux profondes (BIF et schistes noirs) dans une carotte de forage provenant du Ball Assemblage de la ceinture de schistes verts de Red Lake (Ontario, Canada), âgé de 2,93 milliards d'années. Les données sur les éléments majeurs et les REE révèlent que l'accrétion des dolomies s'est produite dans des conditions marines ferrugineuses avec une influence hydrothermale importante et des conditions généralement insuffisantes pour oxyder le Ce. Cependant, les isotopes du fer révèlent un cycle dynamique d'oxydoréduction du fer couvrant ce transect peu profond à profond, avec des valeurs de δ^{56}Fe allant de -2,88‰ à +1,50‰ toutes lithologies confondues. La large gamme et l'évolution stratigraphique des valeurs de δ^{56}Fe sont mieux expliquées par l'appauvrissement en Fe du panache via la précipitation d'oxyde de fer au large, engendrant de faibles valeurs δ^{56}Fe dans le réservoir de Fe(II) résiduel remontant. Des variations séculaires importantes en δ^{56}Fe ont été observées dans les carbonates qui ne peuvent être expliquées facilement par un modèle de distillation de Rayleigh, ni par leur teneur en pyrite, mais qui varient plutôt avec les concentrations de soufre et la composition isotopique stable de ces derniers. Nos données indiquent que les valeurs de $\delta^{56}Fe(II)_{aq}$ sur la plate-forme étaient contrôlées par un facteur indirect reliant les cycles du Fe et du S, que nous suggérons être des variations dans la production primaire. Nos données indiquent un rôle important de la photosynthèse dans la modulation des principaux cycles biogéochimiques de la Terre déjà à 2,93 Ga.

4.1 Introduction

The Great Oxygenation Event (GOE) marks the first significant accumulation of atmospheric oxygen ca. 2.5 to 2.3 Ga, yet multiple redox proxies indicate the establishment of both marine and lacustrine O_2 oases between 2.5 and 3.0 Ga (e.g., (Anbar et al., 2007; Planavsky et al., 2014; Riding et al., 2014; Robbins et al., 2016; Wilmeth et al., 2022). Prior to 2.5 Ga, the discrepancy between persistent mass-independent fractionation of sulfur isotopes (MIF-S) indicating atmospheric anoxia and marine redox proxies implying oxygenic photosynthesis pre-GOE can be explained by either pelagic (Olson et al., 2013) or benthic (Lalonde and Konhauser, 2015) shallow-water and terrestrial O_2-producing communities that had little effect on atmospheric composition. Recently, paired S and Fe isotope data from stromatolite-hosted trace pyrites have indicated the occurrence of oxygenated near-shore shallow marine environments ca. 2.96 Ga, despite clear evidence for atmospheric anoxia (Eickmann et al., 2018).

The above studies converge on the idea that shallow marine environments showing evidence of strong photosynthetic activity are promising targets for identifying robust chemical and isotopic indicators of local oxygen production early in Earth history. However, Archean carbonate platforms, often preserving hundreds of meters of near-continuous stromatolitic carbonate deposition in shallow-water environments, remain largely unexplored for the geochemical and paleoredox signals that they may record.

Recent work on stromatolitic carbonates from the 2.43–2.46 Ga Griqualand Formation, S. Africa, demonstrate the proxy potential of such targets (Heard et al., 2022). Here, modest but appreciable enrichments in Ce and Mn reveal high oxidation potential in the stromatolitic carbonate-depositing environment relative to the enclosing deep-water

banded iron formation (BIF) facies, while strong iron isotope homogeneity in the stromatolite facies (-1.55‰ to -1.45‰) relative to the BIF (-0.07‰ to -1.75‰; data from Thibon et al., 2019) was suggested to indicate quantitative oxidation of Fe in the former. However, this stromatolitic interval spanned only ~1m, and the Fe isotope results are odds with prior work that revealed significant Fe isotope variation (-3.69‰ to 0.08‰) at the platform scale in the underlying Campbellrand-Malmani carbonate platform that is at most 150 Ma younger (Eroglu et al., 2018). It remains to be seen what Earth's earliest thick carbonate platforms, deposited between ~2.93 and 2.80 Ga (Riding et al., 2014) reveal about iron cycling and paleoredox in shallow-water stromatolite-accreting environments.

Accordingly, here we report on the REE and Fe isotope compositions of diverse sediments associated with the shallow-water stromatolitic Archean carbonate platform preserved in the 2.925 to 2.940 Ga Ball Assemblage of the Red Lake Greenstone Belt, Superior Craton, Western Ontario, Canada. This platform is the Earth's first thick (>100 m) accumulation of carbonates, and is interbedded with siltstones, deep-water black shales (pyritic at times), and BIF (McIntyre and Fralick, 2017; Afroz, 2019). The transition between conformable shallow-water and deep-water facies provides an unparalleled opportunity to study the Mesoarchean iron cycle, and the abiotic or metabolic processes driving it, in a continuous chemostratigraphic shallow-to-deep transect.

In this work we focused on two paleoredox proxies of particular promise, cerium (Ce) anomalies and Fe stable isotope compositions. With the exception of Eu, Ce is the only REE for which abundance anomalies occur in aqueous solutions and their precipitates due to redox reactions. Oxidation of Ce(III) to Ce(IV) and subsequent decoupling of Ce from the other REEs due to the formation of less soluble Ce(IV) species and/or preferential

adsorption of Ce(IV) on particle surfaces drives the water-column development and sedimentary preservation of Ce anomalies (Bau and Dulski, 1996). Cerium oxidation requires redox electrode potentials significantly higher that of the Fe(III)/Fe(II) half-cell, and hence, the widespread occurrence of negative Ce anomalies in sediments beginning ca. 2.5 Ga has been used to argue in favor of the presence of oxidized Precambrian surface waters (Towe, 1991; Riding et al., 2014) and its first appearance provides convincing evidence for the origin of cyanobacteria by 2.7 Ga (Riding et al., 2014). Iron stable isotopes also provide important information about ancient Fe cycling that speaks directly to water column paleo-redox (Johnson et al., 2003; Rouxel et al., 2005a; Dauphas et al., 2007). While igneous materials possess a narrow range in δ^{56}Fe, Fe isotope fractionations greater than ~0.5‰/amu are associated exclusively with Fe redox cycling (Beard et al., 2003). We thus also examined the whole-rock Fe stable isotope systematics of oxide-facies BIF and sulfidized BIF (S-BIF), black shales, and stromatolitic dolostones, as well as isolated pyrites and carbonate-associated Fe isolated via a weak-leach technique, in order to understand iron redox cycling and microbial metabolic processes in a unique Archean transgressive sequence that preserves a history of Fe-rich deep waters upwelling onto what constitutes Earth's first thick carbonate platform.

4.2 Methods

See Chapter 3, section 3.2 for major and trace elements, section 3.3 for Fe isotopes, and section 3.4 for S isotopes. All data are available in Appendix A.

4.3 Results and discussion

4.3.1 Major and trace element constraints on paleoenvironmental conditions

The NGI10-031 drill hole captures a wide range of lithologies (iron formations, shales, carbonates) and this lithological diversity is reflected in the wide range in major element compositions. In this sample set, Fe_2O_3 contents ranged from 0.39 to 63.07 wt.%, Al_2O_3 from 0.05 to 25.97 wt.%, and CaO from 0.12 to 30.55 wt.% (Appendix A.1). Certain intervals in both carbonate and shale sections are remarkably sulfur-rich; at depths around 58 m and 80 m, carbonates reach up to 10 wt. % S, largely as fine-grained disseminated pyrite and pyrrhotite, while higher in the core ca. 80 m, shales reach up to 24 wt.% S, where the same sulfur minerals are observed to occur as cm-scale nodules and disseminated bed-parallel layers. The stratigraphic evolution upwards from stromatolitic dolomite to sulfide- and organic-rich shales and then iron formations paints a clear picture of sea-level transgression and provides a shallow to deep perspective on the geochemical zonation of this unique Mesoarchean shoreline.

Trace element compositions from the NGI drill hole provide important additional insights into the paleoenvironment at the time of deposition. PAAS-normalized REE spectra (Fig. 4.1) show multiple characteristics shared by both modern and Archean seawater that confirm the marine origin of these carbonates, notably heavy REE enrichment, positive La anomalies, and positive Y/Ho ratios (German et al., 1990; Bau and Dulski, 1996; Bolhar et al., 2004).

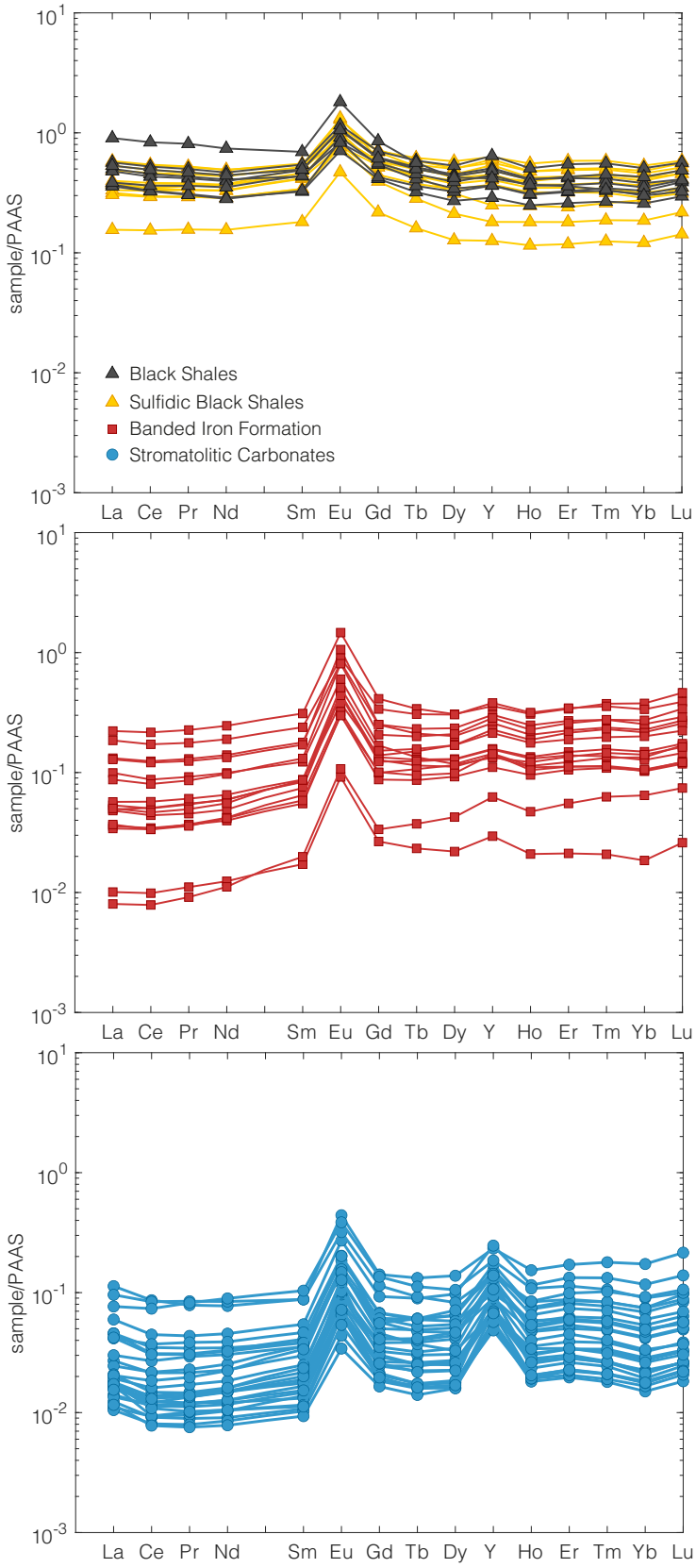

Figure 4.1. Shale-normalized REE + Y patterns of BIF (red squares), stromatolitic dolostones (blue circles), black shales (black triangles) and sulfidic black shales (yellow triangles). BIF and carbonate chemical sediments show clear seawater-like patterns, but with pronounced Eu anomalies indicating the upwelling of hydrothermally influenced basinal waters onto the platform and a clear absence of Ce anomalies reflecting anoxic water column conditions.

These seawater features are most pronounced in weak carbonate digests relative to whole-rock digest of BIF, sulfidic shales, and black shales, the latter two showing flatter (shale-like) spectra and higher total REE concentrations concomitant with their higher concentrations of crustal components. The Red Lake carbonates differ from modern seawater in two important aspects, specifically with regards to the presence of strong Eu anomalies and general absence of Ce anomalies. The existence of Eu anomalies reveals the presence of a high-temperature hydrothermal component in seawater (Bau, 1991), confirming that upwelling basinal fluids affected by hydrothermal venting were likely an important Fe source even to shallow waters, and that the Red Lake carbonate platform likely had a strong connection to the open ocean. This is also observed for the 2.96 Ga shallow-water Sinqeni iron formation (S. Africa; (Alexander et al., 2008). Strong negative cerium anomalies characterize modern oxygenated seawater, and their general absence in the studied section indicates against the presence of free oxygen in the water column (Bau and Dulski, 1996). The localized production of oxygen cannot be ruled out; one might imagine a case where Fe(II) supply exceeded O_2 production, such that the water column remained anoxic and ferruginous even if oxygenic photosynthesis were occurring. In any case, Eh conditions were too reducing, or REE residences times to short, to generate significant amounts of Ce(IV) (Bau and Dulski, 1996) in this particular section. While the absence of cerium anomalies is important evidence for generally reducing water column conditions, it does not conclusively indicate which oxidative mechanisms may have been responsible for BIF deposition. Iron isotopes provide important additional insight into redox structure and iron cycling across and offshore of the platform.

4.3.2 Iron cycling from deep water to the platform: an iron perspective

Iron isotope variations are mainly associated with redox changes (Johnson et al., 2004; Beard and Johnson, 2004), and sediments from the Red Lake Greenstone Belt show clear isotope evidence of iron redox cycling in both shallow and deep-water facies, with $\delta^{56}Fe$ values ranging from -2.88 ‰ to 1.50‰ (Fig. 4.2).

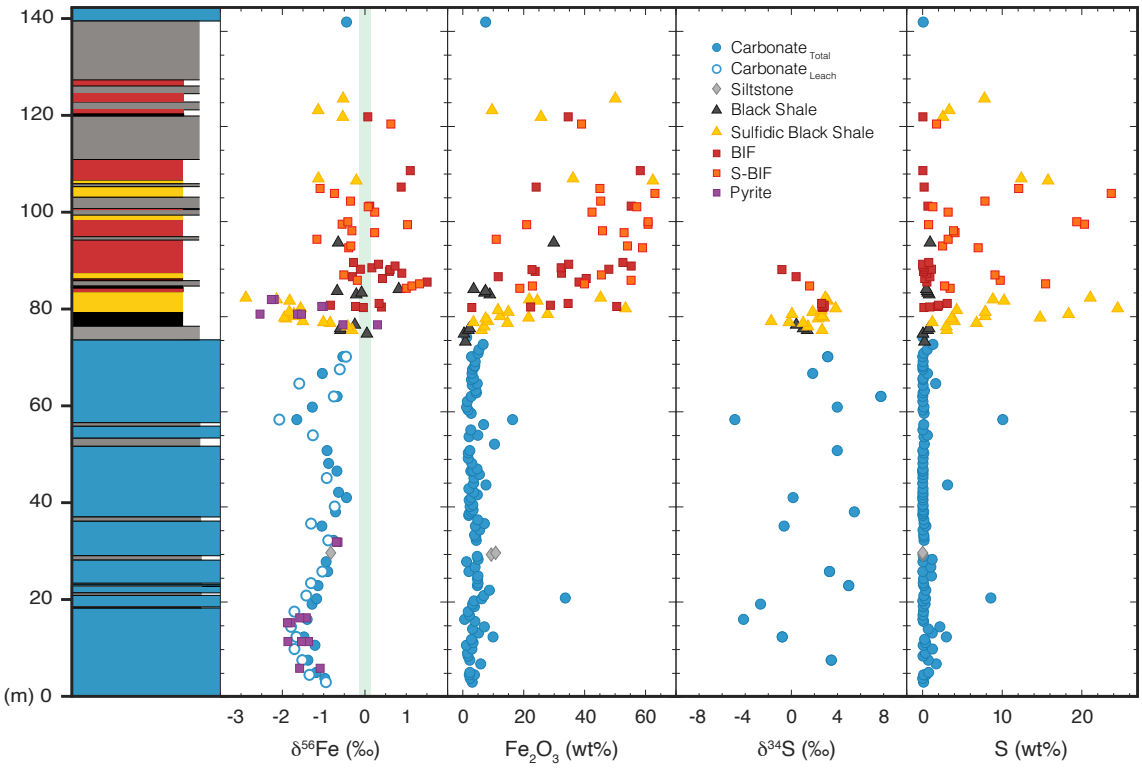

Figure 4.2. Chemostratigraphic profiles of iron isotope compositions ($\delta^{56}Fe$), Fe concentrations, sulfur isotope compositions ($\delta^{34}S$), and S concentrations in the NGI-31 drill core, where shallow water stromatolitic dolostones (blue circles) are overlain by deep-water sediments in the form of shales (black and yellow triangles) and iron formations (red and orange squares) in a shallow-to-deep transgressive sequence.

Indeed, the different lithologies cover a wide range of $\delta^{56}Fe$ values, with BIF spanning -0.84 to 1.5‰, sulfidic black shales from -2.88 to -1.09 ‰, black shales from -1.01 to -0.08 ‰, carbonates from -2.07 to -0.05 ‰, and isolated pyrites from -2.54 to

0.30‰. Assuming a deep-water Fe(II) source close to values of the crust or high-temperature hydrothermal fluids (~0‰; Beard et al., 2003), sedimentary variations away from this value represent a combination of fractionating oxidation, reduction, and mineral precipitation processes onto which reservoir effects may be superposed.

Near-zero to highly positive $\delta^{56}Fe$ values in the BIF are consistent with a near-zero $\delta^{56}Fe$ source that experienced variable degrees of reservoir drawdown. Indeed, oxidative precipitation of $Fe(II)_{aq}$ to $Fe(III)_{ppt}$ by O_2 as well as microbial Fe(II) oxidation by anoxygenic photosynthesis causes enrichment in heavy Fe isotopes in the precipitate by 1 to 2‰ (Croal et al., 2004; Swanner et al., 2015) and up to 2‰ (Bullen et al., 2001; Beard et al., 2003), respectively. The negative BIF values reflect either dissimilatory Fe(III) reduction (DIR) that releases isotopically light Fe(II) (Icopini et al., 2004; Johnson et al., 2004), or alternatively, isotope distillation during oxide precipitation, yielding to low $\delta^{56}Fe$ values in residual Fe(II) pool (Rouxel et al., 2005). In either scenario, the alternance between BIF, sulfidic black shale, and ordinary black shale indicate instability of Fe(II) and/or S(-II) concentrations in the water column. Trendall et al. (2004) suggested that BIF deposition occurs rapidly as a function of iron supply, while shale deposition represents slower deposition under more iron-depleted conditions. The iron isotope compositions are consistent with this model, whereby values become increasingly negative from iron formation to sulfidic shales as $\delta^{56}Fe(II)_{aq}$ decreased with increasingly iron-starved conditions. While there may be important iron isotope fractionation expressed during the precipitation of sulfides (Guilbaud et al., 2011), negative values in the oxide-facies BIF require negative excursions in $\delta^{56}Fe\ (II)_{aq}$, either in the water column (via oxidative Fe(II) depletion) or porewater (via DIR). The non-sulfidic black shales continue the upward trend of iron depletion, recording crustal values for a lack of iron enrichment from seawater. In

a Rayleigh distillation model where $\Delta^{56}Fe_{oxide\text{-}aq}$ is set at 2‰, $\delta^{56}Fe\ (II)_{aq}$ values as low as -3‰ (corresponding to BIF values as low as -1‰) reflect to up to 70% Fe loss by precipitation of oxides in the offshore.

The Fe isotope composition of the carbonates indicates that an exclusively lighter $\delta^{56}Fe(II)_{aq}$ reservoir was consistently upwelled onto the shelf. As Fe(II) substitution into carbonates involves no change in redox state, carbonates are thought to directly record $\delta^{56}Fe(II)_{aq}$ values at the time of their formation (Eroglu et al., 2018). Inferred carbonate $\delta^{56}Fe(II)_{aq}$ values range between -2.07 and -0.05‰ and show clear secular trends up section. This begs the question as to whether these important variations in $\delta^{56}Fe(II)_{aq}$ during the formation of carbonates can be related to ambient concentrations of iron upwelling on the shelf. The assumption that $\delta^{56}Fe(II)_{aq}$ in Precambrian carbonates was controlled by the influence of oxide precipitation on ambient Fe concentrations has been suggested by Eroglu et al. (2018) based on a Rayleigh distillation model applied to carbonates of the 2.6–2.5 Ga Campbellrand carbonate platform. We also applied this approach to our carbonate $\delta^{56}Fe$ dataset. Briefly, dissolved Fe concentrations are estimated from carbonate Fe/Ca ratios using experimentally determined partition coefficients, and a best-fit isotope fractionation factor is determined iteratively using a Rayleigh isotope distillation model (see Eroglu et al. (2018), for details). A best-fit fractionation factor $\delta^{56}Fe_{oxide\text{-}aq} = \delta^{56}Fe(II)_{oxide} - \delta^{56}Fe(II)_{aq} = 0.517$ ‰ was determined for our data, however the fit is poor, which implies that secular variations in the $\delta^{56}Fe$ compositions of the carbonates were not directly related to dissolved Fe concentrations that were upwelled onto the shelf.

Some insight is gained by the additional data provided by isolated pyrites. Guilbaud et al. (2011) proposed that Archean negative Fe isotope excursions may reflect partial

$Fe(II)_{aq}$ utilization and associated fractionation during abiotic pyrite formation, suggesting that there is no need to invoke the production of a large ^{56}Fe-depleted $Fe(II)_{aq}$ pool to explain isotopically light Archean pyrites, and that fractionation during pyrite formation may be attributed exclusively to mineral fractionation. However, at Red Lake the $\delta^{56}Fe$ values from co-occurring pyrites and carbonates are generally within error of one another, indicating that the carbonates and pyrites both recorded ambient marine $\delta^{56}Fe(II)_{aq}$ and that there was no mineral fractionation during pyrite formation. Furthermore, at the broader scale of the entire dataset, no correlation is observed between $\delta^{56}Fe$ and iron contents (Fig. 4.3). Remarkably, however, sulfur seems to play a controlling role in setting $\delta^{56}Fe$ values on the carbonate platform; indeed, $\delta^{56}Fe$ values in carbonates tend to lighter values as sulfur concentrations increase. This is surprising because it implies that sulfur cycling in some way determined Fe isotope compositions of Fe incorporated into these ferruginous carbonates – yet in a manner unrelated to the sulfur isotope composition of the pyrites themselves.

4.3.3 Productivity control over Mesoarchean Fe and S biogeochemical cycling

Coupled $\delta^{56}Fe$-$\delta^{34}S$ data revealed important $\delta^{34}S$ variation only in carbonates (Fig. 4.3), which indicates that shallow water settings where carbonate precipitation was occurring also experienced the most important sulfur redox cycling, with the negative values representing times when the SO_4 pool was largest, while positive values indicate near total-drawdown of the SO_4 pool by sulfate reduction. Moreover, the more important $\delta^{34}S$ variation in the carbonates is linked to $\delta^{56}Fe$ values that tend to become lighter as $\delta^{34}S$ becomes more negative (Fig. 4.3).

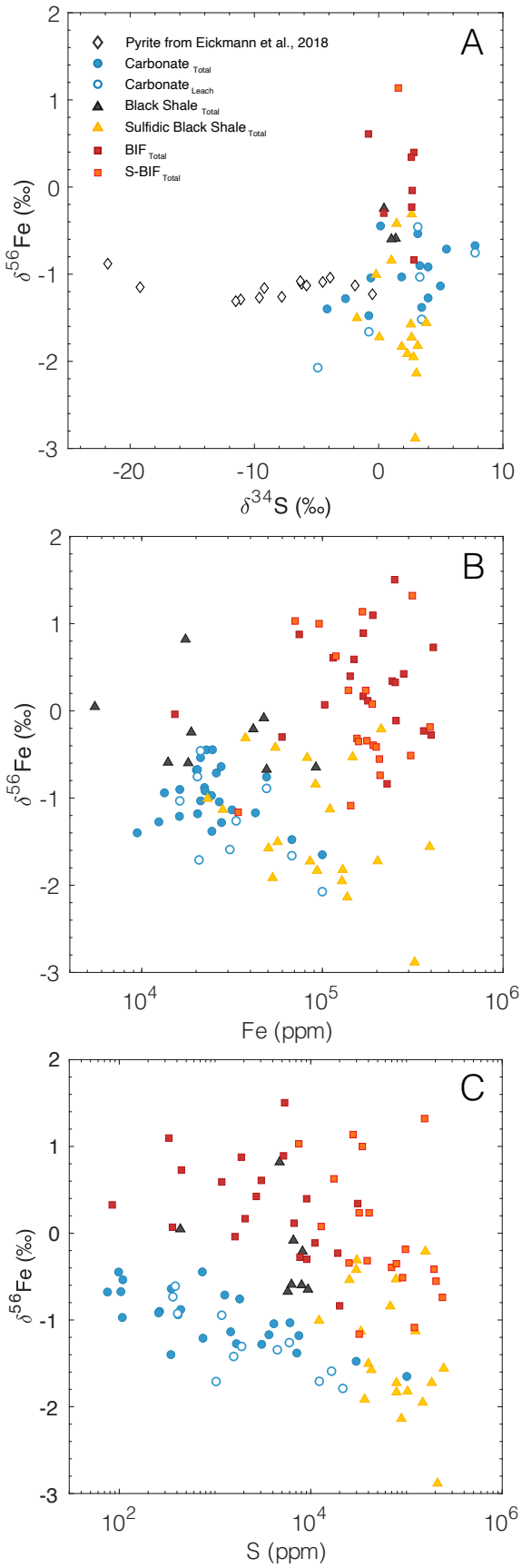

Figure 4.3. Iron stable isotope compositions plotted against sulfur stable isotope compositions (A), iron concentrations (B) and sulfur concentrations (C). Also plotted for comparison are iron and sulfur isotope composition data for isolated pyrites of the 2.96 Ga Chobeni carbonate (Eickmann et al., 2018).

This indicates coupling between the Fe and S redox cycles, whereby when SO_4 concentrations are lowest on the shelf (positive $\delta^{34}S$), Fe upwelled onto the shelf after minimal oxidative processing, whereas conversely, when SO_4 contents on the shelf were highest (most negative $\delta^{34}S$), the aqueous Fe pool was smaller and/or subject to greater losses by oxidative precipitation during upwelling from deep waters onto the shelf. In other words, it appears that sulfate reduction modulated Fe availability on the shelf (where S>Fe), while in the offshore, an abundant Fe pool led to BIF precipitation with generally minimal drawdown of the aqueous Fe(II) reservoir (Fe>S). During deposition of sulfidic black shales at the interface, the cross product of Fe and S concentrations attained the necessary values for abundant pyrite precipitation. The combined dataset paints a picture of a Mesoarchean carbonate platform that experienced non-negligible sulfate reduction in near-shore settings, leading to an euxinic wedge at the platform edge that modulated the ability of deep-water Fe to upwell onto the shelf. The unique insights provided by the shallow to deep transect approach has important implications for the interpretation of potential Archean oxygen oases. While Eickmann et al. (2018) interpreted a similar dataset for the 2.96 Ga Chobeni carbonates of the Pongola Supergroup to represent an oxygen oasis, here we show that Fe isotope variations in shallow water Archean carbonates may not necessarily be attributed to the establishment of a localized oxygen oases, but that offshore Fe processing may strongly influence Fe isotope systematics on the shelf. In the case of Red Lake, we suggest that the data does not permit the resolution of Fe oxidation mechanisms, whether by oxidative photosynthesis, photoferrotrophy, or possibly (but less likely) UV photooxidation (Konhauser et al., 2007; Nie et al., 2017). However, the above observations permit another interesting but overlooked possibility, that being that S-based anoxygenic phototrophy on the shelf is responsible at the same time for the localized accumulation of sulfate, fueling sulfate reduction and generation of the offshore euxinic

wedge that acted as partial barrier to upwelling Fe. The important secular trends in $\delta^{56}Fe$ that we report in the stromatolitic carbonates reveal that even if they may record localized and near-quantitative Fe oxidation in shallow waters at a given point in time (e.g., (Heard et al., 2022), evolution of the Fe isotope composition of upwelling $Fe(II)_{aq}$ over unit-depositional timescales reveals dynamic Fe redox processing in the upwelling environment. As we show here, this processing is also coupled to biogeochemical sulfur cycling, painting a picture where variations in primary productivity drove coupled Fe- and S-biogeochemical cycling in surface waters and shallow-water shelf environments already by 2.93 Ga.

4.4 Conclusion

The Red Lake Greenstone Belt hosts the oldest thick (>100m) accumulation of carbonate in Earth's history and holds significant promise for better understanding biological control over the early evolution of Earth's biogeochemical cycles. In this study, rare earth elements and Fe stable isotope compositions were examined in detailed stratigraphic section to better understand iron precipitation processes as Fe-rich deep waters upwelled onto the shallow carbonate platform. REE results reveal a complete absence of negative Ce anomalies at this locality and thus a largely oxygen-free environment, while positive Eu anomalies indicate the presence of a high temperature hydrothermal component in seawater and therefore a strong connection of the Red Lake carbonate platform to the open ocean by a significant upwelling system. Fe stable isotopes reveal active iron redox cycling, with δ^{56}Fe values ranging from -2.88 to +1.50‰ across this shallow-to-deep transect. The large δ^{56}Fe variations between the different lithologies is best explained by progressive plume depletion by iron oxide precipitation during upwelling, yielding to low δ^{56}Fe values in the residual in Fe(II) pool. Remarkably, important and clear secular variations in δ^{56}Fe are recorded in the carbonates that aren't easily explained a Rayleigh isotopic distillation (when combined with carbonate Fe concentrations), nor by mineral fractionation during pyrite formation. However, carbonate δ^{56}Fe values show remarkable co-variation with S contents, and pyrite S isotope data reveals an active microbial sulfur cycle with appreciable sulfate reduction at times. We suggest that the most parsimonious explanation for observed links between Fe and S cycling at this locality is overarching control by photosynthetic primary production. This work reveals that already by 2.93 Ga, photosynthetic activity both on- and off-shore exerted important control over Earth's major marine biogeochemical cycles, as it does today.

4.5 References

Afroz, M., 2019, Sedimentology and Geochemistry of the 2.93 Ga Basinal Facies of the Red Lake Carbonate Platform: Msc thesis from Lakehead University.

Alexander, B.W., Bau, M., Andersson, P., and Dulski, P., 2008, Continentally-derived solutes in shallow Archean seawater: Rare earth element and Nd isotope evidence in iron formation from the 2.9 Ga Pongola Supergroup, South Africa: Geochimica et Cosmochimica Acta, v. 72, p. 378–394, doi:10.1016/j.gca.2007.10.028.

Anbar, A.D. et al., 2007, A Whiff of Oxygen Before the Great Oxidation Event? Science, v. 317, p. 1903–1906, doi:10.1126/science.1140325.

Bau, M., 1991, Rare-earth element mobility during hydrothermal and metamorphic fluid-rock interaction and the significance of the oxidation state of europium: Chemical Geology, v. 93, p. 219–230.

Bau, M., and Dulski, P., 1996, Distribution of yttrium and rare-earth elements in the Penge and: v. 79, p. 37–55.

Beard, B.L., and Johnson, C.M., 2004, Fe Isotope Variations in the Modern and Ancient Earth and Other Planetary Bodies: Reviews in Mineralogy and Geochemistry, v. 55, p. 319–357, doi:10.2138/gsrmg.55.1.319.

Beard, B.L., Johnson, C.M., Damm, K.L. von, and Poulson, R.L., 2003, Iron isotope constraints on Fe cycling and mass balance in oxygenated Earth oceans:, www.geosociety.org/pubs/ft2003.htm.

Bolhar, R., Kamber, B.S., Moorbath, S., Fedo, C.M., and Whitehouse, M.J., 2004, Characterisation of early Archaean chemical sediments by trace element signatures: Earth and Planetary Science Letters, doi:10.1016/j.epsl.2004.02.016.

Bullen, T.D., White, A.F., Childs, C.W., Vivit, D. v., and Schulz, M.S., 2001, Demonstration of significant abiotic iron isotope fractionation in nature: Geology, v. 29, p. 699, doi:10.1130/0091-7613(2001)029<0699:DOSAII>2.0.CO;2.

Croal, L.R., Johnson, C.M., Beard, B.L., and Newman, D.K., 2004, Iron isotope fractionation by Fe(II)-oxidizing photoautotrophic bacteria: Geochimica et Cosmochimica Acta, v. 68, p. 1227–1242, doi:10.1016/j.gca.2003.09.011.

Dauphas, N., Cates, N.L., Mojzsis, S.J., and Busigny, V., 2007, Identification of chemical sedimentary protoliths using iron isotopes in the 3750 Ma Nuvvuagittuq supracrustal belt, Canada: Earth and Planetary Science Letters, v. 254, p. 358–376, doi:10.1016/j.epsl.2006.11.042.

Eickmann, B., Hofmann, A., Wille, M., Bui, T.H., Wing, B.A., and Schoenberg, R., 2018, Isotopic evidence for oxygenated Mesoarchaean shallow oceans: Nature Geoscience, v. 11, p. 133–138, doi:10.1038/s41561-017-0036-x.

Eroglu, S., Schoenberg, R., Pascarelli, S., Beukes, N.J., Kleinhanns, I.C., and Swanner, E.D., 2018, Open ocean vs. continentally-derived iron cycles along the neoarchean campbellrand-malmani carbonate platform, South Africa: American Journal of Science, v. 318, p. 367–408, doi:10.2475/04.2018.01.

German, C.R., Klinkhammer, G.P., Edmond, J.M., Mura, A., and Elderfield, H., 1990, Hydrothermal scavenging of rare-earth elements in the ocean: Nature, doi:10.1038/345516a0.

Guilbaud, R., Butler, I.B., and Ellam, R.M., 2011, Abiotic pyrite formation produces a large Fe isotope fractionation: Science, v. 332, p. 1548–1551, doi:10.1126/science.1202924.

Heard, A.W., Bekker, A., Kovalick, A., Tsikos, H., Ireland, T., and Dauphas, N., 2022, Oxygen production and rapid iron oxidation in stromatolites immediately predating

the Great Oxidation Event: Earth and Planetary Science Letters, v. 582, doi:10.1016/j.epsl.2022.117416.

Icopini, G.A., Anbar, A.D., Ruebush, S.S., Tien, M., and Brantley, S.L., 2004, Iron isotope fractionation during microbial reduction of iron: The importance of adsorption: Geology, doi:10.1130/G20184.1.

Johnson, C.M., Beard, B.L., Beukes, N.J., Klein, C., and O'Leary, J.M., 2003, Ancient geochemical cycling in the earth as inferred from Fe isotope studies of banded iron formations from the Transvaal Craton: Contributions to Mineralogy and Petrology, v. 144, p. 523–547, doi:10.1007/s00410-002-0418-x.

Johnson, C.M., Beard, B.L., Roden, E.E., Newman, D.K., and Nealson, K.H., 2004, Isotopic Constraints on Biogeochemical Cycling of Fe: Reviews in Mineralogy and Geochemistry, v. 55, p. 359–408.

Konhauser, K.O., Amskold, L., Lalonde, S. V, Posth, N.R., Kappler, A., and Anbar, A., 2007, Decoupling photochemical Fe(II) oxidation from shallow-water BIF deposition: Earth and Planetary Science Letters, v. 258, p. 87–100, doi:10.1016/j.epsl.2007.03.026.

Lalonde, S. v., and Konhauser, K.O., 2015, Benthic perspective on Earth's oldest evidence for oxygenic photosynthesis: Proceedings of the National Academy of Sciences of the United States of America, v. 112, p. 995–1000, doi:10.1073/pnas.1415718112.

McIntyre, T., and Fralick, P., 2017, Sedimentology and Geochemistry of the 2930 Ma Red Lake-Wallace Lake Carbonate Platform, Western Superior Province, Canada: The Depositional Record, v. 3, p. 258–287, doi:10.1002/dep2.36.

Nie, N.X., Dauphas, N., and Greenwood, R.C., 2017, Iron and oxygen isotope fractionation during iron UV photo-oxidation: Implications for early Earth and Mars: Earth and Planetary Science Letters, v. 458, p. 179–191, doi:10.1016/j.epsl.2016.10.035.

Olson, S.L., Kump, L.R., and Kasting, J.F., 2013, Quantifying the areal extent and dissolved oxygen concentrations of Archean oxygen oases: Chemical Geology, v. 362, p. 35–43, doi:10.1016/j.chemgeo.2013.08.012.

Planavsky, N.J. et al., 2014, Evidence for oxygenic photosynthesis half a billion years before the Great Oxidation Event: Nature Geoscience, v. 7, p. 283–286, doi:10.1038/ngeo2122.

Riding, R., Fralick, P., and Liang, L., 2014, Identification of an Archean marine oxygen oasis: Precambrian Research, v. 251, p. 232–237, doi:10.1016/j.precamres.2014.06.017.

Robbins, L.J. et al., 2016, Trace elements at the intersection of marine biological and geochemical evolution: Earth-Science Reviews, v. 163, p. 323–348, doi:10.1016/j.earscirev.2016.10.013.

Rouxel, O.J., Bekker, A., and Edwards, K.J., 2005, Iron isotope constraints on the Archean and Paleoproterozoic ocean redox state: Science, v. 307, p. 1088–1091, doi:10.1126/science.1105692.

Swanner, E.D., Wu, W., Schoenberg, R., Byrne, J., Michel, F.M., Pan, Y., and Kappler, A., 2015, Fractionation of Fe isotopes during Fe(II) oxidation by a marine photoferrotroph is controlled by the formation of organic Fe-complexes and colloidal Fe fractions: Geochimica et Cosmochimica Acta, doi:10.1016/j.gca.2015.05.024.

Thibon, F., Blichert-Toft, J., Tsikos, H., Foden, J., Albalat, E., and Albarede, F., 2019, Dynamics of oceanic iron prior to the Great Oxygenation Event: Earth and Planetary Science Letters, v. 506, p. 360–370, doi:10.1016/j.epsl.2018.11.016.

Towe, K.M., 1991, Aerobic carbon cycling and cerium oxidation: significance for Archean oxygen levels and banded iron-formation deposition: Global and Planetary Change, v. 5, p. 113–123, doi:10.1016/0921-8181(91)90132-G.

Trendall, A.F., Compston, W., Nelson, D.R., De Laeter, J.R., and Bennett, V.C., 2004, SHRIMP zircon ages constraining the depositional chronology of the Hamersley Group, Western Australia: Australian Journal of Earth Sciences, v. 51, p. 621–644, doi:10.1111/j.1400-0952.2004.01082.x.

Wilmeth, D.T., Lalonde, S. v., Berelson, W.M., Petryshyn, V., Celestian, A.J., Beukes, N.J., Awramik, S.M., Spear, J.R., Mahseredjian, T., and Corsetti, F.A., 2022, Evidence for benthic oxygen production in Neoarchean lacustrine stromatolites: Geology, doi:10.1130/G49894.1.

CHAPTER 5:

Comparative Rare Earth Element Systematics from Three Mesoarchean Carbonate Platforms

Abstract

Rare Earth Elements (REE) are powerful paleoenvironmental tracers that are generally well-preserved in carbonate rocks and provide important information on the composition of ancient seawater. Here I describe and compare the REE enrichment characteristics of three Mesoarchean carbonate platforms (Red Lake, Woman Lake and Steep Rock), combining new geochemical data from carbonate samples from the three platforms that were selected for La-Ce geochronology with a larger database of geochemical data from these same sites produced by myself and others in the context of the ERC StG project EARTHBLOOM. All three sites show typical seawater signatures with elevated La/La*, Y/Ho, and Pr/Yb that reflect a variety of environments that were affected differently by particulate flocculation and other estuarine processes. They also show appreciable Eu anomalies indicative of hydrothermal input to contemporaneous seawater. The presence of negative Ce anomalies in all three sites provides strong evidence of redox conditions conducive to Ce oxidation. Bearing the smallest Ce anomalies, the largest Eu anomalies, and relatively high Fe but rather low Mn concentrations, Red Lake is interpreted as weakly oxidizing, with O_2 concentrations buffered by the abundance of Fe from nearby hydrothermal sources. Steep Rock, which shows intermediate Fe and Mn concentrations, seems to capture more oxidizing conditions than Red Lake, with oxidative loss of Fe and Mn occurring in conjunction with increasingly oxic local conditions, as tracked by the Ce anomaly. Woman Lake, richer in Mn and more depleted in Fe, appear to record the most oxidizing conditions, where Mn oxides were delivered directly to the sediment pile from a severely Ce-depleted water column. This study of REE systematics in these carbonate platforms confirms the marine sedimentary origin of these carbonates and reveals that O_2-driven oxidative processes were likely in operation at each of these sites, as revealed by unambiguous evidence for the redox cycling of Ce and Mn.

Résumé

Les terres rares (REE) sont de puissants traceurs paléo-environnementaux qui sont généralement bien conservés dans les roches carbonatées et fournissent des informations importantes sur la composition de l'eau de mer ancienne. Je décris et compare ici les systématiques des REE de trois plateformes carbonatées Mésoarchéennes (Red Lake, Woman Lake et Steep Rock), en combinant de nouvelles données géochimiques provenant d'échantillons carbonatés qui ont été sélectionnés pour la géochronologie La-Ce avec une base de données élargie de ces mêmes sites produites par moi-même et d'autres dans le contexte du projet ERC StG EARTHBLOOM. Les trois sites présentent des signatures typiques de l'eau de mer avec des valeurs élevées de La/La*, Y/Ho et Pr/Yb qui reflètent une variété d'environnements qui ont été affectés différemment par la floculation des particules et d'autres processus estuariens. Elles présentent également des anomalies d'Eu qui indiquent un apport hydrothermal à l'eau de mer contemporaine. La présence d'anomalies négatives de Ce dans les trois sites fournit des preuves fortes de conditions redox propices à l'oxydation du Ce. Un comportement systématique dans les enrichissements en Fer et Mn qui suivent la mise en place des conditions oxydantes tracées par les anomalies en Ce révèle des conditions de plus en plus oxydantes entre les trois sites avec dans l'ordre Red Lake, Steep Rock, puis Woman Lake. Cela montre également l'importance des apports de métaux réduits des eaux profondes, et leur consommation lors de la production de dioxygène, qui régule l'accumulation d'O_2 dans ces trois sites. Cette étude de la systématique des REE dans ces plateformes carbonatées confirme l'origine sédimentaire marine de ces carbonates et montre que des processus d'oxydation induits par l'O_2 étaient probablement en cours sur chacun de ces sites, comme le révèlent les preuves non ambiguës du cycle redox du Ce et du Mn.

5.1 Introduction

The rare earth elements are a group of 17 elements of the periodic table including the 15 lanthanides (with atomic number from 57 to 71) as well as scandium (Sc, Z=21) and yttrium (Y, Z=39). The latter are considered REE because they appear to occur in the same deposits as the lanthanides and to have similar chemical properties. However, with a substantially smaller ionic radii and difference in geochemical behavior, Sc is generally treated separately from the REEs whereas Y, mimicking REE behavior and particularly that of holmium (Ho) due to close similarity in their ionic radii (Qu et al., 2009), is commonly examined in association with the lanthanides (REE+Y or REY) and inserted between dysprosium (Dy) and Ho (Bau and Dulski, 1995). Rare earth elements are generally subdivided into three groups based on their atomic numbers: the light REEs (LREE), including lanthanum (La), cerium (Ce), praseodymium (Pr) and neodymium (Nd); the middle REEs (MREE) including samarium (Sm), europium (Eu), gadolinium (Gd), terbium (Tb), dysprosium (Dy) and holmium (Ho); and the heavy REEs (HREE) including erbium (Er), thulium (Tm), ytterbium (Yb) and lutetium (Lu) (Tostevin et al., 2016; Smrzka et al., 2019). With increasing REE atomic number, for each consecutive atom, the nuclear charge is more positive by one, accompanied by a corresponding increase in the number of electrons present in the inner 4f orbitals. The 4f electrons imperfectly protect each other from the increased positive charge of the nucleus, so that the effective nuclear charge attracting each electron increases steadily in the lanthanide elements, resulting in successive reductions in atomic and ionic radii with values ranging from 1.03 angstroms for La(III) to 0.8 angstroms for Lu(III), the so-called "lanthanide contraction" (Goldberg et al., 1963; Elderfield and Greaves, 1982; Nozaki, 2001). This contraction of lanthanides leads to an increase of the strength of complex formation from La^{3+} to Lu^{3+} (Byrne and Kim, 1990), as well as an increase in electronegativity, and since the ionic radii of the

lanthanides change very little, REEs generally act as geochemical twins, making their separation difficult. However, small differences in complexation behavior between the rare earth elements leads to REE fractionation in natural systems and leading them to adopt unique characteristics specific to low-temperature aqueous environments.

REEs are commonly normalized to chondritic values, or to shale values that are thought to be representative of REEs in the upper continental crust. Normalization by shale eliminates the Oddo-Harkins effect, the notorious odd-even variation in natural abundance of REEs (Schmitt et al., 1963; Wildeman and Haskin, 1965; Piper and Bau, 2013), but also allows an immediate visualization of their fractionation relative to continental crust sources. Several different composite shale values, averaging shale compositions over wide geographic areas, have been used for normalization, such as for example the North American Shale Composite (NASC, Gromet et al., 1984), or Post-Archean Archean Shales (PAAS, Taylor and McLennan, 1985), the former which is employed in this study. To evaluate fractionation between different water masses in the modern ocean, it is recommended to normalize the data to the values of a distinct reference water mass, such as North Pacific Deep Water (NPDW), for example (Alibo et al., 1999a). Normalization by NPDW removes the common seawater characteristics that appear in shale-normalized REE spectra and can be useful for isolating REE fractionation processes relative to the final dissolved product observed in global ocean circulation (Nozaki, 2001), however for ancient seawater reconstruction, where REE systematics may show significant departures from modern values, normalization to a sedimentary reference material representing crustal weathering sources remains *de rigueur*.

The first analyses of REE concentrations and Sm-Nd isotope systematics in seawater were first performed on isolated samples (Goldberg et al., 1963; Hogdahl et al., 1968; Piepgras et al., 1979; Piepgras and Wasserburg, 1980; Elderfield et al., 1981), until the first systematic study of vertical profiles of REE in the North Atlantic Ocean by Elderfield and Greaves (1982) that revealed the REE distribution in the marine water column. Rare earth elements and yttrium (REY) are delivered to the ocean primarily by rivers (which have largely negligible cerium anomalies and a flat continental-type REY pattern as normalized to PAAS, Fig. 5.1) but also by hydrothermal vents (which have flat or HREE-depleted pattern but significant Eu positive anomalies) as well as eolian inputs, and are largely removed by particle scavenging, especially during estuarine flocculation, where several of the characteristic features of seawater are generated (Elderfield et al., 1990; Byrne and Kim, 1990; Douville et al., 1999).

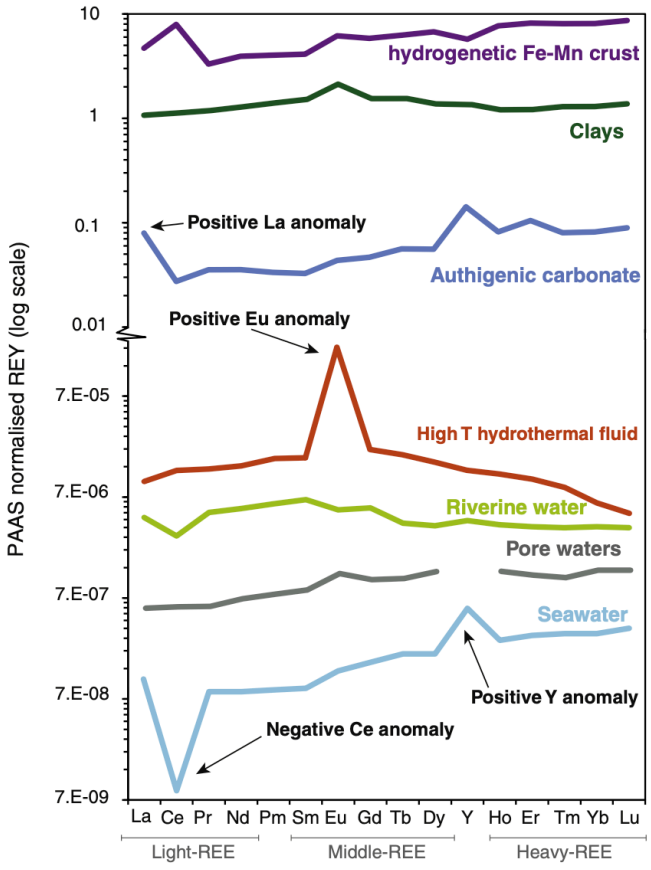

Figure 5.1. Post-Archean Australian Shale (PAAS) normalized REE+Y (REY) patterns showing typical REY signatures and anomalies of La, Ce, Eu and Y in different environments and minerals (Tostevin et al., 2016).

The typical REY profile of seawater is depleted in LREE, with a progressive enrichment in HREE as the consequence of the stronger complexation of carbonate ions with HREE (due to the contraction of lanthanides, explained above), leaving seawater more enriched in HREE (Byrne and Kim, 1990; Zhong and Mucci, 1995). The slope of the REY pattern and therefore the LREE/HREE ratio is commonly measured with the Pr/Yb ratio, with values >1 indicating LREE enrichment and values <1 indicating HREE enrichment (i.e., Pr/Yb values lower than 1 are considered as characteristic of seawater, Lawrence et al., 2006). Deviations from the general tendency of HREE enrichment occur when different REE show a unique chemical property that affects their solubility and removal via scavenging onto Fe and Mn oxyhydroxides, organic matter, and clay particles, which generates in modern seawater the characteristic positive La, Gd and Y anomalies, and negative Ce anomalies in the case of oxic seawater. To correctly identify these abundance anomalies, it is necessary to choose appropriate elemental neighbors for normalization, i.e., the nearest neighbors that do not experience anomalies. For example, when calculating La anomalies, Ce cannot be used because it is also subject to it's own redox-dependent anomalies, and therefore La anomalies are calculated using the projection of expected La determined by the closest anomaly-free REE, specifically Pr and Nd (Bau and Dulski, 1996; Lawrence et al., 2006; Bolhar and van Kranendonk, 2007). Similarly, due to the possible presence of positive La anomalies, Ce anomalies are usually calculated via the projection to expected values from Pr and Nd (Lawrence et al., 2006; Ling et al., 2013; Tostevin et al., 2016). In this study, all anomalies were calculated geometrically (e.g., logarithmically, for straight lines in logarithmic plots) according to Lawrence et al. (2006) with respect expected (non-anomalous) reference values (Ln*) calculated as follows:

$$La^*_n = Pr_n * (Pr_n/Nd_n)^2$$

$Ce^*_n = Pr_n * (Pr_n/Nd_n)$

$Eu^*_n = (Sm^2_n * Tb_n)^{1/3}$

$Gd^*_n = (Tb^2_n * Sm_n)^{1/3}$

Strong positive La anomalies are a consistent characteristic of marine REY patterns and represent a reliable indicator of water chemistry, with $(La/La^*)_N > 3$ for seawater or marine carbonates (Bau and Dulski, 1996; Kamber and Webb, 2001; Shields and Webb, 2004; Kamber et al., 2004) and $(La/La^*)_N <2$ for freshwaters and resulting chemical precipitates (Lawrence et al., 2006; Zhao et al., 2022). Positive lanthanum anomalies are common REY features of marine chemical precipitates inherited from seawater (Bau and Dulski, 1996; Kamber and Webb, 2001), where they develop as the result of the empty 4f electron shell of La that significantly increases its relative stability during complexation in seawater (de Baar et al., 1985a; Byrne and Kim, 1990; Byrne et al., 1996). Positive La anomalies may also result of their release from suspended barite particles (Grenier et al., 2018), or may be generated by the enzymatic activity of methanotrophs (Wang et al., 2020), demonstrating that REE are not immune from so-called “vital effects”, although these remain little explored and poorly understood.

With the exception of Eu, Ce is the only REE to form anomalies due to redox processes. Oxidation of more soluble Ce^{3+} to more insoluble Ce^{4+}, either abiotically (Koeppenkastrop and de Carlo, 1992; Bau, 1999) or via microbial mediation related to microbial Mn oxidation (Moffett, 1990), results in the decoupling of Ce from other REEs, i.e., cerium anomalies (Bau and Dulski, 1996; Ling et al., 2013; Liu et al., 2019). The incorporation of Ce(IV) into MnO_2 minerals results in a CeO_2 coordination state (Goldberg et al., 1963; de Baar et al., 1985a). The true diversity of Ce(IV) coordination in modern

seawater is more complex, involving various phases such as biogenic manganese oxides and organic ligands (Tanaka et al., 2010), Fe-Mn (oxyhydr)oxides, and clays (de Baar et al., 2018). Positive Ce anomalies are found in marine hydrogenetic Fe-Mn crusts (Bau and Dulski, 1996) and in Fe-Mn nodules (Amakawa et al., 1991; Bau et al., 2014) as a result of Ce^{4+} adsorption and scavenging by Fe-Mn (oxyhydr)oxides (German et al., 1995; Bau and Dulski, 1996; de Baar et al., 2018), leaving residual seawater depleted in Ce relative to the other trivalent REE, i.e., negative Ce anomalies (German and Elderfield, 1990). The magnitude of negative Ce anomalies varies within and between modern ocean basins (German and Elderfield, 1990; de Baar et al., 2018), but the general trend of vertical Ce/Ce* values remains rather the same, with a progressive decrease from the surface to deeper ocean waters, i.e., an accentuation of the negative Ce anomaly with depth (Alibo et al., 1999b; Nozaki and Alibo, 2003b; Ling et al., 2013). On the contrary, in restricted marine environments, inland seas, and lakes, negative Ce anomalies develop in oxic surface waters and are rapidly recycled away in anoxic deep waters by reductive dissolution of sinking Fe-Mn hydroxides, concomitant with an increase in dissolved Mn^{2+} and Fe^{2+} (e.g., Bau et al., 1997; de Carlo and Green, 2002). Ce anomalies can also develop in suboxic and anoxic environments underlying oxic surface waters; results from studies in the Saanich Inlet, the Black Sea, and Lake Vanda suggest that Ce anomalies are responsive to the onset of manganous (Mn^{2+}) conditions rather than ferruginous (Fe^{2+}) conditions. For examples of detailed examinations of the water column behavior of Ce in diverse modern ocean basins, marginal seas, and closed basins, the reader is referred to the studies of German and Elderfield (1989) in the Saanich Inlet in Canada, German et al. (1991) in the Black Sea, Bau et al. (1997) in the Mediterranean Sea, Alibo and Nozaki (1999) in the Western North Pacific near Japan, De Carlo and Green (2002) in Lake Vanda, Antarctica, and Nozaki and Alibo (2003a) in the Southern Ocean Southwest of Australia in comparison to South

Atlantic data. During the Archean, the atmosphere as well as the oceans were mostly anoxic, and the negative Ce anomaly was globally absent (i.e., Ce/Ce*=1) in surface waters (e.g., Bau and Dulski, 1996; van Kranendonk et al., 2003; Kamber et al., 2004), although several studies have show its presence locally, suggesting the establishment of so-called "oxygen oases" during the Archean (Riding et al., 2014; Mukhopadhyay et al., 2014; Siahi et al., 2018; Thoby et al., 2019). In the early Proterozoic, when oxygen levels in the atmosphere and surface seawater increased as a result of the Great Oxidation Event (GOE) and exceeded the threshold needed to oxidize Ce^{3+} to Ce^{4+}, negative anomalies began to form, but never exceeded Ce/Ce*= 0.55 in currently available sedimentary records (Fig. 5.2, Liu et al., 2021). Ce anomalies slowly increase towards the end of the Proterozoic, and increase drastically during the Phanerozoic, to eventually reach the magnitude of modern anomalies (ca. 0.4 to 0.2), most likely as a simple reflection of the increase in atmospheric oxygen levels (Wallace et al., 2017; Bellefroid et al., 2018; Liu et al., 2021).

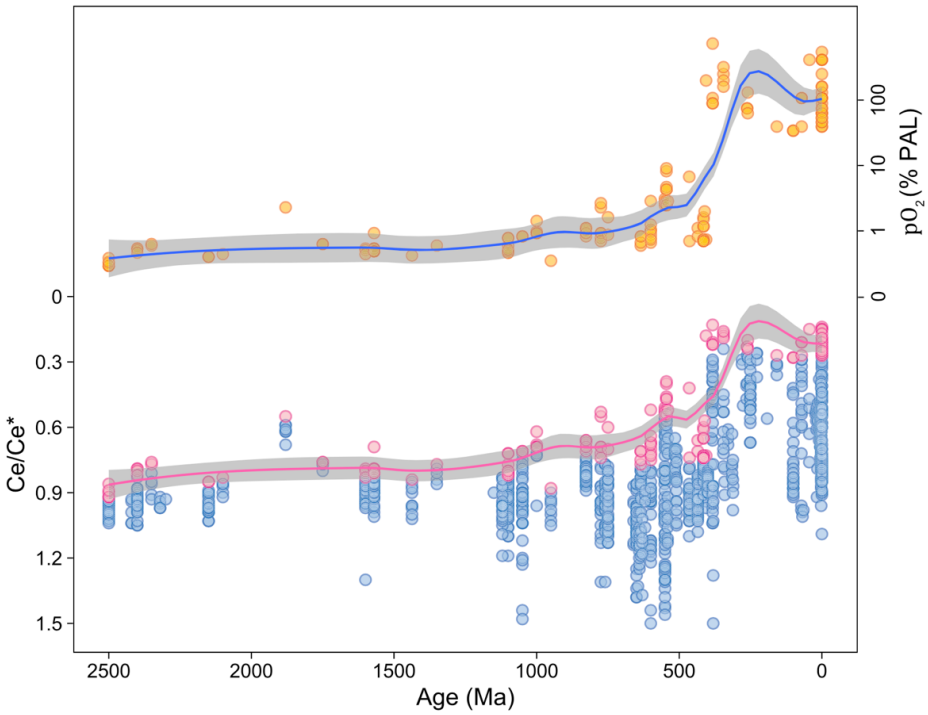

Figure 5.2. Ce/Ce* from marine carbonates and estimated atmospheric evolution of pO_2 from the early Proterozoic to the present (Liu et al., 2021).

Like all other trivalent REEs, europium generally occurs as Eu(III), which is its dominant form in aqueous environments at low temperatures, however it can be reduced to Eu(II) at higher temperatures (above ~250 °C) and at elevated pressures (Bau, 1991). Indeed, at these temperatures, the reduction of Eu(III) occurs at much higher oxygen fugacities (Drake, 1975; Sverjensky, 1984) making Eu(II) the dominant under these conditions. Thus, Eu(III)/Eu(II) ratios in aqueous solutions depend primarily on temperature and, to a lesser extent, on pressure, pH, and REE speciation (Sverjensky, 1984; Bau, 1991). Positive Eu anomalies are thus strongly expressed in modern hydrothermal vent fluids from mid-ocean ridges worldwide (James et al., 1995; Douville et al., 1999; Bau and Alexander, 2009; Craddock et al., 2010; Bau et al., 2010; Johannessen et al., 2017). These Eu excesses in high-temperature (>250 °C) hydrothermal fluids may be further driven by alteration of Ca-rich plagioclase in the oceanic crust that bear significant Eu anomalies (Michard and Albarède, 1986; Bau, 1999; Barrat et al., 2000; Alexander et al., 2008; Sylvestre et al., 2017), or the preferential affinity of Eu(II) in the dissolved phase relative to Eu(III) for sorption onto or reaction with secondary minerals during water-rock interaction (Bau, 1991). Low-temperature fluids generally do not have positive Eu anomalies, and when they occur the anomalies are minor to negative (Bau et al., 2010). Cooling of high-temperature hydrothermal fluids, by conduction or mixing with low-temperature fluids, results in the reoxidation of dissolved Eu^{2+} to Eu^{3+} and the loss of positive Eu anomalies (Bau et al., 2010). Hence, positive Eu anomalies in ancient chemical sediments are generally interpreted as residual signals from high-temperature hydrothermal fluids, and used to identify the high-temperature water-rock interaction occurring beneath the ocean floor (Michard et al., 1983; James et al., 1995; Douville et al., 1999; Kamber and Webb, 2001; van Kranendonk et al., 2003; Bolhar et al., 2004; Bau and Alexander, 2009; Craddock et al., 2010; Bau et al., 2010; Johannessen et al., 2017).

Gd lies midway in the REY series and has very similar vertical concentration distributions to its neighbors Sm, Eu, and Tb in the northwestern Atlantic Ocean and eastern equatorial Pacific Ocean (de Baar et al., 2018; Luong et al., 2018). Its 4f shell is exactly half-filled with 7 electrons, which makes the Gd^{3+} cation particularly stable, with a spherically symmetric ligand field giving rise to a unique hydration pattern in itself (Masuda and Ikeuchi, 1979; de Baar et al., 1985b). This peculiarity is thought to be responsible for the appearance of positive Gd anomalies present in seawater from the Pacific, Atlantic, and Indian oceans when normalized to PAAS (de Baar et al., 2018). That said, both positive and negative Gd anomalies have been observed in seawater (de Baar et al., 1985a, 2018). In addition, two competing phenomena affecting REE solubility in seawater, the varying strengths of REE complexation with carbonate (Luo and Byrne, 2004) as well as the distribution coefficients for REE sorption on most particles, partially cancel out when combined (Schijf et al., 2015). Thus, although much less pronounced than those of La, Ce, and Y (Lawrence et al., 2006; de Baar et al., 2018), the positive Gd anomaly in seawater is thought to be due to very subtle interactions between the inorganic complexation of REE in seawater and the different types and concentrations of particles present in seawater (de Baar et al., 2018). However, the Gd anomaly must be evaluated with caution, as an uncertainty of ± 0.07-0.10 related to a propagation of reproducibility error on REE concentrations show have been shown in one study that 19-40% of the observed Gd anomalies are statistically not significant (Garcia-Solsona et al., 2014). In addition, the inherent uncertainties of the REE database underlying the PAAS reference affects the definition and accuracy of the Gd/Gd* calculation in seawater (de Baar et al., 2018). Furthermore, with positive anomalies between 1.1 and 1.2 in the northern Pacific Ocean (de Baar et al., 2018), 1.22 for the Amazon River (Elderfield et al., 1990; Sholkovitz, 1993), and 1.16 for 12 different rivers (Elderfield et al., 1990), Gd/Gd* does not necessarily

differentiate between fluvial, lacustrine, and marine deposits, and therefore cannot be qualified as unique characteristic of seawater, unlike the strong positive anomalies in La, Y, and LREE/HREE ratios greater than 1 (Lawrence et al., 2006; Bolhar and van Kranendonk, 2007).

The Y anomaly (mass ratio of Y to Ho) is a specific feature of seawater, with the largest anomalies (Y/Ho = 40-80) corresponding to open marine environments and the smallest anomalies (Y/Ho = 33-40) to near shore or restricted environments (de Baar et al., 1985a, 1985b; Bau et al., 1997; Nozaki et al., 1997). Y and Ho have similar charges and ionic radii, with Y^{3+}= 0.900Å and Ho^{3+}= 0.901Å (Shannon, 1976) and act as twins and according to Goldschmidt's rules, and generally behave consistently in different environments (Nozaki et al., 1997; Shahkarami et al., 2017). Igneous rocks and epiclastic sediments thus have generally constant Y/Ho ratios close to the chondritic Y/Ho mass ratio of 28 (molar ratio of 52) (Bau, 1996). However, modern seawater has highly variable and fractionated Y/Ho ratios, with values above 44 (de Baar et al., 1985a; Alibo and Nozaki, 1999; van Kranendonk et al., 2003; Luong et al., 2018), which can be explained by a faster uptake of Ho into calcite compared to Y despite their similarly high affinity for incorporation (Qu et al., 2009). This was attributed to the binding covalency associated with ligand exchange between the two elements during incorporation of $REE(CO_3)^{2-}$ complexes into calcite (Tanaka et al., 2008; Qu et al., 2009). The Y/Ho ratio also varies with salinity, phosphate mineral solubility, and fractionation during chemical weathering, biological processes, and redox cycling (Liu and Byrne, 1997; Hill et al., 2000). Indeed, Y anomalies in riverine, estuarine, and possibly lacustrine waters (Zhang and Nozaki, 1996; Nozaki et al., 1997) are much lower than those in seawater, with Y and Ho concentrations decreasing with increasing salinity (Akagi et al., 1986; Nozaki et al., 1997). In estuarine

environments, Y/Ho variations that cannot only be explained by the mixing of continental crust and marine surface water, suggesting either a preferential release of Y from the sediments or a preferential removal of dissolved Ho in estuaries (Nozaki et al., 1997). In the eastern Mediterranean Sea, Y/Ho ratios have a narrow range between 47 and 48 whether in intermediate oxic or deep waters (Bau et al., 1997), whereas in oxidized Pacific waters Y/Ho ratios are between 46 and 65 (Bau and Dulski, 1995; Luong et al., 2018). In Archean and post-Archean marine sedimentary carbonate rocks, Y/Ho ratios are generally similar to modern seawater with values above 44 (Kamber et al., 2004; Komiya et al., 2008; Planavsky et al., 2010b; Bolhar et al., 2015). The Y anomaly, and specifically a Y/Ho ratio greater than 44, is thus a reliable indicator of deposition in the ocean environment (de Baar et al., 1985a; Alibo and Nozaki, 1999; Kamber and Webb, 2001; van Kranendonk et al., 2003; Bolhar et al., 2004; Kamber et al., 2004; Luong et al., 2018; Li et al., 2019; Zhao et al., 2022).

The full range of REE signatures observed in modern marine basins can be recognized in the ancient sedimentary rock record, as under certain conditions sedimentary rocks can preserve REE signatures reflecting the composition of the waters in which they formed. Chemical sediments, such as carbonates, cherts, iron formations, ironstones, manganese crusts and nodules, are particularly suitable lithologies for preserving paleoenvironmental information as they may derive an important proportion of their REE directly from ancient seawater by adsorption and co-precipitation reactions.

Early work conducted by Dymek and Klein (1988) on banded iron formation (BIF) from the 3.8 Ga Isua Supracrustral Belt, West Greenland, showed partial REE spectra (limited to 8 REEs analyzed by neutron activation analysis, prior to the widespread

adoption of ICP-MS) normalized to chondrites with positive La, Eu anomalies and negative Ce anomalies. In view of the similarity between the REE features of the Isua samples and modern deep-sea hydrothermal deposits, these BIFs were interpreted to be products of precipitation from dilute hydrothermal solutions. Furthermore, the presence of negative cerium anomalies opened the possibility that the ancient oceans may have been substantially more oxidized than previously thought (Dymek and Klein, 1988). In 1996, Bau and Dulski conducted one of the first PAAS-normalized REY studies for samples from the Kuruman and Penge BIF in the Transvaal Supergroup. Both formations exhibit typical seawater characteristics such as HREE enrichment and positive La, Gd, and Y anomalies. They have neither positive nor negative cerium anomalies but show a strong Eu anomaly similar to those found in formations of similar age, interpreted as the influence of a high temperature hydrothermal component (Bau and Dulski, 1996). In 2009, Planavsky et al. examined the 1.89-billion-year-old Gunflint and Bibawik iron formations using redox-sensitive tracers including REE and found positive cerium anomalies and evidence for the presence of Fe-oxidizing bacteria. Subsequently, Planavsky et al. (2010a) conducted a comprehensive and systematic REE study of BIFs by analyzing samples from 18 units dated between 3 and 1.8 billion years ago in order to re-evaluate with new analytical methods the depositional mechanisms and significance of these deposits. These new data suggest a shift in marine redox conditions ca. 1.9 Ga, with older formations showing no appreciable negative Ce anomalies while younger ones do, and that these deposits would have been deposited by microbial oxidation of Fe, implying that the distribution of Fe in the Archean oceans may have been controlled by microbial cycling of Fe rather than by the oxidative potential of shallow marine environments (Planavsky et al., 2010a).

REE geochemistry is also proving to be a powerful tool for constraining the depositional environments of carbonate rocks, for example as demonstrated by Bolhar and Van Kranendonk (2007) in their analysis of carbonates from the Neoarchean Fortescue Group (2.78-2.63 Ga) in the Hamersley Basin, Pilbara Craton, Western Australia. These carbonates lack typical seawater characteristics such as distinct La, Gd anomalies and supra-chondritic Y/Ho ratios, nor do they show LREE depletion relative to HREE unlike seawater, and have thus been interpreted as deposited in a lacustrine environment, or a very shallow lagoon environment dominated by freshwater inflow from rivers (Bolhar and van Kranendonk, 2007). PAAS-normalized REE spectra presented by Allwood et al., (2010) in carbonate and chert samples from stromatolites and associated facies in the 3.43 billion year old Strelley Pool Formation, Pilbara Craton, Western Australia that show consistent REY patterns with an origin associated with hydrothermal and mixed marine-hydrothermal fluid precipitation for the cherts, and a seawater origin for the carbonates with heavy rare earth depletion, positive La and Gd anomalies, absence of negative Ce anomaly and strongly superchondritic Y/Ho ratio. Allwood et al. (2010) therefore concluded that ancient carbonates and associated cherts record the geochemical characteristics of the waters in which they precipitated. While some studies have used REE systematics to show that there are no cerium anomalies in microbial carbonates aged 2.52 to 3.45 Ga, and suggest that free oxygen concentrations in seawater did not exceed trace amounts (Kamber et al., 2014), others have shown strong negative Ce anomalies in 2.80 Ga stromatolitic carbonates from Steep Rock Lake (one of the three sites examined in this study) that were interpreted to represent the presence of an Archean oxygen oasis, with O_2 concentrations in seawater of at least 10.25 uM (Riding et al., 2014). More recently, Wallace et al. (2017) used REE in marine carbonates to trace the history of marine oxygenation over the last 760 million years and demonstrated through the Ce anomaly that Earth's oxygenation was neither

unidirectional nor a simple two-step process, and that oxygen levels reached values comparable to those of the modern world when large land plants and forests appeared (Fig. 5.3).

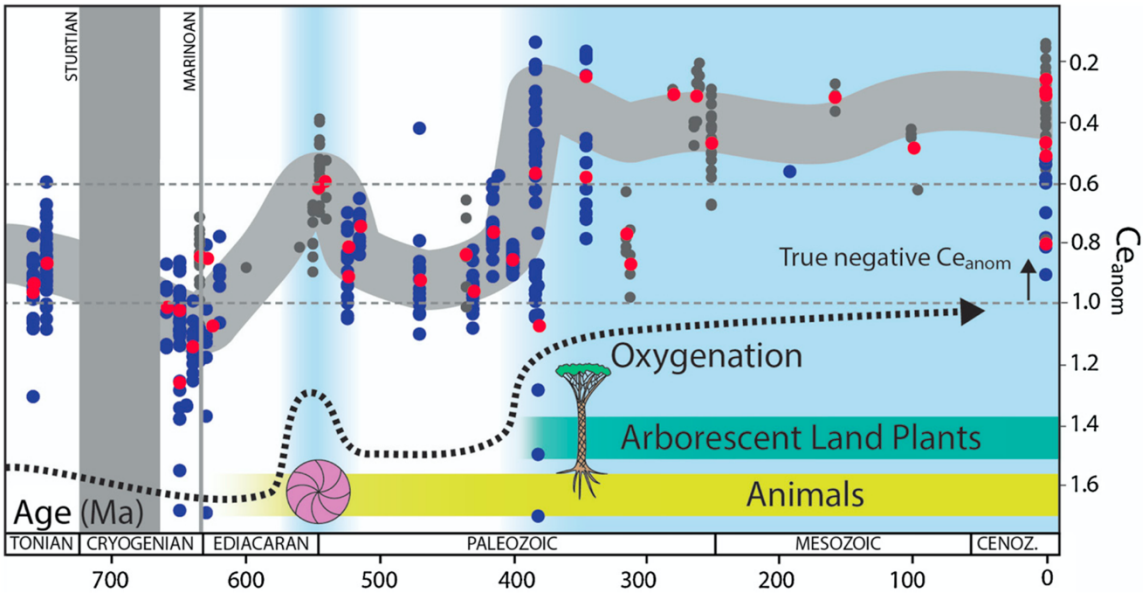

Figure 5.3. Plot of Ce/Ce* accompanied by a schematic of evolving surface oxygenation over the last 760 million years, with the appearance of animals and land plants accompanied by an accentuation of negative cerium anomalies in marine carbonates (Figure from Wallace et al., 2017).

Numerous studies have thus used REE+Y in several chemical sediment types, such as BIFs and carbonates, and demonstrated the great utility of these elements to constrain the depositional environments of these rocks (Dymek and Klein, 1988; Bau and Dulski, 1996; Bolhar et al., 2004; Bolhar and van Kranendonk, 2007; Allwood et al., 2010; Planavsky et al., 2010a; Viehmann et al., 2020), to trace the evolution of oxygen in seawater over time (Wallace et al., 2017; Liu et al., 2021), and argue for the presence of oxygen oases during the Archean (Riding et al., 2014; Mukhopadhyay et al., 2014; Siahi et al., 2018; Thoby et al., 2019).

However, when working with ancient sediments, especially carbonates, care must be taken to ensure that REE signatures are not altered by post-depositional processes or

contaminated during dissolution. Indeed, non-carbonate phases such as clastic detritus (Elderfield et al., 1990; van Kranendonk et al., 2003; Bolhar and van Kranendonk, 2007; Zhao et al., 2009), Fe-Mn(oxyhydr)oxides (Bayon et al., 2004), or phosphates (Byrne et al., 1996) have higher REY concentrations that can weaken the anomalies. Therefore, partial carbonate dissolution with 2.5% (Li et al., 2021) or 5% (Rongemaille et al., 2011) acetic acid for 24 hours at room temperature is recommended as a robust method for recovering pristine REY signatures (Zhao et al., 2022). In this study, carbonate samples have been dissolved in 5% acetic acid according to Rongemaille et al. (2011).

While still poorly understood, post-depositional alteration of REE signatures tends to increase REE contents, alter Ce and Eu anomalies, and enrich preferentially MREE (Shields and Stille, 2001) or LREE (Bonnand et al., 2020). Such preservational issues may not have been considered as seriously as they should have in prior work, as a recent literature compilation study comparing REE data and specifically Ce anomalies from outcrop and core samples show that many outcrop samples have in fact probably been affected by surface weathering (Planavsky et al., 2020). This is consistent with other recent work showing that for certain metal isotope systems (e.g., Mo, Cr, U; Albut et al., 2018; 2019), important redox-dependent fractionation processes indicated in outcrop samples are absent in drill core from the same units. It has also been suggested that early diagenetic alteration may also possibly affect REY concentrations and distributions in sedimentary carbonates (Holser, 1997). However, in their REY study of carbonate successions from Australia, the USA, and Ireland that have undergone several common types of diagenetic alteration, Hood et al. (2018) showed that normalized REY profiles appear to be well preserved during diagenetic recrystallization. Similarly, a study by Liu et al. (2019) on carbonates from drill core collected in the Bahamas, which show the loss or retention of a

variety of primary carbonate proxy signals through a series of different alteration processes, mainly under anoxic conditions, revealed that regardless of mineralogy, diagenetic fluid composition, and redox state, the REY patterns as well as the Ce anomaly in these carbonates remained similar to those in modern oxic seawater, suggesting that REY patterns retain the seawater characteristics recorded in the primary chemical precipitates. In addition, REY compositions in different diagenetic Quaternary carbonates from a deep well drilled on an isolated coral atoll in the South China Sea have very similar REY patterns to seawater that similarly do not vary during diagenetic facies changes (Luo et al., 2021). And since the Ce anomaly did not correlate with any isotopic, elemental, or mineralogical proxies tracing carbonate diagenesis, the Luo et al. (2021) data further support the conservative behavior of the Ce redox proxy in carbonate rocks across diagenetic alteration processes and its robustness for reconstructing past changes in seawater composition.

As described above, REE (henceforth, including Y) are powerful paleoenvironmental tracers that show important resistance to diagenetic and metamorphic alteration, and their systematics in marine chemical sediments reveal important clues to ancient depositional environments, including redox state. Accordingly, REE systematics were examined in a large dataset spanning three Mesoarchean carbonate platforms (Red Lake deposited at 2.93 Ga, Woman Lake deposited at 2.85 Ga, and Steep Rock deposited at 2.80 Ga, all located in the Superior Province in Canada; see Chapter 2) in order to better understand the depositional environments and geochemical conditions in seawater at the time of deposition of these important Mesoarchean carbonate deposits.

5.2 Methods

The data for this study represent a combination of data generated over the 2017-2022 period by the ERC StG EARTHBLOOM team (specifically, by Munira Afroz for the Red Lake industry drill hole samples, Martin Homann for the Red Lake backpack drill core samples, Brittany Ramsay for the Woman Lake samples, and Dylan Wilmeth for the Steep Rock Lake samples, referred to below as the EARTHBLOOM compilation), as well as new analyses made during this thesis (all leach data for the NGI10-31 drill core from Red Lake, additionally discussed in Chapter 4 and included in the EARTHBLOOM compilation, as well new analyses of all samples selected for La-Ce geochronology from the three sites that are highlighted independently in many of the figures below; see also Chapter 6). All were analyzed using the 5% acetic acid weak leach procedure and ElementXR HR-ICP-MS analysis as described in Chapter 3 (see section 3.2.1.2 and 3.2.2.2). All of these data are tabulated in Appendices B.1 and B.2. In places, these new data were compared to other available Archean data extracted from a large literature compilation of major and trace element data from sedimentary carbonates spanning geological time made by (Rigoussen, 2017, M2 thesis, UBO). The reader is referred to that compilation and its detailed annexes (including all data) for further information.

5.3 Results

5.3.1 Mineralogy and distribution of carbonates

Carbonates from Red Lake are mainly composed of dolomite (about 65% of samples, Fig. 5.4-A) while the Woman Lake and Steep Rock carbonates are composed almost entirely of calcite (about 90% of samples, Fig. 5.4-B and C). The high abundance of calcite at Woman Lake and Steep Rock appears unique compared to carbonates of similar ages that appear to be composed primarily of dolomite. The mineralogy of Red Lake samples is consistent with the other Archean sites dominated by dolomite, although it also shows abundant calcite where deposition is inferred to occurred to have in more distal settings (Afroz, 2019).

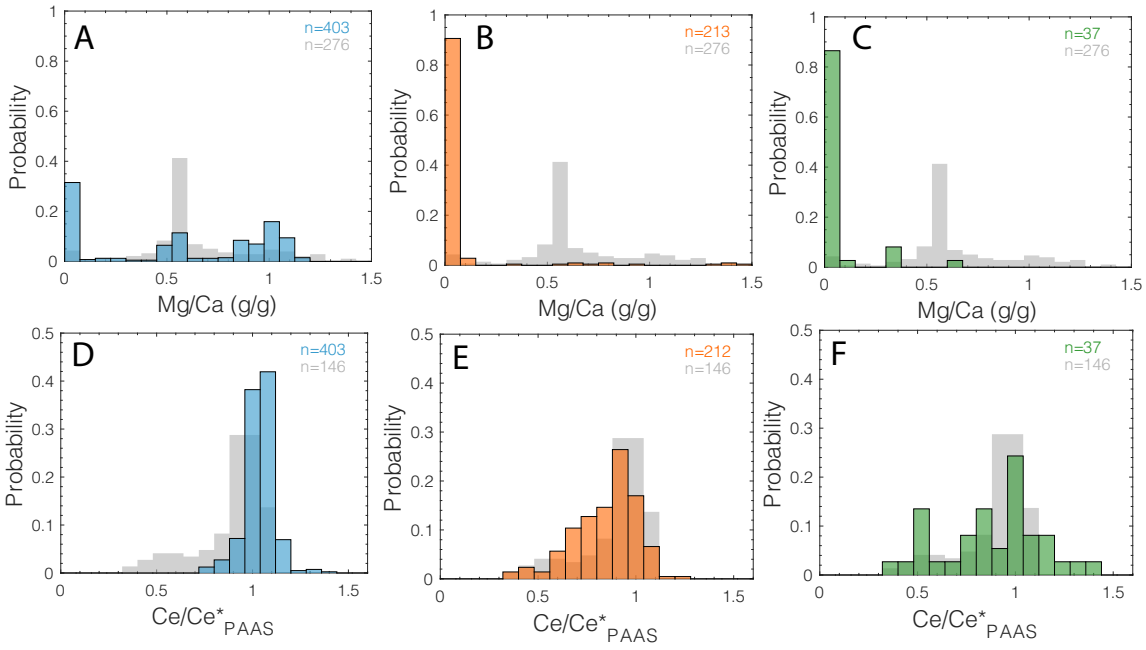

Figure 5.4. Histograms showing the distribution of Mg/Ca and Ce/Ce* values from the Red Lake (blue), Woman Lake (orange), and Steep Rock (green) sites compared to data from other Archean occurrences as compiled by Rigoussen (2017) (grey).

The Red Lake carbonates show few Ce anomalies, either positive or negative, and when they do occur, they are not very pronounced, with Ce/Ce* values ranging from ~ 0.75

to 1.4 (Fig. 5.4-D). Conversely, Woman Lake and Steep Rock show abundant and significant Ce anomalies that are quite pronounced, with Ce/Ce* values ranging from ~ 0.38 to 1.25 and from ~ 0.38 to 1.45, respectively (Fig. 5.4-E and F).

5.3.2 REE patterns

The Red Lake REE spectra show overall depletion of LREEs relative to HREEs as well as anomalies in La, Ce, Eu and Y (Fig. 5.5-A). Lanthanum anomalies range from 0.77 to 5.32, with an average La/La*=1.66. Ce anomalies at Red Lake are not very present with values ranging from 0.75 to 1.40 and an average Ce/Ce*=1.04. Eu anomalies are very pronounced, with values ranging from 0.90 to 19.99 and an average Eu/Eu*=3.14. Y/Ho ratios are highly variable, but relatively high, with values ranging from 24 to 157 and an average value of 70. The REY spectra of Woman Lake show the same overall characteristics as Red Lake, with depletion of LREEs relative to HREEs, and anomalies in La, Ce, Eu and Y (Fig. 5.5-B). La anomalies range from 0.66 to 4.13 with an average value of 2.06. Ce anomalies at Woman Lake are much more numerous and pronounced than those at Red Lake, with values ranging from 0.38 to 1.24 and an average Ce/Ce*=0.84. In contrast, Eu anomalies are much less pronounced at Woman Lake, with Eu/Eu* values ranging from 0.70 to 4.58 and an average of 1.75. Y/Ho ratios range from 22 to 118 with an average value of 70, similar to Red Lake. The Steep Rock REE spectra are composed of the same features as Red Lake and Woman Lake, i.e., depletion of LREEs relative to HREEs and anomalies in La, Ce, Eu and Y (Fig. 5.5-C). The La anomalies at Steep Rock are even more pronounced compared to the other two sites, with La/La* values ranging from 1.11 to 6.87 and a mean value of 3.42. Ce anomalies range from 0.38 to 1.43, with an average Ce/Ce*=0.88. Eu anomalies are less pronounced than those of Red Lake but more pronounced than those of Woman Lake, with Eu/Eu* values ranging from 1.16 to 9.11 and

a mean value of 2.60. Y/Ho ratios range from 34 to 155 and average of 105, significantly higher than the other two sites.

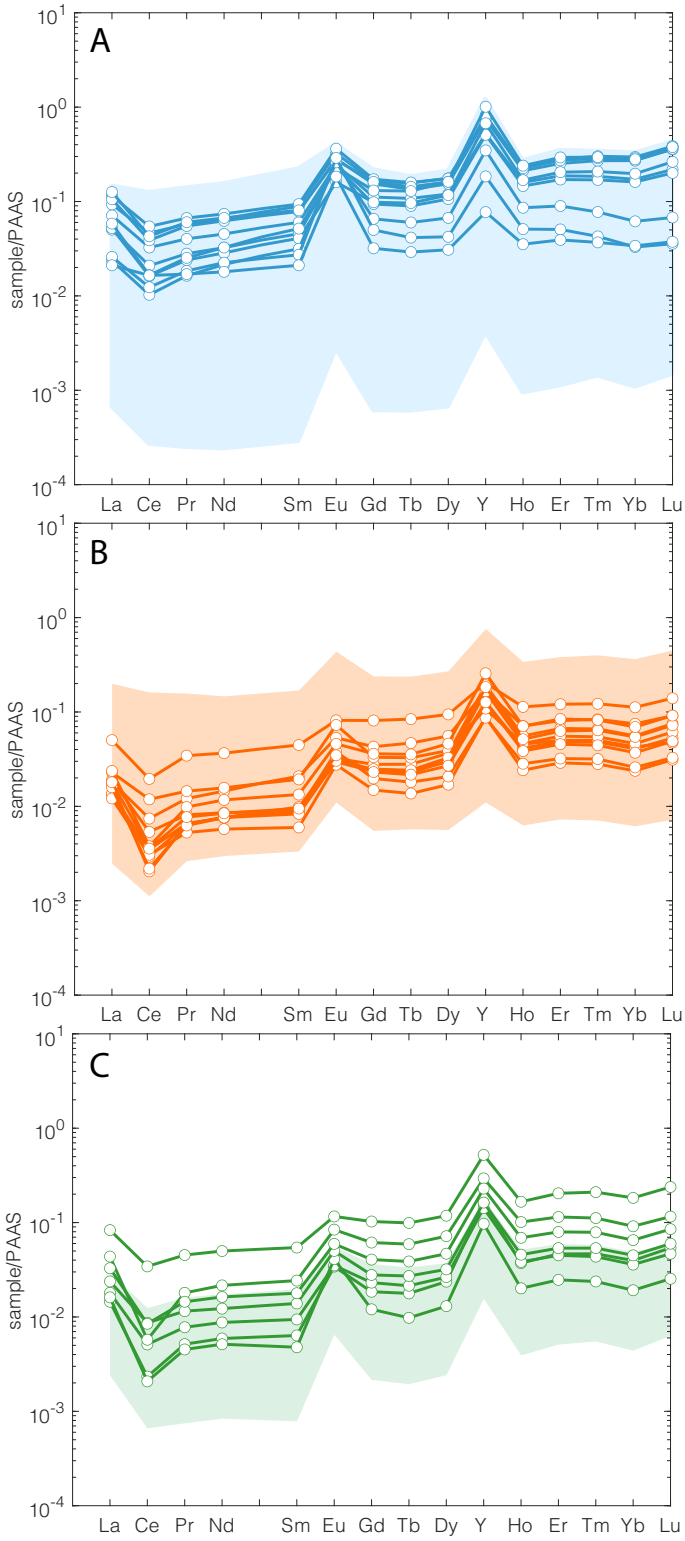

Figure 5.5. PAAS-normalized REE spectra of samples analyzed for La-Ce geochronology (see Chapter 6) from Red Lake (A), Woman Lake (B) and Steep Rock (C). Colored areas correspond to currently available data from each site from the EARTHBLOOM compilation; additional data from Afroz (2019, 2023), this thesis work (Chapter 4), Ramsay (2020), and Wilmeth et al. (2021).

5.3.3 Red Lake

The Red Lake carbonates, composed mostly of microbialitic dolomite (65%) with lesser microbialitic and crystal fan calcite (35%), have Mg/Ca values ranging from 0.002 to 1.18 with an average equal to 0.56. Positive and negative Ce anomalies are more pronounced in calcite samples than in dolomite samples (Fig. 5.6-A). Indeed, Ce/Ce* values vary from 0.89 to 1.2 in the dolomite samples and from 0.75 to 1.40 in the calcite samples. Fe/Mn ratios also show a wide range, varying from 0.25 to 13.11 with an average of 2.57. The positive Ce anomalies appear to be somewhat more pronounced at smaller Fe/Mn ratios and to a lesser extent this also appears to be true for the negative cerium anomaly (Fig. 5.6-B). The Y/Ho ratios have values between 25 and 157 with an average Y/Ho=70. The negative Ce anomalies are clearly more pronounced above Y/Ho=90 and the positive anomalies reach their maximum values (Ce/Ce*>1.2) when Y/Ho is above 120 (Fig. 5.6-C). Fe concentrations in the Red Lake carbonates range from 235 to 70,000 ppm with an average value of about 7000 ppm. There does not appear to be a strong correlation between Fe concentrations and Ce anomalies, although it would appear that Ce anomalies are somewhat more pronounced at lower Fe concentrations (Fig. 5.6-D). Sr concentrations range from 1.8 to 774 ppm with an average of 59 ppm. Ce anomalies clearly appear more pronounced when Sr concentrations are higher (Fig. 5.6-E). Mn concentrations in these carbonates range from 20 to 14,600 ppm with an average value of 3200 ppm, however, Ce anomalies do not appear to correlate with Mn concentrations (Fig. 5.6-F) at this site.

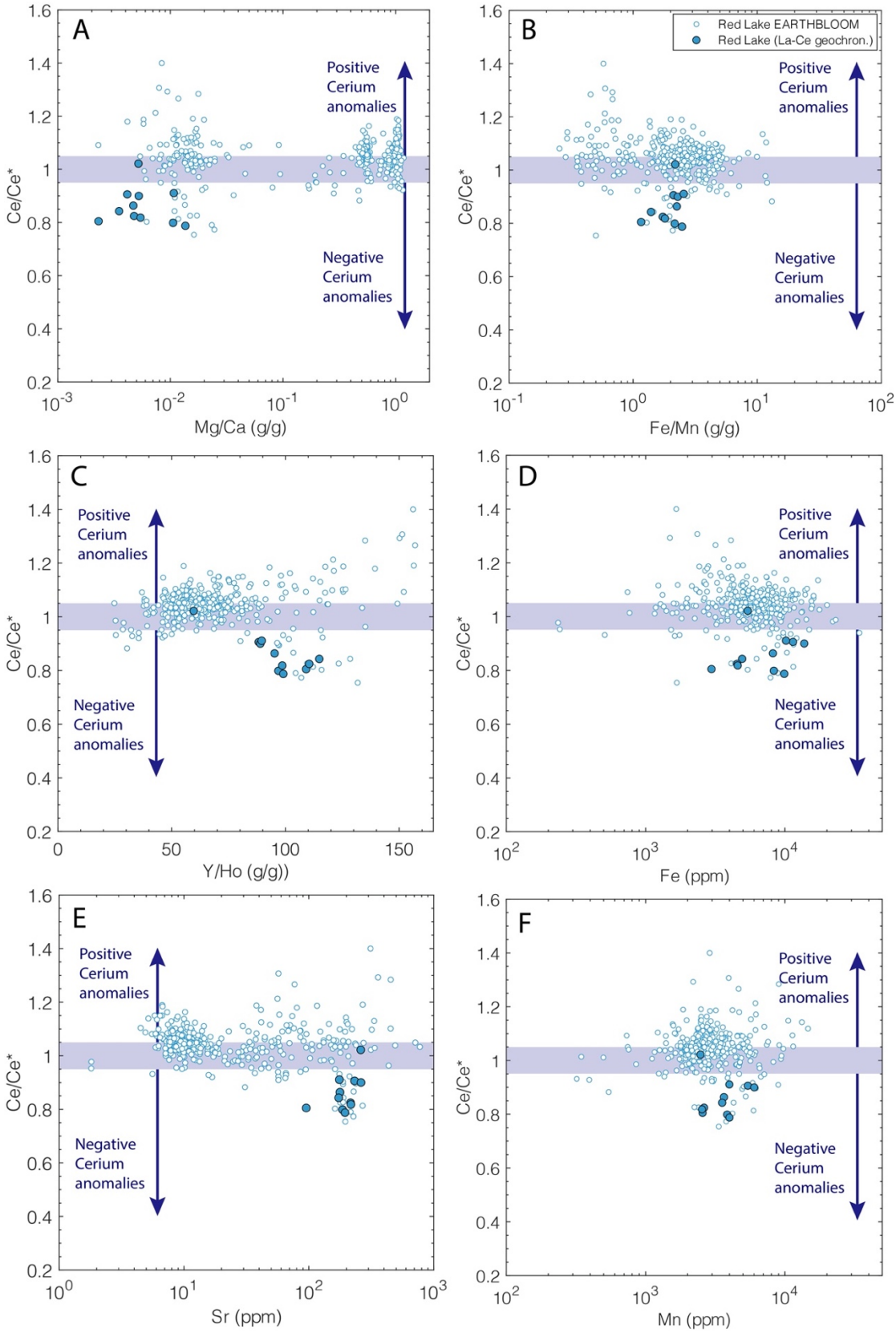

Figure 5.6. Graphs displaying Red Lake Ce anomalies versus Mg/Ca (A), Fe/Mn (B), Y/Ho (C) ratios, and Fe (D), Sr (E), and Mn (F) concentrations. "EARTHBLOOM" data correspond to currently available EARTHBLOOM compilation data from Red Lake generated by Afroz (2019, 2023) and from this thesis work (Chapter 4). "La-Ce geochron." data correspond to the samples selected for La-Ce geochronology and re-analysed independently from their REE systematics in this work (see also Chapter 6).

5.3.4 Woman Lake

The Woman Lake carbonates, composed almost entirely of calcite (90%), have Mg/Ca values ranging from 0.005 to 1.49 and an average equal to 0.08. The numerous strong negative Ce anomalies (Ce/Ce*<0.8) are present only in the calcites (Fig. 5.7-A). Fe/Mn ratios range from 0.04 to 116 with an average of 1.21. Negative Ce anomalies appear to be somewhat more pronounced with smaller Fe/Mn ratios (Fig. 5.7-B). The Y/Ho ratios have values between 22 and 118 with a mean Y/Ho=70. A correlation between Y/Ho and cerium anomalies is clearly visible with a progressive appearance of anomalies when the Y/Ho ratio increases (Fig. 5.7-C). Negative Ce anomalies are strongly accentuated (Ce/Ce* between 0.4 and 0.7) when Y/Ho ratios are above 70. Fe concentrations in the Woman Lake carbonates range from 4 to 16,600 ppm with a mean value of about 1800 ppm. There does not appear to be a strong correlation between Fe concentrations and Ce anomalies (Fig. 5.7-D). Sr concentrations range from 0.3 to 342 ppm with an average of 76 ppm. The strong Ce anomalies appear to be present only in Sr concentrations between 20 and 100 ppm (Fig. 5.7-E). Mn concentrations in these carbonates range from 2 to 28,600 ppm with an average value of 8850 ppm and Ce anomalies appear to become increasingly present and pronounced with increasing Mn concentrations (Fig. 5.7-F).

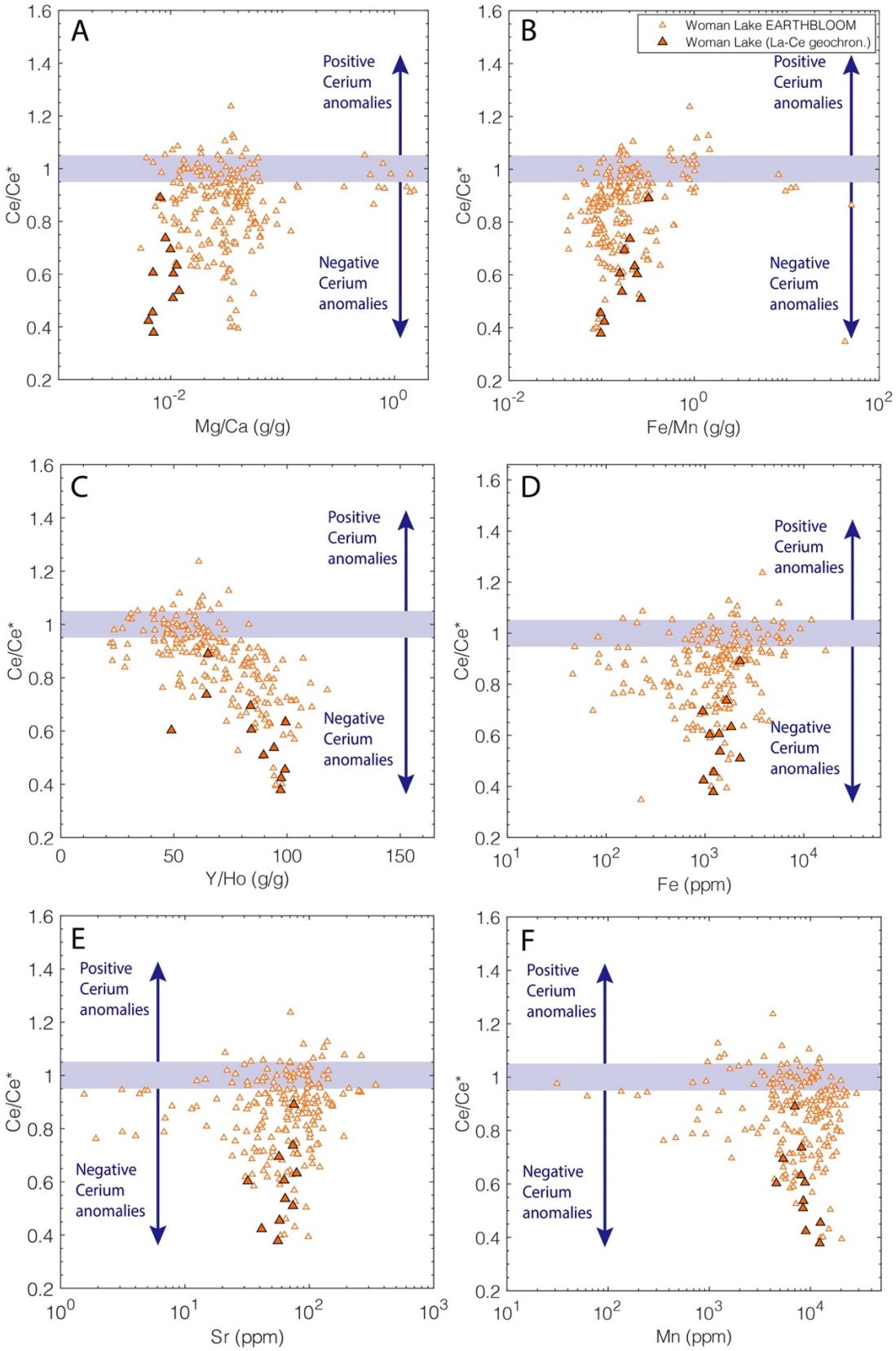

Figure 5.7. Graphs displaying Woman Lake Ce anomalies versus Mg/Ca (A), Fe/Mn (B), Y/Ho (C) ratios and Fe (D), Sr (E), and Mn (F) concentrations. "EARTHBLOOM" data correspond to currently available EARTHBLOOM compilation data from Woman Lake generated by Ramsay (2020). "La-Ce geochron." data correspond to the samples selected for La-Ce geochronology and re-analysed independently from their REE systematics in this work (see also Chapter 6).

5.3.5 Steep Rock

The Steep Rock carbonates, composed almost entirely of calcite (90%), have Mg/Ca values ranging from 0.003 to 0.63 with an average equal to 0.06. Strong negative and positive Ce anomalies are present only in the calcites, and the more Mg-rich carbonates do not show appreciable Ce anomalies (Fig. 5.8-A). Fe/Mn ratios vary from 0.27 to 3.79 with an average of 0.96. Positive Ce anomalies appear more pronounced as Fe/Mn ratio increases, and negative Ce anomalies do not appear to correlate with Fe/Mn ratio (Fig. 5.8-B). The Y/Ho ratios have values between 35 and 155 with an average Y/Ho=105. Ce anomalies appear above Y/Ho=75, and positive Ce anomalies seem to increase with increasing Y/Ho ratio (Fig. 5.8-C). The negative anomalies, however, do not seem to correlate particularly well with the Y/Ho ratio. Fe concentrations in the Steep Rock carbonates range from 392 to 12,700 ppm with an average value of about 3,000 ppm. There does not appear to be a strong correlation between Fe concentrations and Ce anomalies (Fig. 5.8-D). Sr concentrations range from 22 to 1924 ppm with an average of 405 ppm. Ce anomalies only appear at Sr concentrations >60 ppm and the anomalies appear to increase somewhat with increasing Sr concentrations (Fig. 5.8-E). Mn concentrations in these carbonates range from 269 to 8500 ppm with an average value of 3300 ppm, and the pronounced Ce anomalies at low Mn concentrations appear to lessen with increasing Mn concentrations (Fig. 5.8-F).

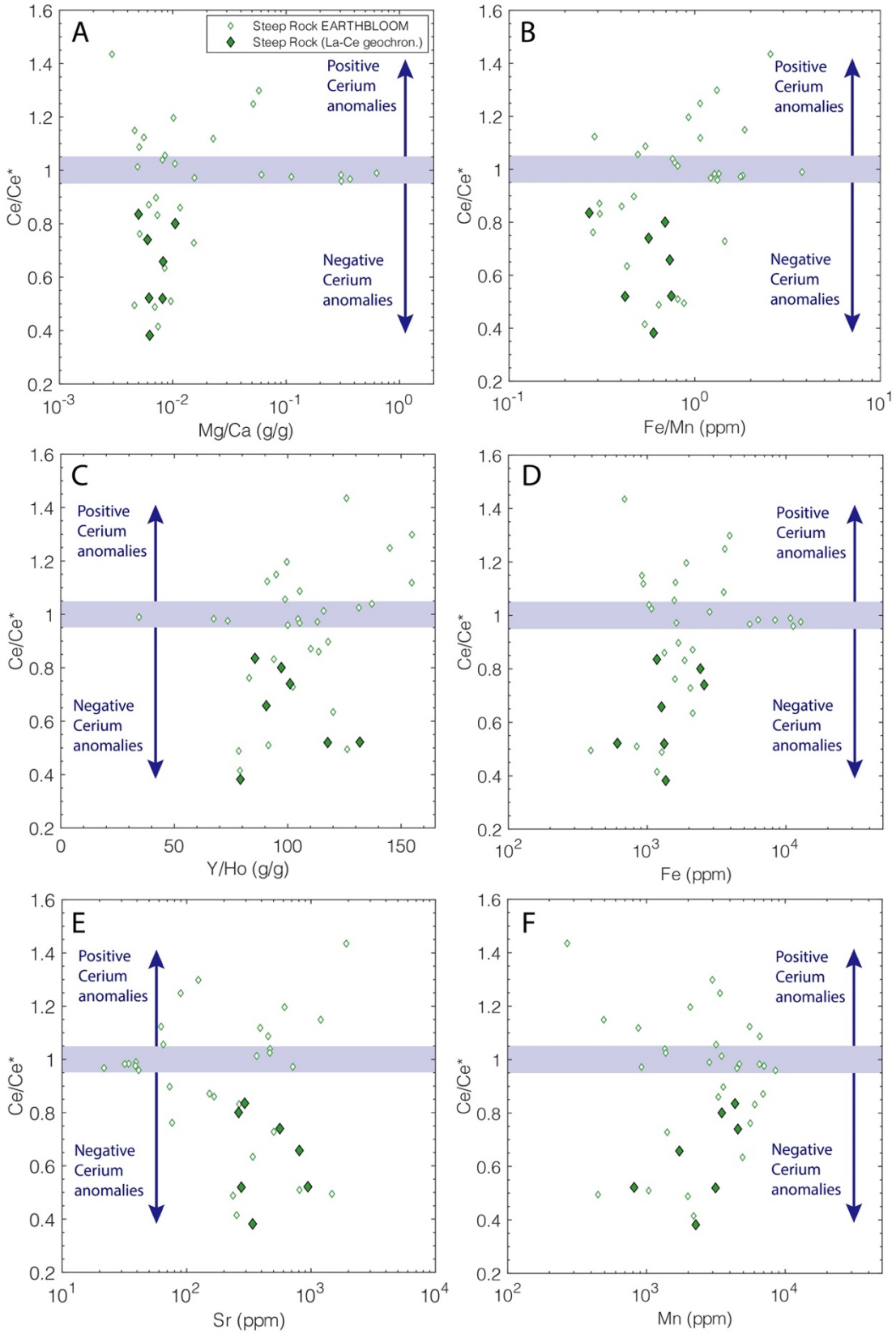

Figure 5.8. Graphs displaying Steep Rock Ce anomalies versus Mg/Ca (A), Fe/Mn (B), Y/Ho (C) ratios and Fe (D), Sr (E), and Mn (F) concentrations. "EARTHBLOOM" data correspond to currently available EARTHBLOOM compilation Steep Rock data from Wilmeth et al. (2021). "La-Ce geochron." data correspond to the samples selected for La-Ce geochronology and re-analysed independently from their REE systematics in this work (see also Chapter 6).

5.4 Discussion

5.4.1 Detrital contamination

Pure chemical sediments contain little REE (generally less than 0.1 to 0.01 PAAS) and are therefore highly susceptible to contamination by detrital components. Despite a careful weak leaching procedure, some clays were also digested, as shown by detectable aluminum (Al) concentrations in the studied samples. In Figure 5.9, Ce, La, and Eu anomalies, as well as the Y/Ho ratios, Pr/Yb ratios, and the total REE concentrations (plus Y) are plotted against Al concentrations to assess the effects of detrital contamination. Two mixing curves between the PAAS pole and two selected chemically pure carbonates are also shown on the different plots. In general, the data reveal very pure chemical sediments with little Al, however, at higher Al concentrations, mixing toward crustal values appears evident. At low Al concentrations, a large variability of "detrital free" endmembers in multiple parameters indicate that the most chemically pure sediments have preserved different REE compositions from contemporaneous seawater. This most likely represents a variety of environmental and redox conditions captured by the carbonates that are discussed in more detail in Sections 5.4.2 and 5.4.3. More specifically, Ce anomalies are most pronounced at low Al concentrations and tend to disappear with increasing Al concentrations (Fig. 5.9-A). La/La* and Y/Ho show very high variability at low Al concentrations, and at higher Al concentrations show clear detrital mixing behavior (Fig. 5.9-B and C). Total REE also scale with Al, but not always as predicted by mixing with PAAS (Fig. 5.9-D). Pr/Yb and Eu/Eu* also show behavior indicative of high variability at low Al, consistent with a wide range of alkalinity and hydrothermal influence in the parent waters, with little detrital influence (Fig. 5.9-E and F). In the following sections, we

consider only the samples showing a negligible effect of detrital mixing on REE proxies, i.e., those below 38 ppm Al (about 0.1% of REE derived from detrital sources).

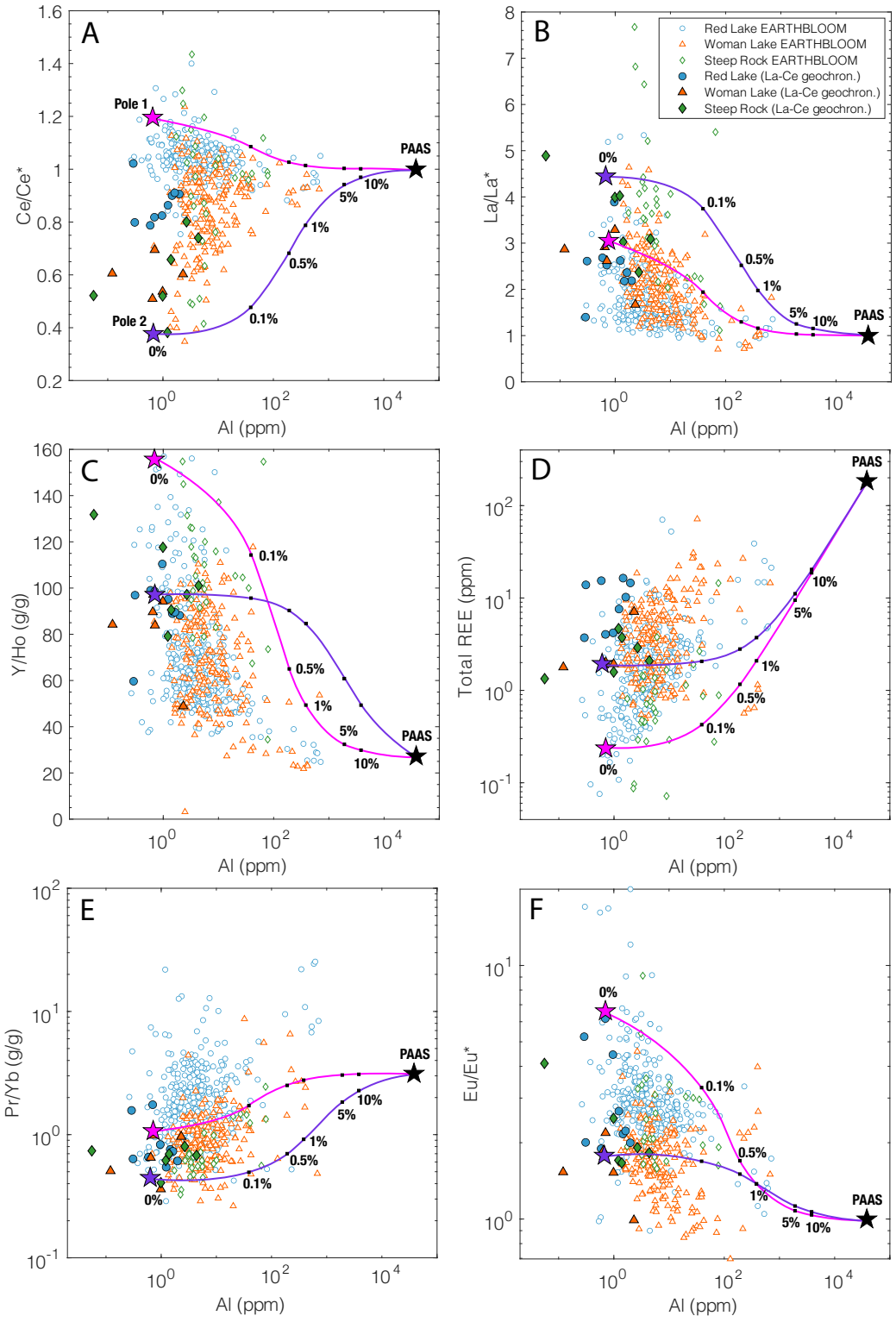

Figure 5.9. Graph showing multiple features of the REE patterns, such as Ce/Ce* (A), La/La* (B), Y/Ho (C), Total REE concentrations (plus Y) (D), Pr/Yb (E) and Eu/Eu* (F) versus Al concentrations for carbonate samples from Red Lake, Woman Lake, and Steep Rock. On each panel, two mixing curves represent mixing between PAAS and two selected pure carbonate endmembers of contrasting composition. The same two selected samples were used for all mixing curves.

5.4.2 Paleoenvironmental context

Rare earth element compositions from Red Lake, Woman Lake and Steep rock provide important insights into the paleoenvironmental context of the diverse carbonates at the time of deposition. PAAS-normalized REE spectra from these three Mesoarchean platforms (Fig. 5.5) show multiple characteristics typical of modern seawater that confirm the marine origin of these carbonates, notably a depletion of LREE compared to HREE, strong positive La and Y anomalies, and in some samples, negative Ce anomalies (German et al., 1990; Bau and Dulski, 1996; Bolhar et al., 2004). Indeed, these three platforms combined have La/La* and Ce/Ce* values ranging from 0.66 to 6.87 and 0.38 to 1.43, respectively, a range comparable to available literature data throughout all geological time (Rigoussen, 2017).

Although calculated independently according to Lawrence et al. (2006), these two anomalies appear to be correlated, whereby positive or negative Ce anomalies are more pronounced as La/La* increases (Fig. 5.10-A). Since positive La anomalies are considered a reliable indicator of aqueous chemistry and correlate with salinity, with lower La/La* values in freshwater (La/La* < 2; Lawrence et al., 2006) and higher values in seawater, i.e., La/La* > 2 (Bau and Dulski, 1996; Kamber and Webb, 2001; Shields and Webb, 2004; Kamber et al., 2004), these values support the marine nature of these carbonates and their formation in an open ocean environment. This is also strongly supported by the Y/Ho ratios ranging from 22 to 157 with an average value of 70, which is well above the minimum Y/Ho=44 value after which the depositional environment is considered fully marine (de Baar et al., 1985a; van Kranendonk et al., 2003; Bolhar et al., 2004; Luong et al., 2018; Li et al., 2019; Zhao et al., 2022).

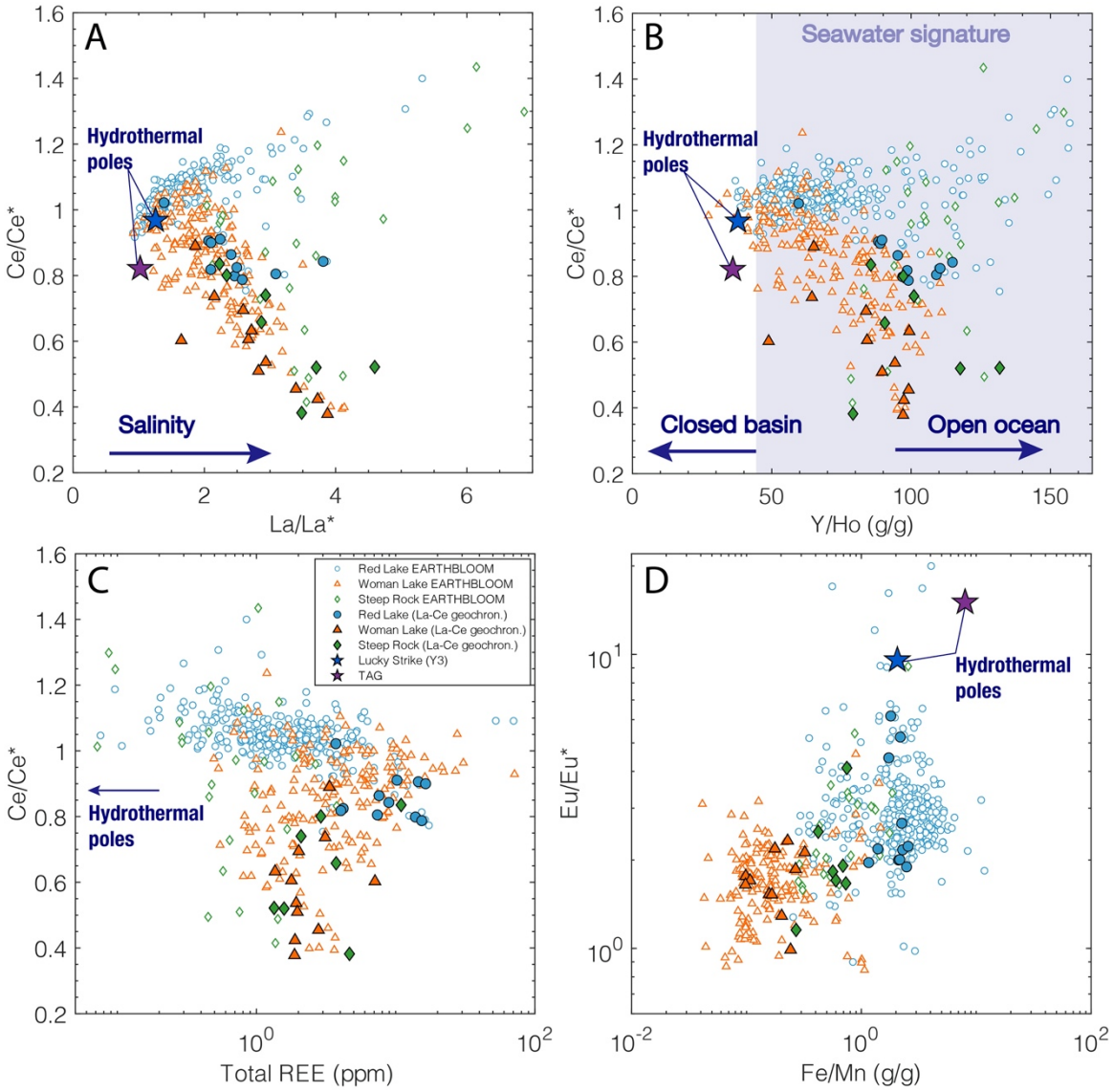

Figure 5.10. Graph with several panels presenting the paleoenvironmental context of the Red Lake, Woman Lake and Steep Rock sites. Two hydrothermal poles are represented and correspond to the Lucky Strike (main smoker Y3) and TAG hydrothermal sites, REE data from Douville et al. (1999) and Fe/Mn data from (Waeles et al., 2017).

The visible correlation between Ce/Ce* and La/La* appears to be equally valid between Ce/Ce* and Y/Ho, with positive and negative Ce anomalies more pronounced as the Y/Ho ratio increases (Fig. 5.10-B). In addition, Y/Ho ratios appear to vary with mineralogy, with dolomites restricted to Y/Ho ratios between 40 and 100 while calcites have ratios ranging from 40 up to 160 (Appendix B.3-A). Furthermore, Y/Ho ratios appear to correlate with Sr concentrations, as Y/Ho ratios are higher at higher Sr concentrations

(Appendix B.3-B), most notably at Red Lake and Steep Rock. Luo et al. (2021) showed that calcified corals had average Y/Ho ratios of 60 and aragonitic corals 118, thus, higher Y/Ho ratios would reflect primary aragonite formation instead of calcite. At Steep Rock, the calcites have Y/Ho ratios between 70 and 155, which according to Luo et al. (2021) would correspond to aragonite, consistent with the findings of Fralick and Riding (2015) who suggested that the high Sr concentrations indicate that Steep Rock carbonates were originally aragonite. In the case of Red Lake, where the carbonates are predominantly dolomite (65%), the remaining 35% of samples that are calcitic in composition today may have originally been calcite when Y/Ho ratios and Sr concentrations are low, or aragonite when Y/Ho ratios and Sr concentrations were high. With Y/Ho values predominantly between 40 and 100, the Woman Lake samples were likely primary calcite precipitates, and indeed, crystal fans indicative of aragonite are rare (absent? Check Ramsay) at this site. The distribution of Ce anomalies, which also seems to be correlated with mineralogy, with very pronounced anomalies in the calcites and inferred former aragonites, would thus similarily indicate important paleoenvironmental control on expression of the Ce anomaly. In addition, the distribution of Ce anomalies does not appear to correlate with total REE concentrations at Woman Lake, but appears to correlate to a lesser extent at Red Lake and Steep Rock, with a predominance of positive anomalies at low total REE concentrations and negative anomalies at rather high total REE concentrations, which likely reflect several depositional environments with varying REE inputs, particulate scavanging intensity, and corresponding water column residence time (see below).

The Red Lake, Woman Lake, and Steep Rock carbonates are distinguished from modern seawater by the presence of strong Eu anomalies, that appear to correlate with the Fe/Mn ratio (Fig. 5.10-D), which is consistent with other Precambrian carbonates. Red

Lake has higher Eu anomalies and Fe/Mn ratios than Woman Lake and Steep Rock, approaching those of modern marine high-temperature hydrothermal systems (data from TAG and Lucky Strike on the mid-atlantic ridge; REE data from Douville et al., 1999 and Fe/Mn data from Waeles et al., 2017). The existence of Eu anomalies revealing the presence of a high-temperature hydrothermal component in the seawater (Bau, 1991), coupled with the high Fe concentrations, confirms that ascending basinal fluids affected by hydrothermal venting were probably a major source of Fe, even in shallow water, and that the Red Lake carbonate platform had a strong connection to the open ocean (Chapter 4). Woman Lake, with lower Eu anomalies and higher Mn than Fe concentrations, was probably situated further from hydrothermal sources than Red Lake. With Eu/Eu* values and Fe/Mn ratios rather intermediate relative to the other two sites, Steep Rock would have been more influenced by hydrothermal fluids present in ambient seawater than Woman Lake, but significantly less so relative to Red Lake.

5.4.3 Redox processes

As described in the results, a subset of samples shows pronounced Ce anomalies, both positive and negative, that provide strong evidence of Ce redox cycling and thus the establishment of conditions sufficiently oxidizing to enable Ce oxidation. The behaviour of other redox-sensitive elements, such as Fe and Mn, also provide information on ancient redox conditions. Fe is rapidly oxidized under mildly oxidizing conditions (Rouxel et al., 2005; Taylor and Konhauser, 2011), and modern seawater is highly depleted in Fe due to rapid Fe(II) oxidation. However, Mn oxidation requires higher oxidation potentials and is also a kinetically slow process, and therefore, even in the modern ocean, Mn oxidation is slow, and the modern dissolved Mn pool is significantly higher than that of Fe (Konhauser,

2007). In this way, Fe/Mn ratios may similarly serve as a redox proxy. A graph of Fe vs. Mn for the three sites shows high Fe and lower Mn for Red Lake, intermediate Fe and Mn for Steep Rock, and lower Fe and even higher Mn for Woman Lake (Fig. 5.11-A). To first order, this suggests that different oxidation potentials characterize these different sites, with Red Lake, Steep Rock, and then Woman Lake attaining progressively higher oxidation potentials in this order. This is also supported by the frequency and magnitude of their Ce anomalies, as well as the behavior of Fe and Mn at each of the three sites when examined individually (Fig. 5.6-; 5.7- and 5.8-D and F).

Red Lake, where the sample set shows the fewest and smallest Ce anomalies, is also the site with the highest Fe concentrations (Fig. 5.11-B) which correlate with the increase in Eu/Eu* (Fig. 5.10-F), suggesting a strong connection to a nearby hydrothermal system (see section 5.4.2 above). The smaller Ce anomalies at Red Lake could be a consequence of lower O_2 concentrations dampened in part by buffering by the abundant Fe(II) supplied by this strong hydrothermal connection. Furthermore, Red Lake shows Fe depletion in samples with minor Ce anomalies that is relatively minor compared to Steep Rock and Woman Lake, both of which show similar and more important levels of Fe depletion concomitant with their more important Ce anomalies.

The behavior of Mn is more complex. In the case of Red Lake, Mn concentrations are relatively static for samples containing significant Ce anomalies compared to the other two sites. This may indicate that Mn redox cycling was minimal at Red Lake compared to the other two sites. Nevertheless, it was almost certainly present, which is supported by both Mo isotopic evidence (Thoby et al., 2019) and the fact that samples with pronounced Ce anomalies tend to be among the most Mn-rich samples at Red Lake (Fig. 5.11-C).

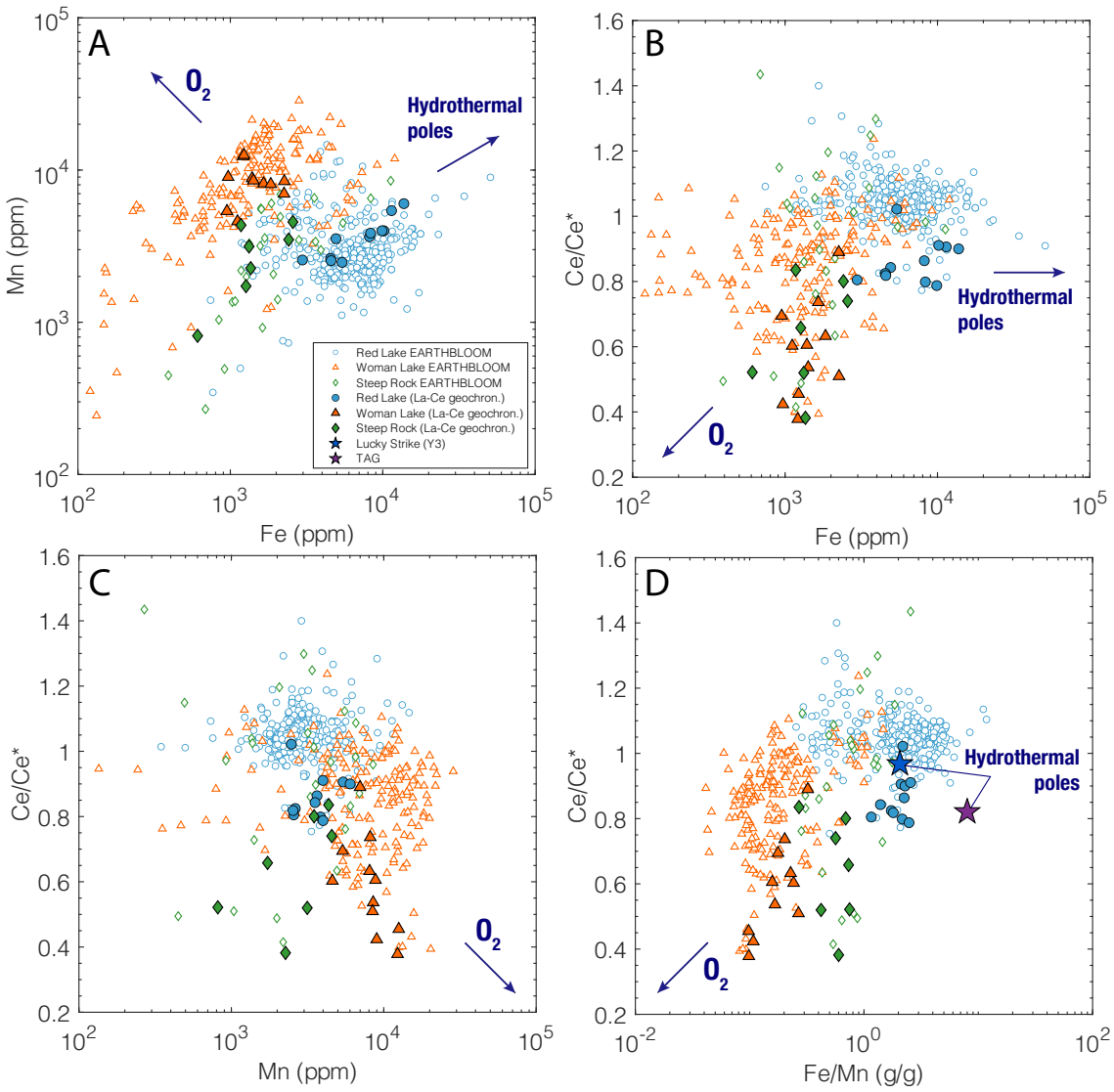

Figure 5.11. REE and Fe-Mn cross plots further indicating important redox processes occurring at the Red Lake, Woman Lake and Steep Rock sites. Two hydrothermal poles are represented that correspond to the Lucky Strike (main smoker Y3) and TAG hydrothermal sites; REE data from Douville et al. (1999) and Fe/Mn data from (Waeles et al., 2017).

At Steep Rock, significant Ce anomalies are observed at low Mn concentrations. This may reflect oxidative precipitative loss of Mn from the water column; however, the analyzed sediments appear to reflect only residual waters that has undergone loss of both Mn and Ce. The Woman Lake case is different, where the magnitude of negative Ce anomalies in the samples increase with increasing Mn content, which may reflect oxidative precipitation of Mn oxides that were delivered directly the sediment pile, resulting in Mn

enrichment. One might assume that this would provide REE with positive Ce anomalies in the sediments, however one can also imagine a scenario where highly Ce-depleted waters produced Mn oxides with negative Ce anomalies, despite the tendency for surface-catalyzed Ce oxidation of the Mn oxide to lead to local Ce enrichment on particle surfaces. Alternatively, a scenario could also be considered where significant sedimentary Mn enrichment due to oxidative Mn precipitation occurred, but that most REEs were derived from the Ce-depleted water column independently from the Mn oxides, as opposed to the sinking Mn oxide phase that would have carried positive Ce enrichment relative to the source water (which may have already been Ce-depleted).

In any case, a clear order of increasing redox potential emerges from this dataset, whereby (1) Red Lake developed weakly oxidizing conditions, expressing minor Ce anomalies accompanied by oxidative Fe loss with no major effect on the dissolved Mn reservoir, followed by (2) Steep Rock, more oxidizing, where Fe and Mn loss occurred in conjunction with increasingly oxic local conditions, as traced by the magnitude of the Ce anomalies, and (3) Woman Lake, where Mn oxides were delivered directly to the sediment pile from a highly Ce-depleted water column. This may not have so much to do with the oxidative capacity of the respective photosynthetic ecosystems at each site, but rather with the different environments preserved at each site, as in all cases, oxygenic photosynthesis is clearly indicated.

As discussed above, the generation of Ce anomalies in the water column at each site appears to be related to specific environments, namely intermediate depth waters that are neither strongly influenced by coastal waters (e.g., low Y/Ho and low La/La) nor completely open to the ocean (high Y/Ho, La/La or Eu/Eu). One possibility is that in a

nutrient-limited world, the most intense productivity was driven by upwelling bringing nutrients from the deep to the margins of continental shelves - as occurs today in the context of modern oxygen minimum zones (OMZs, Kämpf and Chapman, 2016). Alternatively, the reason for this specific paleoenvironmental distribution of large Mesoarchean negative Ce anomalies at the platform-open ocean interface may instead be related to specific aspects of REE cycling in different environments, notably the slow kinetics of Ce oxidation relative to short REE residence times in more particulate-rich coastal environments, the need to physically separate phases bearing positive and negative Ce anomalies, and the burial of these phases without REE recycling and remixing. As discussed further in Chapters 6 and 7, these observations provide important insights into ancient redox cycling and water column chemistry at the dawn of oxygenic photosynthesis, that we will see in Chapter 6, is placed firmly in the Archean by La-Ce geochronology.

5.5 Conclusion

In this chapter, a systematic examination of carbonate REE signatures and corresponding paleoenvironmental implications across three Mesoarchean carbonate platforms, Red Lake (2.93 Ga), Woman Lake (2.85 Ga) and Steep Rock (2.80 Ga), was performed. The REE (plus Y) patterns from these three sites show typical seawater characteristics, such as LREE depletion relative to HREE and strong La and Y anomalies, confirming the marine origin of these carbonates. These carbonate sediments are also chemically very pure, with low REE and Al concentrations. The REE patterns also show strong Eu anomalies, more pronounced at Red Lake than at the other two sites, indicating the presence of a high temperature hydrothermal component in the seawater. Significant Ce anomalies are observed at all three sites, are predominantly present in primary calcites and secondary calcites representing recrystallized aragonite, and are more pronounced at Woman Lake and Steep Rock. The presence of these anomalies provides strong evidence of cerium redox cycling and the establishment of sufficient oxidation conditions for Ce oxidation in the Mesoarchean. These anomalies are also associated with shifts in Fe and Mn abundances, which are also sensitive to redox processes and provide additional information on redox processes that took place in the water column. At Red Lake, which has the smallest magnitude Ce anomalies and the largest Eu anomalies, is rich in Fe and rather poor in Mn, while Steep Rock has intermediate Fe and Mn concentrations, and Woman Lake shows strong Mn enrichment and important Fe depletion. The muted nature of the Ce anomalies at Red Lake may thus be explained by an abundance of hydrothermal Fe that buffered O_2 due to its greater proximity to high temperature hydrothermal sources. Furthermore, Ce anomalies are present at low Mn concentrations at Red Lake and Steep Rock but increase at Woman Lake with increasing Mn concentrations, which can be explained as by increasing redox potential between the sites as follows: (1) at Red Lake,

conditions were more weakly oxidizing, and relatively muted Ce anomalies were accompanied by oxidative loss of Fe with no major effect on the dissolved Mn reservoir, followed by (2) Steep Rock, where conditions were more oxidizing, and oxidative precipitation of Fe and Mn occurred in conjunction with increasingly oxic local conditions as tracked by the magnitude of the Ce anomaly, and finally, (3) at Woman Lake, Mn oxides are delivered directly to the sediment pile from a severely Ce-depleted water column. The differences between these sites were not necessarily related to the oxidative capacity of the respective photosynthetic ecosystems at each site, but may also reflect the different marine environments preserved at each site. This study of rare earth systematics in the Red Lake, Woman Lake, and Steep Rock carbonate platforms supports the marine and primary nature of these carbonates as well as the REE signals that clearly recorded geochemical fingerprints of the Mesoarchean seawater – including the production of free O_2 by oxygenic photosynthesis.

5.6 References

Akagi, T., Kodama, T., Haraguchi, H., Fuwa, K., and Tsubota, H., 1986, Distribution of heavy metals in seawater around the Shikoku Island.: GEOCHEMICAL JOURNAL, v. 20, p. 127–135, doi:10.2343/geochemj.20.127.

Alexander, B.W., Bau, M., Andersson, P., and Dulski, P., 2008, Continentally-derived solutes in shallow Archean seawater: Rare earth element and Nd isotope evidence in iron formation from the 2.9Ga Pongola Supergroup, South Africa: Geochimica et Cosmochimica Acta, v. 72, p. 378–394, doi:10.1016/j.gca.2007.10.028.

Alibo, D.S., and Nozaki, Y., 1999, Rare earth elements in seawater: particle association, shale-normalization, and Ce oxidation: Geochimica et Cosmochimica Acta, v. 63, p. 363–372, doi:10.1016/S0016-7037(98)00279-8.

Alibo, D.S., Nozaki, Y., and Jeandel, C., 1999a, Indium and yttrium in North Atlantic and Mediterranean waters: comparison to the Pacific data: Geochimica et Cosmochimica Acta, v. 63, p. 1991–1999, doi:10.1016/S0016-7037(99)00080-0.

Alibo, D.S., Nozaki, Y., and Jeandel, C., 1999b, Indium and yttrium in North Atlantic and Mediterranean waters: comparison to the Pacific data: Geochimica et Cosmochimica Acta, v. 63, p. 1991–1999, doi:10.1016/S0016-7037(99)00080-0.

Allwood, A.C., Kamber, B.S., Walter, M.R., Burch, I.W., and Kanik, I., 2010, Trace elements record depositional history of an Early Archean stromatolitic carbonate platform: Chemical Geology, v. 270, p. 148–163, doi:10.1016/j.chemgeo.2009.11.013.

Amakawa, H., Ingri, J., Masuda, A., and Shimizu, H., 1991, Isotopic compositions of Ce, Nd and Sr in ferromanganese nodules from the Pacific and Atlantic Oceans, the Baltic and Barents Seas, and the Gulf of Bothnia: Earth and Planetary Science Letters, v. 105, p. 554–565, doi:10.1016/0012-821X(91)90192-K.

de Baar, H.J.W., Bacon, M.P., Brewer, P.G., and Bruland, K.W., 1985a, Rare earth elements in the Pacific and Atlantic Oceans: Geochimica et Cosmochimica Acta, v. 49, p. 1943–1959, doi:10.1016/0016-7037(85)90089-4.

de Baar, H.J.W., Brewer, P.G., and Bacon, M.P., 1985b, Anomalies in rare earth distributions in seawater: Gd and Tb: Geochimica et Cosmochimica Acta, v. 49, p. 1961–1969, doi:10.1016/0016-7037(85)90090-0.

de Baar, H.J.W., Bruland, K.W., Schijf, J., van Heuven, S.M.A.C., and Behrens, M.K., 2018, Low cerium among the dissolved rare earth elements in the central North Pacific Ocean: Geochimica et Cosmochimica Acta, v. 236, p. 5–40, doi:10.1016/j.gca.2018.03.003.

Barrat, J.A., Boulègue, J., Tiercelin, J.J., and Lesourd, M., 2000, Strontium isotopes and rare-earth element geochemistry of hydrothermal carbonate deposits from Lake Tanganyika, East Africa: Geochimica et Cosmochimica Acta, v. 64, p. 287–298, doi:10.1016/S0016-7037(99)00294-X.

Bau, M., 1996, Controls on the fractionation of isovalent trace elements in magmatic and aqueous systems: evidence from Y/Ho, Zr/Hf, and lanthanide tetrad effect: Contributions to Mineralogy and Petrology, v. 123, p. 323–333, doi:10.1007/s004100050159.

Bau, M., 1991, Rare-earth element mobility during hydrothermal and metamorphic fluid-rock interaction and the significance of the oxidation state of europium.:

Bau, M., 1999, Scavenging of dissolved yttrium and rare earths by precipitating iron oxyhydroxide: experimental evidence for Ce oxidation, Y-Ho fractionation, and lanthanide tetrad effect: Geochimica et Cosmochimica Acta, v. 63, p. 67–77, doi:10.1016/S0016-7037(99)00014-9.

Bau, M., and Alexander, B.W., 2009, Distribution of high field strength elements (Y, Zr, REE, Hf, Ta, Th, U) in adjacent magnetite and chert bands and in reference standards FeR-3 and FeR-4 from the Temagami iron-formation, Canada, and the redox level of the Neoarchean ocean: Precambrian Research, v. 174, p. 337–346, doi:10.1016/j.precamres.2009.08.007.

Bau, M., Balan, S., Schmidt, K., and Koschinsky, A., 2010, Rare earth elements in mussel shells of the Mytilidae family as tracers for hidden and fossil high-temperature hydrothermal systems: Earth and Planetary Science Letters, v. 299, p. 310–316, doi:10.1016/j.epsl.2010.09.011.

Bau, M., and Dulski, P., 1995, Comparative study of yttrium and rare-earth element behaviours in fluorine-rich hydrothermal fluids: Contributions to Mineralogy and Petrology, v. 119, p. 213–223, doi:10.1007/BF00307282.

Bau, M., and Dulski, P., 1996, Distribution of yttrium and rare-earth elements in the Penge and Kuruman iron-formations, Transvaal Supergroup, South Africa: Precambrian Research, v. 79, p. 37–55, doi:10.1016/0301-9268(95)00087-9.

Bau, M., Möller, P., and Dulski, P., 1997, Yttrium and lanthanides in eastern Mediterranean seawater and their fractionation during redox-cycling: Marine Chemistry, v. 56, p. 123–131, doi:10.1016/S0304-4203(96)00091-6.

Bau, M., Schmidt, K., Koschinsky, A., Hein, J., Kuhn, T., and Usui, A., 2014, Discriminating between different genetic types of marine ferro-manganese crusts and nodules based on rare earth elements and yttrium: Chemical Geology, v. 381, p. 1–9, doi:10.1016/j.chemgeo.2014.05.004.

Bayon, G., German, C.R., Burton, K.W., Nesbitt, R.W., and Rogers, N., 2004, Sedimentary Fe–Mn oxyhydroxides as paleoceanographic archives and the role of aeolian flux in

regulating oceanic dissolved REE: Earth and Planetary Science Letters, v. 224, p. 477–492, doi:10.1016/j.epsl.2004.05.033.

Bellefroid, E.J., Hood, A. v. S., Hoffman, P.F., Thomas, M.D., Reinhard, C.T., and Planavsky, N.J., 2018, Constraints on Paleoproterozoic atmospheric oxygen levels: Proceedings of the National Academy of Sciences, v. 115, p. 8104–8109, doi:10.1073/pnas.1806216115.

Bolhar, R., Hofmann, A., Siahi, M., Feng, Y., and Delvigne, C., 2015, A trace element and Pb isotopic investigation into the provenance and deposition of stromatolitic carbonates, ironstones and associated shales of the ~3.0 Ga Pongola Supergroup, Kaapvaal Craton: Geochimica et Cosmochimica Acta, v. 158, p. 57–78, doi:10.1016/j.gca.2015.02.026.

Bolhar, R., Kamber, B.S., Moorbath, S., Fedo, C.M., and Whitehouse, M.J., 2004, Characterisation of early Archaean chemical sediments by trace element signatures: Earth and Planetary Science Letters, v. 222, p. 43–60, doi:10.1016/j.epsl.2004.02.016.

Bolhar, R., and van Kranendonk, M., 2007, A non-marine depositional setting for the northern Fortescue Group, Pilbara Craton, inferred from trace element geochemistry of stromatolitic carbonates: Precambrian Research, v. 155, p. 229–250, doi:10.1016/j.precamres.2007.02.002.

Byrne, R.H., and Kim, K.-H., 1990, Rare earth element scavenging in seawater: Geochimica et Cosmochimica Acta, v. 54, p. 2645–2656, doi:10.1016/0016-7037(90)90002-3.

Byrne, R.H., Liu, X., and Schijf, J., 1996, The influence of phosphate coprecipitation on rare earth distributions in natural waters: Geochimica et Cosmochimica Acta, v. 60, p. 3341–3346, doi:10.1016/0016-7037(96)00197-4.

de Carlo, E.H., and Green, W.J., 2002, Rare earth elements in the water column of Lake Vanda, McMurdo Dry Valleys, Antarctica: Geochimica et Cosmochimica Acta, v. 66, p. 1323–1333, doi:10.1016/S0016-7037(01)00861-4.

Craddock, P.R., Bach, W., Seewald, J.S., Rouxel, O.J., Reeves, E., and Tivey, M.K., 2010, Rare earth element abundances in hydrothermal fluids from the Manus Basin, Papua New Guinea: Indicators of sub-seafloor hydrothermal processes in back-arc basins: Geochimica et Cosmochimica Acta, v. 74, p. 5494–5513, doi:10.1016/j.gca.2010.07.003.

Douville, E., Bienvenu, P., Charlou, J.L., Donval, J.P., Fouquet, Y., Appriou, P., and Gamo, T., 1999, Yttrium and rare earth elements in fluids from various deep-sea hydrothermal systems: Geochimica et Cosmochimica Acta, v. 63, p. 627–643, doi:10.1016/S0016-7037(99)00024-1.

Drake, M.J., 1975, The oxidation state of europium as an indicator of oxygen fugacity: Geochimica et Cosmochimica Acta, v. 39, p. 55–64, doi:10.1016/0016-7037(75)90184-2.

Dymek, R.F., and Klein, C., 1988, Chemistry, petrology and origin of banded iron-formation lithologies from the 3800 MA isua supracrustal belt, West Greenland: Precambrian Research, v. 39, p. 247–302, doi:10.1016/0301-9268(88)90022-8.

Elderfield, H., and Greaves, M.J., 1982, The rare earth elements in seawater: Nature, v. 296, p. 214–219, doi:10.1038/296214a0.

Elderfield, H., Hawkesworth, C.J., Greaves, M.J., and Calvert, S.E., 1981, Rare earth element geochemistry of oceanic ferromanganese nodules and associated sediments: Geochimica et Cosmochimica Acta, v. 45, p. 513–528, doi:10.1016/0016-7037(81)90184-8.

Elderfield, H., Upstill-Goddard, R., and Sholkovitz, E.R., 1990, The rare earth elements in rivers, estuaries, and coastal seas and their significance to the composition of ocean waters: Geochimica et Cosmochimica Acta, v. 54, p. 971–991, doi:10.1016/0016-7037(90)90432-K.

Fralick, P., and Riding, R., 2015, Steep Rock Lake: Sedimentology and geochemistry of an Archean carbonate platform: Earth-Science Reviews, v. 151, p. 132–175, doi:10.1016/j.earscirev.2015.10.006.

Garcia-Solsona, E., Jeandel, C., Labatut, M., Lacan, F., Vance, D., Chavagnac, V., and Pradoux, C., 2014, Rare earth elements and Nd isotopes tracing water mass mixing and particle-seawater interactions in the SE Atlantic: Geochimica et Cosmochimica Acta, v. 125, p. 351–372, doi:10.1016/j.gca.2013.10.009.

German, C.R., and Elderfield, H., 1990, Application of the Ce anomaly as a paleoredox indicator: The ground rules: Paleoceanography, v. 5, p. 823–833, doi:10.1029/PA005i005p00823.

German, C.R., and Elderfield, H., 1989, Rare earth elements in Saanich Inlet, British Columbia, a seasonally anoxic basin: Geochimica et Cosmochimica Acta, v. 53, p. 2561–2571, doi:10.1016/0016-7037(89)90128-2.

German, C.R., Holliday, B.P., and Elderfield, H., 1991, Redox cycling of rare earth elements in the suboxic zone of the Black Sea: Geochimica et Cosmochimica Acta, v. 55, p. 3553–3558, doi:10.1016/0016-7037(91)90055-A.

German, C.R., Klinkhammer, G.P., Edmond, J.M., Mura, A., and Elderfield, H., 1990, Hydrothermal scavenging of rare-earth elements in the ocean: Nature, v. 345, p. 516–518, doi:10.1038/345516a0.

German, C.R., Masuzawa, T., Greaves, M.J., Elderfield, ~ H, and Edmond~, J.M., 1995, Dissolved rare earth elements in the Southern Ocean: Cerium oxidation and the influence of hydrography.:

Goldberg, E.D., Koide, M., Schmitt, R.A., and Smith, R.H., 1963, Rare-Earth distributions in the marine environment: Journal of Geophysical Research, v. 68, p. 4209–4217, doi:10.1029/JZ068i014p04209.

Grenier, M., Garcia-Solsona, E., Lemaitre, N., Trull, T.W., Bouvier, V., Nonnotte, P., van Beek, P., Souhaut, M., Lacan, F., and Jeandel, C., 2018, Differentiating Lithogenic Supplies, Water Mass Transport, and Biological Processes On and Off the Kerguelen Plateau Using Rare Earth Element Concentrations and Neodymium Isotopic Compositions: Frontiers in Marine Science, v. 5, doi:10.3389/fmars.2018.00426.

Gromet, L.P., Haskin, L.A., Korotev, R.L., and Dymek, R.F., 1984, The "North American shale composite": Its compilation, major and trace element characteristics: Geochimica et Cosmochimica Acta, v. 48, p. 2469–2482, doi:10.1016/0016-7037(84)90298-9.

Hill, I.G., Worden, R.H., and Meighan, I.G., 2000, Yttrium: The immobility-mobility transition during basaltic weathering: Geology, v. 28, p. 923, doi:10.1130/0091-7613(2000)28<923:YTITDB>2.0.CO;2.

Hogdahl, O.T., Melsom, S., and Bowen, V.T., 1968, Neutron Activation Analysis of Lanthanide Elements in Sea Water, *in* p. 308–325, doi:10.1021/ba-1968-0073.ch019.

Holser, W.T., 1997, Evaluation of the application of rare-earth elements to paleoceanography: Palaeogeography, Palaeoclimatology, Palaeoecology, v. 132, p. 309–323, doi:10.1016/S0031-0182(97)00069-2.

Hood, A. v. S., Planavsky, N.J., Wallace, M.W., and Wang, X., 2018, The effects of diagenesis on geochemical paleoredox proxies in sedimentary carbonates:

Geochimica et Cosmochimica Acta, v. 232, p. 265–287, doi:10.1016/j.gca.2018.04.022.

James, R.H., Elderfield, H., and Palmer, M.R., 1995, The chemistry of hydrothermal fluids from the Broken Spur site, 29°N Mid-Atlantic ridge: Geochimica et Cosmochimica Acta, v. 59, p. 651–659, doi:10.1016/0016-7037(95)00003-I.

Johannessen, K.C., vander Roost, J., Dahle, H., Dundas, S.H., Pedersen, R.B., and Thorseth, I.H., 2017, Environmental controls on biomineralization and Fe-mound formation in a low-temperature hydrothermal system at the Jan Mayen Vent Fields: Geochimica et Cosmochimica Acta, v. 202, p. 101–123, doi:10.1016/j.gca.2016.12.016.

Kamber, B.S., Bolhar, R., and Webb, G.E., 2004, Geochemistry of late Archaean stromatolites from Zimbabwe: evidence for microbial life in restricted epicontinental seas: Precambrian Research, v. 132, p. 379–399, doi:10.1016/j.precamres.2004.03.006.

Kamber, B.S., and Webb, G.E., 2001, The geochemistry of late Archaean microbial carbonate: implications for ocean chemistry and continental erosion history: Geochimica et Cosmochimica Acta, v. 65, p. 2509–2525, doi:10.1016/S0016-7037(01)00613-5.

Kamber, B.S., Webb, G.E., and Gallagher, M., 2014, The rare earth element signal in Archaean microbial carbonate: information on ocean redox and biogenicity: Journal of the Geological Society, v. 171, p. 745–763, doi:10.1144/jgs2013-110.

Kämpf, J., and Chapman, P., 2016, Upwelling Systems of the World: Cham, Springer International Publishing, doi:10.1007/978-3-319-42524-5.

Koeppenkastrop, D., and de Carlo, E.H., 1992, Sorption of rare-earth elements from seawater onto synthetic mineral particles: An experimental approach: Chemical Geology, v. 95, p. 251–263, doi:10.1016/0009-2541(92)90015-W.

Komiya, T., Hirata, T., Kitajima, K., Yamamoto, S., Shibuya, T., Sawaki, Y., Ishikawa, T., Shu, D., Li, Y., and Han, J., 2008, Evolution of the composition of seawater through geologic time, and its influence on the evolution of life: Gondwana Research, v. 14, p. 159–174, doi:10.1016/j.gr.2007.10.006.

Konhauser, K., 2007, Introduction to Geomicrobiology:

van Kranendonk, M.J., Webb, G.E., and Kamber, B.S., 2003, Geological and trace element evidence for a marine sedimentary environment of deposition and biogenicity of 3.45 Ga stromatolitic carbonates in the Pilbara Craton, and support for a reducing Archaean ocean: Geobiology, v. 1, p. 91–108, doi:10.1046/j.1472-4669.2003.00014.x.

Lawrence, M.G., Greig, A., Collerson, K.D., and Kamber, B.S., 2006, Rare earth element and yttrium variability in South East Queensland waterways: Aquatic Geochemistry, v. 12, p. 39–72, doi:10.1007/s10498-005-4471-8.

Li, Y., Li, C., Chu, Z., and Guo, J., 2021, Evaluation and optimisation of the dissolution method for bulk analysis of carbonate neodymium isotopic composition based on chemical leaching of carbonate certified reference materials: Microchemical Journal, v. 171, p. 106880, doi:10.1016/j.microc.2021.106880.

Li, F., Webb, G.E., Algeo, T.J., Kershaw, S., Lu, C., Oehlert, A.M., Gong, Q., Pourmand, A., and Tan, X., 2019, Modern carbonate ooids preserve ambient aqueous REE signatures: Chemical Geology, v. 509, p. 163–177, doi:10.1016/j.chemgeo.2019.01.015.

Ling, H.-F., Chen, X., Li, D., Wang, D., Shields-Zhou, G.A., and Zhu, M., 2013, Cerium anomaly variations in Ediacaran–earliest Cambrian carbonates from the Yangtze

Gorges area, South China: Implications for oxygenation of coeval shallow seawater: Precambrian Research, v. 225, p. 110–127, doi:10.1016/j.precamres.2011.10.011.

Liu, X., and Byrne, R.H., 1997, Rare earth and yttrium phosphate solubilities in aqueous solution: Geochimica et Cosmochimica Acta, v. 61, p. 1625–1633, doi:10.1016/S0016-7037(97)00037-9.

Liu, X.M., Hardisty, D.S., Lyons, T.W., and Swart, P.K., 2019, Evaluating the fidelity of the cerium paleoredox tracer during variable carbonate diagenesis on the Great Bahamas Bank: Geochimica et Cosmochimica Acta, v. 248, p. 25–42, doi:10.1016/j.gca.2018.12.028.

Liu, X.-M., Kah, L.C., Knoll, A.H., Cui, H., Wang, C., Bekker, A., and Hazen, R.M., 2021, A persistently low level of atmospheric oxygen in Earth's middle age: Nature Communications, v. 12, p. 351, doi:10.1038/s41467-020-20484-7.

Luo, Y.-R., and Byrne, R.H., 2004, Carbonate complexation of yttrium and the rare earth elements in natural waters: Geochimica et Cosmochimica Acta, v. 68, p. 691–699, doi:10.1016/S0016-7037(03)00495-2.

Luo, Y., Li, G., Xu, W., Liu, J., Cheng, J., Zhao, J., and Yan, W., 2021, The effect of diagenesis on rare earth element geochemistry of the Quaternary carbonates at an isolated coral atoll in the South China Sea: Sedimentary Geology, v. 420, p. 105933, doi:10.1016/j.sedgeo.2021.105933.

Luong, L.D., Shinjo, R., Hoang, N., Shakirov, R.B., and Syrbu, N., 2018, Spatial variations in dissolved rare earth element concentrations in the East China Sea water column: Marine Chemistry, v. 205, p. 1–15, doi:10.1016/j.marchem.2018.07.004.

Masuda, A., and Ikeuchi, Y., 1979, Lanthanide tetrad effect observed in marine environment.: GEOCHEMICAL JOURNAL, v. 13, p. 19–22, doi:10.2343/geochemj.13.19.

Michard, A., and Albarède, F., 1986, The REE content of some hydrothermal fluids: Chemical Geology, v. 55, p. 51–60, doi:10.1016/0009-2541(86)90127-0.

Michard, A., Albarède, F., Michard, G., Minster, J.F., and Charlou, J.L., 1983, Rare-earth elements and uranium in high-temperature solutions from East Pacific Rise hydrothermal vent field (13 °N): Nature, v. 303, p. 795–797, doi:10.1038/303795a0.

Moffett, J.W., 1990, Microbially mediated cerium oxidation in sea water: Nature, v. 345, p. 421–423, doi:10.1038/345421a0.

Mukhopadhyay, J., Crowley, Q.G., Ghosh, S., Ghosh, G., Chakrabarti, K., Misra, B., Heron, K., and Bose, S., 2014, Oxygenation of the Archean atmosphere: New paleosol constraints from eastern India: Geology, v. 42, p. 923–926, doi:10.1130/G36091.1.

Nozaki, Y., 2001, Rare earth elements and their isotopes in the ocean: Encyclopedia of Ocean Sciences, v. 4, p. 2354–2366.

Nozaki, Y., and Alibo, D.S., 2003a, Dissolved rare earth elements in the Southern Ocean, southwest of Australia: Unique patterns compared to the South Atlantic data.: GEOCHEMICAL JOURNAL, v. 37, p. 47–62, doi:10.2343/geochemj.37.47.

Nozaki, Y., and Alibo, D.S., 2003b, Importance of vertical geochemical processes in controlling the oceanic profiles of dissolved rare earth elements in the northeastern Indian Ocean: Earth and Planetary Science Letters, v. 205, p. 155–172, doi:10.1016/S0012-821X(02)01027-0.

Nozaki, Y., Zhang, J., and Amakawa, H., 1997, The fractionation between Y and Ho in the marine environment: Earth and Planetary Science Letters, v. 148, p. 329–340, doi:10.1016/S0012-821X(97)00034-4.

Piepgras, D.J., and Wasserburg, G.J., 1980, Neodymium isotopic variations in seawater: Earth and Planetary Science Letters, v. 50, p. 128–138, doi:10.1016/0012-821X(80)90124-7.

Piepgras, D.J., Wasserburg, G.J., and Dasch, E.J., 1979, The isotopic composition of Nd in different ocean masses: Earth and Planetary Science Letters, v. 45, p. 223–236, doi:10.1016/0012-821X(79)90125-0.

Piper, D.Z., and Bau, M., 2013, Normalized Rare Earth Elements in Water, Sediments, and Wine: Identifying Sources and Environmental Redox Conditions: American Journal of Analytical Chemistry, v. 04, p. 69–83, doi:10.4236/ajac.2013.410A1009.

Planavsky, N., Bekker, A., Rouxel, O.J., Kamber, B., Hofmann, A., Knudsen, A., and Lyons, T.W., 2010a, Rare Earth Element and yttrium compositions of Archean and Paleoproterozoic Fe formations revisited: New perspectives on the significance and mechanisms of deposition: Geochimica et Cosmochimica Acta, v. 74, p. 6387–6405, doi:10.1016/j.gca.2010.07.021.

Planavsky, N.J., Robbins, L.J., Kamber, B.S., and Schoenberg, R., 2020, Weathering, alteration and reconstructing Earth's oxygenation: Interface Focus, v. 10, p. 20190140, doi:10.1098/rsfs.2019.0140.

Planavsky, N.J., Rouxel, O.J., Bekker, A., Lalonde, S. v., Konhauser, K.O., Reinhard, C.T., and Lyons, T.W., 2010b, The evolution of the marine phosphate reservoir: Nature, v. 467, p. 1088–1090, doi:10.1038/nature09485.

Planavsky, N., Rouxel, O., Bekker, A., Shapiro, R., Fralick, P., and Knudsen, A., 2009, Iron-oxidizing microbial ecosystems thrived in late Paleoproterozoic redox-stratified oceans: Earth and Planetary Science Letters, v. 286, p. 230–242, doi:10.1016/j.epsl.2009.06.033.

Qu, C., Liu, G., and Zhao, Y.F., 2009, Experimental study on the fractionation of yttrium from holmium during the coprecipitation with calcium carbonates in seawater solutions: Geochemical Journal, v. 43, p. 403–414, doi:10.2343/geochemj.1.0036.

Riding, R., Fralick, P., and Liang, L., 2014, Identification of an Archean marine oxygen oasis: Precambrian Research, v. 251, p. 232–237, doi:10.1016/j.precamres.2014.06.017.

Rigoussen, D., 2017, Carbonate geochemistry, new redox tracer analyses through the Precambrian: Msc 2 diss., Université de Bretagne Occidentale (UBO),.

Rongemaille, E., Bayon, G., Pierre, C., Bollinger, C., Chu, N.C., Fouquet, Y., Riboulot, V., and Voisset, M., 2011, Rare earth elements in cold seep carbonates from the Niger delta: Chemical Geology, v. 286, p. 196–206, doi:10.1016/j.chemgeo.2011.05.001.

Rouxel, O.J., Bekker, A., and Edwards, K.J., 2005, Iron isotope constraints on the Archean and Paleoproterozoic ocean redox state: Science, v. 307, p. 1088–1091, doi:10.1126/science.1105692.

Schijf, J., Christenson, E.A., and Byrne, R.H., 2015, YREE scavenging in seawater: A new look at an old model: Marine Chemistry, v. 177, p. 460–471, doi:10.1016/j.marchem.2015.06.010.

Schmitt, R.A., Smith, R.H., Lasch, J.E., Mosen, A.W., Olehy, D.A., and Vasilevskis, J., 1963, Abundances of the fourteen rare-earth elements, scandium, and yttrium in meteoritic and terrestrial matter: Geochimica et Cosmochimica Acta, v. 27, p. 577–622, doi:10.1016/0016-7037(63)90014-0.

Shahkarami, S., Mángano, M.G., and Buatois, L.A., 2017, Discriminating ecological and evolutionary controls during the Ediacaran–Cambrian transition: Trace fossils from the Soltanieh Formation of northern Iran: Palaeogeography, Palaeoclimatology, Palaeoecology, v. 476, p. 15–27, doi:10.1016/j.palaeo.2017.03.012.

Shannon, R.D., 1976, Revised effective ionic radii and systematic studies of interatomic distances in halides and chalcogenides: Acta Crystallographica Section A, v. 32, p. 751–767, doi:10.1107/S0567739476001551.

Shields, G., and Stille, P., 2001, Diagenetic constraints on the use of cerium anomalies as palaeoseawater redox proxies: an isotopic and REE study of Cambrian phosphorites: Chemical Geology, v. 175, p. 29–48, doi:10.1016/S0009-2541(00)00362-4.

Shields, G.A., and Webb, G.E., 2004, Has the REE composition of seawater changed over geological time? Chemical Geology, v. 204, p. 103–107, doi:10.1016/j.chemgeo.2003.09.010.

Sholkovitz, E.R., 1993, The geochemistry of rare earth elements in the Amazon River estuary: Geochimica et Cosmochimica Acta, v. 57, p. 2181–2190, doi:10.1016/0016-7037(93)90559-F.

Siahi, M., Hofmann, A., Master, S., Wilson, A., and Mayr, C., 2018, Trace element and stable (C, O) and radiogenic (Sr) isotope geochemistry of stromatolitic carbonate rocks of the Mesoarchaean Pongola Supergroup: Implications for seawater composition: Chemical Geology, v. 476, p. 389–406, doi:10.1016/j.chemgeo.2017.11.036.

Smrzka, D., Zwicker, J., Bach, W., Feng, D., Himmler, T., Chen, D., and Peckmann, J., 2019, The behavior of trace elements in seawater, sedimentary pore water, and their incorporation into carbonate minerals: a review: Facies, v. 65, p. 41, doi:10.1007/s10347-019-0581-4.

Sverjensky, D.A., 1984, Europium redox equilibria in aqueous solution: Earth and Planetary Science Letters, v. 67, p. 70–78, doi:10.1016/0012-821X(84)90039-6.

Sylvestre, G., Evine Laure, N.T., Gus Djibril, K.N., Arlette, D.S., Cyriel, M., Timoléon, N., and Jean Paul, N., 2017, A mixed seawater and hydrothermal origin of superior-type banded iron formation (BIF)-hosted Kouambo iron deposit, Palaeoproterozoic Nyong series, Southwestern Cameroon: Constraints from petrography and

geochemistry: Ore Geology Reviews, v. 80, p. 860–875, doi:10.1016/j.oregeorev.2016.08.021.

Tanaka, K., Takahashi, Y., and Shimizu, H., 2008, Local structure of Y and Ho in calcite and its relevance to Y fractionation from Ho in partitioning between calcite and aqueous solution: Chemical Geology, v. 248, p. 104–113, doi:10.1016/j.chemgeo.2007.11.003.

Tanaka, K., Tani, Y., Takahashi, Y., Tanimizu, M., Suzuki, Y., Kozai, N., and Ohnuki, T., 2010, A specific Ce oxidation process during sorption of rare earth elements on biogenic Mn oxide produced by Acremonium sp. strain KR21-2: Geochimica et Cosmochimica Acta, v. 74, p. 5463–5477, doi:10.1016/j.gca.2010.07.010.

Taylor, K.G., and Konhauser, K.O., 2011, Iron in Earth Surface Systems: A Major Player in Chemical and Biological Processes: Elements, v. 7, p. 83–88, doi:10.2113/gselements.7.2.83.

Taylor, S.R., and McLennan, Scott.M., 1985, The continental crust: its composition and evolution:

Thoby, M., Konhauser, K.O., Fralick, P.W., Altermann, W., Visscher, P.T., and Lalonde, S. v., 2019, Global importance of oxic molybdenum sinks prior to 2.6 Ga revealed by the Mo isotope composition of Precambrian carbonates: Geology, v. 47, p. 559–562, doi:10.1130/G45706.1.

Tostevin, R., Shields, G.A., Tarbuck, G.M., He, T., Clarkson, M.O., and Wood, R.A., 2016, Effective use of cerium anomalies as a redox proxy in carbonate-dominated marine settings: Chemical Geology, v. 438, p. 146–162, doi:10.1016/j.chemgeo.2016.06.027.

Viehmann, S., Reitner, J., Tepe, N., Hohl, S. v., van Kranendonk, M., Hofmann, T., Koeberl, C., and Meister, P., 2020, Carbonates and cherts as archives of seawater chemistry and habitability on a carbonate platform 3.35 Ga ago: Insights from Sm/Nd

dating and trace element analysis from the Strelley Pool Formation, Western Australia: Precambrian Research, v. 344, p. 105742, doi:10.1016/j.precamres.2020.105742.

Waeles, M., Cotte, L., Pernet-Coudrier, B., Chavagnac, V., Cathalot, C., Leleu, T., Laës-Huon, A., Perhirin, A., Riso, R.D., and Sarradin, P.-M., 2017, On the early fate of hydrothermal iron at deep-sea vents: A reassessment after in situ filtration: Geophysical Research Letters, v. 44, p. 4233–4240, doi:10.1002/2017GL073315.

Wallace, M.W., Hood, A., Shuster, A., Greig, A., Planavsky, N.J., and Reed, C.P., 2017, Oxygenation history of the Neoproterozoic to early Phanerozoic and the rise of land plants: Earth and Planetary Science Letters, v. 466, p. 12–19, doi:10.1016/j.epsl.2017.02.046.

Wang, X., Barrat, J.-A., Bayon, G., Chauvaud, L., and Feng, D., 2020, Lanthanum anomalies as fingerprints of methanotrophy: Geochemical Perspectives Letters, v. 14, p. 26–30, doi:10.7185/geochemlet.2019.

Wildeman, T.R., and Haskin, L., 1965, Rare-earth elements in ocean sediments: Journal of Geophysical Research, v. 70, p. 2905–2910, doi:10.1029/JZ070i012p02905.

Zhang, J., and Nozaki, Y., 1996, Rare earth elements and yttrium in seawater: ICP-MS determinations in the East Caroline, Coral Sea, and South Fiji basins of the western South Pacific Ocean: Geochimica et Cosmochimica Acta, v. 60, p. 4631–4644, doi:10.1016/S0016-7037(96)00276-1.

Zhao, Y., Wei, W., Santosh, M., Hu, J., Wei, H., Yang, J., Liu, S., Zhang, G., Yang, D., and Li, S., 2022, A review of retrieving pristine rare earth element signatures from carbonates: Palaeogeography, Palaeoclimatology, Palaeoecology, v. 586, doi:10.1016/j.palaeo.2021.110765.

Zhao, Y.-Y., Zheng, Y.-F., and Chen, F., 2009, Trace element and strontium isotope constraints on sedimentary environment of Ediacaran carbonates in southern Anhui, South China: Chemical Geology, v. 265, p. 345–362, doi:10.1016/j.chemgeo.2009.04.015.

Zhong, S., and Mucci, A., 1995, Partitioning of rare earth elements (REEs) between calcite and seawater solutions at 25°C and 1 atm, and high dissolved REE concentrations: Geochimica et Cosmochimica Acta, v. 59, p. 443–453, doi:10.1016/0016-7037(94)00381-U.

CHAPTER 6:

Archean origins of oxygenic photosynthesis confirmed by La-Ce geochronology

Abstract

Significant debate exists as to when oxygenic photosynthesis evolved on Earth. Geochemical data from ancient sediments indicates localized or ephemeral photosynthetic O_2 production prior to Great Oxidation Event ca. 2.5-2.3 billion years ago (Ga) and currently suggests Archean origins, around 3 Ga or earlier. However, sedimentary records of the early Earth often suffer from important preservation issues, and a lack of constraints on the timing of oxidation leaves geochemical proxy data for the ancient presence of O_2 open to significant critique. Here we report rare earth element data from three different Archean carbonate platforms preserved in greenstone belts of the NW Superior craton (Canada) that were deposited by the activity of marine photosynthetic bacteria at 2.93 Ga, 2.86 Ga, and 2.80 Ga ago. All three present clear evidence of O_2 production before the GOE in the form of significant depletions in cerium (Ce) reflecting oxidative Ce removal from ancient seawater. For the first time using the ^{138}La-^{138}Ce radiometric isotope geochronometer, we demonstrate clearly for all three sites, and with a high statistical degree of certainty for two of them, that La/Ce fractionation, and thus cerium oxidation, occurred at the time of deposition. These results firmly place the origin of oxygenic photosynthesis in the Mesoarchean, necessitating a revised view of biological and geochemical evolution on Earth.

Résumé

Il existe un débat important sur la date d'apparition de la photosynthèse oxygénique sur Terre. Les données géochimiques des sédiments anciens indiquent une production photosynthétique d'O_2 localisée ou éphémère avant le Grand événement d'oxydation (GOE), il y a environ 2,5 à 2,3 milliards d'années (Ga), et suggèrent actuellement des origines archéennes autour de 3 Ga ou plus tôt. Cependant, les enregistrements sédimentaires de la Terre primitive sont souvent sujets d'altérations d'importantes, et le manque de contraintes sur le moment de l'oxydation laisse les données géochimiques de substitution pour la présence ancienne de l'O_2 ouvertes à d'importantes critiques. Nous présentons ici des données sur les éléments de terres rares (REE) provenant de trois plateformes carbonatées archéennes différentes préservées dans les ceintures de schistes verts au Nord-Ouest du Craton Supérieur (Canada), qui ont été déposées par l'activité de bactéries photosynthétiques marines il y a 2,93 Ga, 2,86 Ga et 2,80 Ga. Toutes trois présentent des preuves évidentes de production d'O_2 avant le GOE sous la forme d'appauvrissements significatifs en cérium (Ce) reflétant l'élimination oxydative du Ce de l'eau de mer ancienne. Pour la première fois, en utilisant le géochronomètre isotopique radiométrique ^{138}La-^{138}Ce, nous démontrons clairement pour les trois sites, avec un degré élevé de certitude statistique pour deux d'entre eux, que le fractionnement La/Ce, et donc l'oxydation du cérium, a eu lieu au moment du dépôt. Ces résultats placent fermement l'origine de la photosynthèse oxygénique au Mésoarchéen, ce qui nécessite une révision de la vision de l'évolution biologique et géochimique sur Terre.

6.1 Introduction

The Great Oxygenation Event (GOE) places a lower limit on the evolution of oxygenic photosynthesis at the time of the first significant accumulation of atmospheric oxygen around 2.5 to 2.3 Ga. However, its upper limit is poorly defined, and multiple redox methods indicate the establishment of marine and lacustrine oxygen oases between 2.5 and 3.0 Ga (Anbar et al., 2007; Planavsky et al., 2014; Riding et al., 2014; Robbins et al., 2016; Eickmann et al., 2018; Thoby et al., 2019; Wilmeth et al., 2022) and perhaps as far back as 3.8 Ga (Rosing and Frei, 2004; Frei et al., 2016). Theoretical considerations support the establishment of pelagic (Olson et al., 2013) and benthic (Lalonde and Konhauser, 2015) oxygen oases, where shallow-water and terrestrial O_2-producing communities may have thrived for hundreds of millions of years before having any effect on atmospheric composition. Molecular clock analyses also support a relatively early origin of oxygenic photosynthesis between 3.5 and 3.0 Ga (Cardona et al., 2019; Boden et al., 2021) but estimates may vary widely, from 4.5 Ga to 2.32 Ga (Fischer et al., 2016; Oliver et al., 2021). In the absence of unambiguous evidence for oxygen photosynthesis during the Archaean in the form of cyanobacterial microfossils or biomarkers, resolution of the question of whether oxygen was present at this time depends largely on geochemical and isotopic proxies.

However, the primary nature of geochemical signals of early photosynthetic O_2 production on Earth is often questionable, given the diverse diagenetic, metamorphic, hydrothermal, and surface oxidative weathering processes that affect the Precambrian sedimentary record. The issue of syngenicity is particularly problematic for sensitive trace metal isotope redox proxies because many sedimentary sequences of paleobiological interest have been in close proximity to oxygen-rich surface conditions for millions of years

or more. On the one hand, many studies have reported trace element or metal isotope evidence for transient free oxygen production prior to the ~2.5–2.3 Ga GOE; first in the 2.5 Ga Mount McRae Shale (Anbar et al., 2007), and in the last decade, pushing it back to the Mesoarchean, often in ~3.0-2.8 Ga sediments (Planavsky et al., 2014; Riding et al., 2014; Crowe et al., 2014; Wang et al., 2018; Thoby et al., 2019). On the other hand, follow-up work has revealed significant concerns regarding the syngenetic nature of many of these signals, whether by the fact that they may be present in surface samples but absent in drill core (Albut et al., 2018, 2019; Planavsky et al., 2020), or showing evidence of remobilization and re-concentration in the later phases of mineralization (Slotznick et al., 2022). Therefore, there is still significant debate regarding when oxygenic photosynthesis arose on Earth.

Recent advances in radiometric isotope geochemistry offer one solution to this problem. At least three currently applied redox tracers (based on U, Re, and Ce) form radiogenic parent-daughter pairs (U-Th-Pb, Re-Os, and La-Ce) that can be used to date the closure of isotope systems on time scales suitable for ancient Earth studies. For example, Li et al. (2012) applied the U-Th-Pb dating system on basalt samples from drill core recovered from over 100 m depth in the Marble Bar region of the Pilbara Craton, Northwestern Australia, to reveal that the hematite present is due to later alteration of the basalts by oxidizing fluids, and not the presence of an Archean O_2-bearing atmosphere, as previously suggested by Hoashi et al. (2009). Samples from this core do not form isochrons in the U-Th-Pb system, indicating post-depositional addition of U or Pb. Modeled U/Th ratios indicate U enrichment during the last 200 Ma, which clearly excludes the possibility that basalt oxidation occurred in the Archean, and ultimately, that these rocks cannot be used to demonstrate an oxygenated atmosphere at that time. Several years later, in what

constitutes a positive confirmation of an ancient paleoredox signal, Kendall et al. (2015) evaluated the Re-Os systematics of the Late Archean Mount McRae Shale from Western Australia. In this intensely studied deposit, a pre-GOE oxygen oasis has been previously identified (Anbar et al., 2007) and since supported by multiple lines of evidence, including stratigraphic trends in Mo, U, Se, as well as S and N (see Kendall et al., (2015) for synthesis). Their results show an evolution of initial $^{187}Os/^{188}Os$ values that indicates the onset, and then termination, of a transient episode of pre-GOE oxidative continental ca. 2.495 Ga, in a unique case where Re-Os isotopic closure is effectively demonstrated to be near syn-depositional.

The La-Ce system is similarly capable of anchoring La-Ce separation processes, and thus including redox reactions, in geological time. La-Ce geochronology was applied for the first time by Tanaka and Masuda (1982) in combination with the Sm-Nd system to determine the age of a gabbro from the upper zone of the Bushveld complex in South Africa, and they determined that the ages obtained with the two systems were consistent within error. These two systems combined were later used for ocean island basalt (OIB) source determination (Dickin, 1987), to constrain the evolution of the moon (Tanimizu and Tanaka, 2002), to characterize the nature of the sediments involved in the genesis of lavas (Bellot, 2016), and to study the behavior of LREE in mid-ocean ridge basalts (MORBs) and OIBs (Schnabel, 2019).

In the La-Ce system, ^{138}La decays via two parallel processes: 34 % of the isotope undergoes β– decay (conversion of a neutron into a proton), transforming into stable ^{138}Ce, while the remaining 66% of ^{138}La disintegrates by electronic capture (conversion of a proton to a neutron by interaction with an electron), leading to the formation of stable ^{138}Ba

(Bortoluzzi and Ferraro, 2020). The long half-life (β-decay; $t^{1/2}$ = 102 x 10^9 years; Sonzogni, 2003) and the low abundance (0.089 %) of ^{138}La generate very small variations in the isotopic ratio ^{138}Ce/^{142}Ce compared to other systems (Bonnand et al., 2019). Figure 6.1 shows the evolution of the ^{138}Ce/^{142}Ce ratio over time as a function of the ^{138}La/^{142}Ce ratio.

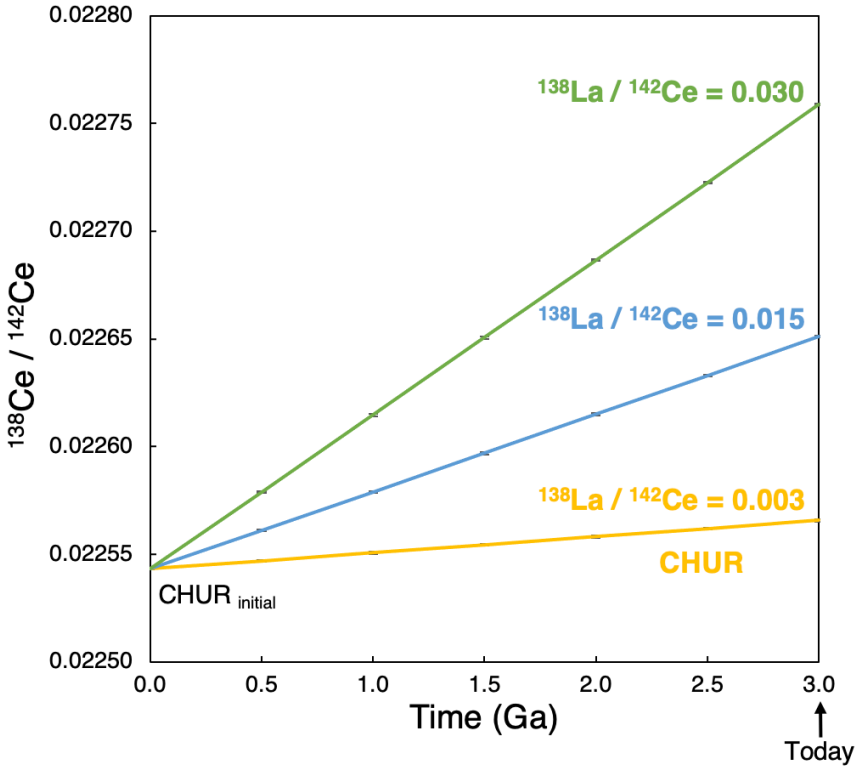

Figure 6.1. Evolution of the ^{138}Ce/^{142}Ce ratio over time and as a function of the ^{138}La/^{142}Ce ratio.

In this figure, we can see that CHUR has a ^{138}La/^{142}Ce ratio of 0.00311447 and a ^{138}Ce/^{142}Ce ratio that has varied in 3 billion years from ^{138}Ce/^{142}Ce $_{initial}$ = 0.02254340 to ^{138}Ce/^{142}Ce $_{modern}$ = 0.02256577 ± 66 (2SD; Israel et al., 2020). If we take a sample with a ^{138}La/^{142}Ce ratio of 0.030, after 3 billion years this sample will have a ^{138}Ce/^{142}Ce ratio of 0.0227589. Therefore, different La/Ce ratios can appreciably influence the evolution of ^{138}Ce/^{142}Ce ratios within a range that may be resolved by modern high-precision mass

spectrometry. This is illustrated graphically in Figure 6.2, which presents the theoretical isochrons of the La-Ce system for $^{138}La/^{142}Ce$ values ranging from 0 to 0.030 and ages from 0.1 to 3 Ga, showing the evolution of the $^{138}Ce/^{142}Ce$ ratio in time as a function of these different initial compositions. The older a sample is, the more the $^{138}Ce/^{142}Ce$ ratio evolves to radiogenic values, and the greater the initial $^{138}La/^{142}Ce$ ratio, the faster this occurs. However, in the best case, i.e., for a ratio $^{138}La/^{142}Ce$ = 0.030 and an age of 3 Ga (representing the upper limit of Mesoarchean carbonates showing extreme negative Ce anomalies examined in this study), the ratio $^{138}Ce/^{142}Ce$ varies by only 0.0002155 from the initial CHUR, which demonstrates that a high level of precision in the measurement is essential for geochronological applications.

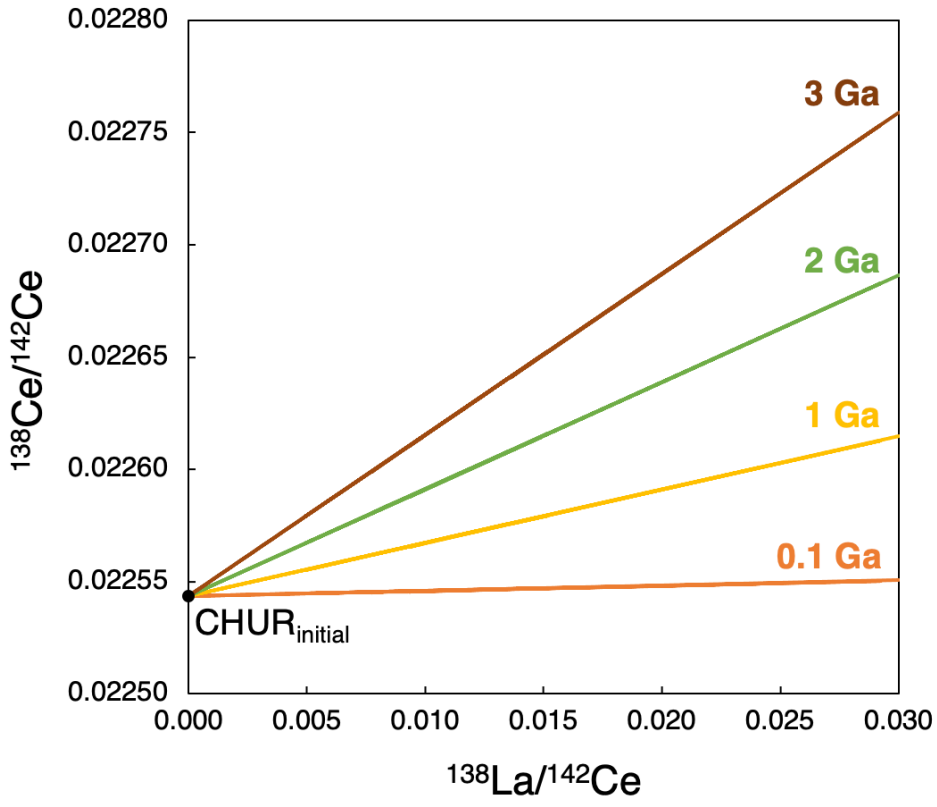

Figure 6.2. Theoretical La-Ce isochrons calculated for several different ages (0.1, 1, 2 and 3 Ga). The evolution of the $^{138}Ce/^{142}Ce$ ratio depends on the age and the $^{138}La/^{142}Ce$ fractionation, the older the samples and the higher the $^{138}La/^{142}Ce$ ratio, the more the $^{138}Ce/^{142}Ce$ ratio becomes radiogenic.

Cerium has 4 stable isotopes (136, 138, 140 and 142) with very contrasted abundances: ^{136}Ce = 0.185%; ^{138}Ce = 0.251%; ^{140}Ce = 88.45%; ^{142}Ce = 11.114% (Lide et al., 2009). Therefore, the high abundance of ^{140}Ce, about 400 times more abundant than the isotopes ^{136}Ce and ^{138}Ce, renders Ce isotopic analysis particularly challenging. In addition, the $^{138}Ce/^{142}Ce$ ratio is readily affected by isobaric interferences on the mass 138 by isotopes of barium and lanthanum that are significantly more abundant in nature than ^{138}Ce. The isotopic mass 142 is additionally prone to interferences from neodymium (Fig. 6.3). Moreover, the isotopic abundances of Ce being so disparate, ^{136}Ce and ^{138}Ce may be affected by peak tailing effects from the strong signal on mass ^{140}Ce during measurement. As a result, a highly efficient chemical separation between Ce and isobaric interfering elements is essential, and additional Ce isotope-specific analytical and instrumental approaches must be adopted, as detailed in Chapter 3.

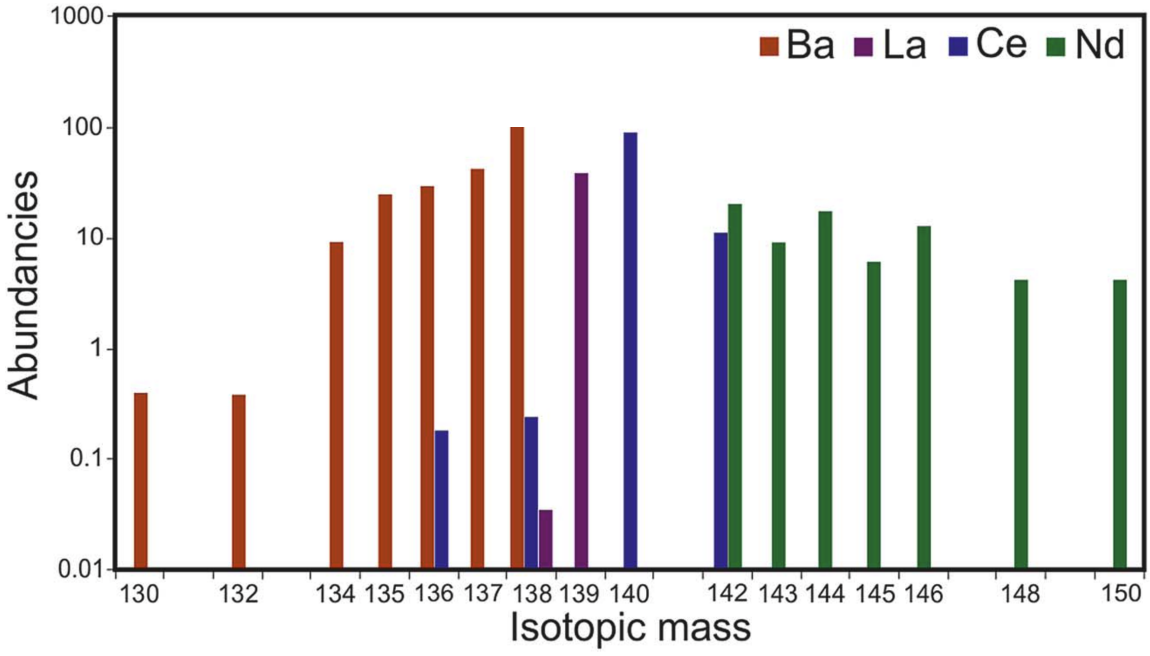

Figure 6.3. Relative isotopic abundances of Ba, La, Ce and Nd normalized to elemental abundances from the primitive mantle (Bonnand et al., 2019).

Although $^{138}Ce/^{142}Ce$ variations are very small in nature and their measurement requires extreme precision, this system is nonetheless very promising for determining the closure age of the La-Ce system and thus the age of generation of Ce anomalies generated by redox processes. Hayashi et al. (2004) were the first to attempt to deduce the origin of negative cerium anomalies and constrain their age of formation in ancient sedimentary rocks using La-Ce isotope systematics. The calculated initial Ce isotopic ratios in samples from the 3.3 Fig Tree and 3.2 Ga Moodies Groups of the Barberton Greenstone Belt, South Africa, indicated that the Ce anomalies could not be primary. Using two different models, they deduced that these negative cerium anomalies appeared during episodes of alteration that took place sometime in the past 1.1 Ga. Recently, Bonnand et al. (2020) constrained the timing of Ce anomalies in 3.22 Ga BIFs from the Moodies Group to the last 100 million years with the La-Ce geochronometer, generating an isochron of 60 ±32 Ma that unquestionably confirms that these anomalies are secondary artefacts of Phanerozoic surface alteration.

Crucially, there exists no proxy evidence at present for the photosynthetic production of O_2 prior to 2.5 Ga that has been confirmed as syndepositional in origin using a radiometric geochronological approach. For this study, we examined multiple carbonate platforms in the Northwest Superior Province (see Chapter 2 for geological context) that all contain geochemical indications of Archean photosynthetic O_2 production in the form of significant negative Ce anomalies (see Chapter 5). Fresh carbonate samples from the 2.93 Ga Red Lake Greenstone Belt (Hofmann, 1985; Corfu and Wallace, 1986; McIntyre and Fralick, 2017), 2.86 Ga Woman Lake Greenstone Belt (Hofmann, 1985; Ramsay et al., 2020), and 2.80 Ga Steep Rock Group (Riding et al., 2014; Fralick and Riding, 2015) were collected in the field from short NQ-size backpack drill cores (Red Lake, Woman Lake) or

from outcrop samples of recent quarry exposures (Steep Rock) and analyzed for their trace element and Ce isotope compositions. All three sites also show unambiguous fossil evidence for photosynthetic bacterial construction by the abundant carbonate microbialites they preserve. Dominated by stromatolitic dolostones, microbialitic and aragonite crystal fan limestones, and associated clastic and chemical sediments (see Chapter 2), these little-explored northern Canadian fossilized microbial ecosystems are at the heart of a trend of increasing thickness in Earth's known sedimentary carbonate deposits through the Paleo- and Meso-archean. Surface exposures often show glacial striations as they were recently exposed to the surface after the last glacial maxima ca. 20 Ka, and thus are excellent targets for Precambrian paleoredox investigation as they have experienced minimal modern surface weathering.

As discussed in Chapter 5, rare earth element (REE) data from all three sites show clear evidence of oxidative processing of cerium (Ce), whereby oxidation of Ce(III) to Ce(IV) under mildly oxidizing conditions, and enhanced particle scavenging of Ce(IV) to organic and mineral surfaces (Bau, 1999). These processes generate characteristic positive and negative anomalies in shale-normalized REE spectra in marine sediments (Bau and Dulski, 1996; Bolhar et al., 2004). This long-studied (e.g., Elderfield and Greaves, 1982; Hoyle et al., 1984; Murphy and Dymond, 1984) and well-understood (German and Elderfield, 1990; Tostevin et al., 2016) redox proxy has been shown to effectively track progressive ocean oxygenation from the Neoproterozoic through the Phanerozoic (Wallace et al., 2017). Post-Archean Australian Shale (PAAS)-normalized REE data for weak leaches of highly pure carbonate samples from all three sites confirm their marine origins via characteristic anomalies in La, Gd, Y/Ho, as well as heavy REE (HREE) enrichment, as well as their open-ocean connection via the presence of Eu anomalies characteristic of

Archean hydrothermally influenced basinal waters. Importantly, samples from all three sites show variable degrees of Ce depletion or enrichment. From a larger REE dataset generated using similar techniques in Brest by multiple collaborators of the ERC StG EARTHBLOOM project (Afroz, 2019; Ramsay, 2020; Wilmeth et al., 2021), a subset of samples was selected for La-Ce isotope analysis. The samples of this subset were selected to generate a maximum range in La/Ce (which inherently includes those samples showing the most significant Ce anomalies) as well as consistent spacing in their La/Ce values, minimal concentrations in detrital-sourced elements such as Al and Ti, and more arbitrarily, on the basis of a visual and numeric assessment of their REE spectral features (e.g., non-flat slopes and clear seawater indicators). Ce/Ce* values in this subset, as calculated using the geometric projection from Pr and Nd according to (Lawrence et al., 2006), range from 0.79 to 1.02 for Red Lake, 0.46 to 0.74 for Woman Lake, and 0.38 to 0.84 for Steep Rock. These anomalies are comparable in magnitude to those found in modern oxygenated seawater (mean Ce/Ce* of 0.36 above 400 m depth as compiled by Wallace et al., 2017) and are some of the largest yet described for Precambrian sediments. See Chapter 5 for a more detailed examination of their REE systematics.

6.2 Methods

See Chapter 3, section 3.2 for trace elements and section 3.5 for Ce isotopes. All uncertainties are provided as 2σ.

6.3 Results and discussion

6.3.1 Variations in La/Ce

The $^{138}Ce/^{142}Ce$ ratios of natural materials show only small variations over time and the largest possible dispersion in $^{138}La/^{142}Ce$ values offers the highest possible precision when evaluating the closure age of the La-Ce system. Figure 6.4 shows the distribution of $^{138}La/^{142}Ce$ ratios in Archean, Proterozoic and Phanerozoic carbonates, as calculated from carbonate REE data compiled by Rigoussen (2017) in comparison with carbonates from the three sites examined in this study.

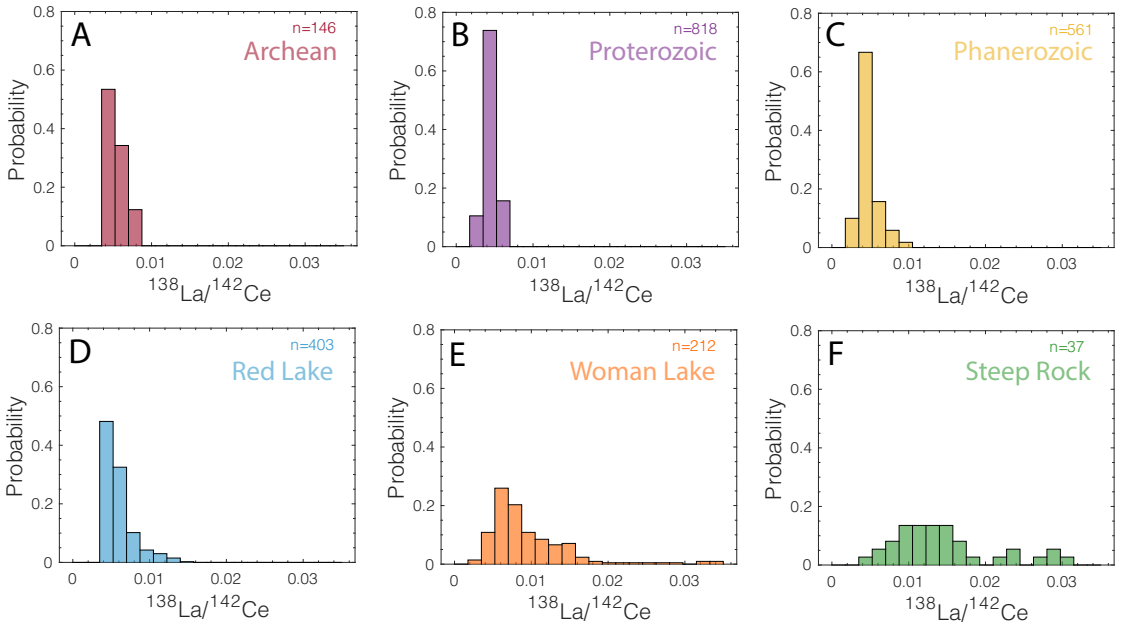

Figure 6.4. Histograms showing the distribution of $^{138}La/^{142}Ce$ ratios from Archean (A), Proterozoic (B) and Phanerozoic (C) carbonates as compiled by Rigoussen (2017) as well as available data from the Red Lake (D), Woman Lake (E) and Steep Rock (F) carbonates.

Compiled data for Archean carbonates show $^{138}La/^{142}Ce$ values between 0.003 and 0.009, with 55% falling in the 0.0035 to 0.0053 bin. Proterozoic carbonates range from 0.002 to 0.007, with 75% of the values falling in the same ~ 0.004 bin. Phanerozoic carbonates have values between 0.002 and 0.010, with over 65% of the values in the ~

0.004 bin. By contrast, the Red Lake carbonates have a range of $^{138}La/^{142}Ce$ values from 0.003 to 0.015 with about 50% of the values in the ~ 0.004 bin. At Woman Lake, values range from 0.002 to 0.034, with the majority of values falling between 0.006 and 0.010. The Steep Rock carbonates show $^{138}La/^{142}Ce$ values between 0.004 and 0.032, with a more even spread of values over the range of the data.

Comparing all of these data, it's immediately apparent that the carbonates from this study (which includes both new data from this thesis as well as other workers on the EARTHBLOOM project, see above) have a much wider range in $^{138}La/^{142}Ce$ than the data in literature, regardless of age. This can be explained by a combination of several factors. First, the carbonates from Red Lake, Woman Lake and Steep Rock are all chemically very pure, and perhaps rather uniquely so; Archean carbonates tend to show evidence of high degrees of carbonate supersaturation and textural evidence of predominately chemical growth modes, such as abundant giant aragonite crystal fans and stromatolites with textures consistent with in-situ chemical sediment encrustation, as opposed to later Proterozoic and Phanerozoic carbonates where such evidence is more rare and stromatolites show a more important role for grain trapping and binding (Grotzinger, 1989). Second, the carbonates examined in this study were digested by a weak leach technique (5% Acetic acid; Rongemaille et al., 2011), which favors the recovery of uncontaminated seawater signatures by avoiding the digestion of clays which tend to flatten the resulting REE spectra and thus attenuate authigenic seawater signatures. While such weak leach methods are slowly enjoying greater adoption by the scientific community, most carbonate REE data in existing literature was obtained via diverse, more aggressive digestions, often total digestion that practically ensures clay dissolution and thus important contamination of authigenic seawater signatures. Finally, the Red Lake, Woman Lake, and Steep Rock

carbonate platforms all preserve a wide range of depositional environments, representing both shallow and deep waters, which also contributes to the diversity of values (see Chapter 5). A closer look at La/Ce fractionation at the three study sites and its relation to La and Ce anomalies (Fig. 6.5) reveals that the La/Ce fractionation is controlled by the different specific behaviors of La and Ce.

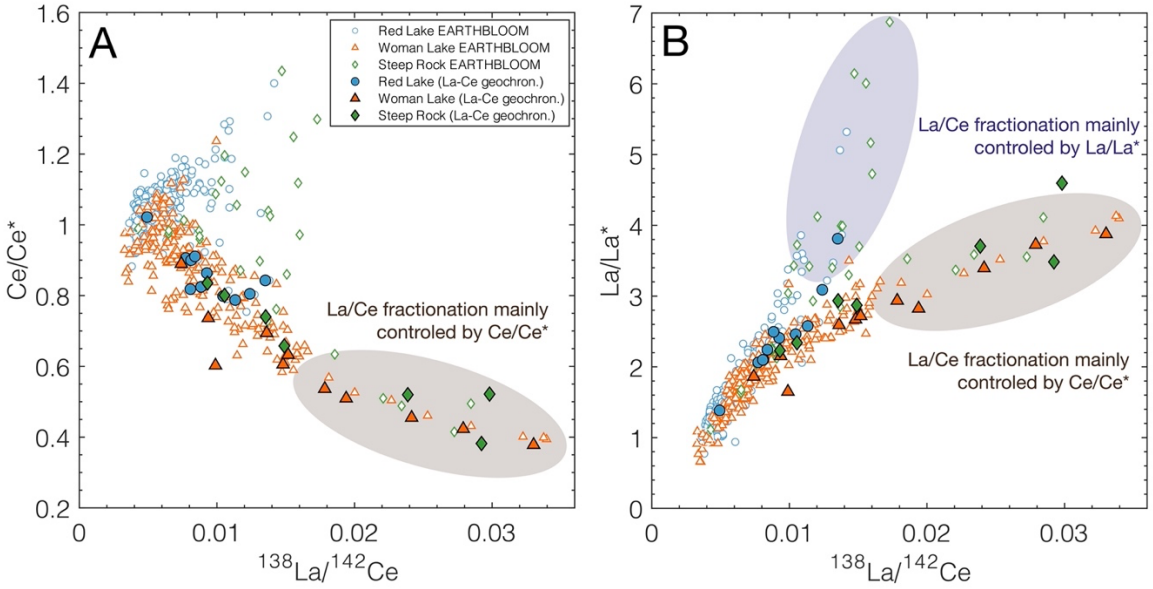

Figure 6.5. Graph showing the controlling factors of the La/Ce fractionation which are the behaviors of Ce and La.

Indeed, as expected, $^{138}La/^{142}Ce$ ratios increase rapidly with increasing magnitude of the negative Ce anomaly (Fig. 6.5-A), and the largest negative Ce anomalies correspond to the highest $^{138}La/^{142}Ce$ values (up to 0.034). Also as expected, in the absence of Ce anomalies, La/Ce ratios do not increase as rapidly with increases in the La anomaly alone (Fig. 6.5-B), as the highest values of La/La*, i.e., La/La*>4.5, have La/Ce ratios that do not exceed 0.018. The behavior of Ce and its ability to form strong anomalies is thus the main factor controlling the fractionation of La and Ce. However, these figures also demonstrate that variations in La/La* alone should be sufficient to enable La-Ce geochronology for sedimentary samples that do not show appreciable Ce anomalies (see Chapter 7) – in which case the La-Ce system is analogous to high-temperature applications.

6.3.2 La-Ce isotope compositions

Plotting the $^{138}La/^{142}Ce$ vs. $^{138}Ce/^{142}Ce$ isotope compositions determined for the three Mesoarchean carbonate platforms for a global look at the combined data from the three sites is highly revealing (Fig. 6.6). Compared to the theoretical isochrons for 0.1 Ga, 1 Ga, 2 Ga and 3 Ga, the data acquired in this thesis clearly demonstrates that the negative Ce anomalies must be very ancient.

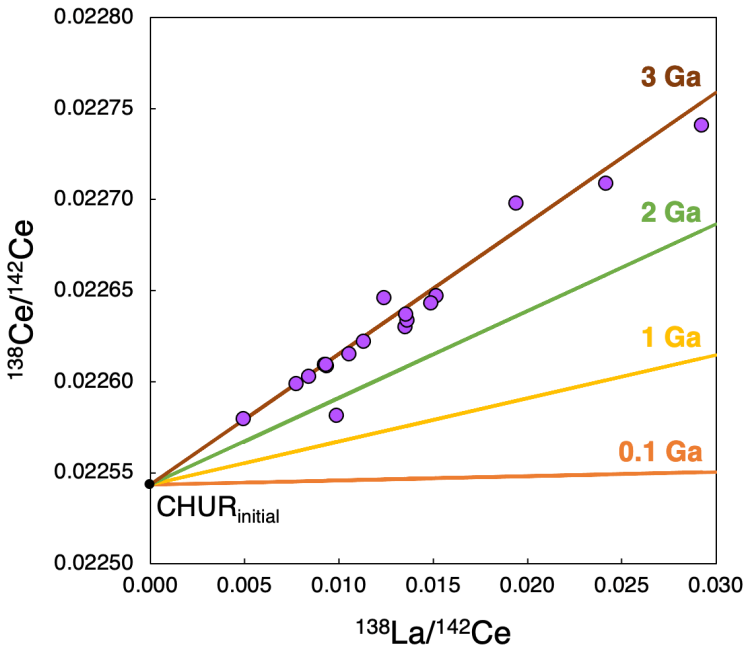

Figure 6.6. Plot of $^{138}Ce/^{142}Ce$ vs. $^{138}La/^{142}Ce$ for the combined dataset (purple circle) from the three study sites (Red Lake, Woman Lake and Steep Rock) superposed on the theoretical La-Ce isochrons calculated for several different ages (0.1, 1, 2 and 3 Ga).

The 18 samples analyzed across the three sites combined have $^{138}La/^{142}Ce$ ratios ranging from 0.005 to 0.029 and $^{138}Ce/^{142}Ce$ ratios ranging from 0.0225796 to 0.0227408. They clearly align with the 3 Ga isochron. These 18 values form a slope of 0.00742 ± 0.00011 with a corresponding age of 3.10 ± 0.05 Ga, an MSWD = 64 and an $\varepsilon^{138}Ce_{initial}$ = -2.78 ± 0.12. When 4 outliers are removed (see below for a discussion on outliers), the remaining 14 values form a slope of 0.00666 ± 0.00010 with a corresponding age of 2.78

± 0.04 Ga, an MSWD = 1.5, and an $\varepsilon^{138}Ce_{initial}$ = 0.56 ± 0.12. This significantly more coherent subset points to an initial $^{138}Ce/^{142}Ce$ that is close to that of CHUR, as expected for a crustal REE source ca. 3 Ga. In the rest of this section only these 14 datapoints are considered; see section 6.3.3 for discussion of the four outlier samples and possible processes driving La-Ce perturbation.

The data from the three different sites form three individual isochrons (Fig. 6.7). The coherent Red Lake samples form a slope of 0.00668 ± 0.00051 with a corresponding age of 2.79 ± 0.21 Ga, a MSWD of 0.19, and an $\varepsilon^{138}Ce_{initial}$ = 0.86 ± 0.12 (Fig. 6.7-A). The Woman Lake samples (without outliers, n=4) form a slope of 0.00686 ± 0.00023 with a corresponding age of 2.87 ± 0.10 Ga, an MSWD of 2.7 and $\varepsilon^{138}Ce_{initial}$ = -0.76 ± 0.12 (Fig. 6.7-B). The Steep Rock samples (n=5) form a slope of 0.00666 ± 0.00015 with a corresponding age of 2.78 ± 0.06 Ga, an MSWD of 2, and $\varepsilon^{138}Ce_{initial}$ = 0.34 ± 0.12. All uncertainties are based on global external errors determined for $^{138}Ce/^{142}Ce$ by repeat analyses of the Ce isotope standard Ce-LMV across all TIMS analytical sessions (2σ = 0.000000144, or 6.37 ppm; n=11), and for $^{138}La/^{142}Ce$ by the highest dispersion obtained between duplicates of weak leach digests of the international geostandard JDo-1 measured across all three HR-ICP-MS analytical sessions (2σ = 0.000358; worst of three duplicate analyses across three sessions).

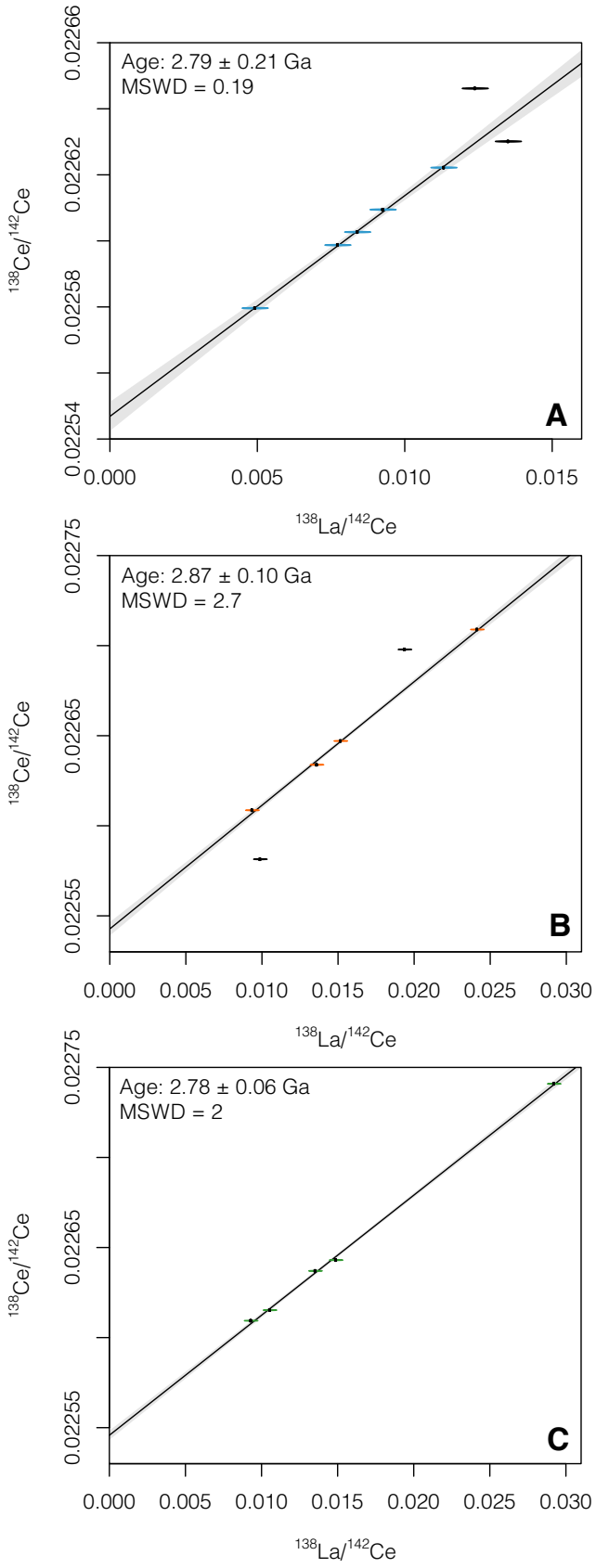

Figure 6.7. La-Ce isochrons and corresponding La-Ce ages for carbonate sample sets showing important Ce anomalies from the (A) Red Lake, (B) Woman Lake, and (C) Steep Rock Mesoarchean carbonate platforms. These ages all fall within error of their respective depositional ages as constrained by zircon U-Pb geochronology (2.93, 2.86, and 2.80 Ga, c.f. chapter 2).

MSWD values of 0.19, 2.7, and 2 for the isochrons from Red Lake, Woman Lake, and Steep Rock, respectively, all meet the criteria for true isochrons considering the F values corresponding to the number of points on the respective isochrons and the number of standard duplicates employed for the global estimation of uncertainties (c.f. Brooks et al., 1972 and Appendix 3 therein). That said, the MSWD value significantly lower than 1 obtained for the Red Lake data indicates that the global analytical uncertainties may be overestimated for these analyses. If this were globally true, and the analytical uncertainties globally overestimated based on the most dispersed repeat analyses of JDo-1 across the various independent sessions, then the true MSWD would be higher for the Woman Lake and Steep Rock isochrons. Above MSWD values of ~3 to 6, according to the tables of Brooks et al. (1972), this would indicate that true dispersion exists in the distribution of $^{138}La/^{142}Ce$ and $^{138}Ce/^{142}Ce$, which would be presumably the result of metamorphic and surface alteration processes affecting $^{138}La/^{142}Ce$ and/or $^{138}Ce/^{142}Ce$ ratios. This may not be unexpected considering that the Red Lake samples experienced upper greenschist to lower amphibolite facies metamorphism, the Woman Lake samples lower to middle Greenschist metamorphism, and the Steep Rock Lake samples experienced lower Greenschist metamorphism (see Chapter 2). The 2σ errors on the isochron ages indeed increase with increasing metamorphic grade. The identification of 4 clear outliers in the combined dataset further suggests that caution is warranted with respect to potential resetting of the La-Ce isotopic system at higher metamorphic grades.

Despite the occurrence of four clear outliers out of 18 analyzed samples, as well as dispersions in the outlier-free isochrons that increase with increasing metamorphic grade, approaching the statistical distinction between strictly isochron behavior and true geological dispersion within identified (and possibly overestimated) analytical

uncertainties, a Mesoarchean origin for the negative Ce anomalies observed in these Mesoarchean carbonate platforms is abundantly clear. All three sites demonstrate with a high statistical certainty (>95%) that the negative Ce anomalies at Red Lake, Woman Lake, and Steep Rock were all formed during the Archean, within error of their independently determined depositional ages (Fig. 6.8 ;see also Chapter 2), and well before the GOE ca. 2.5 to 2.3 Ga. They thus represent primary paleoenvironmental signals of ancient seawater, and as discussed below, constitute highly robust evidence for the production of free oxygen in the marine water column between 2.80 and 2.94 Ga. Before addressing the implications of the most well-preserved samples in section 6.3.4, it is worthwhile to further examine the identified outliers in light of potential mechanisms of perturbation of the La-Ce isotope system.

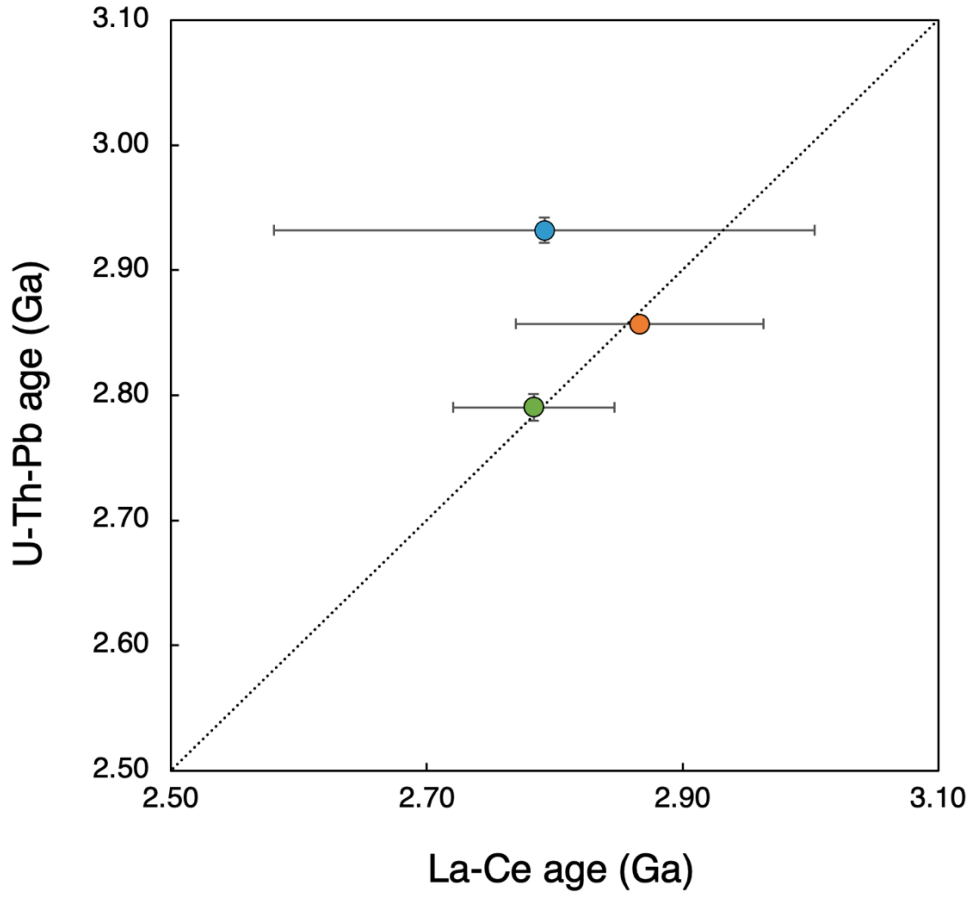

Figure 6.8. Plot of U-Th-Pb age vs. La-Ce age showing that the negative Ce anomalies at Red Lake (blue), Woman Lake (orange), and Steep Rock (green) were all formed during the Archean, within error of their independently determined depositional ages.

6.3.3 Perturbations of the La-Ce system: potential mechanisms and trajectories

Two out of the three sites, namely Red Lake and Woman Lake, show clear outliers (two each) which invite further investigation of the robustness of the La-Ce system and an examination of possible perturbation mechanisms. A variety of later alteration events, such as the addition of external REE from crustal sources, the internal redistribution of REE between different mineral phases, the exchange of REE with metamorphic fluids, and the mobilization of REE to and from infiltrating marine and meteoric waters, could conceivably fractionate La from Ce after deposition by the addition or removal of either La, Ce or both.

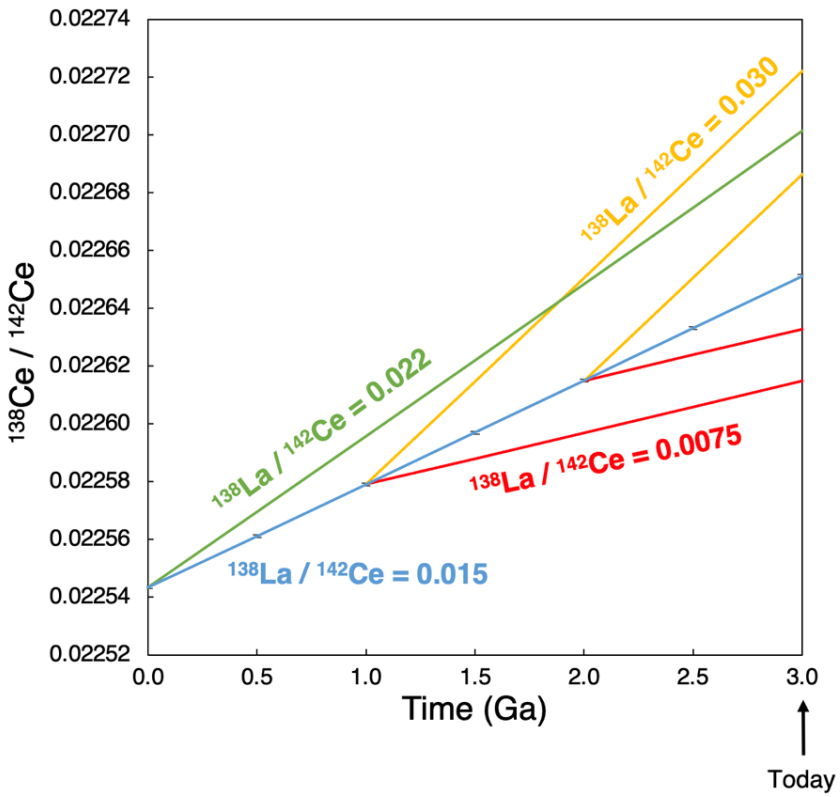

Figure 6.9. Evolution of $^{138}Ce/^{142}Ce$ ratios as a function of time for different perturbation scenarios in the $^{138}La/^{142}Ce$ – $^{138}Ce/^{142}Ce$ system. In green and blue, two unperturbed $^{138}Ce/^{142}Ce$ evolution scenarios with $^{138}La/^{142}Ce$ equal to 0.015 and 0.22, respectively. In red and yellow are $^{138}Ce/^{142}Ce$ evolutionary trajectories for post-depositional perturbations in La/Ce from the arbitrary blue reference line of $^{138}La/^{142}Ce = 0.015$. The red lines represent perturbations that reduce in half the $^{138}La/^{142}Ce$ ratio (to 0.0075) at 1 Ga and 2 Ga after deposition, while the yellow trajectories trace perturbations that double the $^{138}Ce/^{142}Ce$ ratio (to 0.030) at 1 Ga and 2 Ga after deposition.

Figure 6.9 demonstrates how different perturbations of the La/Ce ratio, occurring at different times after deposition, affects the evolution of $^{138}Ce/^{142}Ce$ ratios in time. This figure re-illustrates classic perturbation trajectories for radiogenic isotope systems, very simply adapted here to the La-Ce system. It indicates schematically how later additions of La, or the later emplacement of negative anomalies in Ce, drives $^{138}Ce/^{142}Ce$ ratios to higher values than expected for unperturbed samples. The earlier the perturbation, the more important the effect on $^{138}Ce/^{142}Ce$. Given enough time, a large enough increase in the La/Ce ratio may drive the $^{138}Ce/^{142}Ce$ ratio to surpass that of unperturbed samples that began their evolution at a higher La/Ce ratio than the pre-perturbed sample (c.f. the unperturbed trajectory in green for $^{138}La/^{142}Ce = 0.022$ *vs.* in yellow the perturbation from 0.015 to 0.030 1 Ga after deposition). Conversely, the loss of La, or addition of Ce, lowers La/Ce and leads to trajectories that yield lower $^{138}Ce/^{142}Ce$ ratios than expected in light of the true initial La/Ce ratio (trajectories in red). The addition of REE in near-crustal proportions resembles this category, as it acts to pull the $^{138}La/^{142}Ce$ ratio towards the CHUR value of ~0.004, which is significantly lower than nearly all samples analyzed in this study.

Such alteration processes can readily explain the four outliers in this new dataset, and they may also be responsible for the isochron dispersions (as measured by the MSWD term) that in two out of three cases approach the limits of those expected given the estimated analytical uncertainties. The four identified outliers, two for Red Lake and two for Woman Lake, each falling above and below the 3 Ga isochrons, can be explained by two simple perturbation trajectories. Figure 6.10-A shows the theoretical evolution of $^{138}La/^{142}Ce$ in time; Trajectories A and C represent the evolution of $^{138}Ce/^{142}Ce$ for two different La/Ce ratios that experienced modern perturbation to higher and lower La/Ce

ratios, respectively. Trajectory B represents a late enrichment in La, or more geologically plausible, a late depletion in Ce. Trajectory D represents the opposite – a depletion in La, or an enrichment in Ce (again more geologically plausible), sometime after deposition. Trajectory E represents an unperturbed evolution of the $^{138}Ce/^{142}Ce$ ratio over time for a fairly high $^{138}La/^{142}Ce$ ratio. Figure 6.10-B shows the trajectories of these same $^{138}La/^{142}Ce$ perturbation scenarios in a $^{138}La/^{142}Ce$ vs. $^{138}Ce/^{142}Ce$ plot. These diagrams illustrate schematically how small perturbations in the La/Ce ratio at various times in the post-depositional history may readily account for the outliers observed in this La-Ce isotope dataset.

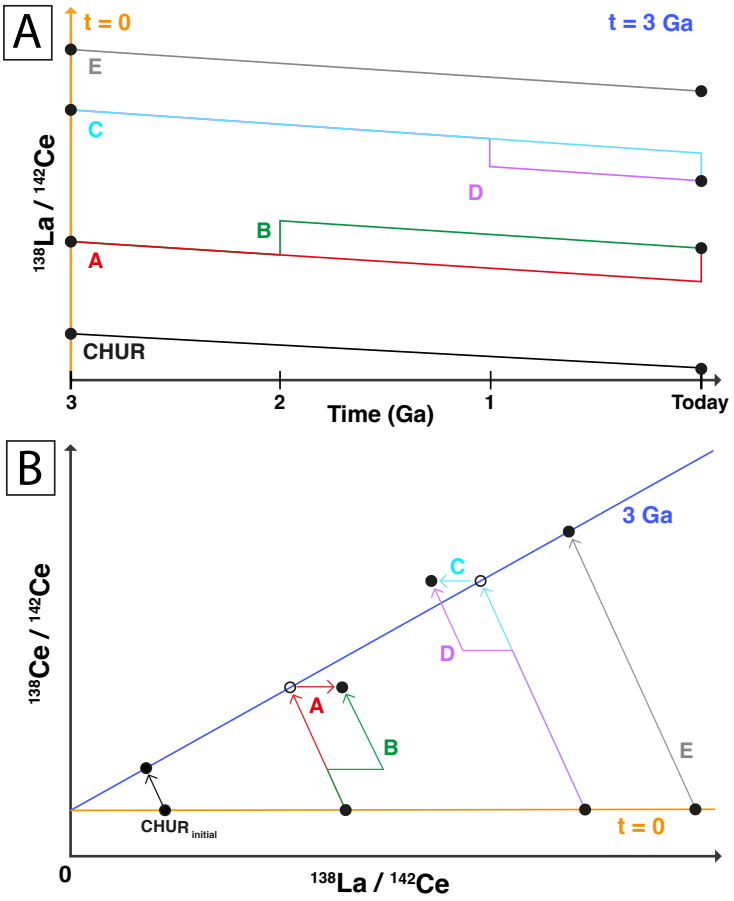

Figure 6.10. Perturbation models showing different scenarios of alteration of the La/Ce ratio (A) and corresponding trajectories on a $^{138}La/^{142}Ce$ vs. $^{138}Ce/^{142}Ce$ plot (B). These two diagrams demonstrate plausible trajectories of two different hypothetical perturbation events that readily explain the outliers identified in this study. CHUR: evolution of material of chondritic composition, approximating the bulk silicate Earth; A and B: perturbation involving an increase in La/Ce, i.e., late La addition or Ce depletion, 1 Ga after deposition in the case of B, and a modern increase in the case of A; C and D: perturbation involving a decrease in La/Ce, i.e., late La depletion or Ce addition, in the case of D 2 Ga after deposition and in the case of C, a modern decrease; E: unperturbed evolution of materials of progressively higher La/Ce ratios.

6.3.4 Oxygenic photosynthesis in the Archean confirmed by La-Ce geochronology

The only process known to generate such large Ce anomalies is the oxidation of Ce(III) to Ce(IV). The oxidation of Ce in aqueous solution occurs at a redox potential close to the Mn(II)/Mn(IV) couple, but appears highly sensitive on the presence of diverse ligands, and is significantly lowered in the presence of Mn oxides where oxidation is surface-catalyzed (de Carlo et al., 1997). Even in modern oxygenated seawater, oxidation is rarely complete (German et al., 1991). Ce oxidation is limited by kinetic factors; under high-pH conditions such as in alkaline lakes, Ce oxidation is significantly accelerated (Möller and Bau, 1993) whereas at circumneutral pH such as in rivers and seawater, oxidation is slow, and largely driven by Mn oxide mineral surface catalysis surfaces (Bau, 1991). Indeed, rivers today transport largely Ce(III) and generally lack significant Ce anomalies except at unusually high pH (Goldstein and Jacobsen, 1988). Upon oxidation, the resulting Ce(IV) is less soluble than its neighbors and rapidly scavenged from solution by surface adsorption onto sinking organic matter, clays, and Fe- and Mn-oxides.

To generate appreciable Ce anomalies in natural waters, several criteria must be met. Physically, particulates bearing surface adsorbed Ce(IV) must be isolated from their formation waters in order for the latter to develop an anomaly in the residual aqueous phase; efficient remineralization of potential Ce(IV) carriers (organic matter, Mn and Fe oxyhydroxides) in shallow water settings such as estuaries prevents efficient sequestration of Ce(IV) from Ce(III). Furthermore, Ce(IV) oxidation rates are generally slow compared to Ce(III) scavenging rates in shallow-water marine environments, and only in waters poor in settling particular matter does the Ce(IV) oxidation rate become important relative to the

rate of Ce(III) removal, also by adsorption (Moffett, 1990). Thus, Ce oxidation may be cryptic in shallow-water, particulate-rich environments, whereas the development of important water column Ce anomalies are favored in offshore environments with slower scavenging of trivalent REE. As discussed in Chapter 5, the observed REE systematics of the three carbonate platforms examined in this thesis are consistent with the above requirements and limitations known from modern environments on the development of water column Ce anomalies.

Chemically, several Ce(III) oxidation pathways are possible, however there are only a few that are relevant to the Precambrian. Firstly, H_2O_2 is an efficient Ce(III) oxidant, however its photochemical production in the Archean atmosphere is thought to have been insignificant relative to other potential oxidants (Pecoits et al., 2015), which are limited to O(-II), and Mn(IV) based on current knowledge. While appreciable Ce anomalies have been generated by adsorption to iron oxyhydroxides under experimental conditions (Bau et al., 2014), Archean seawater was ferruginous in nearly all settings, such that Archean seawater was likely buffered around the relatively low redox potential set by the Fe(II)/Fe(III) couple. The rock record itself further indicates that Ce oxidation by Fe(III) was negligible during the Precambrian, as banded iron formations do not show widespread and appreciable Ce anomalies until the beginning of the GOE ca. 2.5 Ga (Warchola et al., 2018).

Recent experimental work has shown that complexation of REE by organic ligands (specifically, siderophores) during experimental weathering of mafic rocks can generate appreciable Ce anomalies even under anoxic weathering conditions (Kraemer and Bau, 2022). However, only positive Ce anomalies were observed in the aqueous phase by this

mechanism, and considering the low amounts of mobilized REE in these experiments, mass balance considerations limit the potential shifts in Ce abundances in the basalts subjected to weathering. While they were not analyzed, it is highly improbable that appreciable negative Ce anomalies developed anywhere outside of a very fine altered surface layer, if at all. Such mechanisms are unlikely to drive the large magnitude Ce anomalies ($Ce/Ce^* < 0.5$) observed in the current sample set. Furthermore, they would not explain the clear trends between Ce/Ce* and a variety of paleoenvironmental (e.g., La/La, Y/Ho) and redox (Fe, Mn) indicators. This leaves oxidation by O_2 as the most likely explanation for these important and clearly ancient Ce anomalies. This explanation is also highly parsimonious in that it represents the sole mechanism by which important negative Ce anomalies are known to be generated in modern marine environments. As further explored in Chapter 7, these findings have important implications for the evolution of oxygenic photosynthesis on Earth as well as future possible applications of the La-Ce geochronometer to ancient sedimentary rocks.

6.4 Conclusion

In this chapter, the ^{138}La-^{138}Ce radiometric isotope geochronometer was applied to selected samples from three different Archean carbonate platforms preserved in greenstone belts of the NW Superior craton (Canada) that were deposited by the activity of marine photosynthetic bacteria at 2.93 Ga, 2.86 Ga, and 2.80 Ga ago. These three platforms show clear evidence of O_2 production before the GOE in the form of significant depletions in cerium (Ce) reflecting oxidative Ce removal from ancient seawater. Robust La-Ce isochrons were obtained for all three sites and with a high statistical degree of certainty for two of them, that La/Ce fractionation, and thus cerium oxidation, occurred at the time of deposition. These results firmly place the origin of oxygenic photosynthesis in the Mesoarchean, necessitating a revised view of biological and geochemical evolution on Earth.

6.5 References

Afroz, M., 2019, Sedimentology and Geochemistry of the 2.93 Ga Basinal Facies of the Red Lake Carbonate Platform: MSc diss., Lakehead University.

Albut, G., Babechuk, M.G., Kleinhanns, I.C., Benger, M., Beukes, N.J., Steinhilber, B., Smith, A.J.B., Kruger, S.J., and Schoenberg, R., 2018, Modern rather than Mesoarchaean oxidative weathering responsible for the heavy stable Cr isotopic signatures of the 2.95 Ga old Ijzermijn iron formation (South Africa): Geochimica et Cosmochimica Acta, v. 228, p. 157–189, doi:10.1016/j.gca.2018.02.034.

Albut, G., Kamber, B.S., Brüske, A., Beukes, N.J., Smith, A.J.B., and Schoenberg, R., 2019, Modern weathering in outcrop samples versus ancient paleoredox information in drill core samples from a Mesoarchaean marine oxygen oasis in Pongola Supergroup, South Africa: Geochimica et Cosmochimica Acta, v. 265, p. 330–353, doi:10.1016/j.gca.2019.09.001.

Anbar, A.D. et al., 2007, A Whiff of Oxygen Before the Great Oxidation Event? Science, v. 317, p. 1903–1906, doi:10.1126/science.1140325.

Bau, M., 1991, Rare-earth element mobility during hydrothermal and metamorphic fluid-rock interaction and the significance of the oxidation state of europium.:

Bau, M., 1999, Scavenging of dissolved yttrium and rare earths by precipitating iron oxyhydroxide: experimental evidence for Ce oxidation, Y-Ho fractionation, and lanthanide tetrad effect: Geochimica et Cosmochimica Acta, v. 63, p. 67–77, doi:10.1016/S0016-7037(99)00014-9.

Bau, M., and Dulski, P., 1996, Distribution of yttrium and rare-earth elements in the Penge and Kuruman iron-formations, Transvaal Supergroup, South Africa: Precambrian Research, v. 79, p. 37–55, doi:10.1016/0301-9268(95)00087-9.

Bau, M., Schmidt, K., Koschinsky, A., Hein, J., Kuhn, T., and Usui, A., 2014, Discriminating between different genetic types of marine ferro-manganese crusts and nodules based on rare earth elements and yttrium: Chemical Geology, v. 381, p. 1–9, doi:10.1016/j.chemgeo.2014.05.004.

Bellot, N., 2016, Application du système isotopique 138La-138Ce en contexte de subduction intra-océanique : les Petites Antilles et les Mariannes: PhD diss., Université Blaise Pascal-Clermont Ferrand II,.

Boden, J.S., Konhauser, K.O., Robbins, L.J., and Sánchez-Baracaldo, P., 2021, Timing the evolution of antioxidant enzymes in cyanobacteria: Nature Communications, v. 12, p. 4742, doi:10.1038/s41467-021-24396-y.

Bolhar, R., Kamber, B.S., Moorbath, S., Fedo, C.M., and Whitehouse, M.J., 2004, Characterisation of early Archaean chemical sediments by trace element signatures: Earth and Planetary Science Letters, v. 222, p. 43–60, doi:10.1016/j.epsl.2004.02.016.

Bonnand, P., Israel, C., Boyet, M., Doucelance, R., and Auclair, D., 2019, Radiogenic and stable Ce isotope measurements by thermal ionisation mass spectrometry: Journal of Analytical Atomic Spectrometry, v. 34, p. 504–516, doi:10.1039/c8ja00362a.

Bonnand, P., Lalonde, S. v., Boyet, M., Heubeck, C., Homann, M., Nonnotte, P., Foster, I., Konhauser, K.O., and Köhler, I., 2020, Post-depositional REE mobility in a Paleoarchean banded iron formation revealed by La-Ce geochronology: A cautionary tale for signals of ancient oxygenation: Earth and Planetary Science Letters, v. 547, doi:10.1016/j.epsl.2020.116452.

Bortoluzzi, M., and Ferraro, V., 2020, 138La as a useful isotope for gamma spectroscopy without radioactive sources: Spectroscopy Europe, www.spectroscopyeurope.com.

Brooks, C., Hart, S.R., and Wendt, I., 1972, Realistic use of two-error regression treatments as applied to rubidium-strontium data: Reviews of Geophysics, v. 10, p. 551, doi:10.1029/RG010i002p00551.

Cardona, T., Sánchez-Baracaldo, P., Rutherford, A.W., and Larkum, A.W., 2019, Early Archean origin of Photosystem II: Geobiology, v. 17, p. 127–150, doi:10.1111/gbi.12322.

de Carlo, E.H., Wen, X.-Y., and Irving, M., 1997, The Influence of Redox Reactions on the Uptake of Dissolved Ce by Suspended Fe and Mn Oxide Particles: Aquatic Geochemistry, v. 3, p. 357–389, doi:10.1023/A:1009664626181.

Corfu, F., and Wallace, H., 1986, U–Pb zircon ages for magmatism in the Red Lake greenstone belt, northwestern Ontario: Canadian Journal of Earth Sciences, v. 23, p. 27–42, doi:10.1139/e86-004.

Crowe, S.A. et al., 2014, Sulfate was a trace constituent of Archean seawater: Science, v. 346, p. 735–739, doi:10.1126/science.1258966.

Dickin, A.P., 1987, La–Ce dating of Lewisian granulites to constrain the 138La β-decay half-life: Nature, v. 325, p. 337–338, doi:10.1038/325337a0.

Eickmann, B., Hofmann, A., Wille, M., Bui, T.H., Wing, B.A., and Schoenberg, R., 2018, Isotopic evidence for oxygenated Mesoarchaean shallow oceans: Nature Geoscience, v. 11, p. 133–138, doi:10.1038/s41561-017-0036-x.

Elderfield, H., and Greaves, M.J., 1982, The rare earth elements in seawater: Nature, v. 296, p. 214–219, doi:10.1038/296214a0.

Fischer, W.W., Hemp, J., and Johnson, J.E., 2016, Evolution of Oxygenic Photosynthesis: Annual Review of Earth and Planetary Sciences, v. 44, p. 647–683, doi:10.1146/annurev-earth-060313-054810.

Fralick, P., and Riding, R., 2015, Steep Rock Lake: Sedimentology and geochemistry of an Archean carbonate platform: Earth-Science Reviews, v. 151, p. 132–175, doi:10.1016/j.earscirev.2015.10.006.

Frei, R., Crowe, S.A., Bau, M., Polat, A., Fowle, D.A., and Døssing, L.N., 2016, Oxidative elemental cycling under the low O2 Eoarchean atmosphere: Scientific Reports, v. 6, p. 21058, doi:10.1038/srep21058.

German, C.R., and Elderfield, H., 1990, Application of the Ce anomaly as a paleoredox indicator: The ground rules: Paleoceanography, v. 5, p. 823–833, doi:10.1029/PA005i005p00823.

German, C.R., Holliday, B.P., and Elderfield, H., 1991, Redox cycling of rare earth elements in the suboxic zone of the Black Sea: Geochimica et Cosmochimica Acta, v. 55, p. 3553–3558, doi:10.1016/0016-7037(91)90055-A.

Goldstein, S.J., and Jacobsen, S.B., 1988, Rare earth elements in river waters: Earth and Planetary Science Letters, v. 89, p. 35–47, doi:10.1016/0012-821X(88)90031-3.

Grotzinger, J.P., 1989, Facies and evolution of Precambrian carbonate depositional systems: emergence of the modern platform Archetype, *in* Controls on Carbonate Platforms and Basin Development, SEPM (Society for Sedimentary Geology), p. 79–106, doi:10.2110/pec.89.44.0079.

Hayashi, T., Tanimizu, M., and Tanaka, T., 2004, Origin of negative Ce anomalies in Barberton sedimentary rocks, deduced from La-Ce and Sm-Nd isotope systematics, *in* Precambrian Research, Elsevier B.V., v. 135, p. 345–357, doi:10.1016/j.precamres.2004.09.004.

Hoashi, M., Bevacqua, D.C., Otake, T., Watanabe, Y., Hickman, A.H., Utsunomiya, S., and Ohmoto, H., 2009, Primary haematite formation in an oxygenated sea 3.46 billion years ago: Nature Geoscience, v. 2, p. 301–306, doi:10.1038/ngeo465.

Hofmann, H.J., 1985, Archean Stromatolites from Uchi Greenstone Belt, Northwestern Ontario: Geological Association of Canada Special Paper.

Hoyle, J., Elderfield, H., Gledhill, A., and Greaves, M., 1984, The behaviour of the rare earth elements during mixing of river and sea waters: Geochimica et Cosmochimica Acta, v. 48, p. 143–149, doi:10.1016/0016-7037(84)90356-9.

Israel, C., Boyet, M., Doucelance, R., Bonnand, P., Frossard, P., Auclair, D., and Bouvier, A., 2020, Formation of the Ce-Nd mantle array: Crustal extraction vs. recycling by subduction: Earth and Planetary Science Letters, v. 530, doi:10.1016/j.epsl.2019.115941.

Kendall, B., Creaser, R.A., Reinhard, C.T., Lyons, T.W., and Anbar, A.D., 2015, Transient episodes of mild environmental oxygenation and oxidative continental weathering during the late Archean: Science Advances, v. 1, doi:10.1126/sciadv.1500777.

Lalonde, S. v., and Konhauser, K.O., 2015, Benthic perspective on Earth's oldest evidence for oxygenic photosynthesis: Proceedings of the National Academy of Sciences of the United States of America, v. 112, p. 995–1000, doi:10.1073/pnas.1415718112.

Lawrence, M.G., Greig, A., Collerson, K.D., and Kamber, B.S., 2006, Rare earth element and yttrium variability in South East Queensland waterways: Aquatic Geochemistry, v. 12, p. 39–72, doi:10.1007/s10498-005-4471-8.

Li, W., Johnson, C.M., and Beard, B.L., 2012, U–Th–Pb isotope data indicate phanerozoic age for oxidation of the 3.4Ga Apex Basalt: Earth and Planetary Science Letters, v. 319–320, p. 197–206, doi:10.1016/j.epsl.2011.12.035.

Lide, D.R., Baysinger, G., Berger, L.I., Goldberg, R.N., Kehiaian, H. v, Kuchitsu, K., Roth, D.L., and Zwillinger, D., 2009, CRC Handbook of Chemistry and Physics Editor-in-Chief.:

McIntyre, T., and Fralick, P., 2017, Sedimentology and Geochemistry of the 2930 Ma Red Lake-Wallace Lake Carbonate Platform, Western Superior Province, Canada: The Depositional Record, v. 3, p. 258–287, doi:10.1002/dep2.36.

Moffett, J.W., 1990, Microbially mediated cerium oxidation in sea water: Nature, v. 345, p. 421–423, doi:10.1038/345421a0.

Möller, P., and Bau, M., 1993, Rare-earth patterns with positive cerium anomaly in alkaline waters from Lake Van, Turkey: Earth and Planetary Science Letters, v. 117, p. 671–676, doi:10.1016/0012-821X(93)90110-U.

Murphy, K., and Dymond, J., 1984, Rare earth element fluxes and geochemical budget in the eastern equatorial Pacific: Nature, v. 307, p. 444–447, doi:10.1038/307444a0.

Oliver, T., Sánchez-Baracaldo, P., Larkum, A.W., Rutherford, A.W., and Cardona, T., 2021, Time-resolved comparative molecular evolution of oxygenic photosynthesis: Biochimica et Biophysica Acta (BBA) - Bioenergetics, v. 1862, p. 148400, doi:10.1016/j.bbabio.2021.148400.

Olson, S.L., Kump, L.R., and Kasting, J.F., 2013, Quantifying the areal extent and dissolved oxygen concentrations of Archean oxygen oases: Chemical Geology, v. 362, p. 35–43, doi:10.1016/j.chemgeo.2013.08.012.

Pecoits, E., Smith, M.L., Catling, D.C., Philippot, P., Kappler, A., and Konhauser, K.O., 2015, Atmospheric hydrogen peroxide and Eoarchean iron formations: Geobiology, v. 13, p. 1–14, doi:10.1111/gbi.12116.

Planavsky, N.J. et al., 2014, Evidence for oxygenic photosynthesis half a billion years before the Great Oxidation Event: Nature Geoscience, v. 7, p. 283–286, doi:10.1038/ngeo2122.

Planavsky, N.J., Robbins, L.J., Kamber, B.S., and Schoenberg, R., 2020, Weathering, alteration and reconstructing Earth's oxygenation: Interface Focus, v. 10, p. 20190140, doi:10.1098/rsfs.2019.0140.

Ramsay, B., 2020, Environmental Control of Seawater Geochemistry in a Mesoarchean Peritidal System, Woman Lake, Superior Province: MSc diss., Lakehead University.

Ramsay, B., Fralick, P., Bielski, P., Patry, L.A., Sanjofre, P., and Lalonde, S.V., 2020, Facies Control on Geochemistry of the Mesoarchean Carbonate Platform at Woman Lake (Canada): Goldschmidt abstract.

Riding, R., Fralick, P., and Liang, L., 2014, Identification of an Archean marine oxygen oasis: Precambrian Research, v. 251, p. 232–237, doi:10.1016/j.precamres.2014.06.017.

Rigoussen, D., 2017, Carbonate geochemistry, new redox tracer analyses through the Precambrian: Msc 2 diss., Université de Bretagne Occidentale (UBO).

Robbins, L.J. et al., 2016, Trace elements at the intersection of marine biological and geochemical evolution: Earth-Science Reviews, v. 163, p. 323–348, doi:10.1016/j.earscirev.2016.10.013.

Rongemaille, E., Bayon, G., Pierre, C., Bollinger, C., Chu, N.C., Fouquet, Y., Riboulot, V., and Voisset, M., 2011, Rare earth elements in cold seep carbonates from the Niger delta: Chemical Geology, v. 286, p. 196–206, doi:10.1016/j.chemgeo.2011.05.001.

Rosing, M.T., and Frei, R., 2004, U-rich Archaean sea-floor sediments from Greenland – indications of >3700 Ma oxygenic photosynthesis: Earth and Planetary Science Letters, v. 217, p. 237–244, doi:10.1016/S0012-821X(03)00609-5.

Schnabel, C., 2019, 138La-138Ce systematics in terrestrial samples and chondrites: PhD diss., Universität zu Köln.

Slotznick, S.P., Johnson, J.E., Rasmussen, B., Raub, T.D., Webb, S.M., Zi, J.-W., Kirschvink, J.L., and Fischer, W.W., 2022, Reexamination of 2.5-Ga "whiff" of oxygen interval points to anoxic ocean before GOE: Science Advances, v. 8, doi:10.1126/sciadv.abj7190.

Sonzogni, A.A., 2003, Nuclear Data Sheets for A = 138: Nuclear Data Sheets, v. 98, p. 515–664, doi:10.1006/ndsh.2003.0004.

Tanaka, T., and Masuda, A., 1982, The La–Ce geochronometer: a new dating method: Nature, v. 300, p. 515–518, doi:10.1038/300515a0.

Tanimizu, M., and Tanaka, T., 2002, Coupled Ce–Nd isotope systematics and rare earth elements differentiation of the moon: Geochimica et Cosmochimica Acta, v. 66, p. 4007–4014, doi:10.1016/S0016-7037(02)00961-4.

Thoby, M., Konhauser, K.O., Fralick, P.W., Altermann, W., Visscher, P.T., and Lalonde, S. v., 2019, Global importance of oxic molybdenum sinks prior to 2.6 Ga revealed by the Mo isotope composition of Precambrian carbonates: Geology, v. 47, p. 559–562, doi:10.1130/G45706.1.

Tostevin, R., Shields, G.A., Tarbuck, G.M., He, T., Clarkson, M.O., and Wood, R.A., 2016, Effective use of cerium anomalies as a redox proxy in carbonate-dominated marine settings: Chemical Geology, v. 438, p. 146–162, doi:10.1016/j.chemgeo.2016.06.027.

Wallace, M.W., Hood, A., Shuster, A., Greig, A., Planavsky, N.J., and Reed, C.P., 2017, Oxygenation history of the Neoproterozoic to early Phanerozoic and the rise of land plants: Earth and Planetary Science Letters, v. 466, p. 12–19, doi:10.1016/j.epsl.2017.02.046.

Wang, X. et al., 2018, A Mesoarchean shift in uranium isotope systematics: Geochimica et Cosmochimica Acta, v. 238, p. 438–452, doi:10.1016/j.gca.2018.07.024.

Warchola, T., Lalonde, S. v., Pecoits, E., von Gunten, K., Robbins, L.J., Alessi, D.S., Philippot, P., and Konhauser, K.O., 2018, Petrology and geochemistry of the Boolgeeda Iron Formation, Hamersley Basin, Western Australia: Precambrian Research, v. 316, p. 155–173, doi:10.1016/j.precamres.2018.07.015.

Wilmeth, D.T., Fralick, P.W., Riding, R., and Lalonde, S. v, 2021, A Mesoarchean oxygen oasis expanded: new trace element and stable isotope data from the 2.8 Ga Mosher Carbonate, Steep Rock Lake, Canada: Abstract from Goldschmidt .

Wilmeth, D.T., Lalonde, S. v., Berelson, W.M., Petryshyn, V., Celestian, A.J., Beukes, N.J., Awramik, S.M., Spear, J.R., Mahseredjian, T., and Corsetti, F.A., 2022, Evidence for benthic oxygen production in Neoarchean lacustrine stromatolites: Geology, doi:10.1130/G49894.1.

CHAPTER 7:

Conclusion and Perspectives

7.1 Summary of the principal findings

The origin of oxygenic photosynthesis is one of the most important evolutionary events the Earth has ever known. Earth's modern biosphere owes its existence to this planet-defining metabolism, and understanding its origin is a major challenge for Earth system science. However, due to uncertainties about the primary nature of oxygen signals in ancient and weathered rocks, the exact timing of the evolution of oxygenic photosynthesis has remained unresolved. This PhD work focused on new chemical and isotopic signals (Ce anomalies, Fe isotopes, Ce isotopes) preserved in chemical and other marine sedimentary rocks deposited between 2.93 and 2.80 Ga to better understand the evolution of photosynthetic pathways on the early Earth.

After an introductory chapter, a general geological background of the samples examined in this work was detailed in Chapter 2, as well as the analytical methodologies used to obtain the elemental and isotopic data in Chapter 3.

In Chapter 4, major element data, REE compositions, and iron stable isotope chemostratigraphy were presented for an exceptional transgressive sequence spanning more than 70 m of stromatolitic marine carbonate and more than 60 m of deep-water facies (iron formation and black shale) captured in a drill core from the 2.93-billion-year (Ga) Ball Assemblage of the Red Lake Greenstone Belt, Superior Craton, NW Ontario, Canada. Major element and REE data revealed ferruginous marine conditions with significant hydrothermal influence and a combination of Eh conditions and REE residence times that were generally insufficient for Ce oxidation. However, iron isotopes revealed a dynamic iron redox cycle covering this shallow to deep transect, with $\delta^{56}Fe$ values ranging from -2.88‰ to +1.50‰ across all lithologies combined. The wide range and stratigraphic

evolution of $\delta^{56}Fe$ values are best explained by Fe depletion in an upwelling plume via offshore iron oxide precipitation, resulting in low $\delta^{56}Fe$ values in the residual Fe(II) pool. Remarkable large secular variations in $\delta^{56}Fe$ were observed in stromatolitic carbonates that are not easily explained by a Rayleigh distillation model nor by their pyrite content, but rather vary with the samples sulfur concentrations and sulfur stable isotopic compositions. Our data indicate that $\delta^{56}Fe(II)_{aq}$ values on the platform were controlled by an indirect driver linking Fe and S cycles, which we suggest are variations in primary production. This unique dataset indicates an important role for photosynthesis in modulating the Earth's major biogeochemical cycles already at 2.93 Ga.

Chapter 5 presented a systematic REE+Y study describing and comparing the trace element geochemistry of three Mesoarchean carbonate platforms of Red Lake (2.93 Ga), Woman Lake (2.86 Ga), and Steep Rock (2.80 Ga). All three sites show characteristic REE+Y patterns typical of seawater, with LREE depletion relative to HREE and strong La and Y anomalies, confirming the marine origin of these carbonates. Strong Eu anomalies, more pronounced at Red Lake than at the other two sites, indicate the presence of a high temperature hydrothermal component mixed into ambient seawater. The presence of negative Ce anomalies in samples from all three sites provides strong evidence for cerium redox cycling and the establishment of sufficient oxidation conditions for Ce oxidation. Red Lake samples, which have the smallest Ce anomalies and the largest Eu anomalies, have relatively high Fe but rather low Mn concentrations. Steep Rock samples show intermediate Fe and Mn concentrations, while Woman Lake samples tend to be rich in Mn and depleted in Fe. These patterns were interpreted to indicate that Red Lake was weakly oxidizing, with O_2 concentrations buffered by the abundance of Fe from nearby hydrothermal sources, where slight negative Ce anomalies are accompanied by oxidative

losses of Fe without major effect on the dissolved Mn reservoir. Steep Rock samples capture more oxidizing conditions than Red Lake, with oxidative Fe and Mn loss occurring in conjunction with increasingly oxic local conditions, as tracked by the Ce anomaly. Woman Lake samples appear to record the most oxidizing conditions, where Mn oxides were delivered directly to the sediment pile from a severely Ce-depleted water column. This study of rare earth systematics in the Red Lake, Woman Lake and Steep Rock carbonate platforms confirms the marine sedimentary origin of these carbonates and reveals that O_2-driven oxidative processes were likely in operation at each of these sites, as revealed by unambiguous evidence for the redox cycling of Ce and Mn.

In Chapter 6, we applied the ^{138}La-^{138}Ce radiometric isotope geochronometer on selected samples from the three carbonate platforms studied in Chapter 5, with special attention to those showing clear evidence of pre-GOE O_2 production in the form of significant Ce depletions. Robust La-Ce isochrons were obtained for all three sites and constitute clear evidence for all three, and with a high degree of statistical certainty for two of them, that La/Ce fractionation, and thus cerium oxidation, occurred at the time of deposition. These results provide important perspectives for future applications of La-Ce radiometric geochronology, which are elaborated below in section 7.2. They also firmly place the origin of oxygenic photosynthesis in the Mesoarchean, which requires a revised view of biological and geochemical evolution of the early Earth, as further discussed below in section 7.3.

7.2 Implications for La-Ce geochronology

In Chapter 6, high-precision La-Ce isotope compositions are reported for sediment samples bearing negative Ce anomalies from three Mesoarchean carbonate platforms. The

determined $^{138}Ce/^{142}Ce$ values are the most radiogenic reported to date for any Earth material. As described in Chapter 6, the observed range in values corresponds to that expected for samples that experienced important fractionation in La/Ce billions of years ago, and incompatible with a modern (post-depositional) process that might have drove La/Ce fractionation at a later time. Indeed, with the exception of a few outliers, the data can be seen to closely align with the 3.0 Ga La-Ce isochron (Figure 6.6). Furthermore, the data from all three sites define clear isochrons that all fall with error of their known depositional ages previously constrained by U-Th-Pb TIMS analyses on zircons (Figure 6.8). These results constitute an important proof of the potential of the La-Ce geochronometer to date ancient oxidative events affecting sedimentary Ce enrichments, enabled by over a decade of progressive improvements in the analytical methods for La-Ce isotope characterization. These results also offer an important opportunity to evaluate future potential applications as well as potential pitfalls of La-Ce geochronometry going forwards.

This study is the first to report La-Ce isotope compositions from ancient chemical sedimentary carbonates. It is demonstrated here that these samples effectively captured REE from ancient seawater that was characterized by La/Ce ratios that were highly fractionated, similar to seawater today, well outside of the range of crustal materials. Importantly, their widespread in La/Ce is driven not only by the occurrence of negative Ce anomalies, but also by their large spread in La/La*. This characteristic signature of modern and ancient seawater develops during REE scavenging onto flocculating particles, especially across estuarine mixing gradients (Lawrence et al., 2006), and its presence in anoxic marine waters as well as in Archean-age sediments lacking significant Ce anomalies indicates that it develops consistently under marine conditions of all ages regardless of

redox state. Crucially, the presence of La anomalies alone in ancient marine chemical sediments appears to drive sufficient La/Ce fractionation to enable geochronological studies of ancient sediments lacking appreciable Ce anomalies. For example, in Figure 6.5, it can be seen that samples from all three sites *showing no appreciable Ce anomalies* may attain La/Ce ratios that are at least as high as those presented by the Red Lake samples that do show important Ce anomalies (albeit muted relative to the other sites), i.e., $^{138}La/^{142}Ce$ as high as ~0.015. In other words, the presence of important La/La* anomalies alone in ancient chemical sediments should enable radiometric dating by decay of La to Ce with a precision comparable to that obtained for Red Lake (2σ on the isochron of 200 Ma or better) even in the absence of Ce anomalies. This means that the La-Ce isotope system may not only constrain post-depositional processes affecting Ce, but those that affect only La as well. Similarly, the absence of an appreciable Ce anomaly (Ce/Ce* ~1) could be effectively constrained with respect to emplacement age using the La-Ce isotope system. This means that the La-Ce isotope system is likely applicable to a wide variety of ancient sediments, with or without appreciable Ce anomalies, whenever mobility of the LREE needs to be constrained in age, especially redox-dependent mobility. These results are thus highly encouraging for the future application of the La-Ce isotope system to chemical sedimentary rocks regardless of the presence of important Ce anomalies.

The novel La-Ce isotope dataset presented in this thesis also provides new insights into possible post-depositional REE mobility that might affect the La-Ce system. For two out of the three sites, namely Red Lake and Woman Lake, two outliers were clearly identified at each site. These samples show mostly minor but clearly resolved departures from the ca. 3 Ga isochron. In Chapter 6, La/Ce perturbation models are explored, and it is demonstrated schematically that later additions of La and/or Ce can act to raise or lower

the La/Ce ratio and readily explain these outliers by post-depositional processes (c.f. Figures 6.9 and 6.10). Importantly, the presence of outliers in this dataset demonstrates that such processes necessarily affected the sample set. Even when considering only those aliquots not rejected as outliers (14 out of 18 analyzed; those used to generate the isochrons), with the exception Red Lake where analytical errors appear to be overestimated for the obtained isochron (low MSWD of 0.19), the other two isochrons show MSWD values that are relatively elevated (2.7 and 2 for Woman Lake and Steep Rock, respectively). These values approach their respective F value cutoffs (determined by the different numbers of points on each isochron and number of replicates employed) that would designate them as errorchrons instead of isochrons (see Brooks et al., 1972, and F value tables therein). This means that within the analytical uncertainties, they are close to showing behavior in $^{138}La/^{142}Ce$ vs. $^{138}Ce/^{142}Ce$ space that cannot be accounted for strictly by radioactive decay, and that other processes have induced true geological dispersion, for which statistical support is approaching 2σ. In other words, with the exception of Red Lake for which errors appear to be overestimated, even the non-outlier aliquots appear to show evidence for mobility and/or other sources of dispersion in the La-Ce system, despite the coherent ages and small 2σ errors obtained from the isochrons. This is perhaps not surprising considering that both previously published La-Ce isotopic studies of Precambrian metasediments (in both cases >3.2 Ga samples from the Barberton Greenstone Belt; Hayashi et al., 2004; Bonnand et al., 2020) showed significant late perturbation to the La/Ce system, in these cases leading to late negative Ce anomalies. It is further not surprising that due to redox considerations, La and Ce should be separated more readily from each other than Sm from Nd, for example, the Sm-Nd system is widely considered a generally robust source tracer and radiometric dating system that nonetheless may be isotopically perturbed at high metamorphic grades (e.g., Gruau et al., 1996). While La-Ce

isotope systematics nonetheless has strong potential going forwards for constraining in time REE signatures of Ce redox processing, it is important to keep in mind that it is subject to natural processes that may generate true geological dispersion in La and Ce, at the time of deposition or anytime afterwards, beyond that expected by radioactive decay.

7.3 Implications for the origin of oxygenic photosynthesis and early biogeochemical cycling

As detailed in Chapters 5 and 6, certain carbonate samples from three different Mesoarchean carbonate platforms from the NW Superior craton show clear evidence of Ce redox cycling by the presence of mild positive as well as mild to strong negative Ce anomalies. La-Ce geochronology confirms an ancient (pre-GOE) origin of these signals for all three sites, with important implications for our understanding of the timing of the evolution of oxygenic photosynthesis and the early evolution of biogeochemical cycles. As discussed in Chapter 6, even if recent laboratory experiments indicate that it may be possible to generate appreciable Ce anomalies during weathering under anoxic conditions in the presence of siderophores (Kraemer and Bau, 2022), in modern marine environments the water column and sedimentary expression of Ce anomalies stemming from Ce redox cycling is to date, based on currently available data, universally dependent on the presence of O_2. Furthermore, it was seen in Chapter 6 that alternative possible oxidants driving Ce oxidation, e.g., H_2O_2, were unlikely to have been produced in sufficient amounts to drive appreciable Ce oxidation. The presence of important negative Ce anomalies in the Mesoarchean carbonates examined in this study thus indicate that free oxygen was indeed being biologically produced at least as far back as 2.93 Ga.

These findings have important ramifications for our current understanding of Mesoarchean biogeochemical cycling. Firstly, at all three sites, the presence of negative Ce anomalies was far from universal across the hundreds of samples analyzed by the EARTHBLOOM project and examined in this thesis for their REE systematics. Indeed, at Red Lake, only a small number (<20) of samples showed important negative Ce anomalies, and the vast majority came from one site in particular, the Golden Arm site where m-scale domes comprised of alternating carbonate microbialite and carbonate crystal fans outcrop at the lakeshore. This indicates that even at Archean sites where oxygenic photosynthesis is confirmed to been occurring, sedimentary trace element signals for the presence of O_2 may be rare. As discussed in Chapter 6, this is not surprising for the Ce redox proxy considering that even in modern shallow-water environments with abundant water column O_2, Ce(III) oxidation rates may be slow, and only in more open-ocean settings where flocculating particulate concentrations reach a minimum does the Ce(III) oxidation rate exceed the Ce(III) turnover time and permit the water column expression of important Ce anomalies (Moffett, 1990). In other words, it is unlikely that O_2 production was restricted to deeper water environments, but rather it is only here where REE residence times were sufficiently long to permit accumulation of a significant Ce(IV) reservoir in the face of sluggish Ce(III) oxidation kinetics. This observation should help guide future workers in the search for ancient signals of oxygenic photosynthesis using the Ce redox proxy. It also means that early oxygenic photosynthesis may have been cryptic from the point of view of a variety of proxies. The possibility remains open that other proxy systems may reveal the ancient presence of O_2 whereas others indicate anoxic conditions for analysis of the very same sample. It follows that sediments deposited in even more shallow-water environments, where rapid Ce(III) turnover prevents the accumulation of important Ce anomalies, may still hold clues to early O_2 production, and that future work should pay

special attention to lessons obtained from modern oceanography (e.g., redox proxy residence times in different environments) when selecting paleoredox proxies for application to these environments. For shallow-water environments with rapid trace metal and REE turnover, other paleoredox proxies, especially those with rapid oxidation rates relative to anoxic renewal processes, should be explored.

The results of this thesis work also have important bearing on previously published sedimentary records suggested to indicate pre-GOE O_2 production. There exist multiple studies demonstrating convincingly that ancient sedimentary records deposited before the GOE may be subject to later elemental and isotopic modifications during more modern surface weathering (e.g., Albut et al., 2018, 2019; Planavsky et al., 2020; Bonnand et al., 2020). The generally well-preserved samples in this work clearly do not represent such a case, and sheds little insight into modern resetting processes. It does, however, fundamentally change the burden of proof required for claims of pre-GOE O_2 production. Quite simply, now that it has been confirmed with high statistical support that oxygenic photosynthesis was operating in the Mesoarchean, it cannot be said that oxygenic photosynthesis is an unlikely source of ancient signals for free O_2. Rather, the burden of proof should swing in the direction of those claiming that such signals are universally the product of later surface weathering. No longer should claims of pre-GOE oxygenic photosynthesis be shot down by the simple argument that all available records could be explained by later surface weathering. Rather, the most parsimonious explanation for pre-GOE signals of free O_2 production captured in ancient sedimentary rocks should now be that oxygenic photosynthesis was likely recorded, barring robust evidence for the secondary nature of such signals. Adoption of this shift in the current paradigm should help advance research in this domain, as important datasets that may be easily critiqued as

representing “late alteration” with relatively little confirmatory evidence should now enjoy additional support that should act to raise the bar in terms of geochemical or geochronological evidence that might be used to otherwise discredit them.

Finally, in what is likely the most important ramification of this work, these results provide for the first time a chronological anchor point in deep geological time where it may be stated with high certainty that oxygenic photosynthesis had already evolved. Such anchor points are critical for phylogenetic molecular clock reconstructions of the evolution of early microbial metabolism. Such efforts have to date yielded highly discrepant conclusions : the origins of oxygenic photosynthesis is indicated by some studies to have occurred within 100 Ma or so of the GOE itself (Soo et al.; Shih et al., 2017), and thus its evolution may coincide GOE itself, vs. others that indicate its origins as far back as 3.3 – 3.6 Ga or earlier (Cardona et al., 2019; Cardona, 2019; Boden et al., 2021). The data presented in this thesis clearly support the latter, and should enable a new generation of molecular clock reconstructions based on this critical updated timepoint. While it remains to be seen whether it is the O_2-producing activity of direct cyanobacterial ancestors that has been effectively dated by this study, or whether the O_2 was produced by a more ancestral but unrelated group, presumably now extinct, that simply transferred their photosynthetic machinery to the ancestors of modern cyanobacteria. Regardless, this work has placed a new critical anchor point in geological time for early O_2 production, firmly in the Mesoarchean, and should hopefully stimulate further research and insight into the evolution of Earth’s most important microbial metabolism.

7.4 References

Albut, G., Babechuk, M.G., Kleinhanns, I.C., Benger, M., Beukes, N.J., Steinhilber, B., Smith, A.J.B., Kruger, S.J., and Schoenberg, R., 2018, Modern rather than Mesoarchaean oxidative weathering responsible for the heavy stable Cr isotopic signatures of the 2.95 Ga old Ijzermijn iron formation (South Africa): Geochimica et Cosmochimica Acta, v. 228, p. 157–189, doi:10.1016/j.gca.2018.02.034.

Albut, G., Kamber, B.S., Brüske, A., Beukes, N.J., Smith, A.J.B., and Schoenberg, R., 2019, Modern weathering in outcrop samples versus ancient paleoredox information in drill core samples from a Mesoarchaean marine oxygen oasis in Pongola Supergroup, South Africa: Geochimica et Cosmochimica Acta, v. 265, p. 330–353, doi:10.1016/j.gca.2019.09.001.

Boden, J.S., Konhauser, K.O., Robbins, L.J., and Sánchez-Baracaldo, P., 2021, Timing the evolution of antioxidant enzymes in cyanobacteria: Nature Communications, v. 12, p. 4742, doi:10.1038/s41467-021-24396-y.

Bonnand, P., Lalonde, S. v., Boyet, M., Heubeck, C., Homann, M., Nonnotte, P., Foster, I., Konhauser, K.O., and Köhler, I., 2020, Post-depositional REE mobility in a Paleoarchean banded iron formation revealed by La-Ce geochronology: A cautionary tale for signals of ancient oxygenation: Earth and Planetary Science Letters, v. 547, doi:10.1016/j.epsl.2020.116452.

Brooks, C., Hart, S.R., and Wendt, I., 1972, Realistic use of two-error regression treatments as applied to rubidium-strontium data: Reviews of Geophysics, v. 10, p. 551, doi:10.1029/RG010i002p00551.

Cardona, T., 2019, Thinking twice about the evolution of photosynthesis: Open Biology, v. 9, doi:10.1098/rsob.180246.

Cardona, T., Sánchez-Baracaldo, P., Rutherford, A.W., and Larkum, A.W., 2019, Early Archean origin of Photosystem II: Geobiology, v. 17, p. 127–150, doi:10.1111/gbi.12322.

Gruau, G., Rosing, M., Bridgwater, D., and Gill, R.C.O., 1996, Resetting of Sm Nd systematics during metamorphism of > 3.7-Ga rocks: implications for isotopic models of early Earth differentiation: Chemical Geology, v. 133, p. 225–240, doi:10.1016/S0009-2541(96)00092-7.

Hayashi, T., Tanimizu, M., and Tanaka, T., 2004, Origin of negative Ce anomalies in Barberton sedimentary rocks, deduced from La-Ce and Sm-Nd isotope systematics, *in* Precambrian Research, Elsevier B.V., v. 135, p. 345–357, doi:10.1016/j.precamres.2004.09.004.

Kraemer, D., and Bau, M., 2022, Siderophores and the formation of cerium anomalies in anoxic environments: Geochemical Perspectives Letters, v. 22, p. 50–55, doi:10.7185/geochemlet.2227.

Lawrence, M.G., Greig, A., Collerson, K.D., and Kamber, B.S., 2006, Rare earth element and yttrium variability in South East Queensland waterways: Aquatic Geochemistry, v. 12, p. 39–72, doi:10.1007/s10498-005-4471-8.

Moffett, J.W., 1990, Microbially mediated cerium oxidation in sea water: Nature, v. 345, p. 421–423, doi:10.1038/345421a0.

Planavsky, N.J., Robbins, L.J., Kamber, B.S., and Schoenberg, R., 2020, Weathering, alteration and reconstructing Earth’s oxygenation: Interface Focus, v. 10, p. 20190140, doi:10.1098/rsfs.2019.0140.

Shih, P.M., Hemp, J., Ward, L.M., Matzke, N.J., and Fischer, W.W., 2017, Crown group Oxyphotobacteria postdate the rise of oxygen: Geobiology, v. 15, p. 19–29, doi:10.1111/gbi.12200.

Soo, R.M., Hemp, J., Parks, D.H., Fischer, W.W., and Philip Hugenholtz, † On the origins of oxygenic photosynthesis and aerobic respiration in Cyanobacteria:, http://science.sciencemag.org/.

APPENDICES

APPENDIX A:

Appendix to chapter 4

Appendix A.1. **Major element concentration (wt.%) of the 2.94 Ga Red Lake samples.**

Sample	Lithology	Strat-depth (m)	SiO_2	TiO_2	Al_2O_3	Fe_2O_3	MnO	MgO	CaO	Na_2O	K_2O	P_2O_5
NGI 8.4	Carb.	3.15	51.27	0.01	0.11	3.09	0.63	8.95	15.33	0.00	0.01	0.01
NGI 10.5	Carb.	3.93	21.91	0.01	0.05	2.42	0.66	12.96	22.92	0.00	0.02	0.01
NGI 12.5	Carb.	4.68	34.89	0.01	0.24	3.83	0.69	12.24	20.10	0.00	0.00	0.00
NGI 12.5	Carb.	4.68	45.45	0.01	0.10	2.12	0.63	10.72	17.17	0.00	0.00	0.00
NGI 13.85	Carb.	5.19	51.35	0.01	0.06	2.32	0.47	7.82	13.43	n.d.	0.02	0.01
NGI 18.65	Carb.	6.99	17.43	0.01	0.10	5.87	0.74	15.28	24.45	0.00	0.01	0.01
NGI 20.75	Carb.	7.77	24.63	0.01	0.06	2.28	0.61	11.61	19.58	0.00	0.02	0.01
NGI 23.05	Carb.	8.63	20.82	0.01	0.11	1.70	0.71	16.50	24.58	0.00	0.00	0.00
NGI 24.65	Carb.	9.23	34.50	0.01	0.06	1.53	0.55	10.60	16.78	n.d.	0.02	0.01
NGI 27	Carb.	10.11	26.20	0.01	0.10	2.99	0.61	14.86	22.31	0.00	0.01	0.00
NGI 29.1	Carb.	10.90	26.49	0.01	0.05	1.17	0.66	10.52	16.85	n.d.	0.02	0.01
NGI 30.6	Carb.	11.46	65.85	0.01	0.12	3.38	0.48	5.63	10.56	0.00	0.01	0.00
NGI 32.4	Carb.	12.14	33.25	0.01	0.12	2.85	0.72	13.02	20.81	0.00	0.01	0.01
NGI 33.8	Carb.	12.66	23.36	0.02	0.11	9.92	0.84	10.52	20.38	0.00	0.03	0.03
NGI 36	Carb.	13.49	16.77	0.02	0.14	5.15	0.99	16.15	25.43	0.00	0.01	0.01
NGI 38.25	Carb.	14.33	52.56	0.01	0.08	3.19	0.41	7.82	14.06	0.00	0.02	0.01
NGI 39.45	Carb.	14.78	20.04	0.02	0.16	7.08	0.90	14.05	23.52	0.00	0.01	0.02
NGI 42.5	Carb.	15.92	3.69	0.02	0.27	3.97	0.98	19.19	29.70	0.00	0.01	0.01
NGI 43.65	Carb.	16.35	60.09	0.01	0.07	0.59	0.41	5.19	8.57	0.00	0.02	0.01
NGI 46	Carb.	17.23	56.34	0.01	0.12	2.17	0.48	8.35	13.86	0.00	0.01	0.01
NGI 48	Carb.	17.98	10.93	0.01	0.06	1.75	0.92	13.55	23.72	n.d.	0.02	0.02
NGI 50.85	Carb.	19.05	14.90	0.04	0.52	3.82	0.81	17.17	26.00	0.00	0.01	0.01
NGI 52.2	Carb.	19.55	7.08	0.01	0.09	3.20	0.87	15.17	26.34	0.00	0.02	0.02
NGI 54	Carb.	20.23	38.09	0.04	1.32	3.68	0.64	11.38	19.02	0.01	0.00	0.03
NGI 55.2	Carb.	20.68	30.67	0.01	0.15	6.20	0.96	9.50	19.01	0.00	0.03	0.02

Sample	Lithology	Strat-depth (m)	SiO_2	TiO_2	Al_2O_3	Fe_2O_3	MnO	MgO	CaO	Na_2O	K_2O	P_2O_5
NGI 55.65	Carb.	20.85	25.38	0.03	0.40	33.65	2.06	5.63	11.23	0.00	0.01	0.07
NGI 57	Carb.	21.35	13.44	0.02	0.16	6.91	1.26	14.88	27.04	0.00	0.01	0.01
NGI 60	Carb.	22.48	4.12	0.03	0.47	8.72	1.44	15.72	29.24	0.00	0.06	0.02
NGI 62.6	Carb.	23.45	62.08	0.01	0.11	4.77	0.87	4.91	11.39	0.00	0.02	0.01
NGI 64	Carb.	23.97	23.31	0.02	0.24	5.00	1.07	13.94	23.91	0.00	0.01	0.01
NGI 66.45	Carb.	24.89	28.13	0.07	1.30	4.77	0.80	10.32	19.47	0.03	0.28	0.04
NGI 68	Carb.	25.47	62.77	0.01	0.14	4.97	0.53	5.98	11.40	0.00	0.01	0.01
NGI 70.5	Carb.	26.41	11.52	0.01	0.05	2.00	0.82	15.68	26.03	n.d.	0.02	0.01
NGI 73	Carb.	27.35	54.52	0.02	0.19	4.03	0.59	7.87	14.13	0.00	0.02	0.01
NGI 76	Carb.	28.47	3.30	0.01	0.06	1.23	0.74	14.31	24.82	n.d.	0.02	0.01
NGI 77.3	Carb.	28.96	65.01	0.01	0.12	5.03	0.60	5.53	10.74	0.00	0.01	0.01
NGI 79	Carb.	29.59	17.59	0.14	2.77	4.72	0.82	14.65	24.96	0.09	0.44	0.04
NGI 80	Siltstone	29.97	56.95	0.90	17.53	9.33	0.28	5.33	5.23	0.46	2.05	0.26
NGI 81	Siltstone	30.34	55.43	0.93	15.09	10.78	0.24	4.22	2.52	0.37	2.61	0.26
NGI 88	Carb.	32.97	7.82	0.01	0.46	4.41	0.85	7.69	14.25	0.03	0.02	0.02
NGI 89.9	Carb.	33.68	52.56	0.05	6.02	4.24	0.45	7.55	11.46	0.24	0.04	0.02
NGI 91	Carb.	34.09	24.99	0.01	0.11	3.85	0.96	14.00	23.40	0.00	0.01	0.01
NGI 93.8	Carb.	35.14	32.43	0.13	5.03	5.52	0.69	11.01	18.06	0.23	0.01	0.07
NGI 96	Carb.	35.96	47.57	0.01	0.19	4.11	0.61	8.34	15.63	0.00	0.05	0.02
NGI 97.4	Carb.	36.49	12.62	0.02	0.27	7.09	0.98	15.06	26.89	0.00	0.03	0.01
NGI 99.5	Carb.	37.27	6.67	0.02	0.25	4.90	0.91	17.80	28.99	0.00	0.01	0.02
NGI 102	Carb.	38.21	13.81	0.01	0.10	1.94	0.57	17.96	27.03	0.00	0.01	0.01
NGI 103	Carb.	38.58	7.55	0.01	0.10	2.08	0.63	19.19	28.65	0.00	0.01	0.01
NGI 104	Carb.	38.96	8.53	0.01	0.26	2.86	0.82	11.59	20.37	0.01	0.02	0.02
NGI 105	Carb.	39.33	4.68	0.01	0.12	3.37	0.82	19.30	30.04	0.00	0.01	0.01
NGI 107	Carb.	40.08	3.24	0.01	0.10	2.39	0.56	20.42	30.55	0.00	0.01	0.00

Sample	Lithology	Strat-depth (m)	SiO_2	TiO_2	Al_2O_3	Fe_2O_3	MnO	MgO	CaO	Na_2O	K_2O	P_2O_5
NGI 109	Carb.	40.46	6.03	0.01	0.15	3.26	0.72	18.96	29.17	0.00	0.01	0.01
NGI 110.6	Carb.	41.43	5.47	0.01	0.11	2.08	0.63	19.83	29.40	0.00	0.01	0.00
NGI 112	Carb.	41.96	2.10	0.01	0.05	2.81	0.69	15.87	29.12	0.00	0.02	0.02
NGI 113.6	Carb.	42.56	0.79	0.01	0.11	4.76	0.82	18.88	30.53	0.00	0.01	0.01
NGI 115	Carb.	43.08	15.27	0.01	0.10	3.60	0.67	13.78	24.08	n.d.	0.02	0.01
NGI 117	Carb.	43.83	13.02	0.01	0.10	1.98	0.53	18.12	26.93	0.00	0.00	0.00
NGI 119.1	Carb.	44.62	14.09	0.01	0.15	7.60	0.67	15.37	24.96	0.00	0.01	0.01
NGI 120	Carb.	44.95	7.06	0.01	0.11	3.55	0.62	16.82	26.95	0.00	0.02	0.02
NGI 123	Carb.	46.08	15.27	0.02	0.15	3.64	0.66	16.57	26.00	0.00	0.01	0.01
NGI 125	Carb.	46.83	1.86	0.01	0.12	5.44	0.74	18.28	29.82	0.00	0.00	0.01
NGI 126.9	Carb.	47.54	10.52	0.01	0.07	2.61	0.58	15.24	25.05	n.d.	0.02	0.01
NGI 126.9	Carb.	47.54	10.69	0.01	0.12	3.26	0.61	17.82	27.66	0.00	0.01	0.01
NGI 128.1	Carb.	47.99	3.05	0.02	0.19	4.68	0.69	18.90	29.91	0.00	0.01	0.01
NGI 131.2	Carb.	49.15	49.20	0.01	1.07	2.94	0.53	7.26	12.97	0.06	0.02	0.02
NGI 134	Carb.	50.20	61.98	0.01	0.10	1.77	0.46	7.51	12.48	0.00	0.01	0.00
NGI 137	Carb.	51.32	35.63	0.01	0.15	1.78	0.58	13.12	20.30	0.00	0.01	0.00
NGI 138.4	Carb.	51.85	8.65	0.01	0.06	2.30	0.82	15.12	24.85	0.00	0.02	0.01
NGI 142	Carb.	53.19	49.74	0.87	13.58	10.40	0.21	6.24	9.20	0.00	2.06	0.74
NGI 146.2	Carb.	54.77	37.59	0.01	0.15	2.04	0.60	12.43	19.48	0.00	0.01	0.00
NGI 147	Carb.	55.07	35.41	0.01	0.18	4.93	0.76	9.68	18.40	0.00	0.02	0.02
NGI 150	Carb.	56.19	26.05	0.01	0.12	2.61	0.64	14.63	23.08	0.00	0.01	0.01
NGI 153	Carb.	57.31	54.05	0.83	14.31	6.83	0.20	5.90	8.05	0.50	2.79	0.66
NGI 155.8	Carb.	58.36	43.01	0.02	0.56	16.34	0.49	5.86	10.80	0.00	0.12	0.05
NGI 159.3	Carb.	59.67	37.77	0.01	0.14	2.75	0.65	11.91	19.30	0.00	0.01	0.00
NGI 161.2	Carb.	60.39	17.24	0.01	0.10	1.71	0.90	17.02	25.71	0.00	0.01	0.00
NGI 162.8	Carb.	60.99	21.99	0.01	0.07	1.23	0.83	12.72	20.94	n.d.	0.02	0.01

Sample	Lithology	Strat-depth (m)	SiO_2	TiO_2	Al_2O_3	Fe_2O_3	MnO	MgO	CaO	Na_2O	K_2O	P_2O_5
NGI 166	Carb.	62.18	23.18	0.01	0.11	1.49	0.79	15.92	24.06	0.00	0.01	0.00
NGI 168.8	Carb.	63.23	9.79	0.01	0.10	2.73	0.82	15.80	26.15	0.00	0.02	0.02
NGI 170.8	Carb.	63.98	9.80	0.02	0.16	4.46	0.85	17.23	27.71	0.00	0.01	0.01
NGI 172	Carb.	64.43	74.30	0.22	4.89	4.31	0.22	4.00	8.00	0.47	0.11	0.07
NGI 175.1	Carb.	65.59	9.39	0.01	0.11	3.09	0.86	18.40	28.39	0.00	0.01	0.01
NGI 176	Carb.	65.93	58.86	0.01	0.11	4.74	0.48	5.94	11.03	n.d.	0.03	0.02
NGI 178.2	Carb.	66.75	7.40	0.01	0.10	2.82	0.85	18.98	29.42	0.00	0.01	0.01
NGI 179	Carb.	67.05	8.29	0.01	0.11	3.50	0.81	18.43	28.74	0.00	0.01	0.01
NGI 181.7	Carb.	68.07	47.25	0.01	0.11	3.02	0.62	9.41	15.66	0.00	0.03	0.01
NGI 184	Carb.	68.93	8.37	0.01	0.11	3.17	0.79	18.82	29.23	0.00	0.01	0.01
NGI 185.3	Carb.	69.41	3.71	0.01	0.11	3.79	0.84	18.77	30.11	0.00	0.01	0.01
NGI 186.1	Carb.	69.71	7.21	0.01	0.07	3.93	0.79	16.40	28.01	0.00	0.02	0.02
NGI 188 .3	Carb.	70.54	17.59	0.01	0.14	4.06	0.77	15.52	25.43	0.00	0.01	0.01
NGI 191.1	Carb.	71.59	2.24	0.01	0.07	2.84	0.81	17.87	29.66	0.00	0.02	0.01
NGI 193	Carb.	72.30	14.74	0.01	0.15	5.03	0.89	18.25	29.39	0.00	0.01	0.01
NGI 195	Carb.	73.05	13.07	0.01	0.22	5.27	0.65	15.15	25.57	0.00	0.03	0.02
NGI 198	Carb.	74.17	30.68	0.11	3.07	6.67	0.62	8.05	16.43	0.03	0.80	0.02
NGI 199.5	BS	74.73	74.74	0.15	13.45	0.85	0.09	1.73	2.64	0.65	2.71	0.04
NGI 202	Carb.	75.67	76.23	0.15	14.35	1.27	0.04	1.60	2.06	0.59	2.77	0.04
NGI 204	BS	76.42	77.19	0.16	14.28	0.39	0.03	1.08	1.37	0.64	3.10	0.04
NGI 206	SBS	77.17	64.25	0.42	15.26	6.20	0.10	2.50	1.50	0.84	3.19	0.05
NGI 206bis	BS	77.17	66.95	0.47	18.05	1.82	0.05	1.44	1.07	0.81	3.15	0.05
NGI 207	BS	77.54	67.58	0.49	17.71	2.21	0.08	1.54	1.04	0.56	4.17	0.03
NGI 208	SBS	77.92	62.13	0.66	15.38	7.03	0.18	3.03	3.77	0.93	1.90	0.05
NGI 209	BS	78.29	n.d.	n.d.	n.d.	n.d.	n.d.	n.d.	n.d.	n.d.	n.d.	n.d.
NGI 210	SBS	78.67	54.16	0.61	15.92	14.66	0.14	2.27	1.38	0.66	3.24	0.08

Sample	Lithology	Strat-depth (m)	SiO_2	TiO_2	Al_2O_3	Fe_2O_3	MnO	MgO	CaO	Na_2O	K_2O	P_2O_5
NGI 210.4	SBS	78.82	64.24	0.55	17.97	3.46	0.21	2.27	1.75	0.84	3.14	0.04
NGI 211	SBS	79.04	57.16	0.60	18.72	8.23	0.15	2.31	4.01	0.90	2.80	0.10
NGI 212.5	SBS	79.60	63.56	0.44	12.89	7.49	0.20	2.84	1.92	0.83	1.91	0.04
NGI 213	SBS	79.79	42.00	0.50	13.19	21.60	0.31	1.67	2.04	0.70	2.03	0.07
NGI 213.8	SBS	80.09	48.14	0.53	13.60	12.33	0.14	2.66	4.43	1.17	0.92	0.15
NGI 215	SBS	80.54	41.36	0.36	8.27	27.85	0.16	2.61	2.27	0.60	0.28	0.09
NGI 216.2	SBS	80.99	56.79	0.55	13.98	14.95	0.16	0.96	2.07	0.60	2.47	0.08
NGI 217.2	SBS	81.36	66.92	0.36	9.53	11.56	0.35	2.23	2.09	0.67	0.54	0.07
NGI 218.2	SBS	81.74	28.79	0.13	3.43	53.43	0.16	0.96	0.85	0.12	0.17	0.10
NGI 218.7	BIF	81.93	93.95	0.01	0.14	2.95	0.10	0.76	1.69	0.00	0.01	0.01
NGI 219	BIF	82.04	53.10	0.02	0.28	22.26	0.69	5.03	9.59	0.00	0.02	0.05
NGI 219.3	BIF	82.15	26.95	0.09	2.15	50.54	1.71	7.14	4.37	0.00	0.09	0.21
NGI 220	BIF	82.41	59.75	0.03	0.69	28.76	1.11	3.87	4.43	0.00	0.04	0.14
NGI 221	BIF	82.79	48.50	0.05	1.16	34.57	1.76	6.36	4.47	0.00	0.07	0.09
NGI 222.5	SBS	83.35	49.52	0.44	12.68	24.45	0.26	1.12	1.00	0.36	2.12	0.09
NGI 223.2	SBS	83.61	58.73	0.16	5.29	21.82	0.23	6.39	1.92	0.10	0.36	0.07
NGI 224.2	SBS	83.99	29.30	0.19	5.16	45.23	0.08	0.90	1.75	0.39	0.32	0.09
NGI 226	BS	84.66	80.02	0.80	17.79	8.86	0.28	4.46	8.86	0.71	2.57	0.28
NGI 227	BS	85.04	63.20	0.75	16.10	7.11	0.17	3.15	6.20	0.71	2.40	0.25
NGI 227.9	BS	85.37	65.63	0.74	16.04	7.45	0.26	2.48	3.63	0.75	2.16	0.25
NGI 229	BS	85.78	93.31	0.01	0.12	3.55	0.11	0.37	0.70	0.00	0.01	0.01
NGI 229.5	S-BIF	85.97	64.04	0.03	0.56	18.71	0.56	3.63	4.74	0.00	0.04	0.06
NGI 230.8	S-BIF	86.46	61.26	0.04	1.15	22.84	0.64	3.60	4.05	0.01	0.17	0.08
NGI 232	S-BIF	86.91	32.60	0.08	1.89	39.95	0.42	4.53	4.54	0.00	0.28	0.10
NGI 233	BIF	87.28	57.01	0.02	0.20	38.15	0.19	3.38	1.78	0.00	0.02	0.25
NGI 234	S-BIF	87.66	17.12	0.05	1.19	55.24	0.57	5.96	5.17	0.00	0.32	0.20

Sample	Lithology	Strat-depth (m)	SiO_2	TiO_2	Al_2O_3	Fe_2O_3	MnO	MgO	CaO	Na_2O	K_2O	P_2O_5
NGI 235	BIF	88.03	51.64	0.02	0.40	40.50	0.31	4.79	2.78	0.00	0.02	0.22
NGI 236	BIF	88.41	84.07	0.01	0.36	11.62	0.14	1.02	1.76	0.01	0.06	0.04
NGI 237	S-BIF	88.78	43.56	0.03	0.66	45.49	0.28	2.79	2.19	0.00	0.06	0.14
NGI 238	BIF	89.16	63.58	0.02	0.16	32.39	0.18	2.77	2.36	0.00	0.01	0.16
NGI 239	BIF	89.53	73.59	0.01	0.25	23.76	0.13	1.63	2.09	0.00	0.02	0.14
NGI 240	BIF	89.91	73.72	0.10	1.64	22.71	0.07	1.37	0.94	0.05	0.30	0.12
NGI 240.2	BIF	89.98	35.35	0.09	2.83	47.95	0.26	4.29	3.46	0.00	0.70	0.21
NGI 241	BIF	90.28	58.82	0.02	0.30	32.28	0.27	3.75	3.47	0.00	0.03	0.26
NGI 242	BIF	90.65	39.86	0.01	0.15	55.27	0.13	3.22	1.85	0.00	0.02	0.26
NGI 243	BIF	91.03	66.75	0.01	0.14	34.76	0.11	2.07	0.30	0.00	0.01	0.08
NGI 244	BIF	91.40	23.70	0.05	0.86	52.56	0.77	6.31	6.11	0.00	0.09	0.23
NGI 31-1	S-BIF	94.49	2.89	0.04	1.40	59.01	1.58	7.35	4.26	0.00	0.14	0.22
NGI 31-2	S-BIF	94.87	19.37	0.04	1.41	54.06	1.09	7.32	5.94	0.00	0.23	0.13
NGI 31-3	BS	95.56	28.04	1.80	25.97	29.85	0.30	2.18	0.12	0.15	4.36	0.05
NGI 31-4	S-BIF	96.29	83.08	0.04	0.88	10.96	0.18	0.79	1.05	0.01	0.03	0.02
NGI 31-5	S-BIF	98.07	20.18	0.12	2.80	45.86	0.95	8.17	2.68	0.01	0.50	0.25
NGI 31-6	S-BIF	99.45	11.16	0.16	4.29	60.81	0.29	4.43	1.62	0.01	0.93	0.15
NGI 31-7	S-BIF	99.96	10.55	0.16	4.32	60.83	0.43	4.09	2.60	0.01	0.85	0.15
NGI 31-8	S-BIF	97.67	16.78	0.24	6.86	52.95	0.57	5.61	4.04	0.03	1.09	0.16
NGI 31-9	S-BIF	99.35	70.17	0.02	0.24	20.96	0.16	1.80	1.98	0.00	0.01	0.08
NGI 31-10	S-BIF	101.99	37.50	0.11	1.96	42.42	0.43	5.86	4.77	0.03	0.02	0.18
NGI 31-11	S-BIF	103.11	8.98	0.10	2.21	57.11	0.69	5.86	8.34	0.00	0.01	0.29
NGI 31-12	BIF	103.25	6.20	0.04	1.02	55.28	0.92	7.00	9.57	0.00	0.01	0.25
NGI 31-13	S-BIF	104.31	12.48	0.07	2.15	45.26	0.95	8.04	9.35	0.01	0.01	0.10
NGI 31-14	S-BIF	105.93	12.60	0.28	7.94	63.07	1.05	1.11	0.27	0.01	0.96	0.16
NGI 31-15	S-BIF	106.96	33.45	0.54	7.77	45.01	1.77	3.00	1.12	0.04	1.36	0.13

Sample	Lithology	Strat-depth (m)	SiO_2	TiO_2	Al_2O_3	Fe_2O_3	MnO	MgO	CaO	Na_2O	K_2O	P_2O_5
NGI 31-16	BIF	107.26	76.70	0.02	0.16	24.07	0.22	1.06	0.23	0.00	0.01	0.10
NGI 31-17	SBS	108.62	9.42	0.33	6.97	62.41	0.43	4.21	1.31	0.00	0.24	0.34
NGI 31-18	SBS	109.06	39.68	0.39	9.74	36.16	0.38	1.46	2.04	0.89	1.57	0.10
NGI 31-19	BIF	110.71	33.62	0.02	0.18	58.27	0.44	2.88	3.35	0.00	0.01	0.23
NGI 31-20	S-BIF	120.52	58.48	0.02	0.22	38.98	0.51	2.22	1.16	0.01	0.02	0.22
NGI 31-21	SBS	122.00	57.74	0.45	7.96	25.68	1.60	3.42	1.16	0.01	0.21	0.41
NGI 31-22	BIF	122.02	63.58	0.04	0.51	34.60	0.94	3.19	0.28	0.01	0.03	0.07
NGI 31-23	SBS	123.41	89.84	0.02	0.18	9.60	0.05	0.16	0.78	0.00	0.00	0.01
NGI 31-24	SBS	125.86	34.29	0.31	4.23	50.05	1.67	5.29	1.44	0.06	0.03	0.30
NGI 31-25	Carb.	141.96	4.46	0.02	0.13	7.49	0.64	16.06	29.13	0.00	0.01	0.02

Appendix A.2. **REE concentrations (ppm) of the 2.94 Ga Red Lake samples.**

Sample	Lithology	Strat-depth (m)	La	Ce	Pr	Nd	Sm	Eu	Gd	Tb	Dy	Y	Ho	Er	Tm	Yb	Lu
NGI 8.4	Carb.	3.15	0.153	0.246	0.028	0.114	0.025	0.021	0.022	0.040	0.007	0.050	0.012	0.040	0.005	0.032	0.006
NGI 10.5	Carb.	3.93	0.214	0.340	0.038	0.149	0.029	0.020	0.020	0.037	0.005	0.030	0.007	0.023	0.003	0.017	0.003
NGI 12.5	Carb.	4.68	0.326	0.603	0.071	0.302	0.064	0.041	0.042	0.086	0.014	0.092	0.023	0.075	0.011	0.067	0.012
NGI 12.5	Carb.	4.68	0.320	0.596	0.069	0.297	0.064	0.040	0.041	0.085	0.014	0.090	0.022	0.073	0.011	0.064	0.012
NGI 13.85	Carb.	5.19	0.193	0.338	0.039	0.162	0.034	0.021	0.022	0.049	0.008	0.051	0.013	0.039	0.006	0.032	0.006
NGI 18.65	Carb.	6.99	0.356	0.722	0.086	0.377	0.094	0.077	0.078	0.134	0.024	0.166	0.042	0.137	0.020	0.124	0.023
NGI 20.75	Carb.	7.77	0.306	0.532	0.061	0.253	0.052	0.030	0.030	0.071	0.011	0.070	0.017	0.054	0.007	0.044	0.008
NGI 23.05	Carb.	8.63	0.287	0.502	0.057	0.233	0.047	0.028	0.028	0.062	0.010	0.061	0.015	0.046	0.006	0.039	0.007
NGI 24.65	Carb.	9.23	0.239	0.404	0.045	0.185	0.036	0.019	0.020	0.051	0.008	0.048	0.012	0.037	0.005	0.030	0.006
NGI 27	Carb.	10.11	0.223	0.384	0.043	0.177	0.035	0.019	0.019	0.045	0.007	0.040	0.009	0.029	0.004	0.024	0.004
NGI 29.1	Carb.	10.90	0.250	0.430	0.048	0.197	0.038	0.023	0.023	0.050	0.007	0.044	0.010	0.033	0.004	0.027	0.005
NGI 33.8	Carb.	12.66	0.502	0.958	0.116	0.512	0.139	0.124	0.124	0.198	0.039	0.271	0.065	0.215	0.033	0.224	0.043
NGI 36	Carb.	13.49	0.536	1.059	0.127	0.557	0.135	0.090	0.092	0.183	0.032	0.214	0.052	0.173	0.025	0.161	0.029
NGI 38.25	Carb.	14.33	0.381	0.707	0.086	0.383	0.096	0.067	0.067	0.130	0.022	0.145	0.034	0.109	0.015	0.096	0.017
NGI 39.45	Carb.	14.78	0.870	1.602	0.191	0.833	0.220	0.159	0.160	0.286	0.052	0.336	0.078	0.259	0.040	0.279	0.053
NGI 43.65	Carb.	16.35	0.325	0.581	0.067	0.279	0.059	0.038	0.038	0.078	0.012	0.079	0.019	0.061	0.009	0.052	0.009
NGI 46	Carb.	17.23	0.228	0.397	0.047	0.187	0.038	0.020	0.020	0.049	0.008	0.047	0.011	0.035	0.005	0.029	0.005
NGI 48	Carb.	17.98	0.380	0.724	0.084	0.363	0.081	0.045	0.045	0.105	0.016	0.103	0.024	0.077	0.011	0.066	0.012
NGI 50.85	Carb.	19.05	0.340	0.620	0.072	0.293	0.065	0.029	0.029	0.080	0.013	0.080	0.019	0.062	0.009	0.054	0.010
NGI 52.2	Carb.	19.55	0.383	0.700	0.085	0.374	0.093	0.066	0.067	0.130	0.023	0.156	0.039	0.129	0.018	0.114	0.020
NGI 55.2	Carb.	20.68	0.366	0.629	0.078	0.362	0.091	0.065	0.065	0.132	0.022	0.147	0.037	0.119	0.017	0.104	0.020
NGI 57	Carb.	21.35	0.387	0.678	0.080	0.350	0.084	0.060	0.060	0.118	0.020	0.128	0.031	0.098	0.014	0.081	0.014
NGI 60	Carb.	22.48	0.422	0.760	0.091	0.389	0.087	0.059	0.059	0.114	0.018	0.115	0.027	0.086	0.012	0.071	0.013
NGI 62.6	Carb.	23.45	0.652	1.088	0.125	0.517	0.109	0.103	0.104	0.138	0.022	0.137	0.032	0.099	0.014	0.087	0.016
NGI 64	Carb.	23.97	0.491	0.788	0.092	0.388	0.085	0.051	0.052	0.104	0.015	0.087	0.019	0.056	0.007	0.041	0.007

Sample	Lithology	Strat-depth (m)	La	Ce	Pr	Nd	Sm	Eu	Gd	Tb	Dy	Y	Ho	Er	Tm	Yb	Lu
NGI 66.45	Carb.	24.89	1.228	2.138	0.243	0.973	0.178	0.102	0.104	0.207	0.029	0.164	0.036	0.106	0.014	0.087	0.015
NGI 68	Carb.	25.47	0.334	0.494	0.058	0.257	0.060	0.055	0.055	0.093	0.016	0.112	0.028	0.092	0.013	0.079	0.014
NGI 70.5	Carb.	26.41	0.442	0.686	0.079	0.328	0.064	0.046	0.046	0.083	0.011	0.069	0.016	0.048	0.006	0.037	0.007
NGI 73	Carb.	27.35	0.556	0.868	0.103	0.456	0.112	0.083	0.084	0.168	0.029	0.194	0.046	0.144	0.021	0.130	0.024
NGI 76	Carb.	28.47	0.583	0.848	0.092	0.372	0.069	0.041	0.042	0.090	0.012	0.070	0.016	0.049	0.006	0.037	0.006
NGI 77.3	Carb.	28.96	0.666	1.117	0.130	0.571	0.123	0.085	0.085	0.175	0.028	0.177	0.042	0.131	0.018	0.113	0.020
NGI 80	Siltstone	29.97	7.216	15.221	1.805	7.177	1.085	0.202	0.204	1.052	0.111	0.472	0.084	0.194	0.021	0.098	0.012
NGI 81	Siltstone	30.34	4.459	9.197	1.082	4.259	0.588	0.095	0.096	0.571	0.057	0.231	0.042	0.100	0.011	0.055	0.007
NGI 88	Carb.	32.97	0.673	1.250	0.159	0.714	0.157	0.110	0.112	0.194	0.031	0.191	0.044	0.138	0.019	0.118	0.020
NGI 91	Carb.	34.09	0.538	1.035	0.131	0.578	0.127	0.053	0.054	0.142	0.021	0.121	0.024	0.070	0.009	0.055	0.009
NGI 93.8	Carb.	35.14	0.457	0.895	0.116	0.477	0.100	0.054	0.053	0.112	0.017	0.103	0.024	0.074	0.010	0.061	0.010
NGI 96	Carb.	35.96	0.832	1.596	0.188	0.779	0.163	0.097	0.098	0.198	0.032	0.189	0.040	0.121	0.016	0.096	0.016
NGI 97.4	Carb.	36.49	0.531	0.951	0.110	0.472	0.105	0.067	0.067	0.136	0.023	0.152	0.037	0.119	0.017	0.107	0.019
NGI 99.5	Carb.	37.27	0.643	1.189	0.138	0.569	0.106	0.051	0.052	0.119	0.016	0.087	0.018	0.051	0.007	0.039	0.007
NGI 102	Carb.	38.21	0.268	0.452	0.053	0.208	0.037	0.022	0.022	0.041	0.005	0.027	0.006	0.018	0.002	0.013	0.002
NGI 104	Carb.	38.96	0.375	0.566	0.061	0.237	0.039	0.026	0.026	0.052	0.007	0.038	0.009	0.028	0.004	0.021	0.004
NGI 107	Carb.	40.08	0.226	0.360	0.043	0.167	0.029	0.017	0.017	0.034	0.004	0.021	0.005	0.015	0.002	0.011	0.002
NGI 112	Carb.	41.96	0.337	0.426	0.050	0.196	0.033	0.022	0.023	0.047	0.006	0.040	0.010	0.035	0.005	0.027	0.005
NGI 115	Carb.	43.08	0.364	0.635	0.075	0.308	0.063	0.035	0.036	0.090	0.014	0.087	0.022	0.069	0.009	0.056	0.010
NGI 120	Carb.	44.95	0.387	0.541	0.062	0.259	0.049	0.028	0.028	0.066	0.009	0.055	0.013	0.042	0.006	0.032	0.006
NGI 123	Carb.	46.08	0.277	0.520	0.067	0.317	0.076	0.043	0.043	0.118	0.020	0.144	0.037	0.119	0.016	0.100	0.018
NGI 126.9	Carb.	47.54	0.380	0.600	0.073	0.319	0.066	0.041	0.042	0.089	0.014	0.086	0.021	0.065	0.009	0.050	0.009
NGI 131.2	Carb.	49.15	0.346	0.712	0.089	0.391	0.089	0.068	0.068	0.105	0.016	0.095	0.021	0.063	0.008	0.048	0.008
NGI 138.4	Carb.	51.85	0.295	0.538	0.066	0.291	0.064	0.038	0.039	0.084	0.013	0.083	0.021	0.068	0.009	0.057	0.010
NGI 142	Carb.	53.19	4.363	8.423	1.005	4.360	0.920	0.294	0.302	0.878	0.109	0.498	0.086	0.200	0.022	0.120	0.017
NGI 147	Carb.	55.07	0.434	0.736	0.086	0.377	0.088	0.052	0.053	0.126	0.021	0.141	0.035	0.114	0.016	0.096	0.017

Sample	Lithology	Strat-depth (m)	La	Ce	Pr	Nd	Sm	Eu	Gd	Tb	Dy	Y	Ho	Er	Tm	Yb	Lu
NGI 150	Carb.	56.19	0.382	0.609	0.069	0.298	0.062	0.034	0.034	0.078	0.011	0.061	0.014	0.041	0.005	0.030	0.005
NGI 153	Carb.	57.31	4.966	10.056	1.252	5.315	1.101	0.259	0.263	1.026	0.124	0.548	0.092	0.223	0.027	0.166	0.027
NGI 155.8	Carb.	58.36	0.437	0.828	0.102	0.466	0.121	0.074	0.076	0.172	0.032	0.233	0.060	0.204	0.030	0.195	0.034
NGI 159.3	Carb.	59.67	0.332	0.567	0.066	0.279	0.060	0.034	0.035	0.082	0.014	0.092	0.023	0.076	0.011	0.071	0.013
NGI 162.8	Carb.	60.99	0.282	0.429	0.047	0.188	0.034	0.015	0.016	0.047	0.006	0.039	0.010	0.032	0.004	0.026	0.005
NGI 166	Carb.	62.18	0.211	0.310	0.034	0.139	0.024	0.011	0.011	0.031	0.004	0.023	0.006	0.019	0.003	0.015	0.003
NGI 168.8	Carb.	63.23	0.362	0.526	0.055	0.220	0.037	0.021	0.021	0.050	0.007	0.039	0.010	0.032	0.004	0.024	0.005
NGI 170.8	Carb.	63.98	0.462	0.747	0.083	0.350	0.068	0.037	0.037	0.093	0.014	0.092	0.023	0.076	0.010	0.063	0.012
NGI 172	Carb.	64.43	0.347	0.498	0.053	0.206	0.036	0.019	0.019	0.050	0.007	0.041	0.010	0.033	0.004	0.025	0.005
NGI 176	Carb.	65.93	0.421	0.754	0.089	0.403	0.098	0.067	0.068	0.141	0.024	0.162	0.039	0.126	0.018	0.106	0.018
NGI 179	Carb.	67.05	0.381	0.539	0.057	0.231	0.041	0.025	0.026	0.059	0.008	0.053	0.013	0.043	0.006	0.035	0.007
NGI 181.7	Carb.	68.07	0.353	0.598	0.069	0.312	0.082	0.056	0.057	0.138	0.026	0.200	0.053	0.175	0.025	0.162	0.030
NGI 184	Carb.	68.93	0.290	0.361	0.036	0.137	0.023	0.016	0.016	0.031	0.004	0.023	0.005	0.017	0.002	0.012	0.002
NGI 186.1	Carb.	69.71	0.319	0.375	0.036	0.138	0.022	0.017	0.018	0.034	0.004	0.026	0.006	0.017	0.002	0.012	0.002
NGI 188 .3	Carb.	70.54	0.277	0.297	0.028	0.103	0.017	0.017	0.018	0.026	0.004	0.022	0.005	0.017	0.002	0.014	0.002
NGI 191.1	Carb.	71.59	0.240	0.244	0.023	0.085	0.013	0.016	0.016	0.020	0.002	0.013	0.003	0.010	0.001	0.007	0.001
NGI 193	Carb.	72.30	0.464	0.774	0.087	0.356	0.071	0.038	0.038	0.092	0.014	0.085	0.020	0.065	0.009	0.053	0.009
NGI 195	Carb.	73.05	0.657	1.138	0.132	0.575	0.117	0.058	0.058	0.139	0.022	0.137	0.031	0.098	0.014	0.089	0.015
NGI 198	Carb.	74.17	4.068	6.949	0.672	2.405	0.386	0.126	0.129	0.444	0.051	0.248	0.047	0.130	0.016	0.103	0.016
NGI 199.5	BS	74.73	3.569	5.959	0.582	2.006	0.285	0.046	0.048	0.288	0.025	0.080	0.011	0.023	0.003	0.013	0.002
NGI 202	Carb.	75.67	1.478	2.284	0.214	0.659	0.087	0.021	0.021	0.104	0.010	0.039	0.006	0.015	0.002	0.008	0.001
NGI 204	BS	76.42	2.403	3.808	0.336	0.980	0.103	0.018	0.019	0.137	0.011	0.039	0.006	0.014	0.002	0.008	0.001
NGI 206	SBS	77.17	14.836	27.030	2.818	10.084	1.869	0.550	0.563	1.882	0.255	1.316	0.259	0.778	0.117	0.788	0.134
NGI 206bis	BS	77.17	16.823	31.567	3.284	11.712	2.253	0.797	0.896	2.287	0.336	1.858	0.374	1.133	0.169	1.122	0.190
NGI 207	BS	77.54	27.038	50.440	5.330	19.389	3.435	0.990	1.082	3.348	0.445	2.268	0.443	1.353	0.204	1.389	0.245
NGI 208	SBS	77.92	24.308	45.812	4.899	18.037	3.659	1.027	1.036	3.741	0.530	2.809	0.556	1.641	0.234	1.479	0.241

Sample	Lithology	Strat-depth (m)	La	Ce	Pr	Nd	Sm	Eu	Gd	Tb	Dy	Y	Ho	Er	Tm	Yb	Lu
NGI 209	BS	78.29	25.444	48.690	5.157	18.727	3.622	1.018	1.063	3.692	0.526	2.924	0.605	1.850	0.275	1.763	0.295
NGI 210	SBS	78.67	16.950	33.121	3.658	13.724	2.811	0.703	0.709	2.859	0.399	2.119	0.418	1.244	0.182	1.201	0.201
NGI 210.4	SBS	78.82	22.652	43.097	4.593	16.829	3.113	0.874	0.920	3.039	0.418	2.258	0.451	1.375	0.209	1.412	0.243
NGI 211	SBS	79.04	26.256	50.772	5.476	19.599	3.582	1.121	1.130	3.492	0.462	2.300	0.436	1.266	0.188	1.258	0.216
NGI 212.5	SBS	79.60	26.337	51.358	5.623	20.174	3.810	0.850	0.860	3.796	0.534	2.888	0.573	1.703	0.251	1.625	0.270
NGI 213	SBS	79.79	17.874	35.041	3.834	14.289	2.752	0.769	0.767	2.887	0.427	2.395	0.482	1.422	0.204	1.328	0.230
NGI 213.8	SBS	80.09	16.135	31.978	3.574	13.591	2.825	1.047	1.052	3.000	0.451	2.565	0.519	1.577	0.233	1.534	0.264
NGI 215	SBS	80.54	17.899	33.506	3.609	13.588	2.782	0.679	0.680	2.885	0.404	2.131	0.416	1.200	0.171	1.095	0.184
NGI 216.2	SBS	80.99	20.588	40.174	4.309	15.774	3.117	0.865	0.875	3.384	0.511	2.949	0.599	1.814	0.263	1.674	0.273
NGI 217.2	SBS	81.36	13.348	25.643	2.816	10.555	2.058	0.629	0.633	2.173	0.311	1.714	0.342	1.003	0.142	0.896	0.147
NGI 218.2	SBS	81.74	7.109	14.155	1.603	6.051	1.159	0.391	0.392	1.111	0.140	0.690	0.131	0.389	0.058	0.401	0.071
NGI 218.7	BIF	81.93	1.238	2.233	0.250	0.962	0.184	0.085	0.085	0.215	0.028	0.147	0.029	0.084	0.012	0.077	0.013
NGI 219	BIF	82.04	2.334	3.918	0.436	1.734	0.361	0.243	0.243	0.471	0.076	0.473	0.106	0.333	0.048	0.304	0.053
NGI 219.3	BIF	82.15	3.351	6.699	0.817	3.443	0.865	0.488	0.493	1.159	0.200	1.286	0.281	0.878	0.131	0.839	0.142
NGI 220	BIF	82.41	4.549	7.934	0.890	3.514	0.689	0.366	0.370	0.933	0.141	0.849	0.191	0.592	0.084	0.513	0.091
NGI 221	BIF	82.79	3.368	5.764	0.666	2.702	0.564	0.344	0.347	0.761	0.122	0.800	0.189	0.616	0.091	0.591	0.104
NGI 222.5	SBS	83.35	13.492	27.415	3.087	11.705	2.401	0.764	0.763	2.408	0.349	1.962	0.406	1.261	0.192	1.258	0.204
NGI 223.2	SBS	83.61	16.196	31.997	3.644	14.305	3.113	0.751	0.751	3.009	0.384	1.664	0.278	0.780	0.121	0.883	0.168
NGI 224.2	SBS	83.99	14.520	28.872	3.199	11.965	2.297	0.663	0.667	2.179	0.269	1.228	0.221	0.635	0.095	0.650	0.114
NGI 226	BS	84.66	33.266	62.218	6.662	23.017	3.474	1.230	1.296	3.430	0.378	1.695	0.313	0.857	0.118	0.736	0.118
NGI 227	BS	85.04	40.794	76.395	8.270	28.734	4.391	1.518	1.621	4.346	0.475	2.094	0.384	1.061	0.145	0.911	0.148
NGI 227.9	BS	85.37	39.267	74.392	8.019	27.784	4.274	1.443	1.528	4.323	0.486	2.210	0.412	1.127	0.154	0.958	0.154
NGI 229	BS	85.78	0.343	0.690	0.086	0.365	0.084	0.057	0.058	0.106	0.016	0.090	0.018	0.051	0.007	0.044	0.008
NGI 229.5	S-BIF	85.97	3.523	6.308	0.740	3.013	0.608	0.388	0.393	0.715	0.094	0.503	0.102	0.314	0.049	0.345	0.064
NGI 230.8	S-BIF	86.46	6.667	12.837	1.494	6.042	1.259	0.765	0.780	1.485	0.214	1.275	0.263	0.818	0.123	0.822	0.147
NGI 232	S-BIF	86.91	14.991	29.032	3.338	13.290	2.749	1.224	1.225	2.466	0.260	1.024	0.180	0.514	0.077	0.545	0.101

Sample	Lithology	Strat-depth (m)	La	Ce	Pr	Nd	Sm	Eu	Gd	Tb	Dy	Y	Ho	Er	Tm	Yb	Lu
NGI 233	BIF	87.28	2.367	4.582	0.552	2.279	0.516	0.370	0.373	0.684	0.103	0.600	0.124	0.366	0.052	0.331	0.056
NGI 234	S-BIF	87.66	10.036	19.664	2.300	9.392	1.933	1.190	1.199	2.175	0.300	1.643	0.348	1.098	0.174	1.217	0.226
NGI 235	BIF	88.03	2.162	4.615	0.555	2.240	0.520	0.303	0.306	0.739	0.132	0.898	0.209	0.691	0.106	0.696	0.122
NGI 236	BIF	88.41	1.284	2.507	0.294	1.198	0.265	0.192	0.193	0.368	0.060	0.386	0.085	0.264	0.040	0.260	0.045
NGI 237	S-BIF	88.78	5.640	10.890	1.259	5.044	1.048	0.854	0.855	1.325	0.203	1.239	0.278	0.870	0.126	0.805	0.140
NGI 238	BIF	89.16	2.017	4.147	0.489	1.960	0.428	0.287	0.287	0.566	0.089	0.545	0.119	0.372	0.057	0.372	0.065
NGI 239	BIF	89.53	2.009	3.758	0.431	1.754	0.433	0.328	0.330	0.622	0.102	0.641	0.137	0.417	0.059	0.376	0.064
NGI 240	BIF	89.91	1.200	2.422	0.298	1.257	0.314	0.201	0.211	0.419	0.073	0.481	0.106	0.338	0.051	0.346	0.059
NGI 240.2	BIF	89.98	6.544	12.396	1.407	5.652	1.149	0.566	0.584	1.408	0.212	1.264	0.277	0.859	0.129	0.827	0.145
NGI 241	BIF	90.28	1.772	3.387	0.393	1.647	0.416	0.318	0.319	0.637	0.108	0.693	0.152	0.467	0.070	0.464	0.081
NGI 242	BIF	90.65	1.822	3.396	0.407	1.751	0.400	0.267	0.268	0.597	0.094	0.583	0.131	0.402	0.058	0.368	0.063
NGI 243	BIF	91.03	0.403	0.815	0.103	0.469	0.133	0.094	0.097	0.204	0.036	0.250	0.057	0.195	0.032	0.222	0.038
NGI 244	BIF	91.40	4.725	8.866	1.049	4.377	0.949	0.758	0.789	1.323	0.211	1.322	0.301	0.967	0.150	1.014	0.189
NGI 31-1	S-BIF	94.49	10.893	21.052	2.466	9.959	1.988	0.888	0.897	2.030	0.264	1.280	0.262	0.775	0.130	0.930	0.179
NGI 31-2	S-BIF	94.87	3.016	6.076	0.743	3.177	0.825	0.651	0.663	1.201	0.234	1.623	0.408	1.355	0.228	1.549	0.282
NGI 31-3	BS	95.56	13.693	24.991	2.605	8.723	1.327	1.302	1.681	1.607	0.243	1.351	0.295	0.941	0.160	1.145	0.233
NGI 31-4	S-BIF	96.29	1.201	2.601	0.312	1.260	0.336	0.172	0.176	0.420	0.079	0.489	0.107	0.318	0.050	0.319	0.058
NGI 31-8	S-BIF	97.67	14.797	33.848	4.133	16.225	3.511	1.740	1.783	3.930	0.628	3.594	0.788	2.321	0.354	2.248	0.390
NGI 31-5	S-BIF	98.07	13.253	27.523	3.326	13.379	2.758	1.256	1.273	3.196	0.504	3.050	0.743	2.444	0.406	2.782	0.539
NGI 31-9	S-BIF	99.35	3.502	6.565	0.764	3.074	0.712	0.386	0.385	0.875	0.132	0.762	0.170	0.518	0.082	0.527	0.093
NGI 31-6	S-BIF	99.45	16.977	35.949	4.259	16.263	3.237	1.158	1.175	3.404	0.546	3.268	0.740	2.288	0.369	2.409	0.421
NGI 31-7	S-BIF	99.96	18.234	37.948	4.537	17.430	3.500	1.273	1.279	3.532	0.536	3.106	0.692	2.130	0.336	2.199	0.382
NGI 31-10	S-BIF	101.99	6.161	12.815	1.576	6.614	1.760	1.082	1.076	2.326	0.407	2.489	0.567	1.700	0.258	1.606	0.284
NGI 31-11	S-BIF	103.11	13.854	31.165	3.938	15.910	3.390	1.348	1.350	3.614	0.497	2.419	0.474	1.286	0.185	1.203	0.230
NGI 31-12	BIF	103.25	5.894	13.334	1.754	7.465	1.979	0.945	0.937	2.407	0.385	2.073	0.422	1.181	0.174	1.167	0.229
NGI 31-13	S-BIF	104.31	48.088	86.138	9.257	34.855	6.628	2.070	2.064	6.809	0.808	3.521	0.681	1.839	0.269	1.809	0.336

Sample	Lithology	Strat-depth (m)	La	Ce	Pr	Nd	Sm	Eu	Gd	Tb	Dy	Y	Ho	Er	Tm	Yb	Lu
NGI 31-14	S-BIF	105.93	9.190	21.996	2.715	10.364	2.128	0.887	0.900	2.039	0.298	1.547	0.329	0.980	0.152	1.031	0.173
NGI 31-15	S-BIF	106.96	18.871	40.623	4.824	18.576	3.895	1.809	1.803	4.431	0.717	4.200	0.913	2.713	0.411	2.625	0.447
NGI 31-16	BIF	107.26	1.053	1.892	0.224	0.929	0.209	0.133	0.135	0.274	0.039	0.207	0.044	0.116	0.016	0.092	0.017
NGI 31-17	SBS	108.62	26.657	54.644	6.335	24.274	4.353	2.185	2.171	3.983	0.422	1.614	0.300	0.811	0.123	0.832	0.153
NGI 31-18	SBS	109.06	28.545	59.143	6.740	25.092	4.867	1.268	1.287	4.934	0.722	3.834	0.767	2.169	0.324	2.076	0.347
NGI 31-19	BIF	110.71	2.371	4.833	0.617	2.880	0.732	0.478	0.485	1.194	0.218	1.457	0.359	1.106	0.167	1.027	0.184
NGI 31-20	S-BIF	120.52	9.897	17.010	1.880	7.270	1.305	0.526	0.528	1.585	0.220	1.162	0.251	0.726	0.107	0.660	0.113
NGI 31-21	SBS	122.00	56.988	120.21	14.341	56.243	11.920	3.823	3.858	12.362	1.724	8.106	1.474	3.879	0.535	3.273	0.537
NGI 31-22	BIF	122.02	2.759	5.857	0.719	3.128	0.851	0.876	0.884	1.257	0.235	1.489	0.340	1.026	0.160	1.028	0.176
NGI 31-23	SBS	123.41	1.718	3.202	0.354	1.341	0.308	0.264	0.266	0.353	0.048	0.224	0.044	0.117	0.017	0.108	0.018
NGI 31-24	SBS	125.86	21.975	43.282	5.129	20.558	4.534	1.649	1.663	4.739	0.691	3.734	0.796	2.355	0.370	2.337	0.402
NGI 31-25	Carb.	141.96	1.345	2.195	0.279	1.216	0.258	0.237	0.242	0.295	0.041	0.216	0.043	0.110	0.014	0.075	0.013

Appendix A.3. $\delta^{56}Fe$, $\delta^{34}S$, Fe and S concentrations of the 2.94 Ga Red Lake samples in this study (2SD=0.007)

Sample	Lithology	Strat-depth (m)	Digestion	$\delta^{56}Fe$	$\delta^{57}Fe$	$\delta^{34}S$	Fe_2O_3 (%)	Fe (ppm)	S (ppm)
NGI 8.4	Carb.	3.15	Leach	-0.94	-1.48	n.d.	3.09	9229	1174
NGI 10.5	Carb.	3.93	Total	-0.97	-1.37	n.d.	2.42	24318	107
NGI 12.5	Carb.	4.68	Leach	-1.34	-2.10	n.d.	3.83	9016	4471
NGI 13.85	Carb.	5.19	Total	-1.18	-1.73	n.d.	2.32	20376	7501
NGI 20.75	Carb.	7.77	Leach	-1.52	-2.29	n.d	n.d.	6731	n.d.
NGI 20.75	Carb.	7.77	Total	-1.38	-2.20	3.46	2.28	24435	7144
NGI 27	Carb.	10.11	Leach	-1.71	-2.48	n.d.	2.99	4546	12281
NGI 29.1	Carb.	10.90	Total	-1.21	-1.78	n.d.	1.17	16167	748
NGI 33.8	Carb.	12.66	Leach	-1.66	-2.49	n.d.	n.d.	15511	n.d.
NGI 33.8	Carb.	12.66	Total	-1.48	-2.23	-0.79	9.92	67726	29820
NGI 39.45	Carb.	14.78	Leach	-1.79	-2.63	n.d.	7.08	11351	21617
NGI 43.65	Carb.	16.35	Total	-1.40	-1.98	-4.15	0.59	9439	346
NGI 48	Carb.	17.98	Leach	-1.71	-2.58	n.d.	1.75	5886	1025
NGI 52.2	Carb.	19.55	Total	-1.28	-1.86	-2.67	3.20	27647	3071
NGI 55.2	Carb.	20.68	Total	-1.17	-1.66	n.d.	6.20	42576	3652
NGI 57	Carb.	21.35	Leach	-1.42	-2.17	n.d.	6.91	13978	1566
NGI 62.6	Carb.	23.45	Total	-1.14	-1.66	4.97	4.77	31597	1456
NGI 64	Carb.	23.97	Leach	-1.31	-2.04	n.d.	n.d.	13096	n.d.
NGI 70.5	Carb.	26.41	Leach	-1.03	-1.62	n.d.	n.d.	6482	n.d.
NGI 70.5	Carb.	26.41	Total	-0.90	-1.36	3.31	2.00	16241	263
NGI 76	Carb.	28.47	Total	-0.94	-1.38	n.d.	1.23	13350	410
NGI 81	Siltstone	30.34	Total	-0.83	-1.23	n.d.	10.78	79937	85
NGI 88	Carb.	32.97	Total	-0.76	-1.14	n.d.	4.41	49071	1808
NGI 88	Carb.	32.97	Leach	-0.89	-1.34	n.d.	n.d.	17705	n.d.
NGI 96	Carb.	35.96	Total	-1.04	-1.50	-0.63	4.11	26872	4110

Sample	Lithology	Strat-depth (m)	Digestion	$\delta^{56}Fe$	$\delta^{57}Fe$	$\delta^{34}S$	Fe_2O_3 (%)	Fe (ppm)	S (ppm)
NGI 97.4	Carb.	36.49	Leach	-1.30	-1.95	n.d.	7.09	16067	1897
NGI 104	Carb.	38.96	Total	-0.71	-1.04	5.46	2.86	25867	1262
NGI 107	Carb.	40.08	Leach	-0.73	-1.08	n.d.	2.39	5301	363
NGI 112	Carb.	41.96	Total	-0.45	-0.72	0.15	2.81	22817	98
NGI 115	Carb.	43.08	Total	-0.64	-0.91	n.d.	3.60	27496	349
NGI 123	Carb.	46.08	Leach	-0.93	-1.32	n.d.	3.64	7247	407
NGI 126.9	Carb.	47.54	Total	-0.68	-1.01	n.d.	2.61	20076	75
NGI 131.2	Carb.	49.15	Total	-0.88	-1.24	n.d.	2.94	22250	438
NGI 138.4	Carb.	51.85	Total	-0.92	-1.42	3.98	2.30	22417	257
NGI 147	Carb.	55.07	Leach	-1.26	-1.91	n.d.	4.93	11356	5969
NGI 155.8	Carb.	58.36	Leach	-2.07	-3.08	n.d.	n.d.	11417	n.d.
NGI 155.8	Carb.	58.36	Total	-1.65	-2.47	-4.90	16.34	99844	100688
NGI 162.8	Carb.	60.99	Total	-1.27	-1.84	3.98	1.23	12435	1672
NGI 168.8	Carb.	63.23	Leach	-0.75	-1.11	n.d.	n.d.	7751	n.d.
NGI 168.8	Carb.	63.23	Total	-0.67	-0.97	7.76	2.73	20337	104
NGI 176	Carb.	65.93	Leach	-1.59	-2.45	n.d.	4.74	9636	16457
NGI 181.7	Carb.	68.07	Total	-1.03	-1.56	1.85	3.02	21179	6059
NGI 184	Carb.	68.93	Leach	-0.61	-1.00	n.d.	3.17	6966	384
NGI 191.1	Carb.	71.59	Leach	-0.46	-0.66	n.d.	n.d.	7662	n.d.
NGI 191.1	Carb.	71.59	Total	-0.54	-0.71	3.15	2.84	21158	109
NGI 198	Carb.	74.17	Leach	-0.95	-1.39	n.d.	6.67	9045	12900
NGI 204	BS	76.42	Total	0.05	0.13	n.d.	0.39	181	434
NGI 206	SBS	77.17	Total	-0.31	-0.47	2.66	6.20	37506	30257
NGI 206bis	BS	77.17	Total	-0.59	-0.96	1.37	1.82	13987	6284
NGI 207	BS	77.54	Total	-0.60	-0.93	1.03	2.21	18091	8016
NGI 208	SBS	77.92	Total	-0.42	-0.67	1.44	7.03	54871	29806

Sample	Lithology	Strat-depth (m)	Digestion	$\delta^{56}Fe$	$\delta^{57}Fe$	$\delta^{34}S$	Fe_2O_3 (%)	Fe (ppm)	S (ppm)
NGI 209	BS	78.29	Total	-0.25	-0.34	0.43	n.d.	18804	n.d.
NGI 210	SBS	78.67	Total	-0.84	-1.26	1.02	14.66	91521	67700
NGI 210.4	SBS	78.82	Total	-1.01	-1.50	-0.21	3.46	23134	12206
NGI 211	SBS	79.04	Total	-1.50	-2.24	-1.75	8.23	56476	39916
NGI 212.5	SBS	79.60	Total	-1.91	-2.83	2.31	7.49	52992	36469
NGI 213	SBS	79.79	Total	-1.95	-2.88	2.8	21.60	128196	147542
NGI 213.8	SBS	80.09	Total	-1.72	-2.53	2.65	12.33	85419	78565
NGI 215	SBS	80.54	Total	-1.72	-2.52	0.05	27.85	202162	183325
NGI 216.2	SBS	80.99	Total	-1.83	-2.69	1.85	14.95	93446	78700
NGI 217.2	SBS	81.36	Total	-1.58	-2.30	2.59	11.56	50291	42854
NGI 218.2	SBS	81.74	Total	-1.56	-2.31	3.84	53.43	392087	245052
NGI 218.7	BIF	81.93	Total	-0.04	-0.01	2.7	2.95	15250	1615
NGI 219	BIF	82.04	Total	0.40	0.43	2.83	22.26	142483	9055
NGI 219.3	BIF	82.15	Total	-0.23	-0.47	2.66	50.54	363466	19125
NGI 220	BIF	82.41	Total	-0.84	-1.20	2.84	28.76	227999	20011
NGI 221	BIF	82.79	Total	0.34	0.61	2.63	34.57	243351	30899
NGI 222.5	SBS	83.35	Total	-1.82	-2.65	3.14	24.45	129483	102316
NGI 223.2	SBS	83.61	Total	-2.14	-3.14	3.04	21.82	137221	88345
NGI 224.2	SBS	83.99	Total	-2.88	-4.26	2.94	45.23	323959	210658
NGI 226	BS	84.66	Total	-0.21	-0.22	n.d.	8.86	41435	8192
NGI 227	BS	85.04	Total	-0.08	-0.11	n.d.	7.11	47406	6582
NGI 227.9	BS	85.37	Total	-0.67	-0.89	n.d.	7.45	49119	5750
NGI 229	BS	85.78	Total	0.82	1.21	n.d.	3.55	17468	4723
NGI 229.5	S-BIF	85.97	Total	1.00	1.53	n.d.	18.71	95810	34524
NGI 230.8	S-BIF	86.46	Total	1.14	1.75	1.58	22.84	166534	27639
NGI 232	S-BIF	86.91	Total	1.32	1.98	n.d.	39.95	314430	154499

Sample	Lithology	Strat-depth (m)	Digestion	$\delta^{56}Fe$	$\delta^{57}Fe$	$\delta^{34}S$	Fe_2O_3 (%)	Fe (ppm)	S (ppm)
NGI 233	BIF	87.28	Total	1.50	2.31	n.d.	38.15	251097	5331
NGI 234	S-BIF	87.66	Total	-0.19	-0.15	n.d.	55.24	393899	97478
NGI 235	BIF	88.03	Total	0.42	0.74	n.d.	40.50	281890	2697
NGI 236	BIF	88.41	Total	-0.30	-0.41	0.41	11.62	59746	9084
NGI 237	S-BIF	88.78	Total	-0.51	-0.70	n.d.	45.49	308113	90905
NGI 238	BIF	89.16	Total	0.89	1.40	n.d.	32.39	168412	5186
NGI 239	BIF	89.53	Total	0.59	1.02	n.d.	23.76	149431	1174
NGI 240	BIF	89.91	Total	0.61	0.96	-0.82	22.71	114594	3042
NGI 240.2	BIF	89.98	Total	-0.11	-0.05	n.d.	47.95	255518	11048
NGI 241	BIF	90.28	Total	0.17	0.37	n.d.	32.28	168122	2060
NGI 242	BIF	90.65	Total	0.73	1.11	n.d.	55.27	410888	445
NGI 243	BIF	91.03	Total	0.33	0.53	n.d.	34.76	253014	84
NGI 244	BIF	91.40	Total	-0.28	-0.35	n.d.	52.56	399563	7713
NGI 31-1	S-BIF	94.49	Total	-0.39	-0.57	n.d.	59.01	190939	69755
NGI 31-2	S-BIF	94.87	Total	-0.34	-0.49	n.d.	54.06	176202	25102
NGI 31-3	BS	95.56	Total	-0.65	-0.93	n.d.	29.85	91975	9351
NGI 31-4	S-BIF	96.29	Total	-1.16	-1.77	n.d.	10.96	34189	32053
NGI 31-5	S-BIF	98.07	Total	-0.32	-0.47	n.d.	45.86	155356	38822
NGI 31-6	S-BIF	99.45	Total	-0.55	-0.78	n.d.	60.81	206656	203258
NGI 31-7	S-BIF	99.96	Total	-0.41	-0.61	n.d.	60.83	198444	193670
NGI 31-8	S-BIF	97.67	Total	0.23	0.34	n.d.	52.95	173583	40701
NGI 31-9	S-BIF	99.35	Total	1.03	1.51	n.d.	20.96	70589	7489
NGI 31-10	S-BIF	101.99	Total	0.24	0.32	n.d.	42.42	139215	32020
NGI 31-11	S-BIF	103.11	Total	0.08	0.04	n.d.	57.11	188582	12843
NGI 31-12	BIF	103.25	Total	0.12	0.15	n.d.	55.28	178312	6681
NGI 31-13	S-BIF	104.31	Total	-0.35	-0.54	n.d.	45.26	158487	78307

Sample	Lithology	Strat-depth (m)	Digestion	$\delta^{56}Fe$	$\delta^{57}Fe$	$\delta^{34}S$	Fe_2O_3 (%)	Fe (ppm)	S (ppm)
NGI 31-14	S-BIF	105.93	Total	-0.74	-1.12	n.d.	63.07	208527	236983
NGI 31-15	S-BIF	106.96	Total	-1.09	-1.59	n.d.	45.01	143429	120700
NGI 31-16	BIF	107.26	Total	0.88	1.26	n.d.	24.07	74425	1882
NGI 31-17	S-BIF	108.62	Total	-0.21	-0.31	n.d.	62.41	211562	157534
NGI 31-18	S-BIF	109.06	Total	-1.13	-1.66	n.d.	36.16	110081	123942
NGI 31-19	BIF	110.71	Total	1.10	1.64	n.d.	58.27	190134	329
NGI 31-20	S-BIF	120.52	Total	0.63	0.93	n.d.	38.98	118699	17448
NGI 31-21	SBS	122.00	Total	-0.54	-0.79	n.d.	25.68	82336	25346
NGI 31-22	BIF	122.02	Total	0.07	0.08	n.d.	34.60	102954	359
NGI 31-23	SBS	123.41	Total	-1.13	-1.64	n.d.	9.60	28093	33408
NGI 31-24	SBS	125.86	Total	-0.53	-0.76	n.d.	50.05	146852	77690
NGI 31-25	Carb.	141.96	Total	-0.45	-0.65	n.d.	7.49	24622	736
NGI 16.2 py	Pyrite	6.07	Total	-1.09	-1.503	n.d.	n.d.	n.d.	n.d.
NGI 16.2 py	Pyrite	6.07	Total	-1.58	-2.136	n.d.	n.d.	n.d.	n.d.
NGI 31.2 py	Pyrite	11.69	Total	-1.87	-2.629	n.d.	n.d.	n.d.	n.d.
NGI 31.2 py	Pyrite	11.69	Total	-1.37	-2.054	n.d.	n.d.	n.d.	n.d.
NGI 31.2 py	Pyrite	11.69	Total	-1.54	-2.228	n.d.	n.d.	n.d.	n.d.
NGI 41.75 py	Pyrite	15.64	Total	-1.80	-2.566	n.d.	n.d.	n.d.	n.d.
NGI 41.75 py	Pyrite	15.64	Total	-1.88	-2.903	n.d.	n.d.	n.d.	n.d.
NGI 44.5 py	Pyrite	16.67	Total	-1.42	-2.260	n.d.	n.d.	n.d.	n.d.
NGI 44.5 py	Pyrite	16.67	Total	-1.58	-2.410	n.d.	n.d.	n.d.	n.d.
NGI 87 py	Pyrite	32.59	Total	-0.67	-1.164	n.d.	n.d.	n.d.	n.d.
NGI 87 py	Pyrite	32.59	Total	-0.65	-0.923	n.d.	n.d.	n.d.	n.d.
NGI 87 py	Pyrite	32.59	Total	-0.69	-0.921	n.d.	n.d.	n.d.	n.d.
NGI 209 py	Pyrite	78.29	Total	-0.53	-0.613	n.d.	n.d.	n.d.	n.d.
NGI 209 py	Pyrite	78.29	Total	0.30	0.445	n.d.	n.d.	n.d.	n.d.

Sample	Lithology	Strat-depth (m)	Digestion	$\delta^{56}Fe$	$\delta^{57}Fe$	$\delta^{34}S$	Fe_2O_3 (%)	Fe (ppm)	S (ppm)
NGI 215 py	Pyrite	80.54	Total	-2.54	-3.720	n.d.	n.d.	n.d.	n.d.
NGI 215 py	Pyrite	80.54	Total	-1.63	-2.341	n.d.	n.d.	n.d.	n.d.
NGI 215 py	Pyrite	80.54	Total	-1.54	-2.192	n.d.	n.d.	n.d.	n.d.
NGI 219.3 py	Pyrite	82.15	Total	-1.01	-1.449	n.d.	n.d.	n.d.	n.d.
NGI 219.3 py	Pyrite	82.15	Total	-1.05	-1.543	n.d.	n.d.	n.d.	n.d.
NGI 223.2 py	Pyrite	83.61	Total	-2.20	-3.197	n.d.	n.d.	n.d.	n.d.
NGI 223.2 py	Pyrite	83.61	Total	-2.27	-3.307	n.d.	n.d.	n.d.	n.d.

APPENDIX B:

Appendix to chapter 5

Appendix B.1. REE, Al, Ca, Fe, Mn and Mg concentrations (ppm) from the EARTHBLOOM data.

Location	Sample	La	Ce	Pr	Nd	Sm	Eu	Gd	Tb	Dy	Ho	Er	Tm	Yb	Lu	Al	Ca	Fe	Mn	Mg
Red Lake	EBL28-347.38	0.071	0.074	0.007	0.025	0.004	0.005	0.006	NaN	0.005	0.001	0.004	NaN	0.003	NaN	1.11	33710	3426	2504	35810
Red Lake	EBL28-369.52	0.101	0.101	0.009	0.033	0.006	0.009	0.010	0.002	0.010	0.003	0.008	0.001	0.006	0.001	1.42	25518	3523	1971	27158
Red Lake	EBL28-326.38	0.170	0.197	0.018	0.067	0.010	0.009	0.015	0.002	0.012	0.003	0.009	0.001	0.007	0.001	2.51	28974	4132	2489	29144
Red Lake	EBL28-408.29	0.122	0.139	0.013	0.054	0.012	0.010	0.018	0.003	0.018	0.004	0.013	0.002	0.010	0.002	3.73	28723	4581	1860	29437
Red Lake	EBL28-402.89	0.401	0.582	0.052	0.164	0.022	0.017	0.028	0.003	0.018	0.004	0.011	0.002	0.008	0.001	1.39	32821	5919	2702	32679
Red Lake	EBL28-321.64	0.236	0.347	0.035	0.128	0.019	0.015	0.024	0.003	0.019	0.004	0.012	0.002	0.009	0.002	1.79	27936	4620	2134	31830
Red Lake	EBL28-400.3	0.102	0.133	0.014	0.050	0.010	0.009	0.016	0.003	0.016	0.004	0.012	0.002	0.008	0.002	1.85	40817	7007	3326	44732
Red Lake	EBL28-297.73	0.149	0.199	0.020	0.076	0.015	0.020	0.025	0.004	0.027	0.006	0.016	0.002	0.011	0.002	2.78	32832	6246	2652	34407
Red Lake	EBL28-376.8	0.154	0.168	0.016	0.059	0.011	0.014	0.018	0.003	0.020	0.005	0.014	0.002	0.010	0.002	1.72	41751	5272	2985	43363
Red Lake	EBL28-311.35	0.207	0.324	0.035	0.128	0.021	0.012	0.025	0.003	0.019	0.004	0.013	0.002	0.010	0.002	1.75	30272	3863	2196	32057
Red Lake	EBL28-373.40	0.139	0.151	0.015	0.053	0.010	0.014	0.016	0.003	0.019	0.005	0.014	0.002	0.010	0.002	1.91	36245	5420	2877	38706
Red Lake	EBL28-395.56	0.164	0.189	0.018	0.064	0.009	0.005	0.014	0.002	0.012	0.003	0.011	0.002	0.009	0.002	2.89	31589	5216	3135	31784
Red Lake	EBL28-397.02	0.125	0.131	0.012	0.046	0.007	0.006	0.012	0.002	0.013	0.004	0.013	0.002	0.011	0.002	4.44	34269	3936	2902	36373
Red Lake	EBL28-378.10	0.211	0.285	0.029	0.110	0.019	0.018	0.025	0.004	0.022	0.005	0.015	0.002	0.011	0.002	1.82	30513	6013	2377	32196
Red Lake	EBL28-318.36	0.343	0.515	0.053	0.198	0.031	0.023	0.036	0.005	0.025	0.006	0.016	0.002	0.012	0.002	1.52	27322	3533	2136	29529
Red Lake	EBL28-411.24	0.093	0.106	0.011	0.045	0.009	0.007	0.016	0.003	0.020	0.005	0.016	0.002	0.012	0.002	1.28	27791	4221	2490	27945
Red Lake	EBL28-368.09	0.204	0.243	0.024	0.093	0.018	0.017	0.027	0.005	0.029	0.007	0.021	0.003	0.017	0.003	1.98	35508	4832	2980	37961
Red Lake	EBL28-357	0.272	0.379	0.038	0.142	0.025	0.024	0.034	0.005	0.030	0.007	0.021	0.003	0.015	0.002	1.59	33762	4528	2610	34741
Red Lake	EBL28-436.44	0.190	0.290	0.030	0.110	0.020	0.021	0.029	0.005	0.029	0.007	0.020	0.003	0.015	0.003	1.21	27714	5555	2339	28307
Red Lake	EBL28-322.95	0.371	0.560	0.057	0.208	0.034	0.026	0.041	0.006	0.029	0.007	0.019	0.003	0.013	0.002	3.66	35711	6280	2525	38736
Red Lake	EBL28-421.44	0.163	0.225	0.024	0.098	0.021	0.015	0.031	0.005	0.030	0.007	0.021	0.003	0.014	0.003	1.41	28436	3767	1874	31253
Red Lake	EBL28-416.30	0.155	0.188	0.019	0.073	0.014	0.012	0.024	0.004	0.024	0.006	0.019	0.003	0.015	0.003	6.52	31795	5001	2561	34399
Red Lake	EBL28-360.4	0.314	0.352	0.033	0.122	0.021	0.026	0.032	0.005	0.031	0.008	0.024	0.003	0.018	0.003	3.21	33954	4993	2767	35158
Red Lake	EBL28-433.56	0.189	0.254	0.026	0.095	0.019	0.020	0.030	0.005	0.033	0.008	0.024	0.003	0.019	0.003	1.69	33689	5541	2747	32163
Red Lake	EBL28-332.5	0.603	0.862	0.088	0.329	0.057	0.034	0.066	0.009	0.047	0.010	0.026	0.003	0.020	0.003	3.56	38190	4993	2932	38742
Red Lake	EBL28-344.15	0.328	0.527	0.056	0.221	0.043	0.031	0.052	0.008	0.049	0.011	0.033	0.005	0.028	0.005	3.03	31046	5700	2925	30088
Red Lake	EBL28-426.25	0.181	0.244	0.025	0.101	0.022	0.017	0.035	0.006	0.041	0.010	0.030	0.004	0.023	0.004	1.89	36885	6151	3272	39224
Red Lake	EBL28-382.76	0.192	0.256	0.027	0.106	0.022	0.025	0.035	0.006	0.041	0.010	0.031	0.004	0.024	0.004	3.73	34541	9385	2789	33851
Red Lake	EBL28-387	0.350	0.473	0.048	0.178	0.032	0.032	0.044	0.007	0.043	0.010	0.030	0.004	0.024	0.004	2.64	39129	8554	2690	40579
Red Lake	EBL28-362.40	0.311	0.471	0.051	0.203	0.039	0.027	0.053	0.008	0.049	0.012	0.035	0.005	0.026	0.004	3.84	33882	6577	2904	35212
Red Lake	EBL28-365.22	0.293	0.388	0.040	0.154	0.030	0.027	0.047	0.008	0.052	0.013	0.038	0.006	0.031	0.006	3.79	33127	13945	2977	29017
Red Lake	EBL28-429.76	0.192	0.208	0.020	0.078	0.018	0.021	0.037	0.008	0.054	0.013	0.039	0.005	0.029	0.005	1.59	43909	5282	3581	46721
Red Lake	EBL28-389.46	0.337	0.501	0.055	0.218	0.041	0.025	0.054	0.008	0.051	0.012	0.033	0.005	0.025	0.005	4.01	32421	8672	3171	32178
Red Lake	EBL28-308.89	0.287	0.457	0.050	0.199	0.041	0.030	0.061	0.010	0.066	0.016	0.048	0.007	0.036	0.006	1.74	26725	5241	2496	29015
Red Lake	EBL28-451.93	0.406	0.532	0.055	0.206	0.034	0.019	0.049	0.007	0.042	0.010	0.031	0.004	0.023	0.004	7.61	28587	7153	1781	28573
Red Lake	EBL28-351	0.296	0.511	0.057	0.237	0.052	0.032	0.074	0.013	0.083	0.020	0.061	0.009	0.054	0.010	2.28	27630	4406	2446	27598
Red Lake	EBL28-351.93	0.476	0.703	0.074	0.292	0.059	0.036	0.079	0.013	0.083	0.020	0.061	0.009	0.053	0.009	1.76	26773	5699	2540	25596
Red Lake	EBL28-315.64	0.235	0.398	0.046	0.197	0.050	0.033	0.076	0.013	0.084	0.019	0.056	0.008	0.044	0.008	3.80	25772	9640	2268	23191
Red Lake	EBL28-330	0.503	0.748	0.082	0.334	0.073	0.047	0.104	0.017	0.100	0.023	0.067	0.009	0.050	0.009	2.17	30851	11541	3962	28647

Location	Sample	La	Ce	Pr	Nd	Sm	Eu	Gd	Tb	Dy	Ho	Er	Tm	Yb	Lu	Al	Ca	Fe	Mn	Mg
Red Lake	EBL28-443.28	0.456	0.718	0.077	0.301	0.055	0.031	0.079	0.012	0.073	0.018	0.055	0.007	0.043	0.008	6.64	32412	8556	1515	32603
Red Lake	EBL28-446.76	0.487	0.833	0.091	0.350	0.065	0.033	0.092	0.014	0.085	0.021	0.064	0.009	0.049	0.009	4.12	30241	8379	1884	30245
Red Lake	NGI 202	1.410	2.215	0.197	0.595	0.078	0.020	0.096	0.009	0.036	0.006	0.014	0.002	0.008	0.001	585.17	924	235	20	178
Red Lake	NGI 202	1.478	2.284	0.214	0.659	0.087	0.021	0.104	0.010	0.039	0.006	0.015	0.002	0.008	0.001	619.03	941	242	20	184
Red Lake	NGI 191.1	0.240	0.244	0.023	0.085	0.013	0.016	0.020	0.002	0.013	0.003	0.010	0.001	0.007	0.001	4.57	58949	7662	2796	32743
Red Lake	NGI 191.1	0.240	0.244	0.023	0.085	0.013	0.016	0.020	0.002	0.013	0.003	0.010	0.001	0.007	0.001	4.57	58949	7662	2796	32743
Red Lake	NGI 107	0.226	0.360	0.043	0.167	0.029	0.017	0.034	0.004	0.021	0.005	0.015	0.002	0.011	0.002	3.42	53457	5301	1395	32366
Red Lake	NGI 188 .3	0.277	0.297	0.028	0.103	0.017	0.017	0.026	0.004	0.022	0.005	0.017	0.002	0.014	0.002	3.42	55852	8387	2752	32335
Red Lake	NGI 184	0.290	0.361	0.036	0.137	0.023	0.016	0.031	0.004	0.023	0.005	0.017	0.002	0.012	0.002	4.70	50758	6966	2359	27136
Red Lake	NGI 186.1	0.319	0.375	0.036	0.138	0.022	0.017	0.034	0.004	0.026	0.006	0.017	0.002	0.012	0.002	3.99	57499	10205	2810	30743
Red Lake	NGI 102	0.268	0.452	0.053	0.208	0.037	0.022	0.041	0.005	0.027	0.006	0.018	0.002	0.013	0.002	5.42	58810	5093	1975	34561
Red Lake	NGI 166	0.211	0.310	0.034	0.139	0.024	0.011	0.031	0.004	0.023	0.006	0.019	0.003	0.015	0.003	3.29	47792	3873	2615	27217
Red Lake	NGI 10.5	0.214	0.340	0.038	0.149	0.029	0.020	0.037	0.005	0.030	0.007	0.023	0.003	0.017	0.003	3.35	56473	8070	2565	31026
Red Lake	NGI 104	0.375	0.566	0.061	0.237	0.039	0.026	0.052	0.007	0.038	0.009	0.028	0.004	0.021	0.004	22.07	60714	9793	3342	31746
Red Lake	NGI 46	0.228	0.397	0.047	0.187	0.038	0.020	0.049	0.008	0.047	0.011	0.035	0.005	0.029	0.005	4.21	35581	6318	1954	19483
Red Lake	NGI 27	0.223	0.384	0.043	0.177	0.035	0.019	0.045	0.007	0.040	0.009	0.029	0.004	0.024	0.004	1.41	60460	4546	2705	35741
Red Lake	NGI 29.1	0.250	0.430	0.048	0.197	0.038	0.023	0.050	0.007	0.044	0.010	0.033	0.004	0.027	0.005	3.54	51051	5155	2681	30145
Red Lake	NGI 162.8	0.282	0.429	0.047	0.188	0.034	0.015	0.047	0.006	0.039	0.010	0.032	0.004	0.026	0.005	7.61	54593	4633	3413	31193
Red Lake	NGI 172	0.347	0.498	0.053	0.206	0.036	0.019	0.050	0.007	0.041	0.010	0.033	0.004	0.025	0.005	5.65	42519	8217	2073	23249
Red Lake	NGI 8.4	0.153	0.246	0.028	0.114	0.025	0.021	0.040	0.007	0.050	0.012	0.040	0.005	0.032	0.006	2.38	41777	9229	2786	21582
Red Lake	NGI 13.85	0.193	0.338	0.039	0.162	0.034	0.021	0.049	0.008	0.051	0.013	0.039	0.006	0.032	0.006	2.90	34718	5168	1808	20092
Red Lake	NGI 168.8	0.362	0.526	0.055	0.220	0.037	0.021	0.050	0.007	0.039	0.010	0.032	0.004	0.024	0.005	5.05	56156	7751	2925	30056
Red Lake	NGI 168.8	0.362	0.526	0.055	0.220	0.037	0.021	0.050	0.007	0.039	0.010	0.032	0.004	0.024	0.005	5.05	56156	7751	2925	30056
Red Lake	NGI 24.65	0.239	0.404	0.045	0.185	0.036	0.019	0.051	0.008	0.048	0.012	0.037	0.005	0.030	0.006	3.07	54774	5359	2602	32293
Red Lake	NGI 150	0.382	0.609	0.069	0.298	0.062	0.034	0.078	0.011	0.061	0.014	0.041	0.005	0.030	0.005	7.39	51052	6719	2423	28386
Red Lake	NGI 179	0.381	0.539	0.057	0.231	0.041	0.025	0.059	0.008	0.053	0.013	0.043	0.006	0.035	0.007	6.06	52706	5901	2433	29201
Red Lake	NGI 99.5	0.643	1.189	0.138	0.569	0.106	0.051	0.119	0.016	0.087	0.018	0.051	0.007	0.039	0.007	24.71	56248	10702	3129	30843
Red Lake	NGI 93.8	0.457	0.895	0.116	0.477	0.100	0.054	0.112	0.017	0.103	0.024	0.074	0.010	0.061	0.010	41.40	39937	12115	2565	18679
Red Lake	NGI 23.05	0.287	0.502	0.057	0.233	0.047	0.028	0.062	0.010	0.061	0.015	0.046	0.006	0.039	0.007	4.62	58706	4878	2771	32618
Red Lake	NGI 43.65	0.325	0.581	0.067	0.279	0.059	0.038	0.078	0.012	0.079	0.019	0.061	0.009	0.052	0.009	5.18	38308	4218	2112	22698
Red Lake	NGI 91	0.538	1.035	0.131	0.578	0.127	0.053	0.142	0.021	0.121	0.024	0.070	0.009	0.055	0.009	3.89	49269	9358	3563	26297
Red Lake	NGI 70.5	0.442	0.686	0.079	0.328	0.064	0.046	0.083	0.011	0.069	0.016	0.048	0.006	0.037	0.007	4.56	59092	6482	3058	32771
Red Lake	NGI 70.5	0.442	0.686	0.079	0.328	0.064	0.046	0.083	0.011	0.069	0.016	0.048	0.006	0.037	0.007	4.56	59092	6482	3058	32771
Red Lake	NGI 76	0.583	0.848	0.092	0.372	0.069	0.041	0.090	0.012	0.070	0.016	0.049	0.006	0.037	0.006	4.68	67088	5423	3030	37694
Red Lake	NGI 131.2	0.346	0.712	0.089	0.391	0.089	0.068	0.105	0.016	0.095	0.021	0.063	0.008	0.048	0.008	10.23	36603	9860	2270	18807
Red Lake	NGI 50.85	0.340	0.620	0.072	0.293	0.065	0.029	0.080	0.013	0.080	0.019	0.062	0.009	0.054	0.010	27.48	56413	8402	2931	31235
Red Lake	NGI 112	0.337	0.426	0.050	0.196	0.033	0.022	0.047	0.006	0.040	0.010	0.035	0.005	0.027	0.005	3.99	60113	8104	2267	33782
Red Lake	NGI 64	0.491	0.788	0.092	0.388	0.085	0.051	0.104	0.015	0.087	0.019	0.056	0.007	0.041	0.007	14.16	54114	13096	4252	28057
Red Lake	NGI 20.75	0.306	0.532	0.061	0.253	0.052	0.030	0.071	0.011	0.070	0.017	0.054	0.007	0.044	0.008	3.36	64900	6731	3041	37030
Red Lake	NGI 20.75	0.306	0.532	0.061	0.253	0.052	0.030	0.071	0.011	0.070	0.017	0.054	0.007	0.044	0.008	3.36	64900	6731	3041	37030

Location	Sample	La	Ce	Pr	Nd	Sm	Eu	Gd	Tb	Dy	Ho	Er	Tm	Yb	Lu	Al	Ca	Fe	Mn	Mg
Red Lake	NGI 120	0.387	0.541	0.062	0.259	0.049	0.028	0.066	0.009	0.055	0.013	0.042	0.006	0.032	0.006	10.48	56028	9207	1993	31441
Red Lake	NGI 193	0.464	0.774	0.087	0.356	0.071	0.038	0.092	0.014	0.085	0.020	0.065	0.009	0.053	0.009	6.17	54810	10764	2922	29634
Red Lake	NGI 159.3	0.332	0.567	0.066	0.279	0.060	0.034	0.082	0.014	0.092	0.023	0.076	0.011	0.071	0.013	6.46	45229	6658	2481	24227
Red Lake	NGI 12.5	0.320	0.596	0.069	0.297	0.064	0.040	0.085	0.014	0.090	0.022	0.073	0.011	0.064	0.012	3.74	48702	8763	2754	25278
Red Lake	NGI 12.5	0.326	0.603	0.071	0.302	0.064	0.041	0.086	0.014	0.092	0.023	0.075	0.011	0.067	0.012	3.94	49759	9016	2812	27410
Red Lake	NGI 48	0.380	0.724	0.084	0.363	0.081	0.045	0.105	0.016	0.103	0.024	0.077	0.011	0.066	0.012	3.32	56438	5886	3369	31370
Red Lake	NGI 138.4	0.295	0.538	0.066	0.291	0.064	0.038	0.084	0.013	0.083	0.021	0.068	0.009	0.057	0.010	12.51	57441	7353	2999	33125
Red Lake	NGI 170.8	0.462	0.747	0.083	0.350	0.068	0.037	0.093	0.014	0.092	0.023	0.076	0.010	0.063	0.012	8.11	52068	9827	2725	27019
Red Lake	NGI 62.6	0.652	1.088	0.125	0.517	0.109	0.103	0.138	0.022	0.137	0.032	0.099	0.014	0.087	0.016	6.81	40980	20037	5113	16707
Red Lake	NGI 115	0.364	0.635	0.075	0.308	0.063	0.035	0.090	0.014	0.087	0.022	0.069	0.009	0.056	0.010	8.33	49219	9453	2182	27861
Red Lake	NGI 195	0.657	1.138	0.132	0.575	0.117	0.058	0.139	0.022	0.137	0.031	0.098	0.014	0.089	0.015	17.40	56928	11409	2220	30533
Red Lake	NGI 195	0.657	1.138	0.132	0.575	0.117	0.058	0.139	0.022	0.137	0.031	0.098	0.014	0.089	0.015	17.40	56928	11409	2220	30533
Red Lake	NGI 68	0.334	0.494	0.058	0.257	0.060	0.055	0.093	0.016	0.112	0.028	0.092	0.013	0.079	0.014	4.59	33462	10989	2571	16089
Red Lake	NGI 60	0.422	0.760	0.091	0.389	0.087	0.059	0.114	0.018	0.115	0.027	0.086	0.012	0.071	0.013	9.56	45550	15491	4012	22430
Red Lake	NGI 66.45	1.228	2.138	0.243	0.973	0.178	0.102	0.207	0.029	0.164	0.036	0.106	0.014	0.087	0.015	56.07	50411	13320	3289	23255
Red Lake	NGI 60	0.431	0.771	0.091	0.389	0.088	0.061	0.116	0.018	0.115	0.027	0.087	0.012	0.072	0.013	9.69	47173	15712	4132	22248
Red Lake	NGI 126.9	0.380	0.600	0.073	0.319	0.066	0.041	0.089	0.014	0.086	0.021	0.065	0.009	0.050	0.009	4.97	60802	8359	2220	33943
Red Lake	NGI 96	0.832	1.596	0.188	0.779	0.163	0.097	0.198	0.032	0.189	0.040	0.121	0.016	0.096	0.016	11.11	46063	13148	2895	22770
Red Lake	NGI 38.25	0.381	0.707	0.086	0.383	0.096	0.067	0.130	0.022	0.145	0.034	0.109	0.015	0.096	0.017	5.50	36621	7944	2334	19673
Red Lake	NGI 97.4	0.531	0.951	0.110	0.472	0.105	0.067	0.136	0.023	0.152	0.037	0.119	0.017	0.107	0.019	20.20	54583	16067	3355	27792
Red Lake	NGI 57	0.387	0.678	0.080	0.350	0.084	0.060	0.118	0.020	0.128	0.031	0.098	0.014	0.081	0.014	10.29	46590	13978	3740	23209
Red Lake	NGI 88	0.673	1.250	0.159	0.714	0.157	0.110	0.194	0.031	0.191	0.044	0.138	0.019	0.118	0.020	16.13	62184	17705	3811	29700
Red Lake	NGI 88	0.673	1.250	0.159	0.714	0.157	0.110	0.194	0.031	0.191	0.044	0.138	0.019	0.118	0.020	16.13	62184	17705	3811	29700
Red Lake	NGI 176	0.421	0.754	0.089	0.403	0.098	0.067	0.141	0.024	0.162	0.039	0.126	0.018	0.106	0.018	9.14	34215	9636	2371	17029
Red Lake	NGI 147	0.434	0.736	0.086	0.377	0.088	0.052	0.126	0.021	0.141	0.035	0.114	0.016	0.096	0.017	15.50	41886	11356	2786	21241
Red Lake	NGI 18.65	0.356	0.722	0.086	0.377	0.094	0.077	0.134	0.024	0.166	0.042	0.137	0.020	0.124	0.023	2.60	51812	8979	2650	29003
Red Lake	NGI 123	0.277	0.520	0.067	0.317	0.076	0.043	0.118	0.020	0.144	0.037	0.119	0.016	0.100	0.018	4.42	44589	7247	1740	25334
Red Lake	NGI 55.2	0.366	0.629	0.078	0.362	0.091	0.065	0.132	0.022	0.147	0.037	0.119	0.017	0.104	0.020	8.36	44712	16068	3716	20720
Red Lake	NGI 52.2	0.383	0.700	0.085	0.374	0.093	0.066	0.130	0.023	0.156	0.039	0.129	0.018	0.114	0.020	6.79	49575	7110	2632	27902
Red Lake	NGI 142	4.363	8.423	1.005	4.360	0.920	0.294	0.878	0.109	0.498	0.086	0.200	0.022	0.120	0.017	711.31	19845	7400	744	6828
Red Lake	NGI 77.3	0.666	1.117	0.130	0.571	0.123	0.085	0.175	0.028	0.177	0.042	0.131	0.018	0.113	0.020	21.60	39012	12352	3603	17208
Red Lake	NGI 155.8	0.437	0.828	0.102	0.466	0.121	0.074	0.172	0.032	0.233	0.060	0.204	0.030	0.195	0.034	82.81	35096	11417	2556	16902
Red Lake	NGI 153	4.966	10.056	1.252	5.315	1.101	0.259	1.026	0.124	0.548	0.092	0.223	0.027	0.166	0.027	535.52	15344	3883	855	5261
Red Lake	NGI 73	0.556	0.868	0.103	0.456	0.112	0.083	0.168	0.029	0.194	0.046	0.144	0.021	0.130	0.024	10.91	38651	8668	2562	18405
Red Lake	NGI 181.7	0.353	0.598	0.069	0.312	0.082	0.056	0.138	0.026	0.200	0.053	0.175	0.025	0.162	0.030	20.70	43199	7412	2937	22186
Red Lake	NGI 33.8	0.502	0.958	0.116	0.512	0.139	0.124	0.198	0.039	0.271	0.065	0.215	0.033	0.224	0.043	9.64	46246	15511	3131	23245
Red Lake	NGI 33.8	0.502	0.958	0.116	0.512	0.139	0.124	0.198	0.039	0.271	0.065	0.215	0.033	0.224	0.043	9.64	46246	15511	3131	23245
Red Lake	NGI 36	0.536	1.059	0.127	0.557	0.135	0.090	0.183	0.032	0.214	0.052	0.173	0.025	0.161	0.029	9.42	54058	8262	3528	30110
Red Lake	NGI 39.45	0.870	1.602	0.191	0.833	0.220	0.159	0.286	0.052	0.336	0.078	0.259	0.040	0.279	0.053	10.06	55321	11351	3602	28062
Red Lake	PB32-165	0.100	0.149	0.016	0.061	0.010	0.006	0.012	0.002	0.008	0.002	0.006	NaN	0.004	NaN	3.06	23829	5385	1112	26012

Location	Sample	La	Ce	Pr	Nd	Sm	Eu	Gd	Tb	Dy	Ho	Er	Tm	Yb	Lu	Al	Ca	Fe	Mn	Mg
Red Lake	PB32-189.02	0.141	0.229	0.024	0.091	0.016	0.006	0.019	0.003	0.015	0.003	0.010	0.001	0.008	0.001	4.95	20168	8178	1635	19062
Red Lake	PB32-203.5	0.175	0.246	0.025	0.097	0.016	0.008	0.021	0.003	0.016	0.004	0.012	0.002	0.008	0.002	2.67	27841	3355	2628	29173
Red Lake	PB32-24.25	0.273	0.383	0.037	0.132	0.019	0.015	0.026	0.003	0.020	0.005	0.015	0.002	0.012	0.002	3.88	24660	4579	1984	26615
Red Lake	PB32-123.2	0.070	0.128	0.015	0.064	0.016	0.011	0.023	0.004	0.028	0.007	0.021	0.003	0.018	0.003	3.75	8884	7506	1160	6322
Red Lake	PB32-172.93	0.214	0.319	0.033	0.125	0.020	0.009	0.026	0.003	0.020	0.005	0.016	0.002	0.012	0.002	4.98	25285	11811	1401	22830
Red Lake	PB32-167.5	0.190	0.271	0.028	0.109	0.019	0.012	0.024	0.003	0.019	0.005	0.016	0.002	0.013	0.002	2.26	32095	9646	1845	32313
Red Lake	PB32-292.37	0.238	0.302	0.030	0.105	0.018	0.009	0.024	0.003	0.021	0.005	0.017	0.002	0.014	0.003	12.33	29482	6292	2522	29801
Red Lake	PB32-295.80	0.113	0.132	0.013	0.050	0.010	0.010	0.017	0.003	0.018	0.005	0.016	0.002	0.013	0.002	3.75	33018	4244	2582	33393
Red Lake	PB32-159.13	0.192	0.225	0.022	0.086	0.014	0.011	0.023	0.003	0.022	0.006	0.018	0.003	0.015	0.003	1.47	24080	17280	1564	18706
Red Lake	PB32-143.3	0.302	0.512	0.053	0.197	0.035	0.020	0.044	0.007	0.040	0.009	0.026	0.004	0.021	0.004	3.36	28457	7305	2554	27966
Red Lake	PB32-92.2	0.302	0.442	0.045	0.168	0.031	0.018	0.038	0.006	0.034	0.008	0.024	0.003	0.020	0.003	4.94	22196	4134	1841	23317
Red Lake	PB32-48.88	0.286	0.495	0.054	0.207	0.038	0.022	0.043	0.006	0.031	0.007	0.019	0.003	0.014	0.003	4.20	24082	6548	2288	25613
Red Lake	PB32-40.85	0.235	0.345	0.037	0.145	0.030	0.019	0.039	0.006	0.035	0.008	0.022	0.003	0.016	0.003	2.62	19238	6662	2046	18574
Red Lake	PB32-208.58	0.219	0.321	0.034	0.136	0.026	0.017	0.036	0.005	0.031	0.008	0.022	0.003	0.016	0.003	5.45	32942	7516	2895	31773
Red Lake	PB32-201.92	0.272	0.435	0.047	0.178	0.032	0.018	0.041	0.006	0.036	0.009	0.026	0.004	0.021	0.004	5.17	24357	4918	2075	24932
Red Lake	PB32-96.88	0.341	0.580	0.064	0.253	0.048	0.023	0.055	0.008	0.044	0.010	0.028	0.004	0.022	0.004	15.67	26564	4423	2530	29568
Red Lake	PB32-199.28	0.272	0.394	0.042	0.163	0.029	0.017	0.040	0.006	0.034	0.008	0.024	0.003	0.019	0.003	9.96	23876	5265	2113	25052
Red Lake	PB32-71.89	0.241	0.393	0.043	0.174	0.035	0.021	0.044	0.007	0.038	0.009	0.025	0.003	0.020	0.003	4.10	24107	5047	2097	26163
Red Lake	PB32-85.73	0.291	0.462	0.050	0.192	0.039	0.022	0.052	0.008	0.048	0.011	0.031	0.004	0.024	0.004	4.19	24349	7567	2122	24568
Red Lake	PB32-150.8	0.245	0.427	0.048	0.193	0.043	0.025	0.057	0.009	0.053	0.012	0.032	0.004	0.024	0.004	4.89	26586	8677	1873	27690
Red Lake	PB32-90.70	0.309	0.557	0.062	0.248	0.046	0.022	0.055	0.008	0.045	0.011	0.031	0.004	0.025	0.005	5.95	24352	3664	2697	26888
Red Lake	PB32-205.25	0.292	0.448	0.049	0.194	0.035	0.022	0.048	0.007	0.038	0.009	0.025	0.003	0.018	0.003	6.73	29420	7018	2622	28639
Red Lake	PB32-37.56	0.300	0.444	0.049	0.196	0.041	0.027	0.053	0.008	0.045	0.010	0.029	0.004	0.021	0.004	2.19	22232	4379	2372	23675
Red Lake	PB32-70.38	0.277	0.422	0.047	0.199	0.045	0.028	0.060	0.009	0.051	0.011	0.030	0.004	0.020	0.003	3.35	23240	5482	2307	23024
Red Lake	PB32-124.93	0.345	0.536	0.059	0.231	0.043	0.022	0.054	0.007	0.040	0.009	0.026	0.003	0.018	0.003	11.33	23684	9874	2842	21315
Red Lake	PB32-195.5	0.323	0.491	0.052	0.203	0.038	0.025	0.050	0.007	0.044	0.010	0.031	0.004	0.023	0.004	5.84	32946	6765	3253	33463
Red Lake	PB32-44.81	0.364	0.603	0.064	0.247	0.043	0.027	0.056	0.008	0.048	0.011	0.034	0.005	0.026	0.005	3.39	20441	7174	2215	20215
Red Lake	PB32-138.7	0.345	0.629	0.068	0.257	0.049	0.021	0.059	0.009	0.052	0.013	0.037	0.005	0.030	0.005	5.32	25732	7712	4572	24909
Red Lake	PB32-94.1	0.404	0.622	0.066	0.260	0.049	0.022	0.060	0.009	0.049	0.011	0.033	0.005	0.025	0.004	14.03	28248	4245	2927	29674
Red Lake	PB32-128.48	0.304	0.565	0.061	0.236	0.045	0.024	0.061	0.009	0.056	0.013	0.040	0.006	0.032	0.006	2.87	17480	10165	2631	15430
Red Lake	PB32-60.70	0.371	0.709	0.080	0.312	0.059	0.033	0.071	0.010	0.060	0.014	0.039	0.006	0.032	0.006	14.16	22993	5994	2343	22992
Red Lake	PB32-102.13	0.347	0.639	0.073	0.289	0.058	0.035	0.071	0.011	0.063	0.015	0.042	0.006	0.034	0.006	7.43	25854	5566	2861	27127
Red Lake	PB32-43.70	0.315	0.524	0.057	0.234	0.049	0.039	0.070	0.011	0.063	0.015	0.042	0.006	0.030	0.005	2.39	22741	8061	2603	21010
Red Lake	PB32-116.89	0.310	0.536	0.060	0.237	0.046	0.029	0.061	0.009	0.055	0.014	0.040	0.006	0.031	0.005	13.07	26227	4795	3029	28689
Red Lake	PB32-100.4	0.299	0.589	0.071	0.299	0.066	0.031	0.079	0.012	0.074	0.017	0.049	0.007	0.040	0.007	5.98	18932	3933	2081	19382
Red Lake	PB32-190.25	0.277	0.418	0.045	0.179	0.034	0.018	0.044	0.007	0.045	0.012	0.037	0.005	0.031	0.006	9.27	34091	4832	2500	40275
Red Lake	PB32-146.16	0.320	0.442	0.046	0.175	0.031	0.022	0.044	0.007	0.044	0.011	0.036	0.005	0.029	0.005	3.26	28238	8563	2573	28197
Red Lake	PB32-171.2	0.317	0.556	0.063	0.259	0.053	0.028	0.071	0.012	0.073	0.018	0.056	0.008	0.049	0.009	1.75	23391	6429	1260	23197
Red Lake	PB32-212.08	0.421	0.652	0.071	0.282	0.053	0.036	0.071	0.011	0.065	0.015	0.045	0.006	0.033	0.006	9.29	33569	7449	3462	32290
Red Lake	PB32-56.08	0.575	1.050	0.114	0.440	0.079	0.043	0.095	0.013	0.068	0.015	0.040	0.005	0.029	0.005	12.16	25500	8525	2267	26312

Location	Sample	La	Ce	Pr	Nd	Sm	Eu	Gd	Tb	Dy	Ho	Er	Tm	Yb	Lu	Al	Ca	Fe	Mn	Mg
Red Lake	PB32-104.85	0.319	0.575	0.066	0.266	0.053	0.028	0.070	0.011	0.070	0.017	0.054	0.008	0.047	0.009	6.05	27805	3511	3278	29504
Red Lake	PB32-65.66	0.342	0.665	0.079	0.325	0.070	0.040	0.087	0.014	0.082	0.019	0.056	0.008	0.046	0.008	69.48	22096	7782	2300	20457
Red Lake	PB32-39.11	0.333	0.525	0.059	0.246	0.054	0.039	0.075	0.012	0.073	0.017	0.050	0.007	0.037	0.006	10.37	24089	9270	3092	25067
Red Lake	PB32-31.56	0.316	0.601	0.071	0.292	0.065	0.040	0.086	0.014	0.083	0.020	0.058	0.008	0.044	0.008	4.35	24149	7456	1798	23992
Red Lake	PB32-114.1	0.365	0.721	0.084	0.348	0.076	0.040	0.096	0.016	0.096	0.022	0.065	0.009	0.052	0.009	4.24	27644	6753	2970	28168
Red Lake	PB32-121.10	0.535	0.989	0.109	0.418	0.079	0.038	0.097	0.014	0.082	0.019	0.055	0.008	0.041	0.007	10.15	24792	8059	2793	25183
Red Lake	PB32-183.38	1.912	2.276	0.204	0.697	0.100	0.038	0.127	0.017	0.094	0.022	0.068	0.010	0.061	0.011	1.47	21975	14435	1224	14104
Red Lake	PB32-194.05	0.406	0.659	0.073	0.298	0.061	0.039	0.082	0.013	0.085	0.021	0.067	0.010	0.057	0.011	4.64	30533	6428	2833	32011
Red Lake	PB32-67.93	0.251	0.471	0.056	0.241	0.058	0.044	0.087	0.015	0.095	0.023	0.068	0.010	0.056	0.010	2.69	21119	8954	2834	19956
Red Lake	PB32-50.31	0.390	0.819	0.096	0.386	0.084	0.051	0.102	0.017	0.103	0.024	0.069	0.010	0.056	0.009	14.10	24556	9362	2651	23538
Red Lake	PB32-98.57	0.449	0.802	0.095	0.406	0.092	0.046	0.116	0.018	0.110	0.025	0.072	0.010	0.056	0.009	12.44	29867	5903	3276	31854
Red Lake	PB32-197.35	0.400	0.690	0.080	0.332	0.071	0.042	0.101	0.016	0.105	0.026	0.081	0.012	0.072	0.013	6.68	25060	6778	2319	24669
Red Lake	PB32-108.35	0.377	0.698	0.081	0.343	0.078	0.042	0.111	0.020	0.126	0.030	0.088	0.013	0.073	0.013	8.94	20159	7280	2217	18416
Red Lake	PB32-21.50	0.615	1.026	0.108	0.419	0.079	0.046	0.109	0.018	0.113	0.029	0.090	0.013	0.079	0.015	25.08	28024	10088	2462	26034
Red Lake	PB32-34.62	0.331	0.608	0.074	0.312	0.075	0.047	0.106	0.018	0.114	0.027	0.082	0.011	0.065	0.011	6.36	23486	9497	2153	21431
Red Lake	PB32-88.23	0.356	0.632	0.073	0.309	0.074	0.048	0.108	0.019	0.129	0.033	0.102	0.016	0.094	0.017	9.64	33421	8431	2593	33629
Red Lake	PB32-139.87	1.320	2.501	0.257	0.923	0.151	0.056	0.173	0.025	0.146	0.035	0.107	0.016	0.097	0.018	23.67	25224	8683	4862	24880
Red Lake	PB32-112.63	0.449	0.867	0.101	0.422	0.097	0.061	0.136	0.023	0.144	0.034	0.103	0.015	0.086	0.015	5.58	31064	8384	3795	31346
Red Lake	PB32-29.24	0.560	1.030	0.119	0.487	0.110	0.063	0.149	0.025	0.155	0.036	0.106	0.015	0.090	0.016	4.52	20475	7649	2159	19939
Red Lake	PB32-27.50	0.597	1.059	0.119	0.477	0.103	0.058	0.141	0.023	0.141	0.034	0.103	0.015	0.084	0.015	15.96	26245	6926	1916	26821
Red Lake	PB32-62.29	0.600	1.190	0.137	0.543	0.110	0.057	0.142	0.023	0.139	0.034	0.103	0.014	0.085	0.016	21.03	22169	9117	2442	21010
Red Lake	PB32-118.9	0.477	0.875	0.100	0.409	0.088	0.045	0.123	0.020	0.131	0.034	0.105	0.015	0.089	0.016	9.70	24889	6455	3498	26398
Red Lake	PB32-210.2	0.559	0.922	0.107	0.453	0.098	0.060	0.149	0.025	0.168	0.044	0.138	0.020	0.119	0.022	2.81	27520	7112	2698	29429
Red Lake	PB32-148.92	0.502	0.850	0.098	0.413	0.095	0.064	0.148	0.026	0.175	0.045	0.141	0.021	0.122	0.023	5.28	26280	8298	2406	25886
Red Lake	PB33-129.05	0.311	0.382	0.038	0.140	0.023	0.017	0.031	0.004	0.023	0.005	0.016	0.002	0.011	0.002	6.45	28976	4112	2198	29713
Red Lake	PB33-232.46	0.188	0.317	0.034	0.129	0.022	0.011	0.026	0.004	0.022	0.006	0.017	0.002	0.013	0.002	4.63	27198	4883	2221	29550
Red Lake	PB33-116.73	0.200	0.270	0.028	0.110	0.020	0.013	0.028	0.004	0.023	0.005	0.016	0.002	0.011	0.002	2.27	21274	4144	1724	21474
Red Lake	PB33-235.73	0.160	0.199	0.020	0.080	0.018	0.013	0.027	0.005	0.030	0.007	0.021	0.003	0.016	0.003	2.99	28023	7581	1646	29054
Red Lake	PB33-163.13	0.273	0.482	0.053	0.203	0.036	0.016	0.041	0.006	0.030	0.007	0.020	0.003	0.015	0.003	6.99	34009	6715	2433	37461
Red Lake	PB33-112	0.411	0.489	0.046	0.159	0.026	0.019	0.031	0.004	0.023	0.005	0.016	0.002	0.012	0.002	2.43	42062	5686	3184	46904
Red Lake	PB33-238.8	0.230	0.407	0.045	0.177	0.037	0.022	0.053	0.008	0.049	0.011	0.029	0.004	0.021	0.004	4.36	24835	7186	1525	23765
Red Lake	PB33-123.58	0.488	0.584	0.056	0.214	0.035	0.023	0.050	0.006	0.035	0.008	0.023	0.003	0.016	0.003	2.52	25642	5333	2508	26650
Red Lake	PB33-157.17	0.398	0.659	0.072	0.281	0.051	0.024	0.062	0.008	0.045	0.010	0.029	0.004	0.021	0.004	5.93	27235	7189	2371	28284
Red Lake	PB33-224.52	0.419	0.756	0.088	0.347	0.061	0.027	0.067	0.009	0.045	0.010	0.027	0.004	0.019	0.003	7.88	40493	7335	1832	40671
Red Lake	PB33-138.35	0.389	0.512	0.052	0.188	0.034	0.025	0.049	0.008	0.048	0.012	0.036	0.005	0.027	0.005	3.28	34854	7682	2653	33626
Red Lake	PB33-145.63	0.580	0.845	0.085	0.307	0.052	0.029	0.066	0.009	0.054	0.013	0.038	0.005	0.031	0.006	12.62	28944	8320	2705	27388
Red Lake	PB33-134.82	0.623	0.902	0.095	0.376	0.071	0.040	0.091	0.014	0.079	0.019	0.055	0.008	0.043	0.007	3.61	36776	6328	2660	37623
Red Lake	PB33-108.27	0.660	1.063	0.119	0.465	0.082	0.043	0.101	0.014	0.079	0.019	0.055	0.008	0.042	0.007	5.78	31819	5606	2436	32371
Red Lake	PB33-215.68	0.676	1.372	0.161	0.634	0.115	0.053	0.129	0.019	0.105	0.024	0.072	0.010	0.057	0.011	15.36	30861	8166	2136	33143
Red Lake	PB35-231.97	0.165	0.237	0.024	0.088	0.017	0.010	0.022	0.003	0.021	0.005	0.015	0.002	0.014	0.002	3.66	19981	2852	1836	20450

Location	Sample	La	Ce	Pr	Nd	Sm	Eu	Gd	Tb	Dy	Ho	Er	Tm	Yb	Lu	Al	Ca	Fe	Mn	Mg
Red Lake	PB35-91.8	0.362	0.665	0.072	0.258	0.043	0.023	0.047	0.005	0.025	0.005	0.011	0.001	0.007	0.001	6.51	32793	6362	2313	37117
Red Lake	PB35-59.80	0.181	0.243	0.023	0.080	0.014	0.013	0.019	0.003	0.014	0.003	0.009	0.001	0.007	0.001	5.34	28540	8084	2367	29152
Red Lake	PB35-89.77	0.261	0.445	0.048	0.173	0.029	0.020	0.033	0.004	0.020	0.004	0.012	0.002	0.009	0.001	10.46	31282	6246	2165	33946
Red Lake	PB35-58.02	0.313	0.447	0.047	0.175	0.031	0.022	0.041	0.005	0.029	0.007	0.019	0.002	0.012	0.002	6.57	34554	15495	4125	33746
Red Lake	PB35-190.31	0.396	0.570	0.059	0.208	0.035	0.021	0.042	0.006	0.032	0.008	0.022	0.003	0.017	0.003	3.69	32452	8018	2940	32656
Red Lake	PB35-189.2	0.260	0.305	0.030	0.116	0.021	0.016	0.033	0.005	0.030	0.008	0.023	0.003	0.017	0.003	1.65	35727	8538	2902	22665
Red Lake	PB35-47.11	0.244	0.323	0.035	0.131	0.025	0.015	0.038	0.006	0.039	0.010	0.031	0.005	0.028	0.005	2.88	25878	6113	2349	28610
Red Lake	PB35-210	0.855	1.119	0.110	0.380	0.051	0.024	0.063	0.008	0.042	0.011	0.035	0.005	0.031	0.006	8.73	26629	4459	2115	19640
Red Lake	PB35-191.8	0.453	0.548	0.052	0.179	0.028	0.025	0.036	0.005	0.029	0.007	0.022	0.003	0.017	0.003	4.29	44914	7135	3447	27648
Red Lake	PB35-61.20	0.502	0.767	0.079	0.276	0.045	0.030	0.059	0.008	0.042	0.010	0.027	0.004	0.019	0.003	14.44	32819	14246	3420	32950
Red Lake	PB35-43.9	0.281	0.405	0.044	0.172	0.033	0.022	0.049	0.007	0.046	0.012	0.036	0.005	0.031	0.006	13.38	28480	9371	1793	30560
Red Lake	PB35-87.94	0.508	0.979	0.111	0.415	0.075	0.045	0.088	0.012	0.064	0.014	0.039	0.005	0.030	0.005	13.62	28861	8704	1946	32792
Red Lake	PB35-206	1.090	1.687	0.177	0.630	0.090	0.035	0.100	0.012	0.063	0.014	0.042	0.006	0.035	0.006	5.29	31076	4704	2503	28860
Red Lake	PB35-102.03	0.759	1.462	0.167	0.610	0.112	0.061	0.123	0.017	0.082	0.016	0.041	0.006	0.030	0.005	14.23	32689	9005	3055	37912
Red Lake	PB35-188.57	0.593	0.919	0.098	0.360	0.062	0.028	0.075	0.011	0.061	0.014	0.041	0.006	0.033	0.006	1.13	34267	7337	2818	25081
Red Lake	PB35-200.7	1.121	1.786	0.191	0.693	0.117	0.035	0.123	0.016	0.081	0.016	0.044	0.006	0.033	0.005	6.41	31084	5213	2858	32634
Red Lake	PB35-202.4	0.931	1.210	0.119	0.416	0.065	0.031	0.080	0.011	0.059	0.013	0.040	0.005	0.029	0.005	2.78	38677	5199	2805	28931
Red Lake	PB35-98.95	0.695	1.333	0.153	0.570	0.099	0.056	0.112	0.015	0.076	0.017	0.047	0.007	0.038	0.007	41.06	28913	10995	2637	30007
Red Lake	PB35-187.30	0.510	0.762	0.083	0.319	0.061	0.031	0.079	0.012	0.072	0.017	0.050	0.007	0.039	0.007	10.14	39270	7225	3675	32102
Red Lake	PB35-56.57	0.800	1.505	0.174	0.665	0.117	0.054	0.138	0.019	0.099	0.020	0.056	0.008	0.045	0.008	34.60	31631	14953	3929	30994
Red Lake	PB35-92.9	0.768	1.490	0.162	0.590	0.102	0.054	0.123	0.016	0.086	0.019	0.056	0.008	0.047	0.008	33.93	38960	10929	2802	40958
Red Lake	PB35-193.41	0.821	1.402	0.155	0.571	0.104	0.038	0.120	0.018	0.099	0.023	0.063	0.009	0.049	0.008	1.69	30097	5792	2631	18148
Red Lake	PB35-45.10	0.587	0.789	0.084	0.322	0.063	0.036	0.092	0.015	0.091	0.023	0.069	0.010	0.059	0.011	11.38	44160	11628	3586	49780
Red Lake	PB35-198.6	1.154	1.860	0.200	0.732	0.131	0.045	0.152	0.022	0.124	0.028	0.081	0.012	0.068	0.012	3.29	38051	6111	3339	27166
Red Lake	PB35-196.4	2.363	4.305	0.475	1.695	0.249	0.104	0.256	0.031	0.146	0.029	0.077	0.010	0.056	0.009	5.73	43081	7811	3875	38911
Red Lake	PB35-93.80	0.755	1.661	0.206	0.820	0.168	0.076	0.188	0.027	0.143	0.030	0.082	0.011	0.065	0.011	36.83	30674	9746	3101	33035
Red Lake	PB35-195.4	2.695	4.435	0.478	1.722	0.269	0.081	0.283	0.037	0.181	0.037	0.095	0.013	0.069	0.011	4.44	39373	6934	3491	32115
Red Lake	PB35-206.8	1.694	2.505	0.257	0.896	0.121	0.055	0.152	0.019	0.113	0.028	0.092	0.014	0.085	0.016	18.78	41215	6481	2842	23248
Red Lake	PB35-211.5	1.557	2.425	0.265	1.015	0.197	0.099	0.257	0.039	0.227	0.053	0.152	0.021	0.119	0.021	7.28	49780	3608	3108	11228
Red Lake	HA-12	0.032	0.026	0.003	0.010	0.002	0.002	0.003	0.001	0.004	0.001	0.005	0.001	0.004	0.001	0.38	199240	2820	4205	1151
Red Lake	RL Saw 2-2 H1	0.078	0.147	0.019	0.085	0.021	0.008	0.028	0.005	0.036	0.009	0.031	0.005	0.030	0.005	1.37	10177	768	346	143
Red Lake	HA11	0.203	0.210	0.021	0.085	0.015	0.009	0.022	0.003	0.020	0.005	0.017	0.003	0.013	0.003	1.08	254343	7365	10570	2750
Red Lake	RL Saw 2-1 H1	0.101	0.128	0.014	0.055	0.012	0.012	0.020	0.004	0.027	0.007	0.025	0.004	0.023	0.004	1.63	18758	2404	731	514
Red Lake	RL Saw 2-1 H3	0.134	0.255	0.034	0.161	0.040	0.010	0.051	0.010	0.070	0.019	0.066	0.010	0.066	0.011	0.58	18313	1163	498	286
Red Lake	HA-3A-W	0.760	1.002	0.104	0.407	0.059	0.015	0.066	0.008	0.043	0.011	0.034	0.005	0.028	0.005	12.79	210912	1323	5194	1381
Red Lake	HA-2	0.167	0.146	0.015	0.063	0.011	0.007	0.019	0.003	0.023	0.007	0.026	0.004	0.022	0.005	1.36	236273	2671	6194	1365
Red Lake	HA-82	0.670	0.823	0.085	0.332	0.057	0.083	0.085	0.011	0.070	0.017	0.050	0.007	0.036	0.005	1.72	48294	11981	3521	2137
Red Lake	HA-1	0.202	0.163	0.016	0.067	0.011	0.009	0.022	0.004	0.027	0.009	0.031	0.004	0.026	0.005	2.41	252876	3634	6142	1864
Red Lake	RL Saw 2-2 H2	0.234	0.446	0.057	0.262	0.065	0.015	0.084	0.016	0.110	0.028	0.098	0.014	0.090	0.015	0.53	20917	2213	755	516
Red Lake	HA-3A-B	0.468	0.343	0.029	0.108	0.014	0.010	0.024	0.003	0.022	0.007	0.028	0.004	0.022	0.005	8.54	220555	1494	2195	2073

Location	Sample	La	Ce	Pr	Nd	Sm	Eu	Gd	Tb	Dy	Ho	Er	Tm	Yb	Lu	Al	Ca	Fe	Mn	Mg
Red Lake	HA-calc	0.220	0.129	0.012	0.050	0.008	0.005	0.016	0.003	0.022	0.007	0.028	0.004	0.023	0.005	0.74	191732	2349	3948	1521
Red Lake	HA-3	0.389	0.220	0.018	0.071	0.010	0.008	0.021	0.003	0.025	0.009	0.034	0.005	0.028	0.006	3.29	239899	1660	2884	2010
Red Lake	HA2	0.253	0.222	0.025	0.106	0.019	0.011	0.031	0.005	0.036	0.011	0.042	0.006	0.036	0.008	5.16	264494	5000	11328	2143
Red Lake	RL Saw 2-1 H2	1.117	1.705	0.183	0.710	0.139	0.103	0.168	0.026	0.154	0.033	0.098	0.013	0.070	0.011	NaN	86832	3148	3098	605
Red Lake	HA-4	0.779	1.246	0.138	0.529	0.112	0.022	0.135	0.023	0.143	0.032	0.101	0.014	0.078	0.013	4.49	215539	2253	2669	1263
Red Lake	HA-13	0.606	1.085	0.126	0.520	0.127	0.072	0.154	0.029	0.201	0.051	0.175	0.027	0.180	0.034	0.41	130819	7772	5307	2722
Red Lake	HA3-1	1.330	1.306	0.124	0.463	0.069	0.042	0.102	0.013	0.077	0.020	0.068	0.009	0.051	0.010	1.50	284312	3896	13223	4731
Red Lake	HA-7	0.833	0.766	0.072	0.277	0.039	0.021	0.059	0.008	0.054	0.017	0.063	0.009	0.049	0.010	1.36	244652	2771	4700	1016
Red Lake	HA3-3	1.432	1.088	0.095	0.371	0.046	0.027	0.078	0.009	0.060	0.020	0.073	0.010	0.059	0.013	1.67	333638	4100	9034	5918
Red Lake	HA5	1.166	1.225	0.123	0.482	0.088	0.089	0.138	0.021	0.141	0.039	0.131	0.018	0.108	0.020	1.55	231691	3257	7113	4030
Red Lake	HA3-2	1.683	1.995	0.207	0.831	0.154	0.065	0.226	0.036	0.243	0.064	0.214	0.030	0.184	0.035	18.79	324708	4300	14665	4608
Red Lake	17-GA1-01	1.058	1.667	0.200	0.873	0.195	0.103	0.264	0.043	0.276	0.065	0.206	0.028	0.168	0.029	5.28	111042	5998	2394	1548
Red Lake	17-GA1-02	1.187	1.719	0.191	0.758	0.148	0.095	0.205	0.032	0.208	0.050	0.162	0.022	0.133	0.023	3.65	130856	5266	2466	1772
Red Lake	17-GA1-03	1.188	1.689	0.191	0.777	0.158	0.096	0.208	0.031	0.203	0.048	0.151	0.021	0.125	0.022	1.85	128434	4142	2351	1252
Red Lake	17-GA1-04	0.609	0.866	0.102	0.436	0.099	0.055	0.137	0.022	0.149	0.034	0.110	0.015	0.093	0.016	3.02	74667	5508	1696	2373
Red Lake	17-GA1-05	0.953	1.425	0.176	0.796	0.196	0.152	0.269	0.043	0.276	0.064	0.192	0.025	0.146	0.024	NaN	136254	5632	2962	1124
Red Lake	17-GA1-07	0.752	0.980	0.118	0.522	0.121	0.070	0.177	0.029	0.192	0.046	0.146	0.020	0.119	0.021	2.39	114508	4522	2235	1559
Red Lake	17-GA1-08	0.885	0.974	0.106	0.419	0.076	0.093	0.110	0.015	0.091	0.022	0.069	0.009	0.050	0.009	1.75	142334	4931	2141	2364
Red Lake	17-GA1-09	0.677	0.852	0.109	0.492	0.109	0.125	0.150	0.022	0.126	0.028	0.082	0.011	0.057	0.010	1.67	118918	5544	2035	1998
Red Lake	17-GA1-10	0.752	0.907	0.129	0.648	0.179	0.126	0.289	0.053	0.371	0.093	0.310	0.042	0.255	0.042	1.55	126554	6448	2633	1694
Red Lake	17-GA1-11	3.034	3.041	0.425	1.840	0.407	0.188	0.615	0.098	0.669	0.186	0.667	0.098	0.660	0.132	5.32	137109	8829	4940	1504
Red Lake	17-GA1-12	3.989	3.846	0.528	2.251	0.472	0.232	0.719	0.110	0.743	0.205	0.733	0.105	0.679	0.135	3.95	158907	11530	6197	2105
Red Lake	17-GA1-13	2.974	2.760	0.383	1.664	0.352	0.194	0.562	0.090	0.620	0.171	0.599	0.083	0.515	0.101	3.89	129953	13792	5059	4737
Red Lake	17-GA1-14	2.510	2.118	0.318	1.429	0.327	0.217	0.548	0.091	0.647	0.186	0.657	0.091	0.570	0.110	2.11	136963	10337	5230	1842
Red Lake	17-GA1-15	NaN	NaN	NaN	NaN	NaN	0.000	NaN	NaN	NaN	NaN	NaN	NaN	NaN	NaN	NaN	NaN	NaN	NaN	NaN
Red Lake	17-GA1-16	4.716	3.519	0.568	2.510	0.515	0.240	0.841	0.125	0.870	0.249	0.903	0.133	0.886	0.186	NaN	145738	8883	3980	3401
Red Lake	17-GA1-17	5.436	3.740	0.600	2.579	0.509	0.223	0.844	0.132	0.881	0.254	0.919	0.133	0.901	0.189	NaN	143618	7878	3787	3528
Red Lake	17-GA1-18	3.385	2.128	0.356	1.654	0.383	0.198	0.758	0.126	0.939	0.286	1.034	0.144	0.925	0.190	NaN	181648	5399	4202	1118
Red Lake	17GA1-15	4.524	3.343	0.530	2.364	0.495	0.258	0.777	0.115	0.796	0.227	0.828	0.123	0.824	0.178	3.85	156861	11479	5950	1844
Red Lake	17GA1-19	2.316	1.343	0.225	1.105	0.288	0.165	0.610	0.102	0.787	0.241	0.887	0.125	0.782	0.165	1.22	164442	6264	4283	1791
Red Lake	17GA1-20	0.762	0.663	0.115	0.574	0.136	0.146	0.234	0.036	0.247	0.065	0.208	0.025	0.131	0.022	1.70	133938	4120	2397	2001
Red Lake	17GA1-21	0.898	0.855	0.139	0.644	0.130	0.176	0.193	0.027	0.169	0.042	0.125	0.015	0.076	0.013	2.41	137677	4393	2241	2371
Red Lake	17GA1-22	2.799	2.198	0.299	1.337	0.309	0.182	0.611	0.103	0.770	0.230	0.829	0.115	0.721	0.150	5.50	153117	5952	4695	1255
Red Lake	17GA1-23	1.917	1.920	0.257	1.084	0.219	0.128	0.317	0.047	0.311	0.083	0.297	0.045	0.302	0.063	10.56	62781	50893	8959	17753
Red Lake	17GA1-24	1.297	1.292	0.171	0.734	0.154	0.101	0.239	0.038	0.267	0.073	0.253	0.036	0.227	0.044	10.39	55488	34261	6723	15996
Red Lake	17GA1-25	2.548	2.512	0.324	1.422	0.319	0.166	0.513	0.084	0.589	0.156	0.527	0.073	0.440	0.082	9.04	111393	22083	6542	10517
Red Lake	17GA1-26	2.852	2.919	0.368	1.580	0.347	0.169	0.564	0.092	0.636	0.163	0.533	0.073	0.425	0.074	6.56	108383	12273	4454	5007
Red Lake	17GA1-27	0.996	1.121	0.139	0.588	0.125	0.073	0.179	0.028	0.186	0.046	0.145	0.019	0.114	0.021	9.19	34074	23174	3774	8895
Red Lake	17GA1-28	1.123	1.525	0.192	0.869	0.185	0.229	0.243	0.032	0.176	0.035	0.093	0.012	0.057	0.010	1.36	160631	8944	2893	1288
Red Lake	17GA1-29	0.884	1.078	0.113	0.395	0.044	0.136	0.053	0.005	0.024	0.007	0.023	0.003	0.017	0.003	0.79	128311	5661	1668	777

Location	Sample	La	Ce	Pr	Nd	Sm	Eu	Gd	Tb	Dy	Ho	Er	Tm	Yb	Lu	Al	Ca	Fe	Mn	Mg
Red Lake	17GA1-30	0.588	0.817	0.107	0.528	0.137	0.098	0.216	0.036	0.243	0.058	0.175	0.023	0.127	0.021	1.43	94320	8079	2454	1537
Red Lake	17GA1-31	0.959	0.704	0.051	0.137	0.014	0.064	0.032	0.003	0.024	0.007	0.024	0.004	0.018	0.004	2.00	176679	7239	1785	950
Red Lake	17GA1-32	1.408	1.777	0.193	0.797	0.165	0.100	0.252	0.043	0.306	0.081	0.274	0.040	0.245	0.044	4.03	97922	11318	3501	2365
Red Lake	17GA1-33	0.982	1.561	0.180	0.734	0.142	0.160	0.185	0.028	0.180	0.044	0.140	0.020	0.113	0.020	1.28	131717	7056	2988	2231
Red Lake	17GA1-34	0.993	1.585	0.191	0.834	0.182	0.225	0.238	0.037	0.230	0.051	0.152	0.020	0.114	0.019	6.63	120259	10104	3516	3954
Red Lake	17GA1-35	0.814	1.545	0.186	0.806	0.215	0.177	0.315	0.061	0.446	0.117	0.387	0.056	0.355	0.067	230.76	43070	69728	9746	11097
Red Lake	17GA1-36	1.523	2.156	0.240	1.007	0.224	0.149	0.307	0.046	0.273	0.056	0.151	0.018	0.098	0.015	1.90	67636	8143	2386	3388
Red Lake	17-NG-59	0.138	0.211	0.023	0.087	0.014	0.010	0.017	0.002	0.010	0.002	0.007	0.001	0.005	0.001	1.35	28423	3197	1378	23853
Red Lake	17-NG-65	0.237	0.373	0.041	0.159	0.026	0.019	0.032	0.004	0.020	0.005	0.014	0.002	0.011	0.002	2.91	48398	5039	2422	43168
Red Lake	17-NG-63	0.221	0.356	0.040	0.152	0.027	0.017	0.032	0.004	0.023	0.005	0.016	0.002	0.013	0.002	3.82	41971	5050	2047	35165
Red Lake	17-NG-57	0.223	0.349	0.038	0.149	0.025	0.018	0.032	0.004	0.021	0.005	0.016	0.002	0.012	0.002	4.49	48219	7029	2459	42025
Red Lake	17-NG-61	0.231	0.389	0.044	0.172	0.030	0.018	0.036	0.005	0.026	0.006	0.020	0.003	0.015	0.003	3.30	36617	4629	1936	32679
Red Lake	17-NG-69	0.204	0.339	0.037	0.148	0.026	0.018	0.035	0.005	0.030	0.007	0.023	0.003	0.020	0.004	2.57	39421	4764	1951	35258
Red Lake	17-NG-55	0.333	0.501	0.054	0.205	0.034	0.023	0.041	0.005	0.027	0.007	0.020	0.003	0.016	0.003	3.37	57200	7476	2824	48814
Red Lake	17-NG-51	0.256	0.400	0.044	0.172	0.030	0.021	0.040	0.005	0.033	0.008	0.026	0.004	0.020	0.004	3.81	47265	7317	2810	40661
Red Lake	17-NG-67	0.253	0.424	0.047	0.186	0.034	0.022	0.043	0.006	0.037	0.009	0.029	0.004	0.026	0.005	2.76	40367	5454	1971	34956
Red Lake	17-NG-73	0.257	0.439	0.049	0.195	0.037	0.023	0.046	0.006	0.040	0.010	0.033	0.005	0.031	0.006	3.25	37524	4800	1952	33284
Red Lake	17-NG-53	0.410	0.648	0.070	0.271	0.044	0.030	0.054	0.007	0.036	0.009	0.026	0.004	0.019	0.003	4.60	54444	8471	3488	47590
Red Lake	17-NG-03	0.300	0.488	0.055	0.220	0.042	0.023	0.052	0.007	0.042	0.010	0.031	0.004	0.026	0.005	2.11	33296	3869	1450	29990
Red Lake	17-NG-11	0.319	0.525	0.060	0.242	0.048	0.027	0.060	0.008	0.049	0.011	0.034	0.005	0.027	0.005	4.36	43486	5855	2060	38448
Red Lake	17-NG-47	0.269	0.404	0.044	0.179	0.034	0.021	0.046	0.006	0.043	0.011	0.035	0.005	0.030	0.005	3.61	42427	5612	2151	37458
Red Lake	17-NG-01	0.340	0.501	0.056	0.221	0.043	0.025	0.050	0.007	0.041	0.010	0.031	0.004	0.022	0.004	5.42	53434	5088	2394	48421
Red Lake	17-NG-17	0.315	0.512	0.058	0.230	0.044	0.027	0.055	0.008	0.046	0.011	0.033	0.004	0.024	0.004	4.22	50416	6239	2433	44682
Red Lake	17-NG-49	0.264	0.411	0.045	0.182	0.035	0.024	0.048	0.007	0.046	0.012	0.038	0.005	0.032	0.006	3.22	44501	6818	2261	36126
Red Lake	17-NG-15	0.302	0.496	0.056	0.229	0.044	0.026	0.056	0.008	0.048	0.011	0.035	0.005	0.028	0.005	4.73	50325	7682	2509	42398
Red Lake	17-NG-41	0.356	0.540	0.058	0.226	0.039	0.024	0.051	0.007	0.042	0.011	0.034	0.005	0.026	0.005	2.12	32286	5965	2323	27438
Red Lake	17-NG-13	0.275	0.422	0.048	0.192	0.039	0.022	0.049	0.007	0.045	0.011	0.033	0.005	0.026	0.005	4.14	46354	5449	2344	41307
Red Lake	17-NG-71	0.259	0.447	0.052	0.210	0.040	0.024	0.055	0.008	0.049	0.012	0.041	0.006	0.037	0.006	3.40	43173	5232	2312	38727
Red Lake	17-NG-39	0.270	0.427	0.047	0.185	0.034	0.021	0.048	0.007	0.045	0.011	0.038	0.005	0.032	0.006	3.10	29487	5685	1972	25499
Red Lake	17-NG-31	0.254	0.416	0.047	0.193	0.038	0.022	0.052	0.008	0.054	0.014	0.044	0.006	0.039	0.007	2.99	38246	4547	2118	30788
Red Lake	17-NG-09	0.313	0.510	0.058	0.235	0.047	0.026	0.061	0.009	0.057	0.014	0.043	0.006	0.033	0.006	13.73	47129	5951	2188	42292
Red Lake	17-NG-43	0.287	0.424	0.047	0.190	0.037	0.025	0.053	0.008	0.051	0.013	0.042	0.006	0.035	0.006	3.25	44324	7097	2642	37759
Red Lake	17-NG-07	0.302	0.475	0.054	0.223	0.046	0.027	0.059	0.009	0.056	0.013	0.042	0.005	0.032	0.005	5.56	49260	6382	2334	44447
Red Lake	17-NG-05	0.323	0.507	0.057	0.236	0.048	0.026	0.060	0.009	0.057	0.014	0.042	0.006	0.032	0.006	3.93	51329	6212	2281	45230
Red Lake	17-NG-45	0.312	0.473	0.053	0.211	0.041	0.024	0.055	0.008	0.053	0.013	0.043	0.006	0.036	0.007	2.40	50409	5656	2458	42055
Red Lake	17-NG-21	0.354	0.781	0.092	0.379	0.078	0.035	0.092	0.013	0.072	0.017	0.049	0.007	0.039	0.007	4.17	44473	9256	1752	38176
Red Lake	17-NG-19	0.246	0.419	0.048	0.203	0.044	0.026	0.065	0.010	0.063	0.015	0.044	0.006	0.034	0.006	3.21	42549	8779	1789	34069
Red Lake	17-NG-35	0.261	0.411	0.047	0.190	0.039	0.023	0.055	0.009	0.060	0.015	0.051	0.007	0.047	0.009	3.71	37803	4827	1961	32959
Red Lake	17-NG-37	0.285	0.428	0.048	0.197	0.041	0.027	0.060	0.010	0.066	0.017	0.057	0.008	0.053	0.010	5.08	47481	8689	2536	40784
Red Lake	17-NG-27	0.301	0.520	0.060	0.247	0.050	0.029	0.068	0.011	0.068	0.017	0.054	0.008	0.048	0.009	3.74	42904	5682	2204	37737

Location	Sample	La	Ce	Pr	Nd	Sm	Eu	Gd	Tb	Dy	Ho	Er	Tm	Yb	Lu	Al	Ca	Fe	Mn	Mg
Red Lake	17-NG-25	0.362	0.633	0.073	0.302	0.061	0.036	0.079	0.012	0.077	0.019	0.060	0.008	0.054	0.010	3.48	46244	6764	2293	40001
Red Lake	17-NG-33	0.360	0.599	0.068	0.277	0.056	0.030	0.075	0.011	0.075	0.019	0.062	0.009	0.053	0.010	2.88	52208	5681	2789	45755
Red Lake	17-NG-29	0.332	0.554	0.063	0.259	0.052	0.028	0.071	0.011	0.071	0.018	0.059	0.009	0.052	0.009	3.51	43375	5099	2504	38126
Red Lake	PB35-223.4	0.026	0.022	0.002	0.008	0.002	0.002	0.003	0.000	0.003	0.001	0.003	0.001	0.003	0.001	0.55	98099	1984	3535	1445
Red Lake	PB35-144.40	0.027	0.034	0.004	0.016	0.003	0.002	0.005	0.001	0.005	0.001	0.005	0.001	0.004	0.001	1.22	102990	1670	4549	906
Red Lake	PB35-251.12	0.094	0.143	0.016	0.060	0.011	0.006	0.014	0.002	0.012	0.003	0.009	0.001	0.007	0.001	1.01	68535	1556	4431	613
Red Lake	PB35-246.1	0.059	0.061	0.006	0.025	0.005	0.004	0.008	0.001	0.008	0.002	0.008	0.001	0.007	0.001	0.77	75813	2629	2759	863
Red Lake	PB35-185.16	0.100	0.109	0.011	0.044	0.008	0.009	0.012	0.002	0.011	0.003	0.010	0.001	0.008	0.002	0.83	97521	1662	4731	1705
Red Lake	PB35-243.5	0.153	0.193	0.019	0.071	0.013	0.046	0.016	0.002	0.011	0.002	0.006	0.001	0.004	0.001	0.30	73046	1280	2293	860
Red Lake	PB35-149.77	1.008	1.330	0.104	0.260	0.024	0.017	0.033	0.003	0.012	0.003	0.009	0.001	0.008	0.002	2.35	122096	3857	5870	1417
Red Lake	PB35-147.01	0.056	0.047	0.005	0.021	0.004	0.003	0.008	0.001	0.008	0.003	0.008	0.001	0.006	0.001	1.94	109329	2609	4853	1319
Red Lake	PB35-168.42	0.102	0.093	0.010	0.041	0.007	0.004	0.012	0.002	0.012	0.003	0.010	0.001	0.007	0.001	2.18	117686	1700	2366	1913
Red Lake	PB35-245.6	0.186	0.170	0.015	0.051	0.008	0.029	0.011	0.002	0.011	0.003	0.011	0.002	0.009	0.002	0.56	96962	5009	2901	1273
Red Lake	PB35-153.50	0.098	0.074	0.006	0.022	0.003	0.005	0.006	0.001	0.007	0.002	0.007	0.001	0.006	0.001	0.69	111397	5003	2495	1764
Red Lake	PB35-146.2	0.120	0.141	0.014	0.053	0.009	0.006	0.014	0.002	0.014	0.003	0.011	0.002	0.009	0.002	2.22	130400	2614	5494	1290
Red Lake	PB35-225.2	1.340	2.072	0.206	0.662	0.055	0.012	0.058	0.004	0.014	0.003	0.011	0.002	0.009	0.002	1.18	84137	1753	2985	1722
Red Lake	PB35-185.88	0.071	0.052	0.006	0.023	0.004	0.006	0.008	0.001	0.008	0.003	0.009	0.001	0.008	0.002	0.62	96326	2301	1616	1641
Red Lake	PB35-230.03	0.214	0.315	0.033	0.127	0.024	0.014	0.032	0.005	0.030	0.007	0.021	0.003	0.018	0.003	2.31	90724	1821	3600	1678
Red Lake	PB35-156.21	0.101	0.115	0.012	0.048	0.010	0.008	0.016	0.002	0.015	0.004	0.012	0.002	0.010	0.002	2.51	116413	3653	4194	1583
Red Lake	PB35-70.63	0.054	0.045	0.005	0.020	0.004	0.003	0.007	0.001	0.008	0.002	0.008	0.001	0.007	0.001	0.84	110357	4420	4842	1021
Red Lake	PB35-250.8	0.193	0.294	0.031	0.116	0.023	0.015	0.032	0.005	0.030	0.007	0.021	0.003	0.015	0.003	0.26	73968	1184	3325	790
Red Lake	PB35-247.9	0.149	0.211	0.023	0.091	0.018	0.010	0.025	0.004	0.025	0.006	0.020	0.003	0.016	0.003	1.15	75851	1991	2592	1035
Red Lake	PB35-157.76	0.075	0.081	0.009	0.038	0.008	0.006	0.013	0.002	0.014	0.004	0.013	0.002	0.011	0.002	0.96	124137	2763	4569	1411
Red Lake	PB35-68.65	0.136	0.192	0.022	0.086	0.017	0.009	0.022	0.003	0.019	0.004	0.013	0.002	0.010	0.002	2.90	106056	3491	4509	1095
Red Lake	PB35-241.6	0.079	0.082	0.009	0.035	0.007	0.015	0.012	0.002	0.013	0.004	0.013	0.002	0.012	0.002	1.65	115496	2636	1581	1358
Red Lake	PB35-248.4	0.771	1.079	0.107	0.380	0.056	0.016	0.063	0.007	0.032	0.007	0.021	0.003	0.016	0.003	1.18	66257	1348	2149	674
Red Lake	PB35-69.68	0.179	0.169	0.016	0.060	0.011	0.007	0.018	0.002	0.013	0.004	0.011	0.001	0.008	0.002	0.63	105557	3996	3782	1517
Red Lake	PB35-217.9	0.155	0.184	0.020	0.078	0.016	0.007	0.024	0.004	0.022	0.006	0.017	0.002	0.013	0.002	4.58	110740	2297	2966	1180
Red Lake	PB35-151.12	0.594	0.925	0.096	0.340	0.055	0.076	0.067	0.009	0.048	0.010	0.024	0.003	0.013	0.002	0.65	97180	3272	4685	1062
Red Lake	PB35-22.48	0.134	0.082	0.009	0.032	0.006	0.005	0.011	0.002	0.011	0.004	0.012	0.002	0.010	0.002	2.90	157925	2797	3295	2469
Red Lake	PB35-252.30	0.150	0.190	0.021	0.090	0.019	0.010	0.031	0.005	0.037	0.010	0.032	0.005	0.026	0.005	0.59	71722	1235	3227	779
Red Lake	PB35-239.4	0.209	0.283	0.031	0.122	0.025	0.014	0.035	0.006	0.036	0.009	0.028	0.004	0.023	0.004	1.01	108786	1993	2355	1810
Red Lake	PB35-251	0.366	0.583	0.064	0.240	0.045	0.028	0.056	0.009	0.051	0.012	0.035	0.005	0.029	0.005	3.00	105749	3164	5651	1507
Red Lake	PB35-36.84	0.446	0.524	0.049	0.154	0.022	0.057	0.031	0.004	0.024	0.006	0.020	0.003	0.016	0.003	2.00	113988	6201	4747	1829
Red Lake	PB35-162.4	0.105	0.125	0.014	0.056	0.011	0.009	0.018	0.003	0.020	0.006	0.021	0.003	0.018	0.004	1.83	136991	2642	5392	2066
Red Lake	PB35-246.7	0.212	0.287	0.032	0.129	0.028	0.017	0.041	0.007	0.045	0.011	0.036	0.005	0.031	0.006	1.67	74061	2851	3048	810
Red Lake	PB35-177.6	0.623	0.802	0.081	0.285	0.047	0.048	0.060	0.008	0.044	0.010	0.028	0.004	0.021	0.004	2.59	107388	4659	9369	2071
Red Lake	PB35-160.96	0.108	0.080	0.008	0.031	0.005	0.005	0.011	0.002	0.013	0.004	0.016	0.002	0.013	0.003	1.02	135411	3174	4652	1595
Red Lake	PB35-171.14	0.359	0.397	0.038	0.125	0.020	0.018	0.029	0.004	0.023	0.006	0.018	0.003	0.013	0.003	5.61	100098	4076	9453	2213
Red Lake	PB35-163.8	0.181	0.160	0.016	0.058	0.010	0.006	0.017	0.003	0.018	0.006	0.019	0.003	0.015	0.003	3.52	125607	3390	4014	1742

Location	Sample	La	Ce	Pr	Nd	Sm	Eu	Gd	Tb	Dy	Ho	Er	Tm	Yb	Lu	Al	Ca	Fe	Mn	Mg
Red Lake	PB35-180.9	0.151	0.147	0.015	0.059	0.011	0.005	0.019	0.003	0.022	0.007	0.023	0.004	0.019	0.004	2.75	130688	2926	5694	2228
Red Lake	PB35-39.70	0.133	0.137	0.015	0.066	0.014	0.009	0.026	0.004	0.025	0.007	0.021	0.003	0.016	0.003	0.95	110134	2440	4960	1238
Red Lake	PB35-38.4	0.294	0.245	0.020	0.063	0.011	0.009	0.021	0.003	0.024	0.007	0.025	0.004	0.022	0.005	1.33	98532	2717	2380	1507
Red Lake	PB35-237.5	0.477	0.633	0.065	0.240	0.041	0.023	0.057	0.009	0.052	0.013	0.037	0.005	0.030	0.006	2.28	90727	1950	4655	1281
Red Lake	PB35-221.4	0.201	0.146	0.014	0.055	0.010	0.010	0.019	0.003	0.020	0.007	0.023	0.003	0.020	0.004	0.81	105605	2425	3190	2102
Red Lake	PB35-254.38	3.347	6.584	0.745	2.721	0.435	0.088	0.408	0.047	0.199	0.035	0.083	0.011	0.069	0.013	404.90	2999	509	320	242
Red Lake	PB35-176	0.234	0.291	0.032	0.125	0.026	0.015	0.038	0.006	0.041	0.011	0.035	0.005	0.030	0.006	1.16	90820	1589	5567	1293
Red Lake	PB35-73.52	1.866	3.135	0.316	1.043	0.173	0.049	0.196	0.022	0.090	0.016	0.039	0.005	0.025	0.004	2.08	147707	2721	7108	1605
Red Lake	PB35-54.38	1.108	1.332	0.130	0.462	0.075	0.078	0.097	0.012	0.066	0.015	0.042	0.006	0.029	0.005	4.16	144443	7339	7417	2371
Red Lake	PB35-173.2	1.073	1.637	0.176	0.636	0.107	0.136	0.119	0.016	0.083	0.018	0.053	0.007	0.041	0.007	3.15	114008	3221	6593	2041
Red Lake	PB35-184.14	0.375	0.453	0.048	0.185	0.035	0.021	0.054	0.009	0.057	0.016	0.052	0.008	0.046	0.009	2.68	113086	3519	9105	1750
Red Lake	PB35-235.3	0.545	0.606	0.064	0.237	0.041	0.020	0.060	0.009	0.054	0.015	0.046	0.007	0.037	0.007	3.06	114948	1409	2016	2178
Red Lake	PB35-83.7	3.499	7.348	0.816	2.765	0.362	0.090	0.362	0.040	0.186	0.040	0.109	0.015	0.086	0.014	176.24	12724	7128	544	6067
Red Lake	PB35-253.38	0.653	1.048	0.113	0.418	0.073	0.030	0.093	0.013	0.085	0.021	0.067	0.009	0.056	0.011	3.82	73196	1816	4757	578
Red Lake	PB35-182.05	0.566	0.710	0.073	0.287	0.052	0.031	0.076	0.011	0.070	0.018	0.059	0.008	0.047	0.009	1.76	103344	2147	6147	1098
Red Lake	PB35-50.49	10.022	18.242	1.920	6.493	0.774	0.189	0.701	0.059	0.203	0.039	0.104	0.015	0.087	0.014	346.54	6164	1618	394	1054
Red Lake	PB35-227.9	0.680	0.970	0.103	0.398	0.077	0.050	0.108	0.017	0.109	0.026	0.077	0.011	0.060	0.011	1.72	86726	3026	3408	1569
Red Lake	PB35-52.88	0.613	0.806	0.085	0.321	0.064	0.038	0.086	0.014	0.084	0.021	0.064	0.009	0.055	0.010	7.04	114748	4153	4331	2602
Red Lake	PB35-81.15	1.986	3.784	0.449	1.733	0.332	0.135	0.348	0.048	0.231	0.044	0.108	0.014	0.079	0.012	58.25	49734	9736	1362	8360
Red Lake	PB35-48.3	0.767	0.737	0.068	0.234	0.035	0.072	0.054	0.007	0.047	0.014	0.046	0.007	0.038	0.008	4.91	116612	6654	4549	2179
Red Lake	PB35-55.57	3.446	6.447	0.718	2.631	0.409	0.083	0.434	0.056	0.275	0.054	0.140	0.019	0.106	0.017	529.36	8943	1523	1244	1769
Red Lake	PB35-34.20	0.731	0.893	0.090	0.335	0.058	0.053	0.095	0.015	0.101	0.028	0.090	0.013	0.077	0.015	1.25	110337	7115	5030	1257
Red Lake	PB35-31.20	1.689	2.225	0.229	0.838	0.140	0.176	0.168	0.022	0.115	0.026	0.073	0.009	0.049	0.008	2.54	113531	8827	6151	2812
Red Lake	PB35-27.57	1.066	1.611	0.176	0.682	0.136	0.117	0.187	0.029	0.167	0.039	0.117	0.017	0.095	0.018	1.94	93976	6491	6046	1423
Red Lake	PB35-26.43	0.945	1.254	0.135	0.515	0.102	0.075	0.148	0.024	0.158	0.041	0.129	0.019	0.112	0.021	1.17	111092	4825	5833	1492
Red Lake	PB35-178.9	0.685	1.014	0.117	0.492	0.111	0.068	0.166	0.028	0.186	0.048	0.151	0.022	0.129	0.024	1.15	140124	5222	11461	1601
Red Lake	PB35-26.06	1.002	1.269	0.138	0.553	0.112	0.077	0.169	0.026	0.164	0.043	0.132	0.019	0.105	0.020	1.53	142518	5784	7570	1787
Red Lake	PB35-29.37	1.399	2.405	0.293	1.229	0.252	0.202	0.313	0.044	0.240	0.052	0.140	0.018	0.093	0.015	0.61	134429	6206	8250	1160
Red Lake	PB35-24.22	1.175	1.031	0.129	0.519	0.089	0.057	0.141	0.019	0.123	0.036	0.120	0.016	0.095	0.019	13.81	119022	3246	2991	2277
Red Lake	PB35-77.86	16.090	30.703	3.342	13.739	2.218	0.529	2.089	0.203	0.672	0.117	0.284	0.040	0.261	0.048	7.52	131167	742	1398	301
Red Lake	PB35-49.44	2.206	3.181	0.349	1.365	0.273	0.164	0.401	0.064	0.411	0.105	0.332	0.048	0.283	0.053	21.60	98291	8006	5623	1818
Red Lake	PB35-79.6	12.744	23.256	2.348	8.954	1.391	0.407	1.617	0.176	0.742	0.145	0.355	0.043	0.233	0.040	10.87	77414	4994	5618	7105
Red Lake	PB35-184.26	0.851	0.561	0.091	0.386	0.080	0.039	0.165	0.027	0.205	0.068	0.242	0.034	0.204	0.044	2.08	111016	1676	3351	1797
Woman Lake	A-1	0.176	0.283	0.039	0.168	0.036	0.009	0.047	0.008	0.057	0.016	0.050	0.008	0.047	0.009	5.48	4532	83	792	54
Woman Lake	A-10	0.189	0.192	0.032	0.139	0.032	0.009	0.049	0.010	0.071	0.020	0.067	0.010	0.063	0.012	12.02	50606	434	5082	898
Woman Lake	A-12	0.338	0.216	0.035	0.139	0.025	0.013	0.042	0.007	0.051	0.015	0.051	0.007	0.041	0.008	11.67	76421	1083	6718	2878
Woman Lake	A-14	0.559	0.607	0.069	0.239	0.039	0.026	0.062	0.010	0.066	0.019	0.065	0.009	0.056	0.011	4.87	54956	499	5224	608
Woman Lake	A-16	0.366	0.227	0.038	0.152	0.028	0.014	0.048	0.008	0.057	0.017	0.058	0.008	0.048	0.010	5.79	88954	1010	5713	4729
Woman Lake	A-17	0.291	0.162	0.032	0.135	0.025	0.011	0.046	0.008	0.059	0.018	0.061	0.009	0.051	0.010	12.64	80088	754	5679	2636
Woman Lake	A-18A	0.362	0.208	0.036	0.153	0.028	0.016	0.050	0.009	0.065	0.020	0.068	0.010	0.055	0.011	10.78	101895	1267	8360	3356

Location	Sample	La	Ce	Pr	Nd	Sm	Eu	Gd	Tb	Dy	Ho	Er	Tm	Yb	Lu	Al	Ca	Fe	Mn	Mg
Woman Lake	A-18B	0.289	0.264	0.040	0.174	0.039	0.020	0.063	0.012	0.085	0.024	0.080	0.012	0.067	0.013	19.66	72302	258	5557	599
Woman Lake	A-18C	0.341	0.294	0.040	0.161	0.031	0.019	0.048	0.008	0.055	0.015	0.046	0.007	0.038	0.007	3.03	77704	867	6941	2465
Woman Lake	A-18D	0.288	0.223	0.030	0.126	0.025	0.020	0.045	0.008	0.061	0.018	0.059	0.008	0.048	0.010	5.49	64096	242	5865	500
Woman Lake	A-2	0.550	0.516	0.067	0.271	0.049	0.027	0.077	0.013	0.091	0.025	0.084	0.011	0.070	0.014	1.33	46283	666	6618	1438
Woman Lake	A-20A	0.681	1.036	0.133	0.569	0.135	0.032	0.197	0.041	0.289	0.078	0.260	0.039	0.253	0.048	6.48	56092	1045	5449	1830
Woman Lake	A-20B	0.963	1.311	0.159	0.658	0.143	0.061	0.201	0.039	0.261	0.068	0.214	0.032	0.194	0.036	5.50	80761	898	7593	2828
Woman Lake	A-22	0.189	0.102	0.017	0.072	0.013	0.010	0.025	0.004	0.033	0.010	0.033	0.005	0.028	0.005	3.14	70152	465	6291	2002
Woman Lake	A-23A	0.217	0.173	0.029	0.133	0.028	0.011	0.049	0.009	0.065	0.020	0.068	0.010	0.057	0.011	7.05	62791	230	5356	879
Woman Lake	A-23B	0.315	0.171	0.038	0.173	0.037	0.012	0.069	0.013	0.095	0.029	0.101	0.015	0.086	0.018	3.33	82333	652	6289	2465
Woman Lake	A-27	0.264	0.401	0.052	0.205	0.044	0.015	0.059	0.010	0.069	0.018	0.061	0.009	0.060	0.012	7.51	23879	153	2120	204
Woman Lake	A-28	0.654	0.597	0.081	0.305	0.050	0.024	0.077	0.011	0.074	0.020	0.066	0.009	0.052	0.010	11.58	76763	450	6032	2030
Woman Lake	A-3	0.343	0.185	0.029	0.121	0.021	0.012	0.040	0.007	0.050	0.016	0.053	0.008	0.043	0.009	42.24	170232	1310	14620	5133
Woman Lake	A-31	0.447	0.257	0.042	0.170	0.031	0.013	0.057	0.009	0.067	0.020	0.067	0.009	0.054	0.011	6.68	76568	668	4966	2403
Woman Lake	A-32	0.575	0.309	0.062	0.274	0.057	0.023	0.106	0.020	0.146	0.044	0.148	0.021	0.122	0.024	5.41	119047	1589	10497	2540
Woman Lake	A-35A	0.341	0.238	0.050	0.231	0.053	0.016	0.098	0.018	0.140	0.042	0.145	0.021	0.124	0.024	5.77	78682	848	7453	1192
Woman Lake	A-35B	0.431	0.222	0.043	0.172	0.031	0.016	0.055	0.009	0.064	0.019	0.065	0.009	0.050	0.010	2.06	82286	1122	6789	2607
Woman Lake	A-36A	0.412	0.220	0.046	0.200	0.043	0.020	0.084	0.016	0.123	0.037	0.123	0.018	0.106	0.021	3.64	82833	1163	6772	2744
Woman Lake	A-36B	0.732	0.601	0.107	0.494	0.118	0.037	0.185	0.036	0.261	0.070	0.227	0.034	0.208	0.039	3.24	87693	1266	8340	2700
Woman Lake	A-38A	0.585	0.258	0.060	0.274	0.058	0.025	0.121	0.023	0.180	0.057	0.199	0.028	0.164	0.034	6.28	112781	1586	10422	4130
Woman Lake	A-39	0.985	0.738	0.098	0.359	0.059	0.034	0.095	0.014	0.093	0.026	0.084	0.012	0.066	0.013	6.43	85230	1004	6897	2367
Woman Lake	A-41A	0.316	0.372	0.058	0.245	0.054	0.017	0.086	0.016	0.112	0.031	0.104	0.015	0.094	0.018	7.60	36175	304	3023	393
Woman Lake	A-41B	1.276	0.883	0.137	0.521	0.090	0.044	0.143	0.022	0.149	0.043	0.141	0.019	0.110	0.022	8.33	103336	1574	8555	3093
Woman Lake	A-43	0.275	0.141	0.027	0.114	0.021	0.012	0.039	0.006	0.048	0.015	0.049	0.007	0.041	0.008	4.88	55838	945	4410	1910
Woman Lake	A-43	0.369	0.430	0.066	0.277	0.060	0.019	0.099	0.019	0.142	0.041	0.139	0.020	0.123	0.023	7.83	58226	449	4600	695
Woman Lake	A-48A	0.708	0.414	0.065	0.254	0.042	0.022	0.077	0.012	0.083	0.024	0.080	0.011	0.063	0.012	2.04	82937	755	6202	2386
Woman Lake	A-48B	0.417	0.281	0.055	0.245	0.049	0.016	0.089	0.016	0.120	0.036	0.121	0.017	0.101	0.020	4.59	66545	495	5396	1081
Woman Lake	A-5	0.407	0.675	0.084	0.340	0.073	0.017	0.084	0.014	0.084	0.020	0.061	0.009	0.063	0.011	25.67	15326	166	1356	189
Woman Lake	A-52A	0.121	0.129	0.023	0.111	0.029	0.007	0.056	0.012	0.094	0.028	0.096	0.014	0.086	0.016	20.24	35663	150	2255	315
Woman Lake	A-52B	0.756	0.437	0.073	0.285	0.050	0.027	0.088	0.014	0.097	0.028	0.090	0.012	0.071	0.014	8.95	84073	884	6740	2587
Woman Lake	A-56	0.187	0.133	0.025	0.114	0.025	0.007	0.050	0.010	0.078	0.025	0.089	0.013	0.082	0.016	10.79	28573	73	1663	155
Woman Lake	A-9	0.463	0.327	0.043	0.168	0.030	0.011	0.050	0.008	0.053	0.015	0.048	0.007	0.037	0.007	4.12	94297	993	5141	4090
Woman Lake	B-1	0.983	0.998	0.137	0.581	0.121	0.056	0.181	0.035	0.238	0.065	0.210	0.029	0.181	0.034	2.04	51394	1812	7610	2031
Woman Lake	B-10A	2.398	3.188	0.361	1.421	0.280	0.100	0.373	0.064	0.403	0.105	0.345	0.050	0.314	0.059	1.65	53003	1317	5808	1659
Woman Lake	B-10B	1.257	1.624	0.231	1.068	0.263	0.105	0.376	0.083	0.590	0.160	0.541	0.080	0.518	0.102	2.13	52117	1989	7652	2407
Woman Lake	B-5	2.141	2.290	0.310	1.285	0.265	0.134	0.376	0.072	0.484	0.125	0.395	0.056	0.337	0.062	2.08	70282	3339	11812	2745
Woman Lake	B-7	1.259	1.580	0.228	1.017	0.244	0.092	0.341	0.070	0.491	0.130	0.418	0.059	0.364	0.066	6.90	49732	2596	7819	2396
Woman Lake	B-8	1.563	1.711	0.230	0.963	0.196	0.101	0.281	0.052	0.358	0.095	0.302	0.042	0.254	0.047	1.64	52344	2464	8289	2103
Woman Lake	WM 102	0.054	0.131	0.019	0.095	0.023	0.014	0.036	0.006	0.040	0.010	0.030	0.004	0.027	0.005	3.71	221	3650	31	134
Woman Lake	WM 104	0.584	0.587	0.076	0.336	0.075	0.032	0.128	0.024	0.180	0.049	0.163	0.024	0.151	0.028	4.15	66373	1308	5205	1866
Woman Lake	WM 104	1.139	1.106	0.140	0.614	0.136	0.055	0.242	0.044	0.326	0.089	0.300	0.043	0.265	0.052	4.72	178601	2107	10125	2964

Location	Sample	La	Ce	Pr	Nd	Sm	Eu	Gd	Tb	Dy	Ho	Er	Tm	Yb	Lu	Al	Ca	Fe	Mn	Mg
Woman Lake	WM 105x	1.599	1.711	0.211	0.825	0.162	0.085	0.246	0.040	0.265	0.072	0.229	0.033	0.201	0.037	12.79	89135	1016	6721	2303
Woman Lake	WM 105x	3.647	3.656	0.452	1.808	0.344	0.179	0.523	0.080	0.543	0.144	0.473	0.066	0.398	0.077	24.52	266601	1667	17104	3975
Woman Lake	WM 105y	1.566	1.601	0.210	0.889	0.173	0.088	0.277	0.046	0.299	0.083	0.265	0.038	0.225	0.043	8.56	74072	625	4131	1713
Woman Lake	WM 105y	2.587	2.606	0.337	1.408	0.273	0.141	0.437	0.069	0.468	0.128	0.425	0.058	0.345	0.068	12.55	148179	876	7076	2801
Woman Lake	WM 107x	0.616	0.308	0.062	0.275	0.051	0.021	0.102	0.017	0.128	0.041	0.140	0.020	0.119	0.024	4.24	68343	661	5328	1187
Woman Lake	WM 107x	1.485	0.717	0.143	0.635	0.115	0.048	0.247	0.039	0.303	0.096	0.343	0.046	0.277	0.057	1.62	199391	1330	13390	2215
Woman Lake	WM 107y	0.599	0.340	0.061	0.267	0.048	0.022	0.093	0.015	0.112	0.035	0.123	0.017	0.100	0.021	1.76	55806	589	4788	1064
Woman Lake	WM 107y	1.990	1.053	0.190	0.836	0.153	0.068	0.300	0.046	0.355	0.112	0.401	0.054	0.324	0.067	3.50	244343	1757	16520	2917
Woman Lake	WM 108	1.405	1.025	0.142	0.576	0.099	0.037	0.168	0.025	0.163	0.048	0.155	0.021	0.122	0.024	6.28	70420	552	3665	1295
Woman Lake	WM 108	4.433	3.177	0.429	1.739	0.291	0.111	0.497	0.069	0.474	0.137	0.461	0.061	0.352	0.069	18.72	298209	1495	13281	3296
Woman Lake	WM 109	0.917	1.162	0.150	0.604	0.116	0.032	0.168	0.027	0.174	0.049	0.157	0.022	0.131	0.025	12.82	65124	486	4901	1321
Woman Lake	WM 109	2.873	3.578	0.458	1.819	0.345	0.095	0.499	0.076	0.512	0.143	0.478	0.066	0.390	0.076	34.51	285866	1469	16812	3836
Woman Lake	WM 110	1.609	1.925	0.226	0.909	0.176	0.075	0.267	0.044	0.283	0.078	0.252	0.036	0.220	0.042	15.85	80624	840	5031	1470
Woman Lake	WM 110	4.126	4.717	0.565	2.262	0.429	0.184	0.664	0.103	0.691	0.187	0.620	0.088	0.527	0.103	42.19	304218	2021	16042	3623
Woman Lake	WM 111	0.649	0.625	0.081	0.325	0.061	0.028	0.104	0.016	0.112	0.032	0.106	0.015	0.088	0.018	6.65	57110	674	4142	1187
Woman Lake	WM 111	1.770	1.620	0.209	0.848	0.155	0.072	0.261	0.040	0.276	0.080	0.272	0.038	0.221	0.044	21.91	222866	1758	12524	2931
Woman Lake	WM 112	1.261	1.337	0.164	0.645	0.119	0.063	0.191	0.030	0.200	0.055	0.178	0.025	0.149	0.029	4.89	64708	675	4587	1361
Woman Lake	WM 112	2.988	3.076	0.361	1.471	0.265	0.141	0.429	0.064	0.432	0.119	0.395	0.054	0.322	0.063	10.99	225752	1429	11582	2944
Woman Lake	WM 113	0.869	0.973	0.122	0.512	0.107	0.040	0.173	0.030	0.207	0.053	0.163	0.023	0.138	0.025	4.50	53926	736	2763	1016
Woman Lake	WM 113	2.876	3.123	0.379	1.574	0.338	0.124	0.545	0.091	0.632	0.163	0.513	0.071	0.435	0.080	9.00	243757	2192	10771	2951
Woman Lake	WM 114x	1.611	1.947	0.243	1.050	0.236	0.076	0.362	0.067	0.454	0.117	0.367	0.052	0.312	0.057	4.86	88584	1217	6367	1950
Woman Lake	WM 114x	2.880	3.386	0.407	1.747	0.379	0.127	0.614	0.106	0.729	0.187	0.598	0.082	0.502	0.094	10.15	237911	1989	12561	3128
Woman Lake	WM 114y	0.492	0.604	0.077	0.340	0.075	0.029	0.114	0.021	0.139	0.036	0.115	0.016	0.099	0.018	1.63	52098	761	3508	1051
Woman Lake	WM 114y	1.495	1.770	0.222	0.961	0.203	0.082	0.328	0.057	0.396	0.102	0.332	0.046	0.277	0.051	3.20	209937	2140	11881	2760
Woman Lake	WM 115	2.049	2.454	0.298	1.141	0.204	0.102	0.295	0.047	0.296	0.077	0.240	0.034	0.209	0.038	189.69	62727	1409	5789	2641
Woman Lake	WM 115	4.345	5.185	0.640	2.442	0.423	0.220	0.619	0.096	0.628	0.160	0.514	0.071	0.428	0.080	30.44	288589	2898	18386	6310
Woman Lake	WM 116-x	1.744	2.597	0.378	1.632	0.337	0.078	0.494	0.085	0.625	0.183	0.645	0.094	0.582	0.112	11.51	160711	861	11529	1175
Woman Lake	WM 116-y	1.624	0.794	0.148	0.629	0.113	0.054	0.216	0.033	0.238	0.070	0.232	0.032	0.184	0.037	4.13	250196	3743	11624	4613
Woman Lake	WM 116x	0.659	1.004	0.151	0.638	0.136	0.030	0.192	0.034	0.245	0.073	0.252	0.037	0.230	0.045	2.86	34632	279	3297	371
Woman Lake	WM 116y	1.060	0.537	0.102	0.427	0.078	0.038	0.148	0.024	0.174	0.052	0.167	0.024	0.137	0.026	2.79	90230	2451	5688	2641
Woman Lake	WM 124	1.448	1.710	0.222	0.895	0.188	0.089	0.298	0.052	0.351	0.095	0.294	0.041	0.239	0.044	6.19	66195	2138	4397	2115
Woman Lake	WM 124	4.124	4.683	0.589	2.360	0.490	0.234	0.793	0.133	0.927	0.246	0.799	0.106	0.626	0.117	13.93	253197	4653	14046	3726
Woman Lake	WM 125	4.037	4.603	0.551	2.121	0.367	0.102	0.548	0.081	0.543	0.151	0.516	0.073	0.456	0.090	38.59	100059	16640	15974	35435
Woman Lake	WM 126	2.402	5.392	0.601	1.944	0.265	0.042	0.322	0.028	0.100	0.021	0.071	0.012	0.108	0.022	72.46	4776	46	762	419
Woman Lake	WM 126	5.771	13.167	1.385	4.403	0.575	0.092	0.587	0.057	0.210	0.043	0.141	0.024	0.212	0.045	217.04	12010	157	1239	802
Woman Lake	WM 129-Q	0.640	0.770	0.116	0.473	0.094	0.025	0.116	0.016	0.092	0.021	0.064	0.009	0.062	0.012	20.65	8991	417	682	804
Woman Lake	WM 129-R	1.445	1.068	0.173	0.705	0.126	0.056	0.215	0.035	0.238	0.068	0.223	0.033	0.211	0.041	5.16	75608	1949	4979	1653
Woman Lake	WM 129-S	0.167	0.208	0.034	0.146	0.030	0.009	0.047	0.008	0.052	0.014	0.047	0.007	0.044	0.008	8.57	5990	180	467	382
Woman Lake	WM 129-S	0.341	0.434	0.067	0.280	0.057	0.017	0.083	0.014	0.094	0.026	0.087	0.012	0.080	0.016	14.44	16630	552	922	905
Woman Lake	WM 129-x	1.116	0.793	0.141	0.618	0.115	0.051	0.215	0.034	0.251	0.074	0.250	0.034	0.203	0.041	0.69	167945	1361	12357	1988

Location	Sample	La	Ce	Pr	Nd	Sm	Eu	Gd	Tb	Dy	Ho	Er	Tm	Yb	Lu	Al	Ca	Fe	Mn	Mg
Woman Lake	WM 129-z	0.866	0.985	0.145	0.600	0.111	0.036	0.167	0.024	0.159	0.041	0.133	0.018	0.111	0.020	7.74	41532	389	2661	675
Woman Lake	WM 129Q	0.314	0.388	0.059	0.239	0.048	0.013	0.061	0.008	0.046	0.011	0.032	0.005	0.031	0.006	6.25	3251	120	353	386
Woman Lake	WM 129R	3.239	2.369	0.369	1.524	0.270	0.120	0.462	0.071	0.501	0.143	0.496	0.069	0.449	0.089	9.69	243657	3734	12199	3021
Woman Lake	WM 129t	1.952	1.102	0.196	0.832	0.149	0.077	0.283	0.044	0.315	0.093	0.312	0.041	0.248	0.048	1.69	239183	3768	12382	3552
Woman Lake	WM 129t2	2.497	1.266	0.231	0.955	0.162	0.092	0.316	0.048	0.339	0.099	0.328	0.044	0.259	0.052	4.06	267410	4441	14131	4524
Woman Lake	WM 129y	2.018	1.076	0.194	0.809	0.142	0.067	0.274	0.042	0.301	0.089	0.297	0.041	0.241	0.048	2.42	216708	3321	11631	3895
Woman Lake	WM 130	0.533	0.298	0.045	0.194	0.034	0.015	0.071	0.011	0.082	0.026	0.091	0.013	0.075	0.015	2.55	184168	1826	10835	3051
Woman Lake	WM 32	0.103	0.244	0.032	0.123	0.026	0.012	0.029	0.004	0.021	0.004	0.012	0.002	0.012	0.002	271.02	92	106	2	60
Woman Lake	WM 36	0.107	0.234	0.027	0.101	0.021	0.009	0.025	0.003	0.015	0.003	0.008	0.001	0.008	0.001	227.45	28	85	9	41
Woman Lake	WM 43	0.180	0.389	0.049	0.208	0.057	0.050	0.068	0.011	0.057	0.011	0.030	0.004	0.029	0.005	401.52	1407	5610	685	1304
Woman Lake	WM 44	0.093	0.227	0.031	0.137	0.036	0.017	0.038	0.006	0.028	0.005	0.013	0.002	0.011	0.002	348.76	202	693	62	146
Woman Lake	WM 47	0.186	0.375	0.047	0.187	0.046	0.026	0.055	0.008	0.039	0.008	0.020	0.003	0.019	0.003	411.69	422	2457	196	542
Woman Lake	WM 57	0.154	0.219	0.026	0.118	0.024	0.009	0.038	0.007	0.044	0.011	0.038	0.005	0.031	0.006	2.23	18875	233	1416	219
Woman Lake	WM 57	0.296	0.404	0.048	0.204	0.043	0.015	0.068	0.011	0.076	0.020	0.067	0.009	0.052	0.010	6.89	48226	466	2460	430
Woman Lake	WM 61	0.130	0.213	0.024	0.088	0.013	0.004	0.018	0.002	0.013	0.003	0.011	0.002	0.011	0.002	4.24	1605	48	135	50
Woman Lake	WM 61	0.253	0.411	0.046	0.166	0.026	0.008	0.031	0.004	0.026	0.006	0.021	0.003	0.020	0.004	16.69	4241	132	243	115
Woman Lake	WM 63	1.009	1.464	0.176	0.693	0.127	0.052	0.184	0.028	0.177	0.045	0.141	0.020	0.118	0.022	3.38	57547	1793	5664	1468
Woman Lake	WM 63	3.128	4.485	0.524	2.088	0.378	0.154	0.532	0.081	0.517	0.132	0.425	0.058	0.349	0.066	8.85	258448	5316	20008	4458
Woman Lake	WM 65	0.903	1.222	0.133	0.513	0.094	0.033	0.143	0.023	0.152	0.040	0.130	0.018	0.110	0.021	8.67	59670	1212	4941	1040
Woman Lake	WM 65	2.016	2.650	0.280	1.098	0.198	0.069	0.304	0.049	0.330	0.087	0.281	0.039	0.237	0.045	12.24	163349	2134	12302	1695
Woman Lake	WM 66	0.511	0.663	0.069	0.257	0.046	0.026	0.065	0.010	0.060	0.015	0.046	0.007	0.039	0.007	5.52	34200	967	1597	964
Woman Lake	WM 66	1.251	1.606	0.163	0.620	0.104	0.057	0.148	0.022	0.138	0.035	0.110	0.015	0.087	0.016	11.86	105164	1942	3469	1953
Woman Lake	WM 67	1.874	2.741	0.339	1.477	0.340	0.073	0.520	0.104	0.699	0.166	0.515	0.081	0.557	0.111	18.58	15108	3488	3273	11910
Woman Lake	WM 67	5.532	8.113	0.955	4.090	0.938	0.217	1.495	0.284	1.981	0.474	1.508	0.226	1.569	0.307	27.51	66106	11984	11886	35779
Woman Lake	WM 69	3.458	5.623	0.614	2.377	0.359	0.057	0.490	0.079	0.588	0.182	0.746	0.129	0.964	0.193	128.80	114818	876	9212	802
Woman Lake	WM 71A	0.419	0.638	0.074	0.290	0.056	0.015	0.084	0.016	0.120	0.039	0.151	0.026	0.192	0.041	14.16	18927	83	932	157
Woman Lake	WM 71A	1.189	1.915	0.211	0.841	0.164	0.038	0.223	0.040	0.291	0.090	0.358	0.060	0.443	0.092	42.49	58494	205	1953	356
Woman Lake	WM 73	0.530	0.630	0.076	0.310	0.064	0.020	0.106	0.021	0.149	0.039	0.120	0.017	0.108	0.020	2.64	73631	1125	4297	1700
Woman Lake	WM 73	1.044	1.218	0.145	0.600	0.119	0.039	0.207	0.037	0.272	0.071	0.233	0.033	0.201	0.038	4.53	218991	1961	10328	3141
Woman Lake	WM 74	1.930	1.789	0.238	1.000	0.186	0.086	0.317	0.054	0.379	0.108	0.362	0.052	0.314	0.060	1.59	58961	1050	4218	960
Woman Lake	WM 74	5.370	4.889	0.632	2.676	0.481	0.224	0.849	0.136	0.975	0.278	0.943	0.132	0.797	0.154	2.60	232536	2736	12727	2463
Woman Lake	WM117x	0.157	0.163	0.029	0.134	0.034	0.010	0.061	0.014	0.107	0.032	0.111	0.016	0.100	0.019	5.14	11196	148	1538	159
Woman Lake	WM117y	1.807	1.077	0.172	0.685	0.117	0.057	0.195	0.033	0.223	0.064	0.208	0.029	0.168	0.032	4.33	71033	1275	12019	2579
Woman Lake	WM14x	1.175	1.998	0.221	0.864	0.172	0.072	0.205	0.034	0.195	0.045	0.136	0.019	0.115	0.020	10.63	74885	9200	10793	4188
Woman Lake	WM14y	0.591	1.076	0.125	0.524	0.120	0.040	0.141	0.026	0.156	0.039	0.121	0.018	0.113	0.021	11.42	48332	6107	7883	2927
Woman Lake	WM14z	0.563	0.895	0.096	0.366	0.072	0.032	0.089	0.015	0.094	0.023	0.074	0.011	0.073	0.013	9.04	50425	6004	6304	2568
Woman Lake	WM15	0.541	0.920	0.109	0.429	0.092	0.037	0.099	0.016	0.091	0.021	0.066	0.010	0.057	0.010	14.27	65159	6889	8073	2672
Woman Lake	WM16-x	0.530	0.829	0.088	0.310	0.052	0.055	0.076	0.012	0.077	0.020	0.067	0.010	0.064	0.012	2.66	57550	5872	6565	2015
Woman Lake	WM16-y	0.222	0.292	0.029	0.105	0.019	0.010	0.028	0.005	0.029	0.008	0.027	0.004	0.025	0.005	4.09	45435	4967	5140	1974
Woman Lake	WM16-z	0.878	1.072	0.117	0.467	0.079	0.026	0.123	0.020	0.130	0.035	0.109	0.015	0.087	0.016	2.89	41400	1152	7309	1400

Location	Sample	La	Ce	Pr	Nd	Sm	Eu	Gd	Tb	Dy	Ho	Er	Tm	Yb	Lu	Al	Ca	Fe	Mn	Mg
Woman Lake	WM17	0.603	0.831	0.079	0.259	0.039	0.020	0.051	0.007	0.033	0.007	0.022	0.003	0.018	0.003	3.10	37694	4336	4288	1495
Woman Lake	WM18	0.402	0.649	0.071	0.280	0.056	0.022	0.072	0.013	0.082	0.020	0.066	0.010	0.063	0.012	4.45	33032	3189	5893	873
Woman Lake	WM21	0.466	0.375	0.033	0.126	0.021	0.015	0.036	0.006	0.036	0.010	0.031	0.004	0.024	0.004	2.47	42540	3815	4257	1474
Woman Lake	WM23-x	0.334	0.478	0.055	0.237	0.062	0.039	0.082	0.017	0.117	0.030	0.099	0.015	0.090	0.016	1.81	46390	1852	1256	2177
Woman Lake	WM23-y	0.231	0.244	0.025	0.102	0.023	0.021	0.039	0.007	0.050	0.015	0.050	0.007	0.043	0.008	1.43	42663	1740	1217	1530
Woman Lake	WM55x	7.590	11.295	1.272	4.776	0.840	0.311	1.108	0.183	1.107	0.278	0.864	0.125	0.762	0.139	27.37	63762	3942	17606	3426
Woman Lake	WM55y	5.345	7.956	0.915	3.409	0.610	0.183	0.801	0.136	0.849	0.228	0.763	0.112	0.707	0.128	14.83	36230	3687	11873	4883
Woman Lake	WM58x	0.273	0.327	0.034	0.135	0.026	0.013	0.038	0.007	0.049	0.014	0.047	0.008	0.047	0.009	2.63	50939	5604	5225	1878
Woman Lake	WM58y	1.234	1.345	0.136	0.529	0.082	0.033	0.145	0.023	0.155	0.043	0.135	0.017	0.097	0.018	4.16	55160	2121	9676	1686
Woman Lake	WM58z	0.147	0.193	0.023	0.102	0.021	0.008	0.035	0.007	0.048	0.014	0.044	0.006	0.036	0.007	2.21	5707	148	964	107
Woman Lake	WM60	4.943	9.220	0.999	3.462	0.561	0.149	0.675	0.093	0.470	0.107	0.323	0.048	0.310	0.055	38.35	16905	6436	7056	13803
Woman Lake	WM63	2.071	2.947	0.352	1.424	0.281	0.063	0.393	0.072	0.494	0.131	0.418	0.061	0.388	0.072	31.98	13134	7300	9659	18130
Woman Lake	WM64	2.818	4.228	0.478	1.837	0.334	0.110	0.432	0.072	0.423	0.107	0.330	0.046	0.280	0.052	9.81	41625	2794	8718	2473
Woman Lake	X-16-R	1.582	1.578	0.221	0.897	0.184	0.052	0.293	0.055	0.389	0.116	0.396	0.058	0.349	0.071	14.17	96409	1711	19521	4741
Woman Lake	X-19-M	0.975	0.852	0.107	0.413	0.068	0.052	0.114	0.018	0.127	0.037	0.124	0.017	0.095	0.019	10.38	127961	1366	10718	3078
Woman Lake	X-20-M	2.460	3.475	0.493	2.242	0.550	0.212	0.857	0.176	1.261	0.336	1.093	0.163	1.023	0.193	676.96	248553	3812	19515	10451
Woman Lake	X-20-N	1.054	1.273	0.165	0.664	0.128	0.067	0.198	0.034	0.236	0.063	0.202	0.029	0.165	0.031	12.28	101634	1622	8944	2845
Woman Lake	X-21-M	0.551	0.366	0.062	0.261	0.048	0.022	0.091	0.015	0.113	0.036	0.124	0.016	0.090	0.018	15.17	84844	735	8027	1904
Woman Lake	X-21-N	0.874	0.797	0.123	0.500	0.091	0.027	0.142	0.022	0.149	0.043	0.140	0.020	0.114	0.022	39.34	86211	774	8884	2572
Woman Lake	X-23-X	0.441	0.259	0.049	0.205	0.035	0.016	0.067	0.011	0.084	0.027	0.098	0.014	0.079	0.016	4.72	70021	754	7059	1705
Woman Lake	X-24A-M	0.708	0.442	0.064	0.251	0.041	0.024	0.074	0.011	0.078	0.024	0.082	0.011	0.058	0.011	4.32	147883	1420	15226	3629
Woman Lake	X10A-x	0.551	0.371	0.056	0.232	0.043	0.021	0.077	0.014	0.103	0.030	0.100	0.014	0.082	0.017	2.40	69423	1557	7902	3979
Woman Lake	X10A-y	0.729	0.488	0.072	0.294	0.056	0.025	0.095	0.017	0.120	0.035	0.113	0.016	0.093	0.018	3.92	71053	1376	8120	4085
Woman Lake	X10B-Q	0.739	0.593	0.083	0.348	0.069	0.030	0.121	0.023	0.160	0.046	0.150	0.021	0.125	0.024	9.07	77136	1902	11866	2955
Woman Lake	X10B-R	0.870	0.701	0.087	0.345	0.060	0.033	0.104	0.018	0.122	0.034	0.113	0.015	0.089	0.018	2.23	68828	1482	10337	2370
Woman Lake	X10B-S	1.099	0.905	0.116	0.466	0.087	0.045	0.144	0.026	0.178	0.050	0.163	0.023	0.136	0.026	4.11	71437	1764	11381	2709
Woman Lake	X10B-t	1.662	1.573	0.200	0.806	0.157	0.072	0.253	0.046	0.318	0.088	0.287	0.041	0.240	0.047	2.61	84016	1531	9263	4172
Woman Lake	X10B-u	1.131	1.268	0.165	0.672	0.142	0.059	0.215	0.042	0.283	0.077	0.248	0.036	0.216	0.042	2.64	72564	1253	8996	2208
Woman Lake	X10B-v	2.503	2.902	0.361	1.419	0.276	0.107	0.391	0.073	0.466	0.120	0.379	0.053	0.309	0.057	3.13	90020	2563	15820	4652
Woman Lake	X10B-w	1.334	1.672	0.217	0.925	0.215	0.074	0.330	0.070	0.486	0.133	0.439	0.065	0.390	0.075	7.66	82446	1771	14193	3056
Woman Lake	X12	0.622	0.678	0.097	0.430	0.100	0.041	0.166	0.038	0.301	0.089	0.303	0.044	0.262	0.048	11.88	84760	1243	14711	889
Woman Lake	X14-x	1.210	0.744	0.118	0.459	0.077	0.035	0.136	0.023	0.157	0.047	0.154	0.021	0.120	0.023	5.66	71355	1307	10250	4539
Woman Lake	X14-y	1.821	1.278	0.199	0.796	0.144	0.056	0.242	0.042	0.296	0.089	0.299	0.041	0.244	0.049	7.73	97933	1532	13624	4686
Woman Lake	X16-Q	1.215	1.140	0.156	0.595	0.104	0.032	0.152	0.024	0.154	0.042	0.134	0.019	0.107	0.020	5.39	69165	1148	13591	3596
Woman Lake	X18	1.503	0.928	0.150	0.627	0.115	0.052	0.198	0.034	0.238	0.070	0.229	0.032	0.186	0.037	3.44	80258	1735	9858	5073
Woman Lake	X19-x	2.249	2.256	0.306	1.242	0.224	0.107	0.332	0.059	0.383	0.105	0.343	0.047	0.277	0.053	2.35	108558	2055	19125	4382
Woman Lake	X19-y	2.096	2.204	0.309	1.338	0.302	0.083	0.466	0.097	0.681	0.191	0.635	0.091	0.556	0.107	5.86	137052	2527	21836	5536
Woman Lake	X2	1.662	1.589	0.216	0.845	0.165	0.082	0.246	0.046	0.301	0.080	0.253	0.035	0.201	0.038	6.59	90047	2768	15754	4899
Woman Lake	X20-x	2.180	2.710	0.331	1.329	0.247	0.135	0.372	0.067	0.450	0.122	0.396	0.057	0.335	0.064	4.94	78319	2139	13967	3578
Woman Lake	X20-y	2.917	3.394	0.406	1.599	0.290	0.177	0.458	0.084	0.563	0.152	0.494	0.070	0.416	0.079	4.47	94458	2794	17973	4375

Location	Sample	La	Ce	Pr	Nd	Sm	Eu	Gd	Tb	Dy	Ho	Er	Tm	Yb	Lu	Al	Ca	Fe	Mn	Mg
Woman Lake	X21-x	NaN	NaN	NaN	NaN	NaN	NaN	NaN	NaN	NaN	NaN	NaN	NaN	NaN	NaN	NaN	NaN	4	NaN	NaN
Woman Lake	x21-y	1.274	0.985	0.127	0.491	0.083	0.039	0.127	0.020	0.122	0.035	0.114	0.016	0.090	0.018	3.28	70432	1169	14261	3272
Woman Lake	X21-z	3.629	3.720	0.469	1.859	0.339	0.092	0.483	0.077	0.480	0.129	0.419	0.056	0.327	0.063	5.58	96292	1526	15528	3423
Woman Lake	X23B	1.231	1.023	0.133	0.525	0.089	0.042	0.136	0.021	0.134	0.038	0.125	0.017	0.098	0.020	5.21	70252	1409	14204	3286
Woman Lake	X23C	1.760	1.415	0.224	0.910	0.174	0.049	0.287	0.052	0.371	0.113	0.386	0.055	0.334	0.066	9.51	70816	1570	14975	4451
Woman Lake	X23D-x	1.013	0.358	0.088	0.377	0.069	0.037	0.138	0.026	0.203	0.064	0.225	0.032	0.190	0.038	6.05	77270	1722	15737	2631
Woman Lake	X23D-y	1.361	0.321	0.106	0.481	0.088	0.044	0.183	0.035	0.272	0.087	0.302	0.042	0.249	0.051	4.03	88790	1658	20340	3559
Woman Lake	X23E-w	0.882	0.209	0.069	0.312	0.056	0.030	0.121	0.023	0.180	0.059	0.212	0.030	0.176	0.036	1.77	57354	1169	12565	1967
Woman Lake	X23E-x	1.069	0.265	0.086	0.383	0.070	0.035	0.144	0.026	0.202	0.064	0.222	0.031	0.183	0.037	1.35	58324	1157	13276	2157
Woman Lake	X23E-y	1.236	0.347	0.106	0.479	0.090	0.042	0.188	0.037	0.294	0.098	0.353	0.050	0.294	0.060	1.69	71520	1406	15190	2437
Woman Lake	X23E-z	1.119	0.354	0.099	0.440	0.085	0.038	0.169	0.032	0.253	0.081	0.281	0.039	0.233	0.046	1.41	61146	1186	12565	2354
Woman Lake	X24-Q	1.524	1.468	0.203	0.814	0.156	0.067	0.247	0.043	0.297	0.086	0.286	0.040	0.236	0.047	2.81	57193	1062	11559	1375
Woman Lake	X24-Q	4.603	5.013	0.593	2.378	0.440	0.149	0.650	0.111	0.695	0.191	0.620	0.085	0.500	0.097	10.55	69971	1091	9762	2538
Woman Lake	X24-R	2.740	1.862	0.277	1.132	0.191	0.090	0.326	0.055	0.388	0.119	0.400	0.056	0.328	0.066	3.12	100352	1930	19939	3352
Woman Lake	X24-S	2.458	1.558	0.244	0.952	0.161	0.074	0.287	0.051	0.387	0.131	0.477	0.068	0.401	0.083	7.99	85754	1789	18120	3257
Woman Lake	X24-t	2.822	2.219	0.313	1.240	0.218	0.098	0.345	0.057	0.388	0.114	0.386	0.054	0.319	0.064	4.80	89739	1688	18279	3154
Woman Lake	X24-u	2.223	1.905	0.262	1.060	0.189	0.080	0.298	0.050	0.333	0.098	0.325	0.045	0.270	0.053	5.43	66104	1282	12574	2509
Woman Lake	X24-v	2.106	1.999	0.268	1.087	0.205	0.078	0.322	0.057	0.392	0.110	0.366	0.053	0.318	0.063	2.96	51634	918	11302	1583
Woman Lake	X24-x	3.021	2.618	0.324	1.320	0.244	0.093	0.396	0.067	0.442	0.122	0.395	0.055	0.330	0.066	4.51	46589	857	4254	2928
Woman Lake	X24A-R	0.923	0.756	0.110	0.460	0.087	0.032	0.145	0.026	0.176	0.052	0.172	0.025	0.145	0.028	5.12	49480	667	9169	1240
Woman Lake	X24A-S	1.196	0.810	0.106	0.412	0.068	0.034	0.118	0.019	0.126	0.037	0.126	0.017	0.098	0.020	3.17	74352	1442	15504	3031
Woman Lake	X24A-t	1.189	0.811	0.126	0.519	0.095	0.039	0.161	0.028	0.197	0.060	0.200	0.028	0.162	0.033	5.64	79462	1807	16929	3914
Woman Lake	X24A-W	1.076	0.676	0.089	0.347	0.058	0.028	0.104	0.017	0.111	0.034	0.111	0.015	0.084	0.017	2.53	61820	1055	9612	2557
Woman Lake	X29	1.256	1.725	0.218	0.868	0.183	0.039	0.249	0.045	0.299	0.082	0.280	0.043	0.285	0.056	25.87	14060	6275	6275	19299
Woman Lake	X3-Q	20.228	33.678	3.177	9.636	1.144	0.236	1.467	0.157	0.675	0.147	0.422	0.061	0.366	0.063	32.26	94486	4505	22185	13013
Woman Lake	X3-R	1.093	1.929	0.230	0.951	0.194	0.068	0.269	0.048	0.321	0.083	0.263	0.037	0.220	0.039	4.57	31132	432	7278	447
Woman Lake	X30	1.504	1.388	0.186	0.758	0.139	0.063	0.218	0.037	0.247	0.068	0.226	0.031	0.185	0.037	5.67	50237	2307	9734	5024
Woman Lake	X31	1.672	1.884	0.233	0.926	0.171	0.087	0.255	0.045	0.290	0.079	0.254	0.036	0.211	0.040	4.44	63125	2659	12846	3372
Woman Lake	X32	2.721	2.423	0.340	1.345	0.239	0.116	0.367	0.060	0.392	0.111	0.360	0.051	0.296	0.058	7.11	58441	2845	14371	4189
Woman Lake	X33	2.409	2.151	0.312	1.255	0.229	0.094	0.347	0.060	0.403	0.116	0.400	0.056	0.334	0.067	21.95	77089	3244	18172	5333
Woman Lake	X34	0.784	0.314	0.073	0.310	0.058	0.028	0.109	0.019	0.140	0.043	0.148	0.021	0.120	0.025	1.84	52491	1823	7175	2898
Woman Lake	X6-Q	6.175	10.285	1.172	4.336	0.725	0.179	0.921	0.151	0.927	0.253	0.825	0.117	0.695	0.131	26.31	95849	2824	28577	3300
Woman Lake	X6-R	4.838	9.506	1.029	3.633	0.616	0.134	0.744	0.118	0.712	0.201	0.729	0.116	0.774	0.147	75.73	69196	1554	22839	1700
Woman Lake	X6-S	4.588	8.704	0.943	3.359	0.570	0.118	0.702	0.116	0.724	0.195	0.652	0.098	0.603	0.108	36.17	62714	1388	21325	1590
Woman Lake	X8-x	1.459	1.385	0.159	0.629	0.114	0.059	0.190	0.033	0.218	0.060	0.190	0.026	0.147	0.028	3.78	104849	2608	15993	4713
Woman Lake	X8-y	0.193	0.240	0.031	0.135	0.031	0.011	0.050	0.010	0.077	0.023	0.081	0.013	0.085	0.018	7.92	22737	631	3964	562
Steep Rock	8-20	2.980	5.577	0.632	2.451	0.552	0.194	0.676	0.106	0.565	0.113	0.299	0.042	0.258	0.041	78.07	123564	10767	2844	77737
Steep Rock	8-21 (1)	0.244	0.301	0.034	0.129	0.024	0.011	0.034	0.005	0.034	0.009	0.028	0.004	0.025	0.005	79.25	266914	12763	7034	29729
Steep Rock	8-21 (2)	0.235	0.289	0.033	0.127	0.024	0.011	0.034	0.005	0.034	0.009	0.028	0.004	0.026	0.005	40.82	223122	6310	4678	13517
Steep Rock	8-24	0.092	0.074	0.008	0.034	0.006	0.005	0.011	0.002	0.013	0.004	0.014	0.002	0.012	0.003	3.85	344928	3557	6560	1749

Location	Sample	La	Ce	Pr	Nd	Sm	Eu	Gd	Tb	Dy	Ho	Er	Tm	Yb	Lu	Al	Ca	Fe	Mn	Mg
Steep Rock	8-25	0.021	0.022	0.002	0.010	0.002	0.001	0.003	NaN	0.003	0.001	0.003	0.001	0.002	0.001	8.95	273290	2818	3478	1339
Steep Rock	8-26	0.194	0.084	0.017	0.074	0.013	0.009	0.031	0.005	0.038	0.013	0.045	0.007	0.038	0.008	5.69	385812	2128	4928	3274
Steep Rock	8-44A	0.644	0.593	0.069	0.269	0.043	0.029	0.068	0.009	0.053	0.016	0.053	0.008	0.047	0.010	27.46	198373	8343	6526	60591
Steep Rock	8-44A (2)	0.892	0.816	0.096	0.377	0.061	0.040	0.097	0.012	0.076	0.022	0.077	0.011	0.067	0.014	35.29	265414	11278	8503	81611
Steep Rock	8-44B	0.381	0.349	0.041	0.161	0.026	0.017	0.041	0.005	0.033	0.010	0.034	0.005	0.029	0.006	20.15	118713	5476	4493	43506
Steep Rock	8-31	0.193	0.054	0.014	0.059	0.010	0.013	0.020	0.003	0.022	0.007	0.025	0.004	0.020	0.004	3.10	362974	392	448	1667
Steep Rock	8-32	0.315	0.215	0.030	0.128	0.023	0.009	0.044	0.007	0.052	0.017	0.060	0.009	0.050	0.010	5.54	304406	2126	6926	1875
Steep Rock	8-33	0.118	0.060	0.007	0.028	0.004	0.005	0.010	NaN	0.011	0.004	0.014	0.002	0.012	0.003	65.42	279028	937	875	6346
Steep Rock	SR-1A	0.438	0.238	0.021	0.088	0.012	0.030	0.032	0.005	0.037	0.014	0.052	0.008	0.045	0.010	3.35	310273	687	269	904
Steep Rock	SR-1B	0.535	0.356	0.039	0.173	0.027	0.024	0.058	0.009	0.066	0.020	0.069	0.010	0.055	0.011	3.22	271239	916	493	1252
Steep Rock	SR-2A	0.486	0.143	0.046	0.214	0.040	0.018	0.083	0.013	0.098	0.029	0.095	0.013	0.075	0.014	5.47	293936	1176	2188	2180
Steep Rock	SR-2B	0.548	0.307	0.052	0.232	0.043	0.019	0.085	0.014	0.103	0.032	0.107	0.015	0.089	0.017	8.93	313520	1585	5599	1604
Steep Rock	SR-2AX	0.495	0.169	0.046	0.215	0.041	0.017	0.082	0.013	0.101	0.030	0.100	0.014	0.083	0.016	3.43	303991	1273	1988	2113
Steep Rock	SR-5A	0.155	0.118	0.012	0.054	0.010	0.008	0.020	0.003	0.024	0.008	0.026	0.004	0.023	0.004	5.58	252967	1914	2067	2568
Steep Rock	SR-5B	0.255	0.198	0.022	0.097	0.018	0.009	0.036	0.006	0.046	0.014	0.050	0.007	0.044	0.009	1.74	232487	1599	5540	1294
Steep Rock	SR-7	0.158	0.111	0.013	0.053	0.009	0.005	0.018	0.003	0.021	0.008	0.025	0.004	0.021	0.005	3.46	291921	1569	3176	2498
Steep Rock	SR-9	0.038	0.020	0.002	0.009	0.001	0.001	0.004	NaN	0.004	0.002	0.007	0.001	0.006	0.001	2.32	205728	3623	3388	10559
Steep Rock	SR-10	0.037	0.017	0.002	0.008	NaN	0.002	0.003	NaN	0.004	0.002	0.006	0.001	0.005	0.001	2.24	219907	3931	2986	12646
Steep Rock	SR-16	0.268	0.097	0.024	0.107	0.020	0.011	0.041	0.007	0.051	0.016	0.054	0.007	0.044	0.009	4.59	363127	841	1038	3494
Steep Rock	SR-18A	1.121	0.988	0.142	0.589	0.109	0.040	0.169	0.026	0.174	0.051	0.169	0.024	0.138	0.027	6.01	346775	1861	6040	2537
Steep Rock	SR-18B	0.219	0.128	0.021	0.091	0.016	0.008	0.030	0.005	0.035	0.011	0.036	0.005	0.030	0.006	5.18	233537	2046	1411	3593
Steep Rock	SR-19 (1)	0.115	0.067	0.008	0.032	0.005	0.004	0.011	0.001	0.011	0.004	0.015	0.002	0.012	0.003	10.05	270911	1031	1358	2202
Steep Rock	SR-19 (2)	0.115	0.067	0.008	0.032	0.005	0.004	0.011	0.002	0.012	0.004	0.015	0.002	0.013	0.003	2.71	258585	1075	1377	2700
Steep Rock	SR-20A	0.171	0.091	0.013	0.054	0.009	0.005	0.019	0.003	0.023	0.008	0.028	0.004	0.024	0.005	3.61	282823	1331	3297	3285
Steep Rock	SR-20B	0.272	0.136	0.018	0.081	0.013	0.009	0.030	0.005	0.037	0.013	0.046	0.006	0.038	0.008	3.87	350043	1625	921	5445
Steep Rock	SR-20C	0.173	0.106	0.014	0.062	0.011	0.005	0.020	0.003	0.022	0.007	0.025	0.004	0.021	0.004	3.22	235525	1681	3575	1676

<u>Appendix B.2.</u> REE, Al, Ca, Fe, Mn and Mg concentrations (ppm) of Red Lake, Woman Lake and Steep Rock selected and analyzed for La-Ce geochronology.

Location	Sample	La	Ce	Pr	Nd	Sm	Eu	Gd	Tb	Dy	Ho	Er	Tm	Yb	Lu	Al	Ca	Fe	Mn	Mg
Red Lake	17-GA1-11	3.556	3.683	0.510	2.218	0.492	0.232	0.764	0.121	0.825	0.231	0.803	0.124	0.835	0.165	1.981	483979	11421	5414	2003
Red Lake	17-GA1-12	4.390	4.331	0.590	2.504	0.521	0.261	0.802	0.122	0.820	0.230	0.785	0.119	0.778	0.153	1.461	496056	13762	6018	2596
Red Lake	17-GA1-13	2.718	2.590	0.355	1.534	0.334	0.176	0.520	0.083	0.562	0.158	0.534	0.076	0.485	0.094	1.632	336926	10186	3989	3616
Red Lake	17-GA1-14	1.926	1.665	0.247	1.099	0.253	0.164	0.438	0.069	0.497	0.144	0.487	0.069	0.454	0.086	1.232	308441	8197	3647	1444
Red Lake	17-GA1-16	4.033	3.090	0.486	2.115	0.435	0.203	0.715	0.104	0.720	0.209	0.722	0.111	0.765	0.156	0.308	348290	8324	3850	3678
Red Lake	17-GA1-17	4.819	3.406	0.533	2.271	0.447	0.200	0.752	0.110	0.757	0.223	0.780	0.118	0.811	0.166	0.588	356706	9892	3994	4845
Red Lake	17-GA1-18	1.997	1.291	0.212	0.967	0.226	0.115	0.457	0.074	0.547	0.167	0.583	0.085	0.556	0.113	0.000	282907	2971	2565	652
Red Lake	17GA1-19	2.228	1.320	0.223	1.103	0.287	0.165	0.609	0.099	0.757	0.237	0.835	0.121	0.789	0.162	0.000	387680	4931	3542	1358
Red Lake	17GA1-20	0.903	0.817	0.144	0.729	0.175	0.188	0.305	0.046	0.314	0.085	0.256	0.032	0.174	0.029	0.962	435768	4551	2627	2073
Red Lake	17GA1-21	0.989	0.982	0.163	0.763	0.151	0.209	0.233	0.032	0.198	0.050	0.144	0.017	0.093	0.015	0.701	433195	4581	2540	2348
Red Lake	17GA1-33	0.806	1.310	0.150	0.610	0.117	0.133	0.149	0.022	0.144	0.035	0.112	0.015	0.096	0.016	0.290	307516	5404	2475	1597
Woman Lake	A-20A	1.922	1.556	0.304	1.242	0.248	0.059	0.379	0.065	0.441	0.112	0.344	0.050	0.316	0.060	2.311	176139	1114	4601	1866
Woman Lake	A-32	0.514	0.278	0.058	0.256	0.053	0.021	0.109	0.018	0.139	0.041	0.138	0.020	0.115	0.023	0.121	302540	1390	8826	2111
Woman Lake	A-36B	0.692	0.591	0.107	0.492	0.115	0.038	0.200	0.036	0.261	0.070	0.231	0.034	0.211	0.039	0.000	331445	1652	8152	2979
Woman Lake	A-38A	0.519	0.233	0.057	0.257	0.054	0.023	0.130	0.022	0.171	0.055	0.191	0.027	0.157	0.032	0.985	305224	1418	8523	3643
Woman Lake	A-43	0.463	0.244	0.047	0.195	0.033	0.020	0.069	0.011	0.079	0.024	0.082	0.011	0.067	0.013	0.000	327758	1842	8073	3727
Woman Lake	A-52B	0.725	0.426	0.072	0.290	0.050	0.027	0.092	0.014	0.097	0.028	0.091	0.013	0.073	0.014	0.707	256946	950	5368	2568
Woman Lake	B-5	0.875	0.945	0.128	0.532	0.107	0.053	0.154	0.025	0.183	0.045	0.143	0.021	0.120	0.020	0.000	323820	2251	6987	2618
Woman Lake	X23D-y	0.672	0.163	0.057	0.261	0.048	0.023	0.111	0.018	0.142	0.046	0.158	0.022	0.130	0.026	0.659	387886	1212	12321	2735
Woman Lake	X23E-y	0.608	0.174	0.055	0.258	0.046	0.022	0.115	0.019	0.153	0.051	0.179	0.026	0.153	0.031	0.000	283238	968	8994	1798
Woman Lake	X23E-z	0.906	0.300	0.087	0.396	0.074	0.033	0.168	0.027	0.216	0.070	0.240	0.034	0.196	0.039	0.000	384082	1228	12542	2659
Woman Lake	X34	0.688	0.284	0.068	0.287	0.053	0.025	0.108	0.017	0.126	0.038	0.130	0.018	0.104	0.021	0.646	411325	2260	8445	4325
Steep Rock	8-26	0.554	0.186	0.045	0.200	0.035	0.024	0.086	0.014	0.111	0.037	0.133	0.019	0.112	0.023	0.987	323927	1326	3147	2635
Steep Rock	8-31	0.688	0.407	0.069	0.296	0.052	0.024	0.108	0.016	0.124	0.038	0.128	0.018	0.101	0.020	4.367	409739	2574	4560	2457
Steep Rock	8-32	0.616	0.165	0.040	0.174	0.027	0.027	0.056	0.008	0.061	0.020	0.070	0.010	0.054	0.011	0.055	357077	610	815	2206
Steep Rock	SR-2A	1.667	0.457	0.159	0.732	0.135	0.060	0.286	0.045	0.336	0.100	0.327	0.046	0.258	0.050	1.210	401037	1360	2266	2512
Steep Rock	SR-16	0.909	0.690	0.102	0.416	0.077	0.036	0.130	0.021	0.149	0.045	0.153	0.022	0.127	0.026	2.673	331578	2415	3490	3486
Steep Rock	SR-18A	3.178	2.733	0.400	1.692	0.302	0.083	0.478	0.076	0.553	0.165	0.582	0.086	0.515	0.102	0.000	316239	1175	4348	1578
Steep Rock	SR-18B	1.254	0.674	0.128	0.552	0.099	0.042	0.189	0.030	0.219	0.068	0.227	0.032	0.184	0.037	1.393	406019	1267	1728	3338

Appendix B.3. **Mg/Ca ratios (A) and Sr concentrations (B) plotted against Y/Ho ratios.**

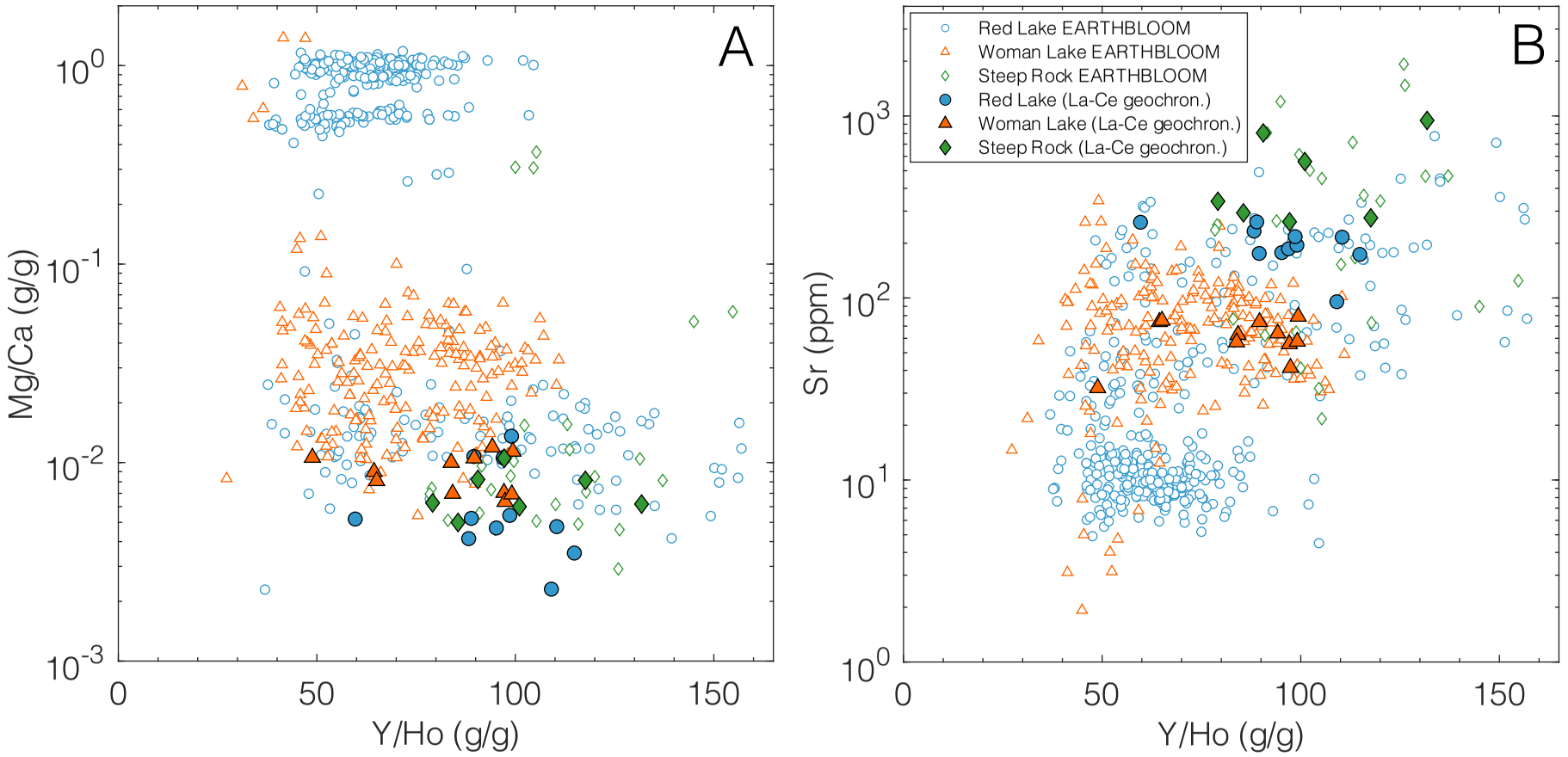

APPENDIX C:

Appendix to chapter 6

Appendix C.1. La-Ce isotope compositions for carbonates from Red Lake, Woman Lake and Steep Rock. Uncertainties are 0.00035707 (2σ) for $^{138}La/^{142}Ce$, 0.00000014 (2σ) for $^{138}Ce/^{142}Ce$, and 0.12 (2σ) for $\varepsilon^{138}Ce_{initial}$.

Location	Sample Name	Ce/Ce*	$^{138}La/^{142}Ce$	$^{138}Ce/^{142}Ce$	$^{138}Ce/^{142}Ce_{initial}$	$\varepsilon^{138}Ce_{initial}$
Red Lake	17-GA1-11	0.922	0.0077322	0.0225987	0.0225471	0.90
	17-GA1-13	0.925	0.0084034	0.0226027	0.0225465	0.67
	17-GA1-14	0.885	0.0092640	0.0226095	0.0225476	1.14
	17-GA1-17	0.797	0.0113288	0.0226222	0.0225465	0.66
	17-GA1-18	0.835	0.0123906	0.0226462	0.0225634	8.14
	17-GA1-19	0.918	0.0135155	0.0226301	0.0225398	-2.31
	17-GA1-33	1.025	0.0049252	0.0225796	0.0225467	0.75
Woman Lake	A-20A	0.605	0.0098944	0.0225814	0.0225135	-13.97
	A-36B	0.767	0.0093683	0.0226086	0.0225443	-0.31
	A-43	0.638	0.0151787	0.0226471	0.0225430	-0.92
	A-52B	0.696	0.0136141	0.0226338	0.0225405	-2.03
	X23E-z	0.472	0.0241517	0.0227089	0.0225433	-0.78
	X34	0.515	0.0193946	0.0226978	0.0225648	8.77
Steep Rock	8-31	0.752	0.0135436	0.0226370	0.0225468	0.80
	SR2A	0.398	0.0292293	0.0227409	0.0225462	0.52
	SR16	0.804	0.0105533	0.0226152	0.0225449	-0.04
	SR18A	0.844	0.0093126	0.0226094	0.0225473	1.03
	SR18B	0.668	0.0148994	0.0226430	0.0225438	-0.56

Appendix C.2. Isochron data (slope, MSWD, Age, $\varepsilon^{138}Ce_{initial}$) for Red Lake, Woman Lake, Steep Rock and the three sites combined.

Isochrones	n=	Slope	Slope error	MSWD	Intercept	Intercept error	Age (Ga)	± (Ga)	$^{138}Ce/^{142}Ce_{CHUR\ t}$	$\varepsilon\ ^{138}Ce_{initial}$
All three sites	18	0.00742	0.00011	64	0.0225364	0.0000016	3.10	0.05	0.0225427	-2.78
All three sites (without outliers)	14	0.00666	0.00010	1.5	0.0225463	0.0000015	2.78	0.04	0.0225450	0.56
Red Lake	5	0.00668	0.00051	0.19	0.0225469	0.0000044	2.79	0.21	0.0225450	0.86
Woman Lake	4	0.00686	0.00023	2.7	0.0225427	0.0000038	2.87	0.10	0.0225444	-0.76
Steep Rock	5	0.00666	0.00015	2	0.0225458	0.0000025	2.78	0.06	0.0225450	0.34

Appendix C.3. Results of the radiogenic Ce isotopic compositions of the reference materials Ce LMV (n=11) and two rock reference materials JDo-1 (n=3) and BHVO-2 (n=3).

Sample	$^{138}Ce/^{142}Ce$	2σ
Ce LMV	0.02256992	0.00000021
Ce LMV	0.02256967	0.00000023
Ce LMV	0.02256973	0.00000023
Ce LMV	0.02257032	0.00000029
Ce LMV	0.02257010	0.00000027
Ce LMV	0.02256979	0.00000021
Ce LMV	0.02256993	0.00000045
Ce LMV	0.02256941	0.00000029
Ce LMV	0.02256968	0.00000020
Ce LMV	0.02256984	0.00000019
Ce LMV	0.02256974	0.00000022
JDo-1	0.02258475	0.00000030
JDo-1	0.02258422	0.00000023
JDo-1	0.02258491	0.00000030
BHVO-2	0.02256335	0.00000024
BHVO-2	0.02256344	0.00000018
BHVO-2	0.02256333	0.00000023

DOCTORAT SCIENCES BRETAGNE DE LA MER LOIRE ET DU LITTORAL

UBO Université de Bretagne Occidentale

Titre : Contraindre l'évolution précoce des voies photosynthétiques de la Terre : une approche isotopique

Mots clés : Archéen, photosynthèse, oxygène, géochronologie La-Ce

Résumé : Ce travail de thèse s'est concentré sur de nouvelles signatures géochimiques et isotopiques préservées dans des roches sédimentaires chimiques et d'autres sédiments marins du Craton Supérieur canadien, déposés entre 2,93 et 2,8 Ga, afin de mieux comprendre l'évolution des voies photosynthétiques sur la Terre primitive.
La chimiostratigraphie isotopique du fer des carbonates stromatolithiques et des sédiments d'eaux profondes préservés dans une carotte de la ceinture de schistes verts de Red Lake (2,93 Ga) révèle un cycle complexe d'oxydoréduction du fer sur un transect de faible profondeur à grande profondeur, avec un couplage entre le cycle du fer et du soufre qui est mieux expliqué par l'activité photosynthétique marine.
Les données de REE de trois plateformes carbonatées (2,93 Ga Red Lake, 2,86 Ga Woman Lake et 2,80 Ga Steep Rock Lake) représentant les plus anciennes plateformes carbonatées épaisses connues sur Terre, fournissent des preuves de processus estuariens, d'apports hydrothermaux et, surtout, de la production d'oxygène libre, comme le montrent d'importantes anomalies négatives en Ce d'une ampleur sans précédent pour l'Archéen. La géochronologie La-Ce de haute précision a été appliquée avec succès aux échantillons des trois sites, produisant trois isochrones claires qui datent le fractionnement La/Ce, et donc l'oxydation du Ce, au moment du dépôt.

Title : Constraining the Early Evolution of Earth's Photosynthetic Pathways: An Isotopic Approach

Keywords : Archean, photosynthesis, oxygen, La-Ce geochronology

Abstract : This PhD work focused on novel geochemical and isotopic signatures preserved in chemical sedimentary rocks and other marine sediments from the Canadian Superior Craton, deposited between 2.93 and 2.8 Ga, to better understand the evolution of photosynthetic pathways on the early Earth. Iron isotope chemostratigraphy of stromatolitic carbonates and deep-water sediments preserved in drill core from the 2.93 Ga Red Lake Greenstone Belt reveals complex iron redox cycling across a shallow-to-deep transect, with coupling between Fe and S cycling that is best explained by offshore photosynthetic activity. Comparative REE systematics of three Mesoarchean carbonate platforms of the Superior Craton (2.93 Ga Red Lake, 2.86 Ga Woman Lake, and 2.80 Ga Steep Rock Lake) and representing Earth's earliest known large carbonate platforms, provide clear evidence for estuarine processes, hydrothermal inputs, and crucially, for the production of free oxygen, as tracked by important negative Ce anomalies of unprecedented magnitude for the Archean. High-precision La-Ce geochronology was successfully applied to samples from all three sites, yielding three clear isochrons that constrain the timing of La/Ce fractionation, and thus Ce oxidation, to the time of deposition. These results constitute the first geochronological constraint on the origin of oxygenic photosynthesis and place it firmly within the Mesoarchean, with important implications for our current understanding of Earth's biological and geochemical evolution.